

The relevance of lipid droplet biogenesis to the hepatitis C virus replication organelle

DISSERTATION

Submitted to the department of Chemistry

Faculty of mathematics, informatics and natural sciences

University of Hamburg

With the aim of achieving a doctoral degree Doctor rerum naturalium

By

Isabelle Reichert

Hamburg, January 2024

First examiner	Prof. Dr. Kay Grünewald
Second examiner	Prof. Dr. Caroline Barisch
Examination committee	Prof. Dr. Kay Grünewald Prof. Dr. Caroline Barisch Prof. Dr. Wolfram Brune Dr. Gabrielle Vieyres Dr. Pietro Scaturro
Date of disputation	26 th of April 2024
Approval for publication	26 th of April 2024

The experimental work and preparation of this dissertation were performed (i) at the Institute of Experimental Virology, Twincore at the Hanover Medical School (MHH) from 19. August 2019 to 10. October 2020 and (ii) at the Leibniz Institute for Experimental Virology (LIV) at the University of Hamburg from 10th of October 2020 to 8th of January 2024 under supervision of Dr. Gabrielle Vieyres, Prof. Dr. Kay Grünewald, and Prof. Dr. Thomas Pietschmann.

I. List of publications

Vieyres G, Reichert I, Carpentier A, Vondran FWR, Pietschmann T. The ATGL lipase cooperates with ABHD5 to mobilize lipids for hepatitis C virus assembly. PLOS Pathogens. 2020 Jun 15;16(6):e1008554.

Reichert I, Lee J, Weber L, Fuh M, Schlaeger L, Rößler S, Kinast V, Schlienkamp S, Conradi J, Vondran F, Scaturro P, Steinmann E, Bartenschlager R, Pietschmann T, Heeren J, Lauber C, Vieyres G. Lipid droplet biogenesis modulates the formation of the hepatitis C virus replication organelle, *in preparation*.

M

m/v	Mass concentration
MBOAT	Membrane-bound O-acyltransferase
MeOH	Methanol
MFI	Mean fluorescence intensity
MGAT	Monoacylglycerol transferase
μM	Micromolar
mM	Millimolar
MMV	Multimembrane vesicle
MOI	Multiplicity of infection
mRNA	Messenger RNA
MTBE	Methyl-tert-butyl-ester
MTT	3-(4,5-Dimethylthiazol-2-yl)-2,5-diphenyltetrazoliumbromid
MUFA	Monounsaturated fatty acid

N

NBD	Nitrobenzoxadiazole
nM	Nanomolar
NS	Non-structural
NTP	Nucleoside triphosphate

O

OA	Oleic acid
ORF	Open reading frame
OSBP	Oxysterol binding protein

P

PA	Phosphatidic acid
PAGE	Polyacrylamide gel electrophoresis
PBS	Phosphate buffered saline
PBST	PBS-Tween
PC	Phosphatidylcholine
PCR	Polymerase chain reaction
PE	Phosphatidylethanolamine
PEI	Polyethylenimine
PFA	Paraformaldehyde
PFU	Plaque forming unit
PI	Phosphatidylinositol
PI4P	Phosphatidylinositol-4-phosphate
PKCε	Protein kinase C epsilon
PL	Phospholipid
PUFA	Polyunsaturated fatty acid

R

RLU	Relative light unit
RNA	Ribonucleic acid
RO	Replication organelle
RT-qPCR	Reverse transcription quantitative real-time PCR

S

SARS-CoV-2	Severe acute respiratory syndrome coronavirus 2
SCD-1	Stearoyl-CoA 9-desaturase
SD	Standard deviation
SDS	Sodium dodecyl sulfate
SEM	Standard error of the mean
SFig.	Supplementary figure
SGR	Subgenomic replicon
shRNA	Small hairpin RNA
SL	Sphingolipid
SM	Sphingomyelin
+ssRNA	Positive-sense single-stranded RNA

T

TAG	Triacylglycerol
TBEV	Tick-borne encephalitis virus
TCID50	Tissue culture infection dose 50
TEM	Transmission electron microscopy
Tet	Tetracycline
Tet-O	Tet-operator
Tet-R	Tet-repressor

U

U	Unit
UFA	Unsaturated fatty acid
UTR	Untranslated region

V

v/v	Volume percent
-----	----------------

W

WB	Western blot
WHO	World health organization
WNV	West Nile virus

Z

ZIKV	Zika virus
------	------------

II. Table of contents

1. ZUSAMMENFASSUNG	1
2. ABSTRACT	2
3. INTRODUCTION	3
3.1. Hepatitis C Virus	3
3.2. Viral replication organelles	5
3.3. Lipids involved in the replication organelle formation	7
3.4. Lipid droplet biogenesis and functions	10
3.5. Diacylglycerol – O-acyltransferase (DGAT) proteins	12
3.6. Lipid droplet hijacking by HCV	15
3.7. Aim of this study	17
4. RESULTS	18
4.1. Characterization of the antiviral phenotype of DGAT expression	18
4.2. Cellular determinants of the DGAT2 antiviral activity	25
4.3. Viral determinants of the DGAT2 antiviral activity	41
4.4. Attempts to reverse the DGAT2 inhibitory phenotype	51
4.5. Effect of DGAT expression and HCV infection on the localization of host cell lipids	56
4.6. Changes of the host cell lipidome upon DGAT protein expression, OA treatment or HCV infection	64
5. DISCUSSION	78
5.1. HCV infection is inhibited by DGAT2-mediated LD biogenesis	78
5.2. DGAT1 overexpression has a mild effect on HCV infection	79
5.3. The localization of DGAT2 at LDs is not important for the antiviral phenotype	80
5.4. DGAT2 overexpression affects HCV replication and the formation of the HCV replication organelle	81
5.5. The inhibitory effect of DGAT2 expression is specific for HCV	82
5.6. The balance of neutral and membrane lipids is affected by DGAT protein expression and OA treatment	83
5.7. Re-localization of DAG is unlikely responsible for the antiviral effect of DGAT2	85
5.8. HCV infection and DGAT2 overexpression upregulate similar membrane lipid classes and highly unsaturated phospholipid species	85
5.9. DGAT2 overexpression depletes saturated and MUFA-PL-species, essential for the HCV RO formation	87
5.10. Model, conclusions and future outlook	89

6. MATERIALS.....	93
6.1. Nucleotides	93
6.2. Bacteria	94
6.3. Eukaryotic cell lines.....	95
6.4. Viruses.....	96
6.5. Antibodies	97
6.6. Buffers	98
6.7. Reagents and Kits.....	100
6.8. Software	102
7. METHODS	103
7.1. Molecular biology methods.....	103
7.2. Cell culture methods.....	111
7.3. Virological methods	113
7.4. Statistics	116
8. BIBLIOGRAPHY	117
9. SUPPLEMENTARY INFORMATION.....	134
9.1. Supplementary figures.....	134
9.2. List of toxic chemicals	137
10. ACKNOWLEDGEMENTS.....	139
11. DECLARATION	140

III. Abbreviations

A

AA	Arachidonic acid
ACAT	Acyl-CoA-cholesterol O-acyltransferases
AGPAT	1-acylglycerol-3-phosphate O-acyltransferase
ALA	Alpha-linoleic acid
ATP	Adenosine triphosphate

B

BODIPY	4,4-difluoro-4-bora-3a,4a-diaza-s-indacene
BSA	Bovine serum albumine

C

CER	Ceramide
CERT	Ceramide transfer protein
Chol	Cholesterol
CHX	Cycloheximide
CLEM	Correlated light electron microscopy

D

Dacl	Daclatasvir
DAG	Diacylglycerol
DAPI	4,6-diamidino-2-phenylindole
DCER	Dihydroceramide
DENV	Dengue virus
DGAT	Diacylglyceride O-acyltransferase
DHA	Docosahexaenoic acid
DMEM	Dulbecco's modified eagle medium
DMSO	Dimethyl sulfoxide
DMV	Double membrane vesicle
DNA	Deoxyribonucleic acid
DOG	Diocanoylglycerol
Dox	Doxycycline

E

EPA	Eicosapentaenoic acid
ER	Endoplasmic reticulum
EtOH	Ethanol

F

FA	Fatty acid
FACS	Fluorescence-activated cell sorting
FCS	Fetal calf serum
FFA	Free fatty acid
FFU	Focus forming unit
Fig.	Figure

G

G.V.	Gabrielle Vieyres
G3P	Glycerol-3-phosphate
GAPDH	Glyceraldehyde 3-phosphate dehydrogenase
GFP	Green Fluorescent protein
GPAT	Glycerol-3-phosphate-acyl-transferase

H

HA	Human influenza hemagglutinin
HCER	Hydroxyceramide
HCoV	Human Coronavirus
HCV	Hepatitis C virus
HEV	Hepatitis E virus
hpi	Hours post infection
hpt	Hours post transfection

I

IF	Immunofluorescence
IRES	Internal ribosome entry site
IVT	<i>In vitro</i> transcript

K

kb	Kilobases
kDa	Kilodalton

L

LA	Linoleic acid
LB	Lysogeny broth
LCER	Lactosylceramide
LC-ESI-MS/MS	Liquid chromatography electrospray ionization tandem mass spectrometric
LD	Lipid droplet
LGTV	Langat virus
lyso-PL	Lyso-phospholipid

1. Zusammenfassung

Ein gemeinsames Merkmal der Infektion mit positiv einzelsträngigen RNA-Viren ist die Umstrukturierung der Wirtszellmembranen zur Bildung viraler Replikationsorganellen (RO). Im Fall der Hepatitis-C-Virus (HCV) Infektion wird dieses RO als "Membrannetz" bezeichnet und beinhaltet Doppelmembranvesikel (DMVs), die vom endoplasmatischen Retikulum (ER) entstammen. Außerdem sind Lipidtröpfchen (LDs) häufig mit dem HCV-Membrannetz assoziiert. So ist das Protein Diacylglycerin-O-Acyltransferase 1 (DGAT1), ein entscheidendes Enzym der LD Bildung, für die Morphogenese von HCV erforderlich. Jedoch stellten wir fest, dass die Überexpression des DGAT1-Isoenzyms, DGAT2, die HCV-Infektion stark hemmt. In folgender Studie wollen wir die viralen und zellulären Faktoren bestimmen, die für diesen hemmenden Effekt verantwortlich sind.

Es stellte sich heraus, dass DGAT2 spezifisch den Replikationsschritt des HCV hemmt, während es die Replikation anderer RNA-Viren der *Flaviviridae*, *Hepeviridae* und *Coronaviridae* nur minimal behindert. Wir brachten die Inhibition des HCV mit defekter DMV-Bildung in Verbindung. Die enzymatische Aktivität von DGAT2 war für diese Inhibition erforderlich. Jedoch genügte bloße LD-Akkumulation nicht, um die HCV-RNA-Replikation zu behindern. Die Analyse mehrerer DGAT2-Mutanten ergab, dass die retikuläre und nicht die LD-Lokalisation für den antiviralen Effekt von DGAT2 entscheidend ist. Da beide, DMVs und LDs, aus der ER-Membran entstammen, stellen wir die Hypothese auf, dass die DGAT2-induzierte LD-Biogenese die ER-Lipidlandschaft verändert und so die DMV-Bildung beeinträchtigt. Wir nutzten eine Kombination von Lipidomics, fluoreszierendem Lipid-Biosensor-Imaging und Lipidsupplementierung, um die Lipidspezies zu identifizieren, die an der DGAT2-Sensitivität von HCV beteiligt sind. Interessanterweise wurden verschiedene Lipidklassen, insbesondere Phospholipide, bei der HCV-Infektion, aber auch bei DGAT2-Expression erhöht. Dabei wurden insbesondere Phospholipide mit stark ungesättigten Fettsäureketten unter beiden Bedingungen stimuliert, was auf eine gemeinsame Nutzung derer für die DMV- und LD-Biogenese hindeutet. Andererseits wurden durch die Expression von DGAT2 bestimmte Lipide, insbesondere Oleyl-Phospholipide, dezimiert, die bei der Bildung von HCV RO eine wesentliche Rolle spielen.

Insgesamt suggerieren unsere Ergebnisse, dass der Lipidaustausch während der DGAT2 initiierten LD-Biogenese nicht nur neutrale Lipide, sondern auch die Zusammensetzung der Membranlipide beeinflusst, was sich nachteilig auf die RO-Bildung auswirkt. Die Lipidveränderungen, die wir global in DGAT2-exprimierenden Zellen beobachteten, könnten unter physiologischen Bedingungen lokal, in ER-Subdomänen, relevant sein. Darüber hinaus könnte der erhöhte Lipidfluss zwischen ER und LDs bei übermäßiger LD-Biogenese, z.B. während der Steatohepatitis, von Bedeutung sein. Schließlich scheint die durch die DGAT-Proteine vermittelte LD-Biogenese die räumliche Kompartimentierung der HCV-Replikations- und Assemblierungsorte innerhalb des Membrannetz zu regulieren.

2. Abstract

A hallmark of plus-strand RNA virus infection is the reshuffling of host cell membranes to form viral replication organelles. In the case of hepatitis C virus (HCV) infection, this replication organelle is called “membranous web” and appears as accumulation of double membrane vesicles (DMVs) that are derived from the endoplasmic reticulum (ER) membrane. Furthermore, lipid droplets (LDs) are often associated with the HCV membranous web and play an important role during the HCV morphogenesis. As such, the diacylglycerol-O-acyltransferase 1 (DGAT1) protein, which catalyzes the rate-limiting step of the triglyceride synthesis important for LD biosynthesis, is required for the assembly of HCV particles. Surprisingly, we found that the overexpression of the DGAT1 isozyme, DGAT2, strongly inhibits HCV infection. In this study, we aim to identify the viral and cellular determinants behind this inhibitory phenotype.

We found that DGAT2 specifically inhibits the replication step of the HCV viral life cycle, while it had minimal effect on the replication of other RNA viruses of the *Flaviviridae*, *Hepeviridae* and *Coronaviridae* families. Using correlated light electron microscopy, we could correlate this phenotype to a defect in DMV formation. While this effect depended on the enzymatic activity of DGAT2, the mere LD accumulation was not sufficient to hamper HCV RNA replication. Analysis of a series of DGAT2 mutants revealed that reticular rather than LD association of DGAT2 is crucial to its antiviral activity. Since both DMVs and LDs are derived from the ER membrane, we hypothesize that the DGAT2-induced LD biosynthesis alters the ER lipid landscape and thereby impairs the DMV formation. We used a combination of lipidomics analysis, fluorescent lipid biosensor imaging and lipid supplementation assays to identify key lipid species involved in the DGAT2 sensitivity of HCV.

Interestingly, various membrane lipid classes, especially phospholipids were enhanced upon HCV infection, but also DGAT2 overexpression. Thereby, especially phospholipids with highly unsaturated fatty acyl chains were stimulated in both conditions, suggesting a co-utilization of these lipids for both DMV and LD biogenesis. On the other hand, excess DGAT2 expression depleted certain lipid species, in particular oleyl-phospholipids, which might play an essential role during the HCV replication organelle formation.

Altogether, our results indicate that lipid exchanges during DGAT2 mediated LD biogenesis influence not only the neutral but also membrane lipid composition, deleterious for the HCV replication organelle formation. The lipid changes observed globally in DGAT2 expressing cells might be relevant locally in specific ER subdomains, in physiological conditions. Furthermore, the increased lipid flux between ER and LD compartment upon exaggerated LD biogenesis may be important during steatohepatitis. Altogether, LD biogenesis mediated by the DGAT proteins might govern the spatial compartmentalization of HCV replication and assembly sites within the membranous web.

3. Introduction

3.1. Hepatitis C Virus

Hepatitis C virus (HCV) is an enveloped, positive-sense single-stranded (+ssRNA) RNA virus and the leading cause of chronic liver disease [1]. According to the world health organization (WHO) about 1.5 million people are infected with HCV annually [2]. In untreated infected individuals, HCV leads to chronic liver infection in about 70 % of all cases, which can develop into liver cirrhosis and liver cancer [3]. HCV belongs to the *Flaviviridae* family, genus *Hepacivirus*, and circulates in seven clinically relevant genotypes differing in their global distribution and severity [4]. The two highly steatogenic genotypes 3 and 1 are the most prevalent, accounting for 30 % and 46 % of all infections, respectively [4]. Since its identification in 1989, research in the field of HCV infection significantly advanced after the establishment of a functional HCV cell culture model that utilizes the genotype 2a isolate JFH1 or an HCV chimera of JFH1 and the J6 strain of the same genotype 2a (Fig. 1A) [5,6]. Besides this so-called Jc1 and other full-length viruses, several subgenomic replicons of various HCV strains are available and provide useful tools for studying the function of the individual viral proteins and dissecting the viral life cycle (Fig. 1) [7].

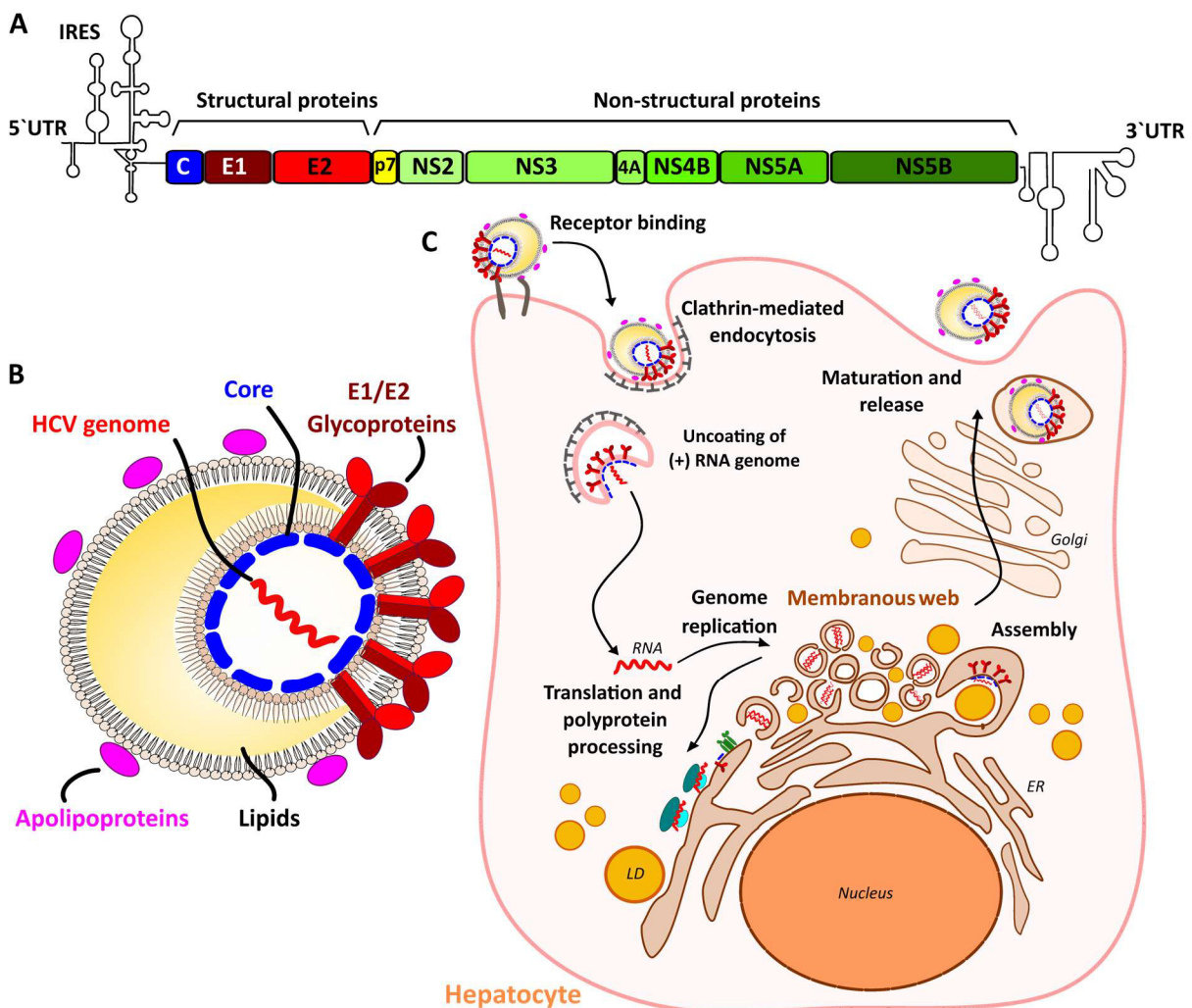


Figure 1: Hepatitis C virus genome, particle and life cycle. (A) The positive sense single stranded RNA genome of Hepatitis C virus (HCV) encodes one open reading frame (ORF) enclosed by two untranslated regions (UTRs) at the 5' and 3' end. The 5'-UTR forms the internal ribosome entry site (IRES) required for translation of the viral genome. The ORF encodes three structural proteins (Core (C), envelope glycoproteins (E1, E2)) and 7 non-structural proteins (p7, NS2-NS5B) that are required for viral replication and assembly. (B) The HCV lipo-viro particle resembles the structure of lipoproteins, as they not only consist of the viral genome, the capsid forming Core protein and the glycoproteins E1 and E2 but possess a neutral lipid envelope decorated by apolipoproteins. (C) Schematic presentation of the HCV life cycle. The HCV entry occurs after binding to a multiple receptor complex on the host cell surface. After clathrin-mediated endocytosis, the viral genome is uncoated and translated at the ER membrane. The replication of the viral RNA occurs in virus induced replication organelles (ROs) at the HCV membranous web. The assembly of HCV virions requires the interplay with lipid droplets (LDs) that are tightly associated with the membranous web. The matured virions are released via the Golgi secretory pathway.

HCV enters the target cell by binding to several receptors at the cell surface, including the CD81 receptor (Fig. 1C) [8,9]. Following clathrin-mediated endocytosis, the 9.6 kB long +ssRNA genome is released into the cytoplasm and directly translated at the endoplasmic reticulum (ER) [10,11]. Besides a single open reading frame (ORF), the HCV genome encodes 5' and 3' untranslated regions (UTR), which support viral translation and replication and are important for the genome's stability (Fig. 1A) [12]. Importantly, a highly conserved structural region called internal ribosome entry site (IRES) is located at the 5'-UTR and is required for binding of the viral RNA to the ribosomal 40S subunit to initiate translation (Fig. 1A) [13,14]. The translation product of the ORF is a poly-protein of 3000 amino acid residues, that is cleaved by host proteases into 10 mature proteins [15]. Consistent with other members of the *Flaviviridae* family, HCV encodes three structural proteins (the capsid protein Core and envelope glycoproteins E1 and E2) and seven non-structural proteins (NS2, 3, 4A, 4B, 5A, 5B and p7) (Fig. 1A) [15]. While the structural proteins are crucial for the formation of the enveloped HCV particle, the non-structural proteins play various roles during HCV replication and particle morphogenesis (Fig. 1B) [15]. The replication of the HCV genome occurs at a virus induced replication organelle (RO), that consists of double and multimembrane vesicles (DMVs and MMVs) derived from the ER membrane (Fig. 1C) [16–19]. DMVs are considered as the site of RNA replication since newly synthesized viral RNA has been detected within these compartments [20]. Following replication, HCV hijacks the host cell lipoprotein synthesis pathway, thereby gaining apolipoproteins to assemble into a low-density “lipo-viro-particle” (Fig. 1B) [21–23]. The newly formed virions are then released through the Golgi-dependent secretory pathway [24] and eventually circulate in the bloodstream either as free particles or associated with lipoproteins in order to escape from the innate immune response [25,26]. Subsequently, HCV can be transmitted to other individuals by percutaneous exposure to infected blood or blood-derived body fluids [27].

Despite intense research effort, to date, no vaccine against HCV infection is available [28]. In the last years, the development of several antiviral treatments led to decreasing numbers of patients suffering from HCV-caused chronic hepatitis [29]. However, the global availability of these highly expensive

treatments is limited and evolution of antiviral-drug-resistant strains has been observed [28]. Continuous study of HCV including the interaction with host factors and its close relation to the liver metabolism is therefore still highly demanded and required for the development of further antiviral treatments. One crucial strategy is to exploit the viral manipulated lipid pathways leading to the formation of HCV RO.

As numerous viruses have developed similar strategies to exploit the lipid pathways of the host cell, the formation of HCV replication organelle (RO) can also serve as a model for other emerging viruses of the *Flaviviridae*, especially arthropod-borne viruses, and *Coronaviridae*, such as the recently emerged severe acute respiratory syndrome coronavirus type 2 (SARS-CoV-2), which also rely on the formation of viral ROs [20,30,31].

3.2. Viral replication organelles

The formation of virus ROs is a hallmark of +ssRNA viruses and believed to create a protective microenvironment for the viral replication and assembly step. ROs do not only provide a locally restricted compartment to concentrate viral and host proteins required for replication, but simultaneously shield the viral RNA genome from innate immune sensors [32].

Based on numerous electron microscopy studies, different architectures of ROs have been revealed. These can be divided into (i) the membrane invagination type, which includes structures formed by single membrane invaginations whose contents are connected to the cytosol, and (ii) the membrane protrusion type including double membrane vesicles (DMV) (Fig. 2). The latter most likely results from both membrane protrusion and invagination, leading to a specialized organelle that resembles the structure of autophagosomes [33].

Different host cell organelles including the ER, the Golgi apparatus, mitochondria, lysosomes and the plasma membrane can serve as substrate for the formation of ROs [30,34]. The ER membrane is one of the most frequently utilized sources for viral RO, which is encouraged by some of the intrinsic properties of the ER, such as the ER-to-cytosol translocation machinery and the constant membrane budding and fission processes that allow dynamic restructuring [35].

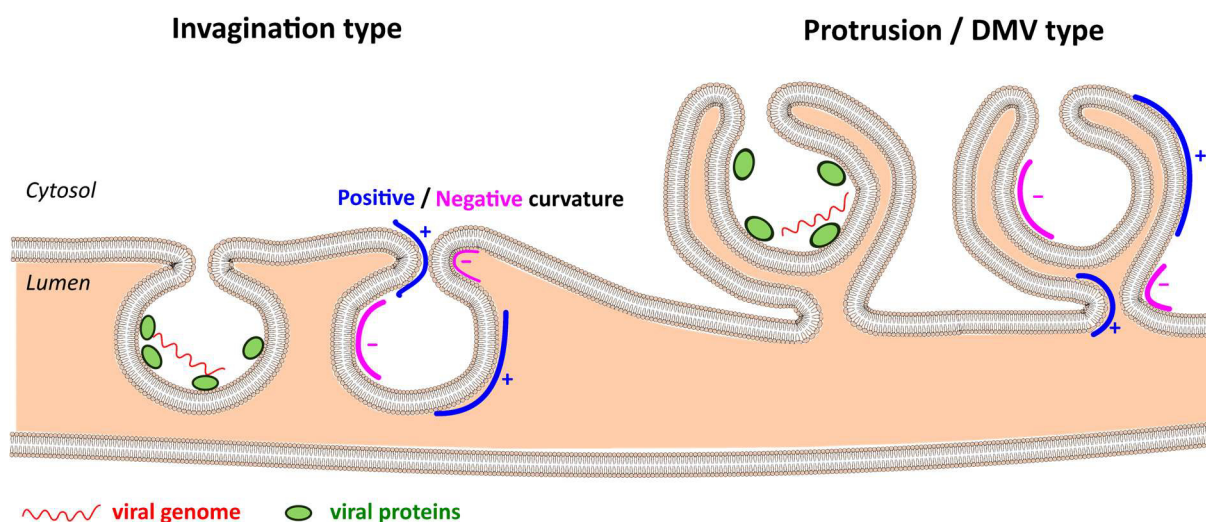


Figure 2: Replication organelle (RO) types. Based on the direction of curvature – away or towards the cytosol - ROs are classified into invagination and protrusion type. In both cases, an interplay of positive (blue) and negative (pink) membrane shaping is essential for the formation of the viral ROs. For the protrusion type, double membrane vesicles (DMVs) are represented here.

Various *Flaviviridae*, including Dengue virus (DENV), Zika virus (ZIKV), tick-borne encephalitis virus (TBEV), Langat virus (LGTV) and West-Nil virus (WNV) induce ER-derived convoluted membranes as well as single membrane vesicles or tubules [36–38]. Moreover, DMVs and MMVs, as in the case of HCV and also various coronaviruses, are formed at the ER membrane [30,39].

The size of DMVs is heterogeneous in both HCV- and SARS-CoV-2-infected cells, ranging from 100 to 300 nm [30]. DMVs are often attached to the ER and some of them have pores that span the double membrane [39]. For SARS-CoV-2, these pores are formed by a protein complex that includes the viral nsp3 protein [40]. These openings may allow the passage of newly synthesized viral RNA so that it can be packaged into newly formed viral particles at the virus assembly site [39].

The mechanisms underlying the formation of different ROs are not fully understood. Often, an interplay of various viral proteins and sometimes also replicating viral RNA is required for the biogenesis of these highly complex membranous structures. Viral transmembrane proteins such as HCV NS4B accumulate at the viral RO site and thereby enable membrane bending [31]. Of note, the biogenesis of the HCV membranous web involves the concentrated action of several viral proteins. As such, also ectopic expression of the HCV NS5A protein triggers DMV formation [41–43]. However, ectopic expression of the entire NS3-5B polyprotein is required to mimic the formation of an RO that is indistinguishable from the membranous web formed during HCV infection. [41]. Besides viral factors, several host proteins are employed for the DMV biosynthesis.

As such, biogenesis factors of autophagosomes, that are also surrounded by a double membrane, are partially utilized by SARS-CoV-2 and HCV for DMV formation cases [33]. However, the conventional macroautophagy pathway is dispensable for the HCV and SARS-CoV-2 DMV synthesis [33].

Importantly, host proteins that are involved in lipid biosynthesis and trafficking contribute to the vast membrane remodeling of viral ROs. Global lipidomic studies and lipid biosensors have proved to be useful in understanding the virus-induced changes of the host cell lipidome [31,44–47].

3.3. Lipids involved in the replication organelle formation

Lipid membranes are composed of a variety of lipid species that differ in their headgroup, which determines the lipid class, as well as in their fatty acyl chain length and saturation (Fig. 3A and B). The composition of these lipids influences the biophysical properties of the membrane, such as curvature, fluidity, protein binding capacity and charge [48–50]. The formation of viral ROs requires high flexibility and bending of the host cell membrane towards and away from the cytosol (positive and negative curvature, respectively) to form vesicles or membrane invaginations (Fig. 3C) [30,43]. Changes of the lipid landscape not only accompany but also enable these vast membrane reshuffling events at the viral RO [30,51,39,43].

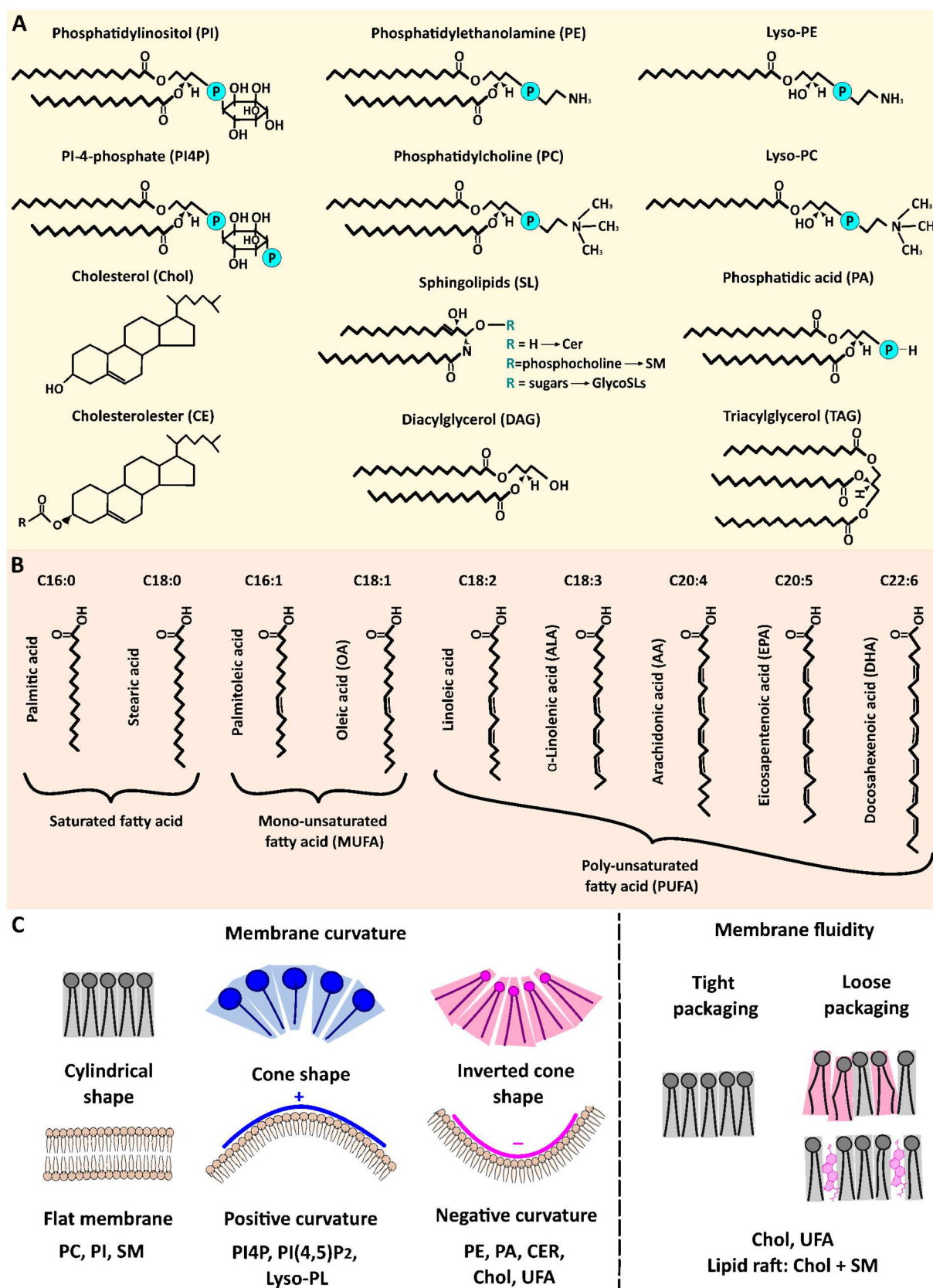


Figure 3: Lipid structures and effects on lipid membranes. (A) Structure representation of major lipid classes distinguished by their headgroup chemistry. (B) Nomenclature of common fatty acids and their classification into saturated, mono-unsaturated (MUFA) and polyunsaturated (PUFA) fatty acids. (C) Influence of the lipid intrinsic curvature on lipid membrane curvature (left panel) and membrane fluidity (right panel). UFA, unsaturated fatty acid; Lyso-PL, lyso-phospholipids.

Similar strategies and patterns are used by different viruses to adapt the lipid landscape of the host cell in favor of the formation of viral RO. One prominent example is the conversion of phosphoinositide (PI) to phosphoinositide-4-phosphate (PI4P) by the action of PI-kinases [52,53]. In the case of HCV, PI4-III kinase- α is recruited by NS5A to the viral RO site, which is crucial for the DMV biogenesis and viral replication [52,54]. PI4P plays a fundamental role as lipid signaling molecule and is bound by various lipid transfer proteins, such as oxysterol binding protein and ceramide transferase (CERT) [55]. The recruitment of these proteins to the HCV membranous web increases the local levels of cholesterol (Chol) and ceramide (CER), respectively [56–58].

Chol is accumulated at the perinuclear region in HCV-infected cells and required for the integrity of the membranous web [20,57]. Enhanced Chol incorporation leads to increased membrane fluidity by intercalating with the phospholipid bilayer [59]. Apart from HCV, the RO formation of DENV, WNV, and ZIKV also depends on Chol enrichment [34,60,61].

In combination with sphingomyelin (SM) or PLs with long, saturated fatty-acyl chains, Chol can form so-called lipid rafts (Fig. 3C.), specialized lipid domains that are important for the formation of the HCV RO [62]. Accordingly, SM has been shown to be critical for the DMV formation of HCV [58]. SM is synthesized from the precursor ceramide (CER), which is trafficked to the HCV RO by CERT [63]. Due to its cone shape, CER itself has an intrinsic negative curvature which might be important for the curvature of viral ROs of HCV, ZIKV and WNV [64,65,46].

The most abundant lipids in eukaryotic lipid membranes are phosphatidylcholine (PC) and phosphatidylethanolamine (PE). While saturated PC species have a rather cylindrical shape important for flat bilayer membranes, PE species possess an intrinsic negative curvature (Fig. 3C). The ratio of PC to PE content has been shown to regulate the fluidity of lipid bilayers and is crucial for the lipoprotein and energy metabolism [66,67]. Various RNA viruses enhance the *de novo* biogenesis of PC and PE, which is probably required for the massive increase of membrane biogenesis during RO formation [68,69]. Also in HCV-infected cells, PC accumulation is observed at the membranous web and enhanced by the upregulation of phosphokinase C [68].

Moreover, the selective increase of mono-unsaturated fatty acyl- (MUFA), and polyunsaturated long fatty acyl (PUFA)- PE and PC species was reported by several studies in HCV-infected cells [44,45]. In line with this, the inhibition or downregulation of several fatty acid elongases and desaturases is detrimental for HCV replication [44,70,71].

Of note, many of the biosynthesis pathways of the aforementioned lipid classes are highly interconnected, which allows the dynamic regulation of local lipid enrichment and depletion. An important bridging point is the phosphatidic (PA) lipid, that serves as lipid precursor of various glycerolipids including PC, PE, and PI [72]. PA is a relatively small, negatively charged phospholipid with intrinsic negative curvature and can also act as a signaling molecule by binding to various proteins [73].

The *de novo* biogenesis of PA is mediated by acylglycerol phosphate acyltransferases (AGPATs) [72]. Recently, the importance of AGPAT1 and AGPAT2 and the accumulation of PA for the formation of the HCV and SARS-CoV-2 RO has been demonstrated [31]. However, the exact role of PA in the formation of viral ROs is not yet fully understood [31].

PA can also be phosphorylated by Lipin proteins to produce diacylglycerol (DAG) [74]. Similar to PA, DAG possesses signaling functions and an intrinsic negative curvature [75,76]. Therefore, DAG plays an important role in the formation of the nuclear envelope and in extreme membrane curvature required for fusion [77]. However, DAG has not yet been associated with the formation of viral ROs.

More importantly, esterification of DAG with acyl-CoA leads to the formation of the neutral triacylglycerol lipid (TAG) – which is catalyzed by diacylglycerol acyl transferases (DGAT) [78]. TAGs are the main component of lipid droplets (LDs), ubiquitous cellular organelles that play an important role in cellular fat storage and energy homeostasis. The formation of these LDs is upregulated during various RNA virus infections, including HCV, and LDs are associated with the HCV membranous web [79–81]. However, in contrast to picornaviruses or DENV [82,83] the function of LDs for the biogenesis of the HCV RO is not yet known [41,79].

3.4. Lipid droplet biogenesis and functions

LDs possess a unique structure, consisting of a neutral lipid Core encircled by a PL monolayer. The biogenesis of LDs occurs at the ER membrane and starts with the synthesis of the neutral lipids cholesteryl ester (CE) and TAG [84]. CE results from acylation of free Chol by acyl-CoA-cholesterol O-acyltransferases (ACATs) [85]. TAG on the other hand is synthesized by sequential acylation from glycerol-3-phosphate (G3P) and three fatty acids (FAs) (Fig. 4A) [84]. In detail, G3P is acylated by glycerol-3-phosphate-acyl-transferase (GPAT) and 1-acylglycerol-3-phosphate O-acyltransferase (AGPAT) to PA [72]. Lipin dephosphorylates PA to DAG, which is then further acylated to TAG [78]. The esterification of DAG to TAG is mediated by either DGAT1 or DGAT2 and forms the rate-limiting step in the cascade of TAG biogenesis (Fig. 4A) [78].

Accumulated TAG and CE eventually coalesce and form ER-embedded oil-lenses, that can transit into budding LDs (Fig. 4B) [84,86]. The latter step is dependent on the oligomeric Seipin protein, which forms a cage-like structure to entrap TAGs at the LD-ER interface and stabilizes the connection between the ER and LD organelle (Fig. 4B) [87,88]. In some cell types, a fraction of LDs detaches from the ER membrane (Fig. 4B) [89]. However, the involved factors and mechanisms behind this membrane fission process are not yet fully understood [89].

The contact between ER membrane and LD contributes to the maturation of LDs, which are supplied with further lipids through ER-LD contact sites. Additionally, LD growth is thought to be stimulated by local TAG synthesis at the LD surface, which is mediated by various lipogenic proteins such as GPAT4

and DGAT2 that can be localized to the LD surface [90]. In line with this, Phosphate Cytidyltransferase 1A (PCYT1A) which catalyzes a rate-limiting step of PC synthesis, associates with LDs that are deficient in PC and is thereby activated. This mechanism is crucial to maintain phospholipid homeostasis in expanding LDs [91].

The degradation of LDs is mediated through the action of lipases, such as the lipase adipose triglyceride lipase (ATGL) and its activator 1-acylglycerol-3-phosphate *O*-acyltransferase (ABHD5) (Fig. 4B) [92,93]. ATGL hydrolyzes TAG to DAG and a FA [94], which can either serve in energy homeostasis via β -oxidation, membrane lipid synthesis, or as lipid signaling molecules. Another mechanism for the degradation of lipids within LDs is lipophagy, which involves the engulfment of LDs by autophagosomal membranes, followed by fusion with lysosomes where the TAG are hydrolyzed by lysosomal acid lipases to free FAs (FFAs) (Fig. 4B) [93,95].

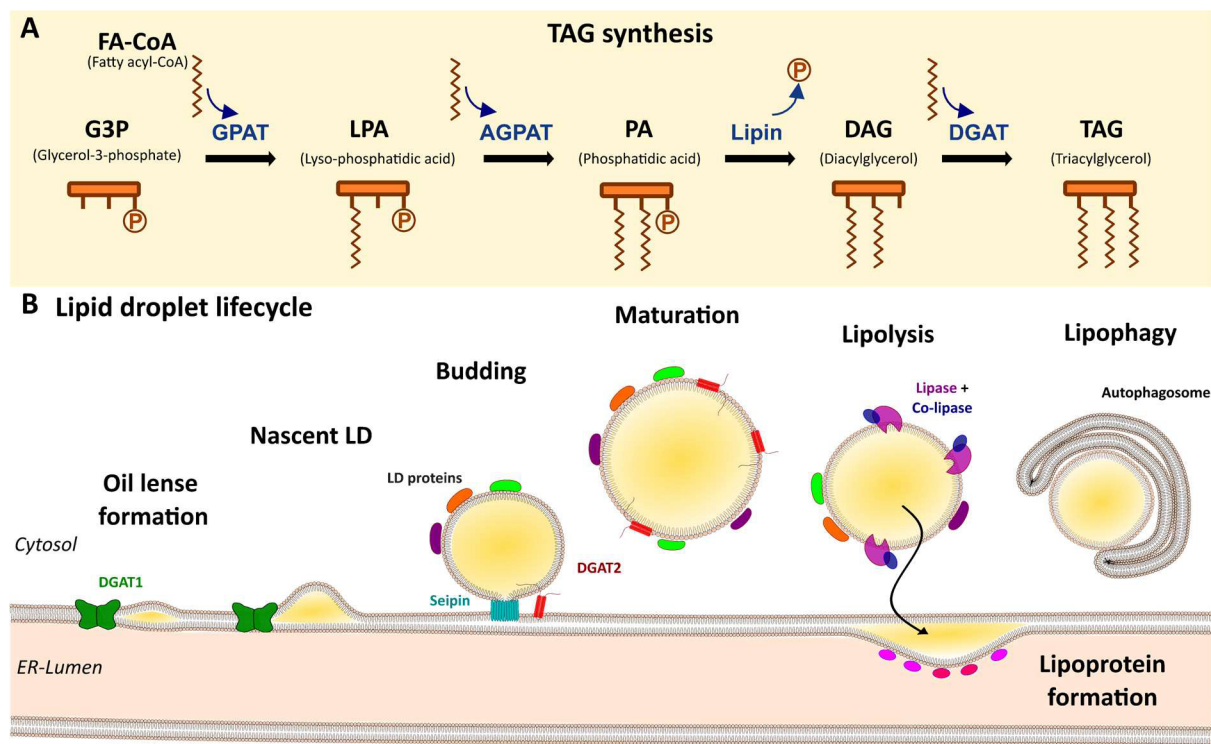


Figure 4: Biosynthesis of triacylglycerol (TAG) and the formation of lipid droplets (LDs). (A) TAG is formed from Glycerol-3-phosphate (G3P) in consecutive acylation steps involving glycerol-3-phosphate-acyl-transferase (GPAT), 1-acylglycerol-3-phosphate *O*-acyltransferase (AGPAT), Lipin and diacylglycerol-*O*-acyltransferase (DGAT) proteins. The catalysis of DAG to TAG mediated by DGAT proteins is the rate-limiting step of the formation of TAG. (B) The lipid droplet life cycle starts with the accumulation of TAG between the ER-leaflets mediated by DGAT. Eventually, the accumulated neutral fats of these oil lenses coalesce and form nascent LDs. The budding of LDs likely involves Seipin, which connects the LD with the ER membrane by forming a neck-like structure. In some cases, mature LDs detach from the ER membrane but are thought to be able to grow via action of DGAT2 or fusion with other LDs. LDs are degraded by lipolysis, involving cellular lipases and co-factors, or a specialized autophagosomal process, called lipophagy. The lipase mediated mobilization of fatty acids (FAs) from the LDs are crucial for the formation of lipoproteins at the ER.

Both expansion and shrinkage of LDs are highly dynamic processes and regulate the LD size dependent on cell type, nutritional condition, and cell developmental state within short time scales. This results in a highly diverse LD pool, that can differ in size, lipid content and protein coating, even within an individual cell [96].

LDs are in contact with many other cell organelles such as the ER membrane, mitochondria, peroxisomes and lysosomes via various membrane bridges and protein tethers [89,97,98]. The proteins involved in these LD contact sites are often related to LD biogenesis or breakdown [89,97]. As such, the aforementioned Seipin is an important membrane bridging protein between LDs and the ER membrane [99,87]. Through these multiple contact sites, LDs play an important role in the inter-organellar communication and transport of lipids and proteins. Thus, in contrast to early findings that underrated LDs as mere fat storage bodies, it is now clear that LDs are highly dynamic organelles that not only function in the energy homeostasis and the availability of membrane building blocks [84]. LDs also protect the cell from the toxic effects of excess FFAs, called lipotoxicity [84,100]. Moreover, recently the role of LDs in the protection from pathogens by acting as innate immune hubs has been demonstrated [101]. On the contrary, various pathogens also hijack the LD life cycle for their replication [102–104].

3.5. Diacylglycerol – O-acyltransferase (DGAT) proteins

The synthesis of TAG is an essential step in the LD biogenesis and catalyzed by either DGAT proteins, DGAT1 or DGAT2. In a reversible reaction, DGAT proteins esterify an acyl-CoA-activated FA to the glycerol backbone of DAG and thereby convert the polar membrane lipid into a neutral lipid, which functions as main energy storage in various organisms. Furthermore, TAG also acts as FA source for PL biosynthesis and the binding of FFAs as TAG protects the cell from lipotoxicity [84,100]. Interestingly, despite knowledge of DGAT activity for several years, it was not until 1998 that the first DGAT protein, DGAT1, was found and cloned from mouse (*Mus musculus*), followed by the discovery of DGAT2 from the soil fungus *Umbelopsis ramanniana* in 2001 [105,106]. DGAT proteins are present in various organisms including various bacteria, fungi, plants, and animals [107]. In mammals, both DGAT proteins are ubiquitously expressed by different cell types, but mainly by adipocytes and hepatocytes, which are involved in fat storage or lipoprotein secretion [105,108].

Although they catalyze the same enzymatic reaction, DGAT1 and 2 do not share sequence homology and are from different protein families [107]. DGAT1 has a molecular weight of 55 kilodaltons (kDa) and belongs to the membrane-bound O-acyltransferase (MBOAT) family [78]. As is characteristic of this family, DGAT1 has several transmembrane domains that are required for its incorporation into the ER membrane (Fig. 5A). While the N-terminus of DGAT1 faces towards the cytosol, the C-terminus extends into the ER lumen and harbors a highly conserved histidine residue that most likely marks the active side of the enzyme (Fig. 5A) [109]. Recently, the protein structure of DGAT1 was solved and revealed

that DGAT1 forms a homodimer via its N-terminus [110]. The acyl-CoA-activated substrate binds to the cytosolic side of DGAT1 and the acyl-residue reaches into a hydrophobic channel within the protein, where the active histidine residue is located (Fig. 5A) [110]. After the esterification, the formed TAG products is thought to be released towards the ER-lumen (Fig. 5A) [110].

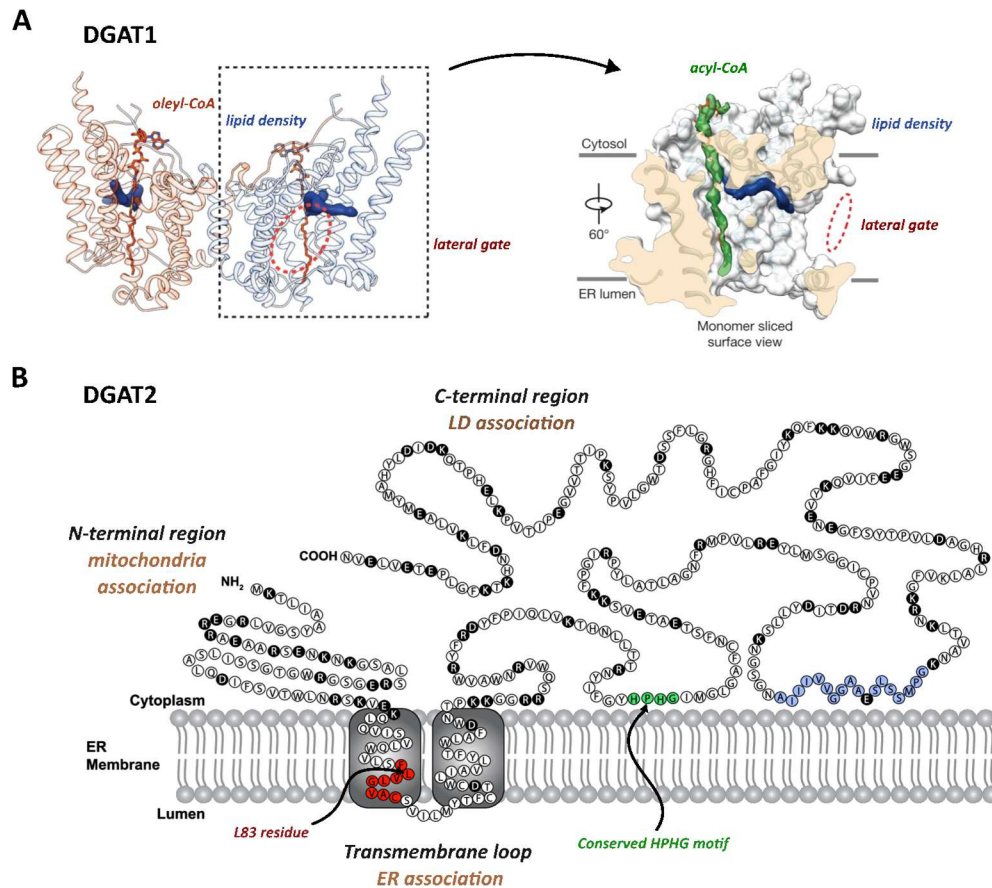


Figure 5: Schematic overview of DGAT1 and DGAT2 protein structures and domains. (A) Left panel: Cryo-electron microscopy structure of human DGAT1 dimer indicating an unidentified lipid-shaped density (blue) residing in the DGAT1 central cavity. The lateral gate (red dashed circle) and oleoyl-CoA molecules (sticks) are shown. Right panel: Surface representation of a DGAT1 monomer showing the orientation of the lipid-like density (blue) in the DGAT1/acyl-CoA complex structure. **(B)** Model of DGAT2 protein topology. The protein's transmembrane domain allows the insertion into the ER membrane, while both N and C-terminus of DGAT2 are faced towards the cytosol. While residues at the N-terminus were shown to be required for the localization of DGAT2 at mitochondria, some hydrophobic regions in the C-terminus are important for the protein's localization at LDs. The putative neutral lipid-binding domain including L83 is shown in red, the conserved HPGG domain in green, and a possible amphipathic α -helix in blue. Positively or negatively charged amino acids are shown in black. Modified and reprinted from (A) Sui et al. 2020 [110] and (B) Stone et al. 2006 [111] with permission according to CC BY 4.0 license (<https://creativecommons.org/licenses/by/4.0/>).

DGAT2 belongs to another protein family that also includes the monoacylglycerol transferase (MGAT) protein [108]. DGAT2 is a 45 kDa protein and probably forms homodimers [112]. In contrast to DGAT1, the crystal-structure of DGAT2 is not yet solved, but due to extensive studies of the protein topology, the functions of several residues within the DGAT2 protein are known (Fig. 5B) [111,113,114]. DGAT2 has two alpha-helices that are connected by a short loop and form the transmembrane region of the

protein, whereas the majority of the protein, including N- and C-terminus are exposed to the cytosol (Fig. 5B) [113]. Within the transmembrane domain, DGAT2 possesses a conserved lipid binding residue (leucine 83), that is crucial for the catalytic activity of DGAT2 (Fig. 5B) [111]. Another putative lipid binding motif is located at the C-terminus: the consensus amino acid sequence HPHG (located at residues 161-164 in human DGAT2) which is conserved among many DGAT2 family members (Fig. 5B) [111]. While the transmembrane domain of DGAT2 is required for localization at the ER-membrane, the C-terminal region is believed to interact with LDs via its amphipathic α -helix [111,113]. In fact, especially after oleic acid supplementation, DGAT2 is not only localized at the ER membrane but also forms rings around LDs, which are characteristic for the localization at these organelles [113–116]. In line with this, deletion of the C-terminal region abolishes this LD-localization [113,114,116]. The association of DGAT2 at LDs is believed to be important for localized TAG synthesis at expanding LDs [113]. Interestingly, DGAT2 was shown to act as an anchor protein between ER and LD together with the ER-resident FATP1 protein [117]. Moreover, DGAT2 is associated with mitochondria, and a recent study reported that CRISPR-Cas9 FLAG-tagged endogenous DGAT2 is primarily present at mitochondria-associated membranes [109]. The interaction with mitochondria is dependent of the N-terminal region of the DGAT2 protein [114].

Due to their different localization, DGAT1 and DGAT2 have been suggested to be responsible for the biogenesis of different LD subsets [90]. While DGAT1 is thought to account for the ER-localized biogenesis of nascent LDs formation, DGAT2 may be more involved in the maturation of cytosolic LDs [90]. Additionally, a study using radiolabeled lipid precursors in combination with either DGAT1 or DGAT2 inhibition showed that both enzymes have different substrate preferences: While DGAT1 preferentially utilizes exogenous, saturated FA, DGAT2 has a preference for *de novo* synthesized FAs [118,119]. Therefore, it has been suggested that DGAT2 acts upstream, utilizing FA from the *de novo* lipogenesis pathway, while DGAT1 would primarily function in re-esterifying released products from the TAG hydrolysis at LDs, while utilizing already present or exogenous FAs [120].

3.6. Lipid droplet hijacking by HCV

Besides their cellular functions, various microbes utilize the LD biogenesis pathways to access the cellular energy and membrane homeostasis, as well as LD resident proteins and contact sites. HCV has a peculiar relationship with the LD lifecycle (Fig. 6) and is one of the best studied examples for the interaction of viral pathogens with LDs [23,121,122].

LD accumulation is a hallmark of HCV infection and manifests clinically as hepatic steatosis, which contributes to the development of liver fibrosis and cancer [3]. Indeed, expression of the HCV Core protein is sufficient to cause accumulation of LDs by protecting them from lipolysis mediated by ATGL and ABHD5 [123].

In addition to the Core protein, the localization of NS5A on the surface of the LDs is essential for HCV assembly and is supported by the action of various host factors such as PLIN2 and PLIN3, but also DGAT1 [124–126] (Fig. 6). Importantly, DGAT1 is required for Core and NS5A LD loading and strengthens the interaction of both viral proteins at the LD surface [126,127]. Interestingly, the enzymatic activity of DGAT1 is crucial for its role as assembly factor [126,127]. In contrast, DGAT2, which catalyzes the same enzymatic reaction, is dispensable for HCV assembly [126].

While the LD surface serves as platform to concentrate the HCV assembly factors, the final formation and budding of the viral particles are thought to occur in an early secretory compartment, presumably the ER, by hijacking the lipoprotein pathway [23] (Fig. 6). Here, LD lipolysis mediated by ATGL and ABHD5 is essential and most likely required for the mobilization of TAGs for the formation of the lipoviro-particle [128,129]. Subsequently, the entanglement of LDs within the membranous web helps to bring together viral proteins, lipids and the newly synthesized viral genome and is believed to facilitate the spatio-temporal coupling of virus replication and morphogenesis [79].

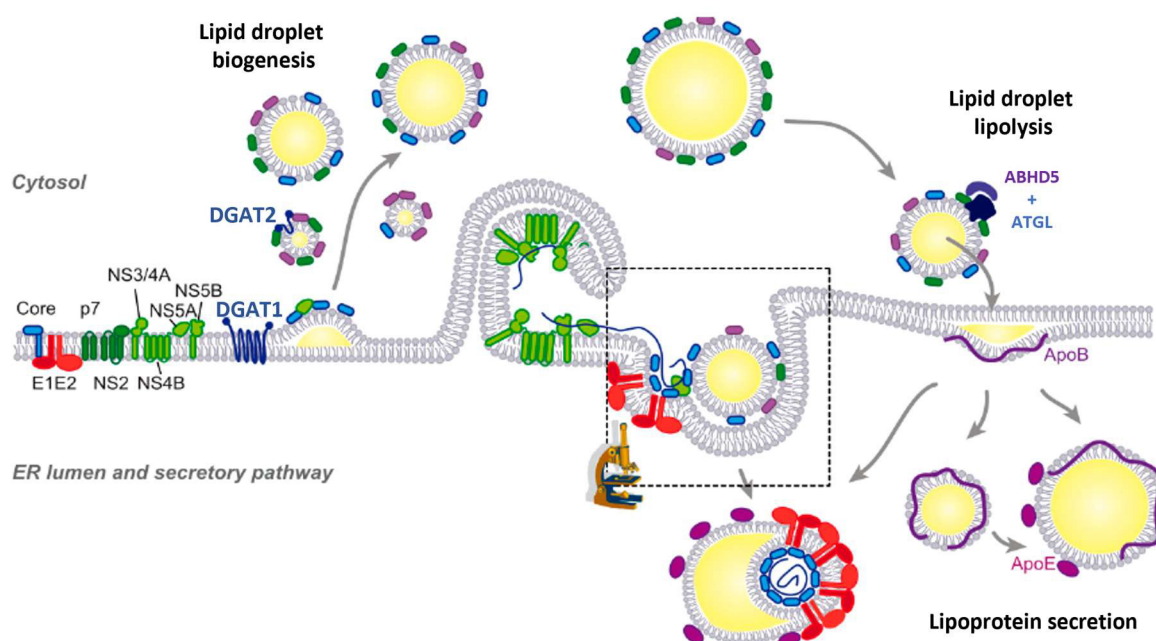


Figure 6: Hijacking of the lipid droplet life cycle for HCV particle formation. While the HCV polyprotein is translated and located at the ER membrane, HCV Core and NS5A proteins are loaded to LDs. The association of NS5A and Core to the LD surface is dependent on the ER-resident DGAT1 protein. Thus, the biogenesis of nascent, DGAT1-mediated LDs rather than cytosolic, DGAT2-mediated LDs is thought to play a role in the concentration of HCV assembly factors. The morphogenesis of HCV is thought to occur at the lipoprotein formation site in close proximity to the HCV ROs. Therefore, neutral lipids of LDs are thought to be mobilized by the ATGL lipase and its co-factor ABHD5 and required for the formation of the HCV lipo-viro-particle. Modified and reprinted from [23] with permission according to CC BY 4.0 license (<https://creativecommons.org/licenses/by/4.0/>)

3.7. Aim of this study

Viral infections can lead to drastic metabolomic changes in the infected host cell. These are often the result of redirected lipid pathways associated with the reprogramming of the cell for highly effective viral particle production. In particular, +ssRNA viruses such as HCV have evolved various strategies to hijack the lipid biogenesis of the host cell [130,43]. Through restructuring of cell membranes and organelles, viral compartments that serve as replication and assembly platforms for viral progeny are formed. Several viral pathogens also utilize LDs as source of membrane lipids and energy reservoir [122]. In the case of HCV, LDs are tightly associated with the membranous web, and play an important role as an assembly platform [127,131]. Additionally, LDs provide lipids for the formation of the HCV lipo-viro-particle [23]. Importantly, the LD biogenesis protein DGAT1 was identified as an essential host factor for HCV and the accumulation of LDs has previously been ascribed a supportive function [123,125–127].

Strikingly, prior experiments have shown that excess LD biogenesis mediated by DGAT2 overexpression was deleterious for HCV infection. So far, the role of DGAT2 for the HCV life cycle is unknown. Therefore, the main subject of this thesis is to decipher the mechanism behind the intriguing antiviral effect of DGAT2 overexpression and to tackle the different roles of DGAT1 and DGAT2 in the HCV life cycle. Subsequently, we will address both cellular and viral determinants of the antiviral activity of DGAT2 expression.

In detail, we will examine the importance of the catalytic activity and subcellular localization of DGAT2 for the inhibitory effect on HCV infection. Additionally, we will test the phenotype in other HCV susceptible cell lines. On the viral side, we aim to determine the affected life cycle step, the timing of the antiviral effect and the responsiveness of various HCV genotypes and other +ssRNA viruses to DGAT overexpression. Furthermore, we will test the impact of the DGAT proteins on the lipid landscape by using lipid biosensors and lipidomic analysis.

Therefore, the aim of this thesis is to utilise DGAT2 overexpression system to gain insights into the tightly regulated relation between HCV replication, LD biosynthesis and lipid homeostasis which holds promise for the development of antiviral therapeutics [122].

4. Results

4.1. Characterization of the antiviral phenotype of DGAT expression

4.1.1. Effect of DGAT protein expression on HCV infection

DGAT1, which catalyzes the esterification of DAG to form TAG stored within LDs, is crucial for virion morphogenesis [126,127]. Loss of DGAT1 leads to severe HCV assembly defects and thereby reduces the release of infectious HCV particles [126]. Although DGAT2, the isoform of DGAT1, catalyzes the same enzymatic reaction as DGAT1, it is not able to fulfill the function as HCV assembly factor [126]. To characterize the effect of DGAT2 on HCV replication, we generated stable cell lines expressing human DGAT2 or DGAT1 from the hepatoma cell line Lunet N hCD81. Additionally, we tested two previously published DGAT2 variants with mutations within the putative neutral lipid binding site (L83A) or a highly conserved acidic sequence (HPH161-163AAA) [111], in order to assess the importance of the catalytic activity for the inhibitory effect of DGAT2. Subsequently, we analyzed the effect of DGAT expression on HCV replication in a whole replication cycle assay utilizing the Renilla luciferase reporter virus JcR2a (Fig. 7A and B).

Strikingly, DGAT2 overexpression inhibited HCV replication 13-fold in the first round of replication and 100-fold in the second round relative to the control (Fig. 7C and D). Furthermore, both DGAT2_L83A and DGAT2_HPH161-163AAA had a reduced effect on HCV infection compared the wildtype protein, suggesting that the catalytic activity of DGAT2 is essential for the inhibitory effect (Fig. 7C and D). Also, DGAT1 overexpression mildly inhibited HCV replication (Fig. 7C and D), which was unexpected due to its known pro-viral function as HCV assembly factor [126,127]. However, the strong inhibition in the first round of infection suggests that both DGAT2 and DGAT1 overexpression inhibited viral replication already before the release of viral progeny (Fig. 7A). Of note, expression of all tested DGAT constructs mildly reduced cell viability at later times post seeding which is, however, unlikely to cause the observed strong HCV replication inhibition (SFig. 1).

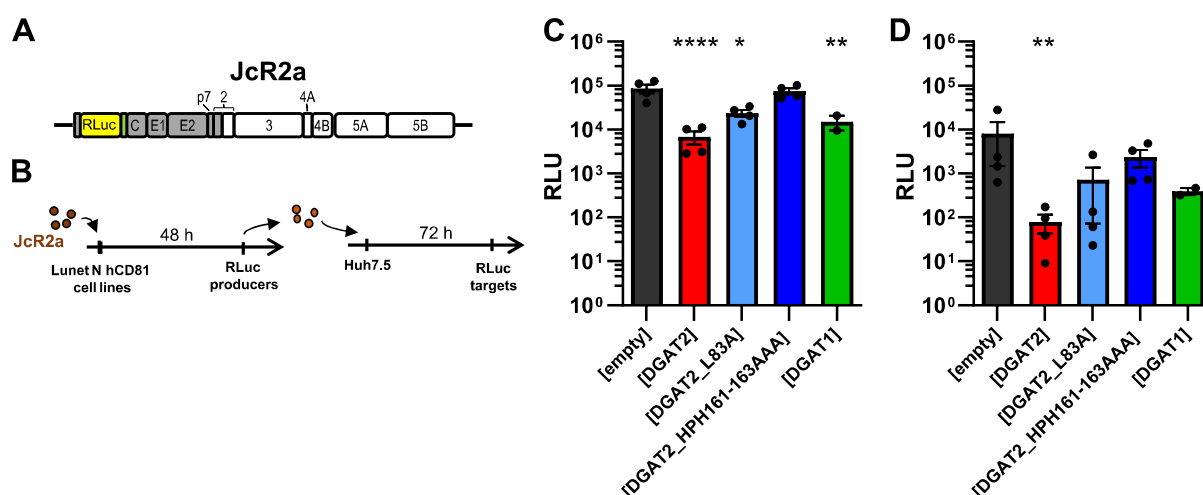


Figure 7: Effect of DGAT expression on HCV replication and cell viability. (A) HCV Renilla luciferase (RLuc) reporter construct of genotype 2a. The construct is a chimera of two genotype 2a HCV strains. Grey areas correspond to J6 and white areas to JFH1 genome. **(B)** Overview of HCV whole replication cycle experiment. Lunet N hCD81 cells stably expressing empty vector control, DGAT2, the two mutants DGAT2_L83A or DGAT2_HPH161-163AAA, or DGAT1 were infected with JcR2a virus for 48 hours (h) and cell lysates were harvested for luciferase assay. Supernatants of infected cells were transferred to naïve Huh-7.5 cells. Cell lysates were harvested 72 hpi. **(C)** Luciferase values of first and second round of infection are depicted as relative light units (RLU). Mean \pm SEM of $n=2-4$ are shown. Statistically significant differences of log-transformed values compared to [empty] control group (ANOVA, Dunett's test) are indicated by asterisks.

In order to test the successful expression of the DGAT constructs, we analyzed the DGAT1 and DGAT2 RNA expression levels in the stable cell lines by using RT-qPCR (Fig. 8). Additionally, we measured the expression levels of endogenous DGAT1 and DGAT2 RNA also in primary human hepatocytes (Fig. 8).

As expected, the DGAT1 mRNA increased 10-fold in the Lunet N hCD81 [DGAT1] cells compared to the control cells (Fig. 8A). Moreover, we detected elevated DGAT2 mRNA expression in all stable cell lines except for DGAT2_HPH161-163AAA, due to impairment of primer binding (Fig. 8B). The DGAT2 mRNA expression was ~ 3 -fold increased for Lunet N hCD81 [DGAT2] cells while comparable to the average endogenous DGAT2 expression level within primary human hepatocytes (Fig. 8B). Curiously, we also observed elevated DGAT2 mRNA levels in Lunet N hCD81 [DGAT1] cells (Fig. 8B). This effect might be caused by a cross-talk of DGAT1 and DGAT2 transcription, as co-regulation of both enzymes has been described before [132].

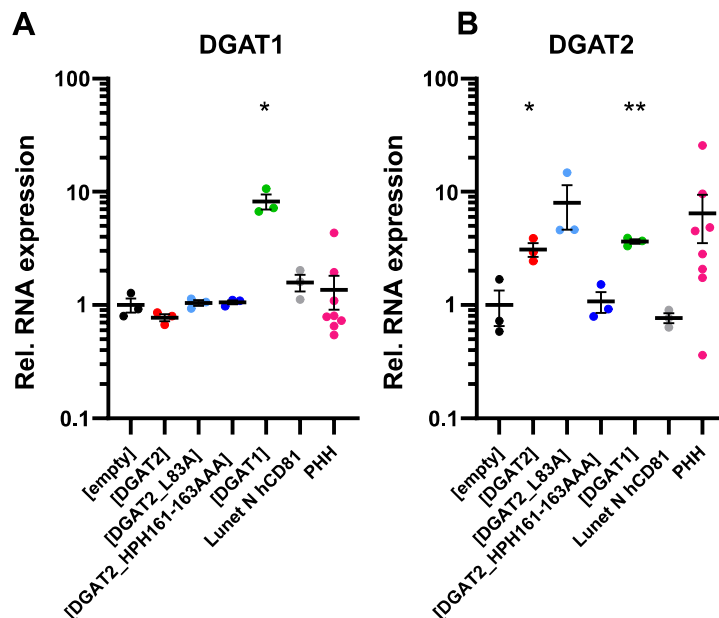


Figure 8: DGAT2 and DGAT1 RNA expression in Lunet N hCD81 stable cell lines and primary human hepatocytes (PHH). Relative expression of either DGAT1 (A) or DGAT2 (B) mRNA was measured by primer-probe RT-qPCR. RNA expression was measured in Lunet N hCD81 cells stably expressing empty, DGAT2, DGAT_L83A, DGAT2_HPH161-163AAA and DGAT1 and normalized to the average DGAT mRNA expression levels in empty vector expressing cells. Additionally, expression levels in naïve Lunet N hCD81 and PHH were determined. Mean \pm SEM of $n=3$ or $n=8$ for PHH donors are shown. Statistically significant differences (Welch's test) in the stable DGAT protein-expressing cell lines compared to the [empty] control group are indicated by asterisks.

The above shown experiments were performed by Gabrielle Vieyres (G.V.) prior to this study. In the following, we elucidated the role of DGAT protein expression for HCV replication by (i) characterizing the antiviral phenotype, (ii) determining the cellular and viral determinants of the antiviral activity, and by (iii) investigating the influence of DGAT expression and HCV infection on the host cell lipid landscape.

4.1.2. Detection of the DGAT proteins

In order to verify the overexpression of DGAT2 on protein level, we tested different commercially available DGAT2 antibodies by Western Blot (WB) and immunofluorescence (IF) staining (Fig. 9). However, all of the tested antibodies failed to detect both endogenous and ectopically expressed DGAT2 in the utilized Lunet N hCD81 cell lines (Fig. 9). The unsuccessful staining with the commercial antibodies has been reported by others [133,134]. Of note, the expression of DGAT1 in the stable Lunet N hCD81 cell lines could be detected by WB (Fig. 9A).

Subsequently, to enable the detection and localization of the ectopically expressed DGAT2 constructs, we cloned HA-tagged DGAT constructs tested their expression by WB and IF (Fig. 9B and C). Note that the HA-tagged constructs were cloned by G.V.

We detected HA-tagged DGAT2, DGAT2-L83A and DGAT2-HPH161-163AAA by WB at the approximate size of 46 kDa (Fig. 9A). Moreover, HA-DGAT2 expression resulted in a cytoplasmic, reticular staining detected by anti-HA IF (Fig. 9C).

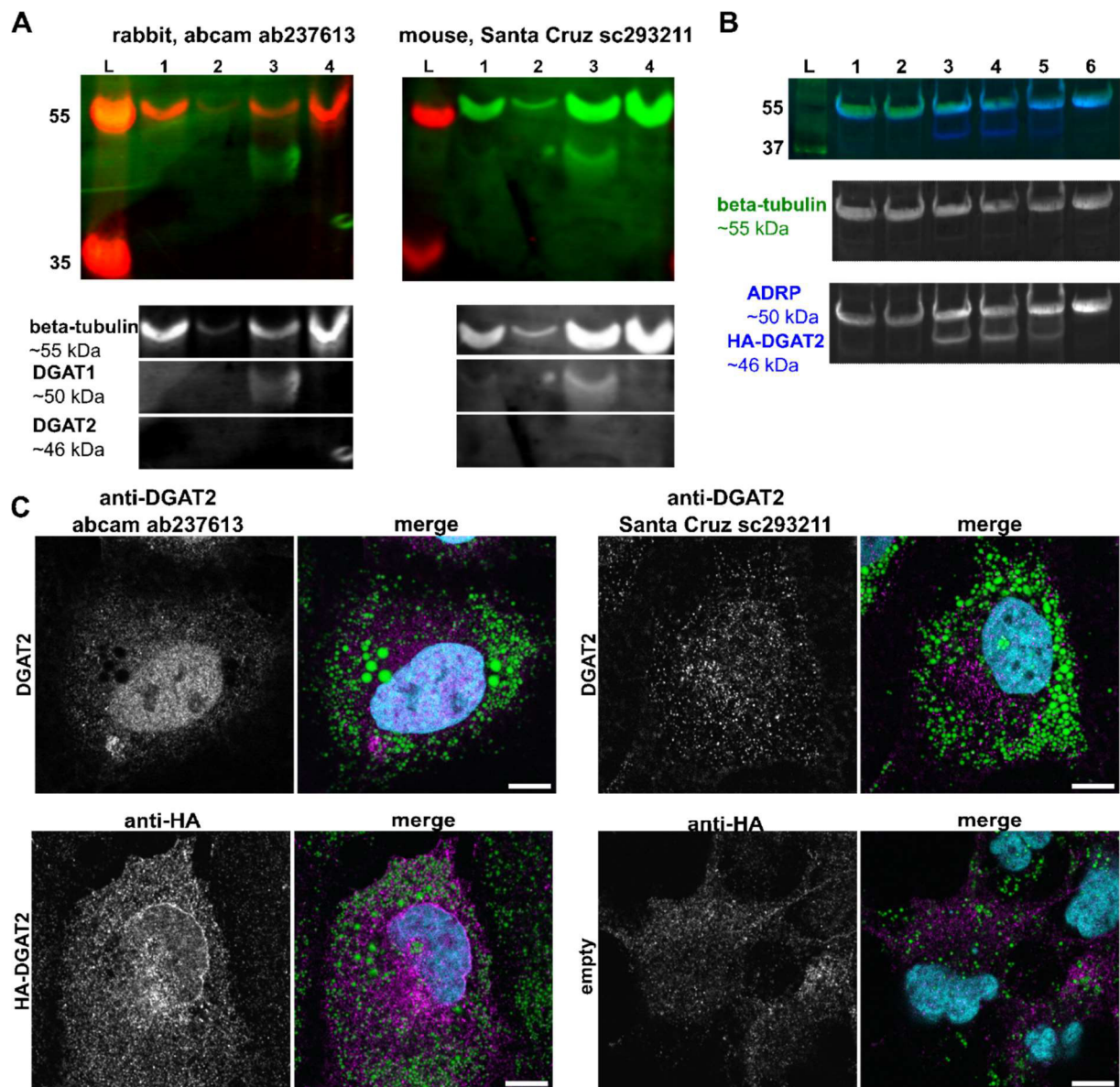


Figure 9: Detection of DGAT2 by Western Blot and immunofluorescence. **(A)** Test of different commercially available DGAT2 antibodies by Western Blot (WB). Cell lysates of Lunet N hCD81 [DGAT2] (lanes 1, 2), [DGAT1] (lane 3) or [empty] (lane 4) cells were tested with fluorescent WB using anti-DGAT2 poly-clonal rabbit (Abcam, ab237613) (left panel) or mono-clonal mouse (Santa Cruz, sc293211) primary antibodies and Starbright secondary antibodies. Beta-tubulin (55 kDa) and DGAT1 (~50 kDa) were co-stained. Note that in lane 2 only one fifth of usual cell lysate was loaded. **(B)** Lunet N hCD81 cells were transduced with lentiviruses to express DGAT2 (lanes 1), Flag-DGAT2 (2), HA-DGAT2 (3), HA-DGAT2_L83A (4), HA-DGAT2_HPH161-163AAA (5) or empty control vector (6). Protein expression was tested with fluorescent WB using anti-HA (mouse, HA11 Biolegend) antibody. Beta-tubulin (55 kDa) and adipose differentiation-related protein (ADRP) (~50 kDa) were co-stained. **(C)** Lunet N hCD81 cells were transduced with lentiviruses to express DGAT2 (upper panel), HA-DGAT2 (bottom left) or empty vector control (bottom right). DGAT2 (upper panel) or HA-DGAT2 staining (lower panel) was tested using the indicated antibodies (magenta). Lipid droplets were co-stained with the LD dye BODIPY 493/503 (green) and nuclei with DAPI (blue). Note that different DGAT2 antibody concentrations were tested in parallel (results for highest ab dilutions are shown) and representative images of at least two independent experiments are depicted. Scale bar, 10 μ m.

4.1.3. Antiviral effect of transiently expressed tagged DGAT proteins

After confirming the expression of the tagged DGAT proteins, we tested whether the N-terminal tags influence the antiviral activity of DGAT (Fig. 10A). Subsequently, we expressed the untagged and HA-tagged DGAT proteins in Lunet N hCD81 cells by lentivirus transduction and assessed the influence of the different constructs on JcR2a replication by luciferase assay (Fig. 10B).

As seen previously, overexpression of DGAT2 significantly decreased viral replication, already starting at 24 hpi (Fig. 10B), while the mutation of the putative lipid binding sides L83A or HPH161-163AAA partially restored viral replication. Importantly, the additional N-terminal HA tag did not impair the inhibitory phenotype of DGAT2 and both mutants (Fig. 10B). Furthermore, we observed no difference between HA-tagged and untagged DGAT1 in their effect on JcR2a replication (Fig. 10B). Of note, in contrast to earlier results, the transient expression of both DGAT1 and HA-DGAT1 only had a mild, but no statistically significant effect on HCV replication.

In summary, the HA-tagged DGAT2 and DGAT1 constructs are suitable tools to study the antiviral effect of DGAT on HCV replication.

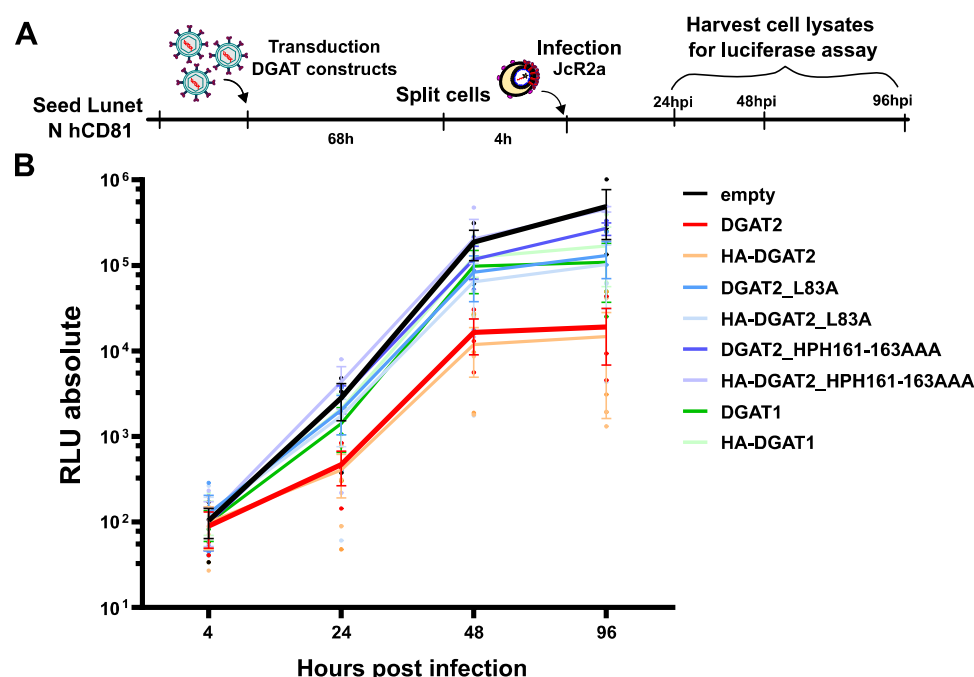


Figure 10: Influence of tagged DGAT proteins on HCV replication. (A, B) Lunet N hCD81 cells were transduced with lentiviruses to express untagged or HA-tagged DGAT2, DGAT2_L83A, DGAT2_HPH161-163AAA or DGAT1. 72 h after transduction, cells were infected with JcR2a. To assess the effect of the expressed constructs on viral replication, cell lysates were harvested at 4, 24, 48 and 96 hours post infection (hpi) for luciferase assay. (B) Results of luciferase assay. Mean ± SEM of n=3 are shown.

Since we observed a cross regulation of the mRNA expression of DGAT2 in DGAT1-overexpressing cells earlier (Fig. 8), we tested the mRNA levels of both DGAT1 and DGAT2 also in the transient expression set-up (Fig. 11). The RT-qPCR on the extracted total RNA was performed by Laura Weber.

As expected, transient expression of either DGAT2 or DGAT1 resulted in increased levels of their corresponding mRNA. However, in contrast to the results obtained in the stable cell lines, we did not observe an upregulation of DGAT2 mRNA upon transient expression of DGAT1 (Fig. 11). In fact, the opposed DGAT mRNA levels were mildly but consistently downregulated (Fig. 11). Therefore, the cross-regulation of DGAT2 mRNA seems to be only relevant in stably expressing cells.

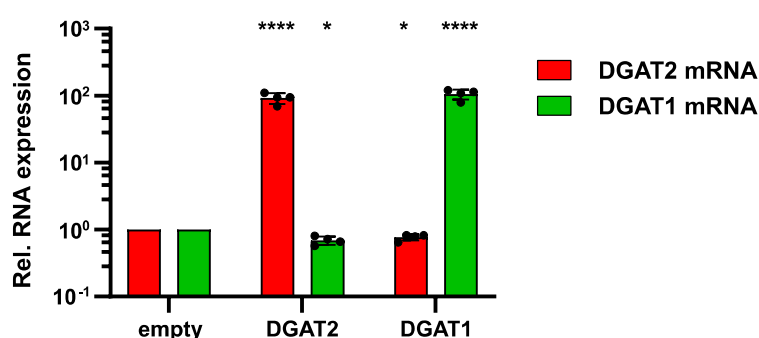


Figure 11: DGAT mRNA levels in transient expression. Lunet N hCD81 cells were transduced with lentiviruses to express empty vector control plasmid, DGAT2 or DGAT1 and cell pellets were harvested 48 h post transduction. DGAT2 (red) and DGAT1 (green) mRNA expression levels were measured by RT-qPCR. Values are normalized to the average DGAT1 or DGAT2 mRNA expression levels in control transduced cells. Mean \pm SEM of $n = 3$. Statistically significant changes of log-transformed values compared to empty control group (Welch's t-test) are indicated by asterisks.

4.1.4. Effect of inhibition of endogenous or ectopically expressed DGAT proteins on HCV replication

Due to the strong restriction of HCV infection upon DGAT2 expression, we wondered whether HCV replication would benefit from blocking the endogenous DGAT2 activity. Additionally, we tested whether the antiviral phenotype of stable DGAT1 and DGAT2 expression can be reversed by treatment with small molecule inhibitors (Fig. 12). Subsequently, we added small molecule inhibitors of DGAT2 and DGAT1 to the Lunet N hCD81 stable cell lines before and after infection with JcR2a (Fig. 12A). We tested the cytotoxicity of the applied inhibitors beforehand (Fig. 12B). Note that this experiment was carried out by G.V..

Interestingly, apart from a mild elevation of viral replication at 40 nM, the addition of DGAT2 inhibitor did not strongly affect viral replication in the Lunet N hCD81 [empty] cells, indicating that the endogenous levels of DGAT2 did not restrict HCV replication. In contrast, treatment of DGAT2-overexpressing cells with the DGAT2 inhibitor significantly increased viral replication up to 3-fold

compared to the untreated control (Fig. 12C). In DGAT1-overexpressing cells, neither inhibitor could rescue replication, despite a mild but not significant positive effect on viral replication upon DGAT2 inhibitor treatment (Fig. 12C). Furthermore, we observed a cytotoxic effect upon addition the DGAT1 inhibitor at high concentrations, which most likely caused the decrease of viral replication (Fig. 12B and D). Together with the observed phenotype of the DGAT2 mutants (Fig. 7 and Fig. 10), these results indicate that the enzymatic activity of DGAT2 is important for the inhibitory effect on HCV replication.

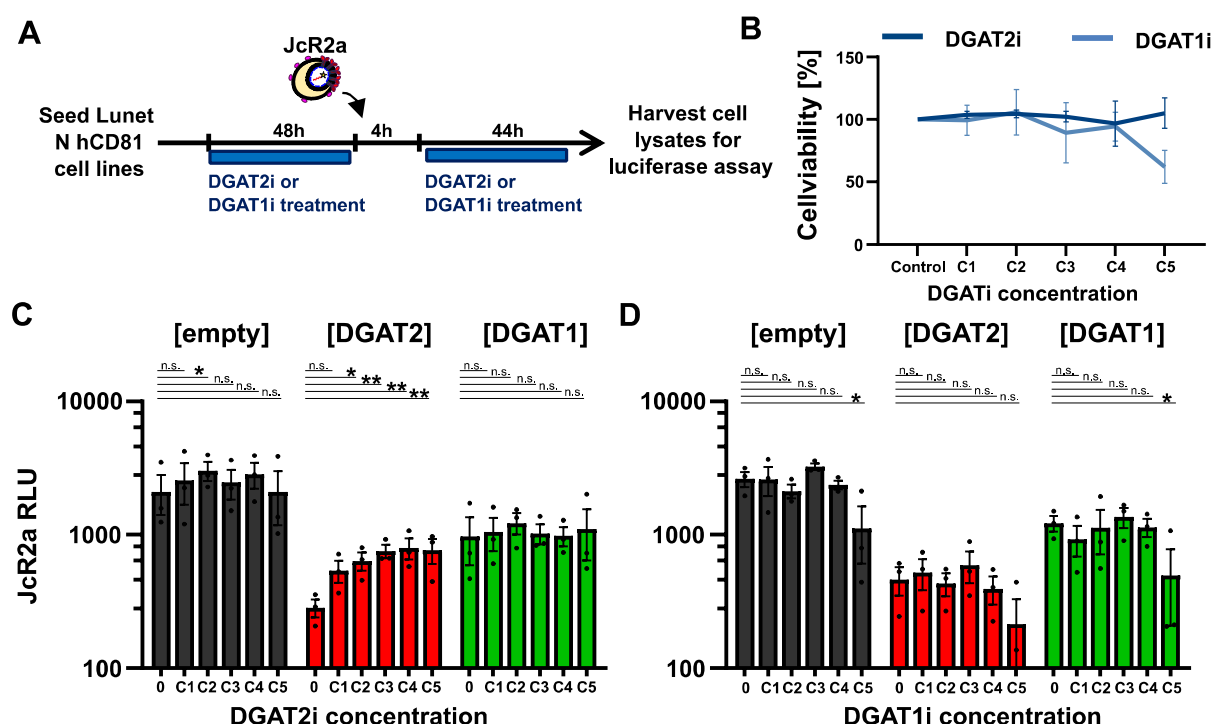


Figure 12: DGAT antiviral activity in presence of DGAT inhibitors. (A-D) Lunet N hCD81 [empty], [DGAT2] and [DGAT1] were treated with either DGAT2 or DGAT1 small molecular inhibitors (DGAT2i and DGAT1i) 48 h prior to and 4 h post JcR2a infection. Cell lysates were harvested 48 hpi. Inhibitors were dissolved in DMSO vehicle control, and five different concentrations were tested (C1-C5; DGAT2i: 0,008, 0,04, 0,2, 1, 5 μ M; DGAT1i: 0,08, 0,4, 2, 10, 50 μ M). **(B)** Cell viability of Lunet N hCD81 [empty] cells upon DGAT inhibitor treatment measured via MTT assay. Relative values normalized to vehicle control are depicted. Mean \pm SD of $n = 3$. **(C,D)** JcR2a replication measured by luciferase assay. Mean \pm SEM of $n = 3$. Statistically significant changes calculated of log-transformed values compared to 0 μ M inhibitor (ANOVA, Dunnet's test) are indicated by asterisks.

4.2. Cellular determinants of the DGAT2 antiviral activity

4.2.1. Effect of DGAT protein expression on LD accumulation

DGAT1 and 2 play important roles in LD biogenesis by mediating the synthesis of triacylglycerols, stored in LDs [78]. This is reflected by the accumulation of LDs in DGAT-expressing cells [135]. As shown above, the disruption of the catalytic activity of DGAT2 by mutation of the highly conserved putative lipid binding domains led to decreased antiviral activity of DGAT2 upon overexpression (Fig. 7). This suggests that the catalytic activity of DGAT2 is required for the inhibitory effect on HCV replication. Here, we assessed the catalytic activity of the DGAT proteins indirectly by measuring the effect on the LD content by a flow cytometry assay (Fig. 13). Following a previously published protocol [128], we mixed Lunet N hCD81 cell lines overexpressing DGAT1, DGAT2, DGAT2_L83A or DGAT2_HPH161-163AAA mixed with an internal reference cell line - Lunet N hCD81 stably expressing mRuby2 - prior flow cytometry (Fig. 13A). This allowed the comparison of the LD content (stained with the neutral fat dye BODIPY 493/504) of each condition independent of staining variations (Fig. 13B). In addition, we stimulated LD accumulation also by oleic acid (OA) in combination with bovine serum albumin (BSA), which served as a positive control of increased LD content. The FACS experiment was performed by G.V..

As expected, we observed an 60 % increase of LD content upon DGAT2 expression relative to the control cells. The DGAT2 mediated LD accumulation was comparable to a high dose OA induction (Fig. 13C). Interestingly, DGAT2_L83A only moderately stimulated LD growth while DGAT2_HPH161-163AAA mutant did not affect the LD content (Fig. 13C). Furthermore, the effect of DGAT1 overexpression on the LD content was milder in comparison to DGAT2 and not statistically significant (Fig. 13C). Strikingly, the effect of the overexpression of each of the shown constructs correlated with the antiviral activity (Fig. 7). These results confirm that the DGAT2 inhibitory effect is dependent on the protein catalytic activity and correlates with the accumulation of LDs.

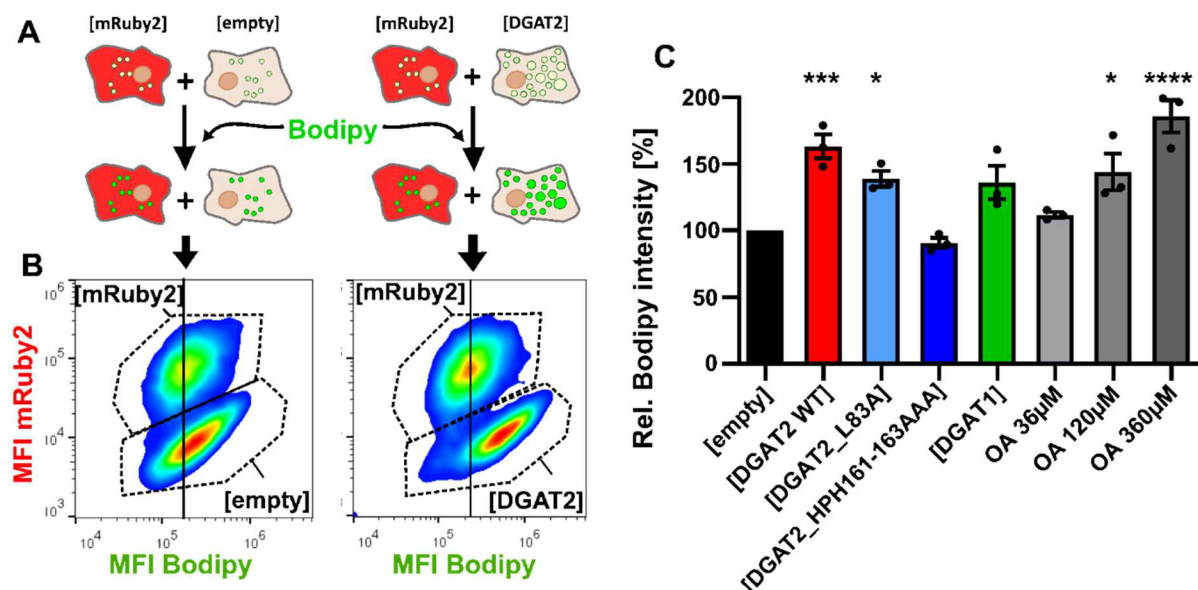


Figure 13: Effect of DGAT expression on LD accumulation measured by flow cytometry. (A) Stable Lunet N hCD81 cells expressing the DGAT constructs or empty vector control were harvested and mixed with mRuby2-positive reference cells prior staining with the LD dye BODIPY 493/503. BODIPY and mRuby2 signal intensities were measured by flow cytometry. (B) Example plots of flow cytometry assay to determine the LD amount in the tested cell lines. BODIPY mean fluorescence intensity (MFI) was compared in each sample between the cells of interest (mRuby2-negative, bottom gate) and the mRuby2-positive reference cell population (top gate). The vertical line was added to highlight the shift in BODIPY signal between the DGAT2-overexpressing and the reference cells, in the plot on the right. (C) Relative LD amount in the DGAT-overexpressing or OA-treated (36, 120, 360 μ M, combined with bovine serum albumin (BSA)) cell lines. Values were normalized to [empty] control cells ($n = 3$). Statistically significant changes compared to [empty] control group (ANOVA, Dunnett's test) are indicated by asterisks.

Since the accumulation of LD appears to cause the antiviral effect on the expression of DGAT proteins, we next investigated whether the accumulation of LDs induced by the addition of OA could also trigger the inhibition of HCV infection (Fig. 14). We subsequently tested the effect of OA addition prior or after infection with HCV (Fig. 14A).

In contrast to DGAT2 overexpression, the addition of OA had a mild effect on JcR2a infection in pretreated cells (Fig. 14B). While the effect appeared to be dose-dependent, it was not statistically significant, and the highest concentration tested of 200 μ M OA resulted in a maximum ~ 1.6 -fold reduction in JcR2a luciferase levels (Fig. 14B). Moreover, treatment of the cells with OA after infection did not impair JcR2a replication (Fig. 14C). Therefore, the accumulation mediated by OA addition could not reproduce the strong antiviral effect caused by DGAT2 overexpression.

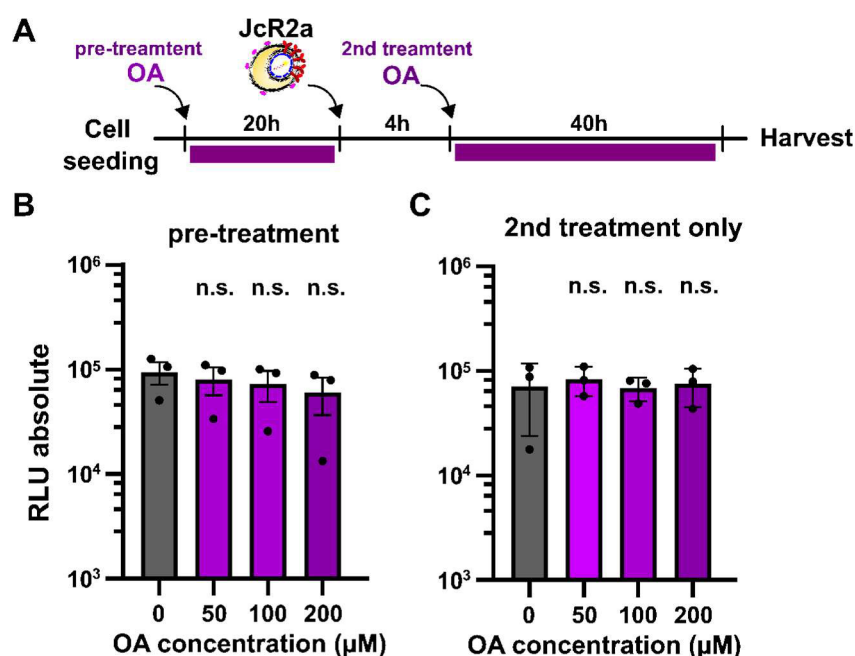


Figure 14: Effect of oleic acid (OA) treatment on HCV infection. (A) Stable Lunet N hCD81 [empty] cells were seeded and infected with JcR2a on the next day. Cells were treated with OA starting at either 20 h before infection ((B), pretreatment) or only 4 hpi ((C), 2nd treatment only). OA was supplemented in 0, 50, 100 or 200 μ M concentrations combined with 30 μ g BSA. Cell lysates were harvested 48 hpi and virus replication was measured by luciferase assay. Mean \pm SEM of $n = 3$. No statistically significant differences of the log-transformed values (ANOVA, Dunnett's test) compared to 0 μ M OA treatment were detected.

4.2.2. Effect of DGAT protein expression on LD size and numbers

LDs are dynamic organelles that range in size and abundance. The constant growth and shrinkage of LDs is influenced by both biophysical and biochemically regulated processes. Consequently, the cellular LD landscape harbors various LD subsets with distinct biophysical properties and protein coats [96]. To assess not only the global changes in LD content (Fig. 13), but also the differential effects on LD quantity and size, we characterized the LD landscape upon DGAT1 and DGAT2 protein expression by fluorescence microscopy (Fig. 15). Accordingly, we seeded the stable DGAT protein-expressing Lunet N hCD81 cell lines together with Lunet N hCD81 [mRuby2] reference cells and acquired images for automated LD analysis (Fig. 15). We used the mRuby2 signal to create a binary mask for each image in order to distinguish mRuby2-positive control cells from the cells of interest (Fig. 15). In the next step, the nuclei and LDs of both cell lines were automatically segmented, followed by analysis of the signal intensity and object sizes using Cell Profiler (Fig. 15). Note that the experiment and microscopy part were performed by G.V., while the analysis pipeline was established in this PhD thesis.

We observed significant shifts in the LD size distribution in both DGAT2- and DGAT1-overexpressing cells, leading to an increase in large LD fractions and a decrease in the smallest LD fractions. (Fig. 16B). This effect is reflected in the expansion of the total cellular LD area in both DGAT2 and DGAT1-expressing cells and is consistent with the overall increase of BODIPY intensity measured by flow cytometry assay (Fig. 13). Furthermore, confirming earlier results (Fig. 13), the LD accumulation was dependent on the DGAT2 catalytic activity.

Interestingly, DGAT1 and DGAT2 overexpression exhibited a very similar effect on the LD area (Fig. 16C). Of note, the absolute LD counts were not significantly affected by neither of the DGAT constructs (Fig. 16D). In summary, overexpression of both DGAT proteins stimulated LD growth dependent on the catalytic activity. These results indicate that the antiviral activity of DGAT2 correlates with the effect on LD accumulation. Additionally, while previous publications reported different influences of DGAT1 or DGAT2 downregulation on the LD profile [90], we did not detect striking differences between DGAT1 and DGAT2 overexpression on the LD profile in this study.

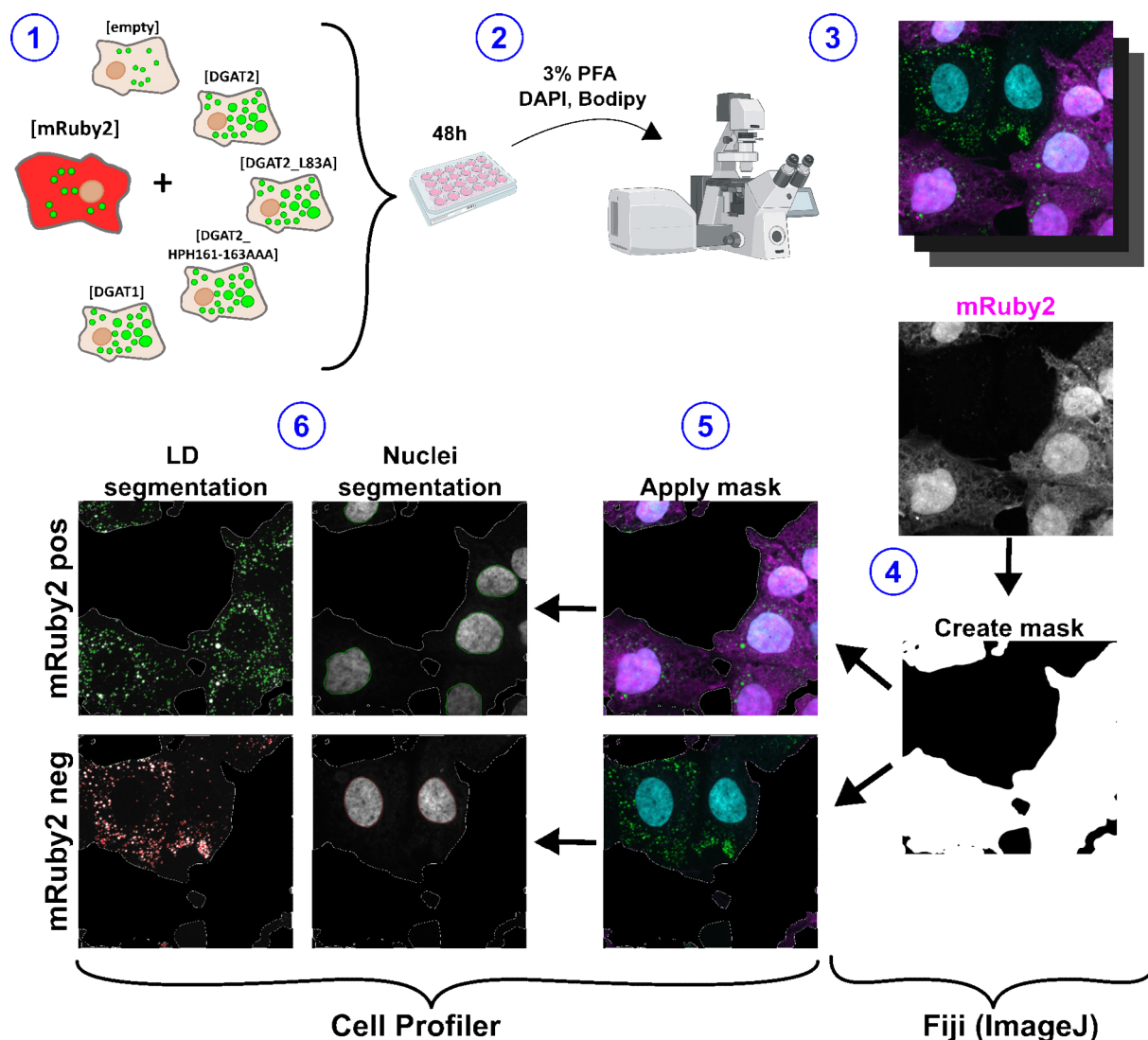


Figure 15: LD quantification by automated image analysis. Pipeline to assess LD sizes and numbers per cell by fluorescence microscopy. (1) Stable Lunet N hCD81 cells expressing the DGAT constructs or empty vector control were co-seeded with mRuby2-positive reference cells. (2) Cells were fixated with paraformaldehyde (PFA) and stained with the LD dye BODIPY 493/503 and the nucleus stain DAPI before imaging. (3) 10 images per condition were taken and processed with a Fiji (ImageJ) macro for object segmentation. The red fluorescence signal of the [mRuby2] cells was utilized to create binary masks. (5) By applying the binary masks to the other fluorescence channels, the fluorescent signal of the cells of interest (mRuby2 neg) was distinguished from control cells (mRuby2 pos). (6) Nuclei and LD of both mRuby2 pos and neg cells were segmented via Cell profiler. Images with low quality leading to crude segmentation errors were excluded. Segmented objects were analyzed upon their size and fluorescence intensity using Cell Profiler.

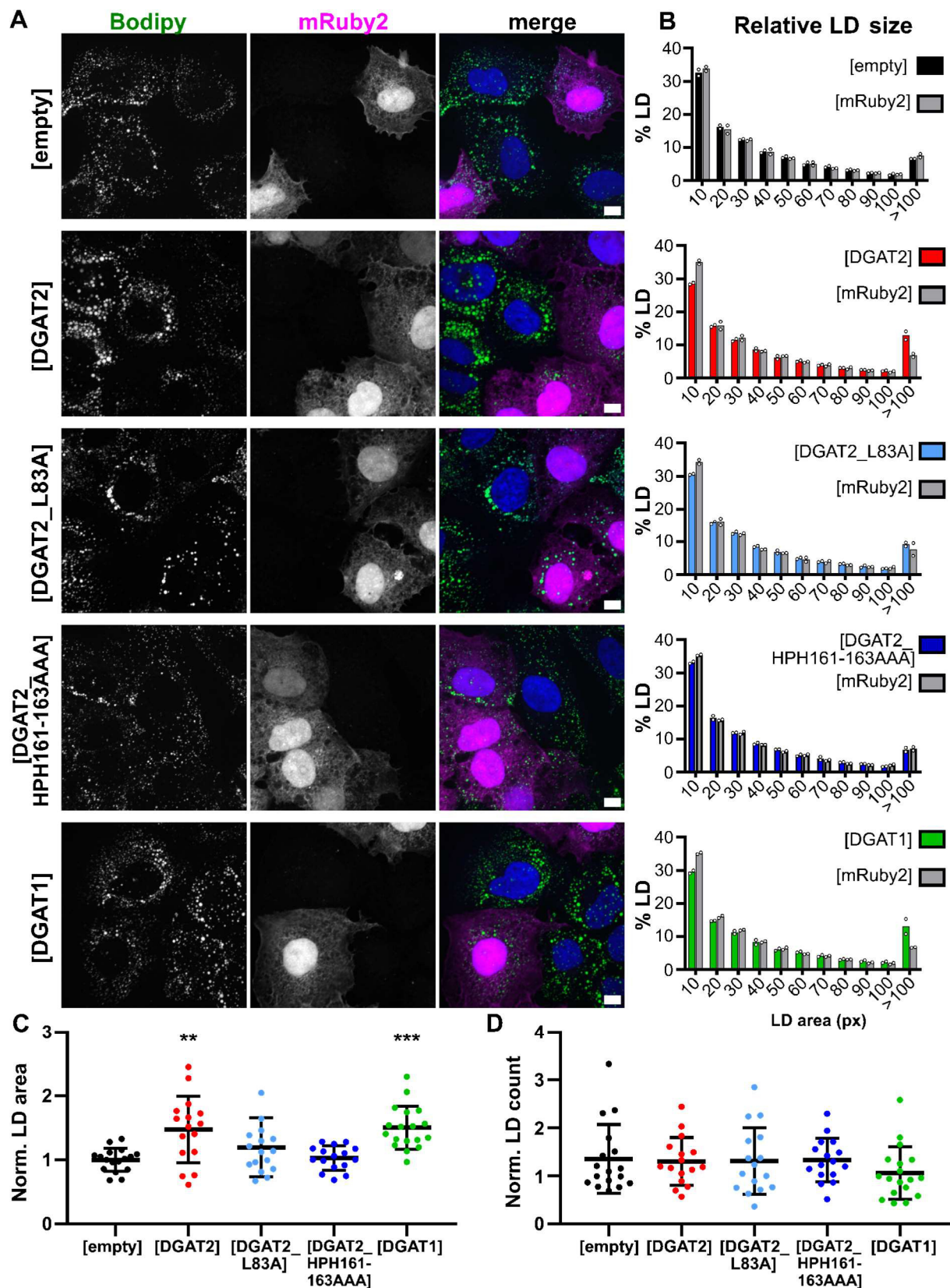


Figure 16: Effect of DGAT expression on the LD profile. (A) Lunet N hCD81 cells stably expressing [empty], [DGAT2], [DGAT2_L83A], [DGAT2_HPH161-163AAA] or [DGAT1] were co-seeded with mRuby2-positive reference cells. Cells were fixed and stained with BODIPY 493/503 and DAPI. Representative images of 2 biological repeats. Scale bar, 10 μ m. (B)-(D) Results of LD quantification following the pipeline shown in Fig. 15. (B) Histograms of relative LD sizes in the Lunet N hCD81 DGAT cell lines (colored bars) compared to the mRuby2-positive cells (grey bars), $n = 2$. X-axis indicates the LD area in pixels. (C) LD area and (D) LD count per cell in Lunet N hCD81 DGAT

cell lines normalized to the mRuby2-positive cells. Each dot represents value for one quantified image of two independent replicates (16-18 images per condition, mean \pm SD are indicated). Results of statistical analysis (ANOVA, Dunnett's test) are indicated by asterisks.

4.2.3. Effect of subcellular localization on the antiviral activity of DGAT2

The ER membrane is the main site of LD biogenesis, and several enzymes that are important for the production of neutral CE and TAG lipids stored in LDs are localized at the ER [136]. Interestingly, in contrast to the ER-bound DGAT1 protein, DGAT2 was reported to localize not only at the ER, but also at LDs and mitochondria, where it catalyzes the local synthesis of TAG [113–115]. Subsequently, we assessed the association of DGAT2 with any of these three organelles and tested the importance of the sub-cellular localization for the antiviral activity of the protein.

We first examined the localization of both HA-tagged DGAT1 and DGAT2 proteins by IF (Fig. 17 and Fig. 18). We co-stained LD, ER, and mitochondria organelles to facilitate the analysis of the subcellular localization of both proteins (Fig. 17 and Fig. 18). We tested the localization of both proteins in both untreated and cells treated with OA, which was reported to enhance the LD localization of the DGAT2 mouse ortholog [115].

As expected, HA-DGAT1 showed a reticular, cytoplasmic signal that strongly overlapped with the ER-membrane but not with mitochondria (Fig. 17A and B). The web-like localization of DGAT1 also enclosed some LDs and thus also occasionally overlapped with the LD-resident adipose differentiation-related protein (ADRP) especially in OA treated cells, (Fig. 17C-F). However, unlike ADRP, HA-DGAT1 did not form ring-like structures, characteristic for LD association, suggesting that the overlap of LD markers with HA-DGAT1 signal was due to ER-embedded LDs and not free LDs (Fig. 17D and F).

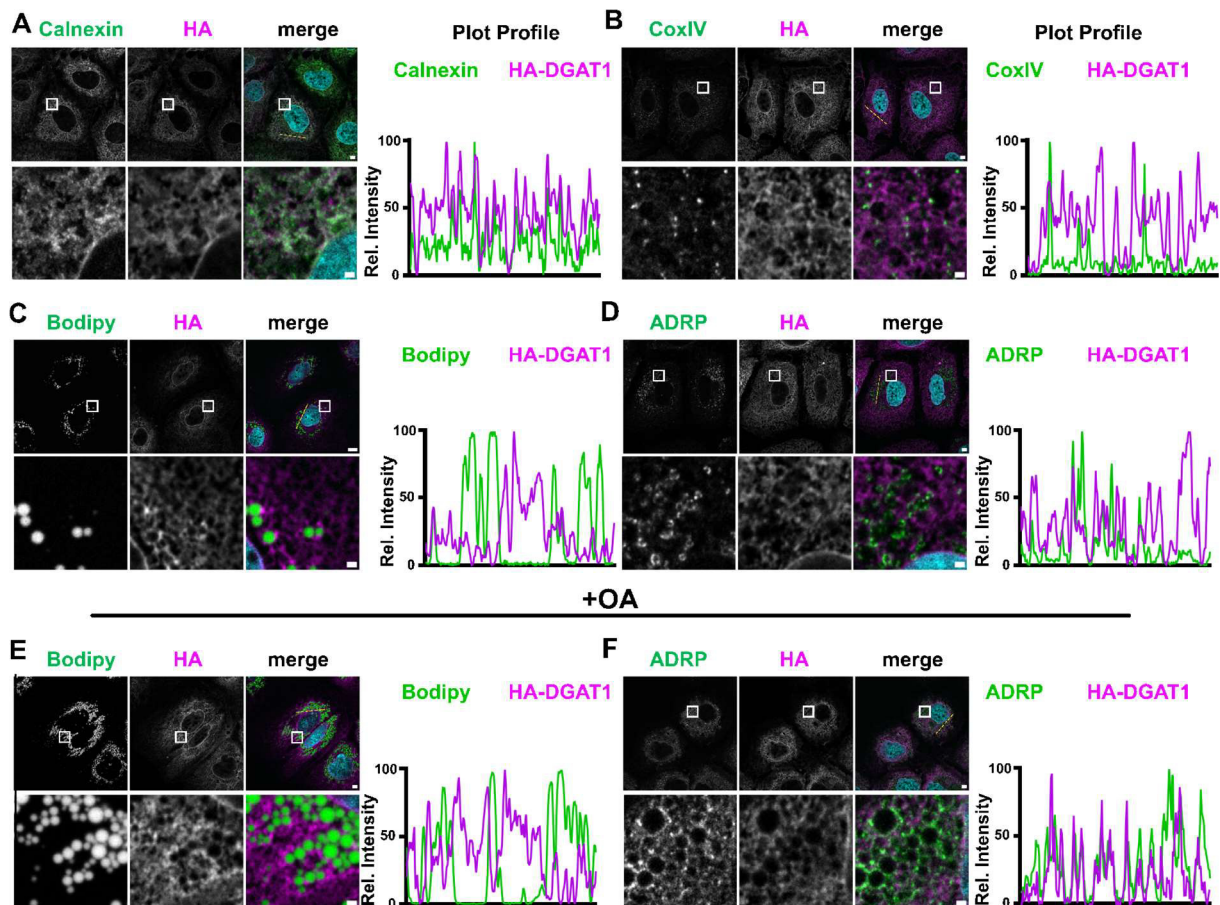


Figure 17: Subcellular localization of HA-DGAT1. (A-F) Lunet N hCD81 cells were transduced with lentiviruses to express HA-DGAT1. In (E) and (F), cells were treated with 360 μ M oleic acid (OA) 6 h prior to fixation. HA-DGAT2 was detected with anti-HA immunofluorescence staining and depicted in magenta. ER (Calnexin, (A)), mitochondria (CoxIV (B)) and LDs (BODIPY 493/503 (C,D), ADRP (D,F)) were co-stained and depicted in green. Nuclei were stained with DAPI and depicted in blue. The white box area in overview images (upper row of images in each panel) is enlarged in the lower row. Intensity plot profiles were computed along the depicted dotted line. Representative images of at least 3 independent experiments are shown.

In comparison to HA-DGAT1, the IF signal of HA-DGAT2 was much weaker but also localized at the ER membrane (Fig. 18A). The nuclear envelope was particularly covered by HA-DGAT2 signal (Fig. 18A). Furthermore, we detected HA-DGAT2 in close proximity to LDs and additional stimulation of LD biogenesis by OA facilitated the detection of HA-DGAT2 at the LD-surface, as described by others [113,115] (Fig. 18C and D). In contrast to HA-DGAT1, the ring-like structures of the HA-DGAT2 signal were very similar to the structures detected in the ADRP staining and overlapped strongly with the BODIPY signal in the OA-treated cells, suggesting an LD association in addition to localization at the ER membrane (Fig. 18C-F). Moreover, HA-DGAT2 signal also partially overlapped with the mitochondria marker, but the association was not as clear as for ER or LD surface (Fig. 18B). Of note, HA-DGAT2 often accumulated in an LD-free perinuclear region, which could hint towards Golgi-association (Fig. 18A). However, did not verify this observation in this study with corresponding Golgi markers.

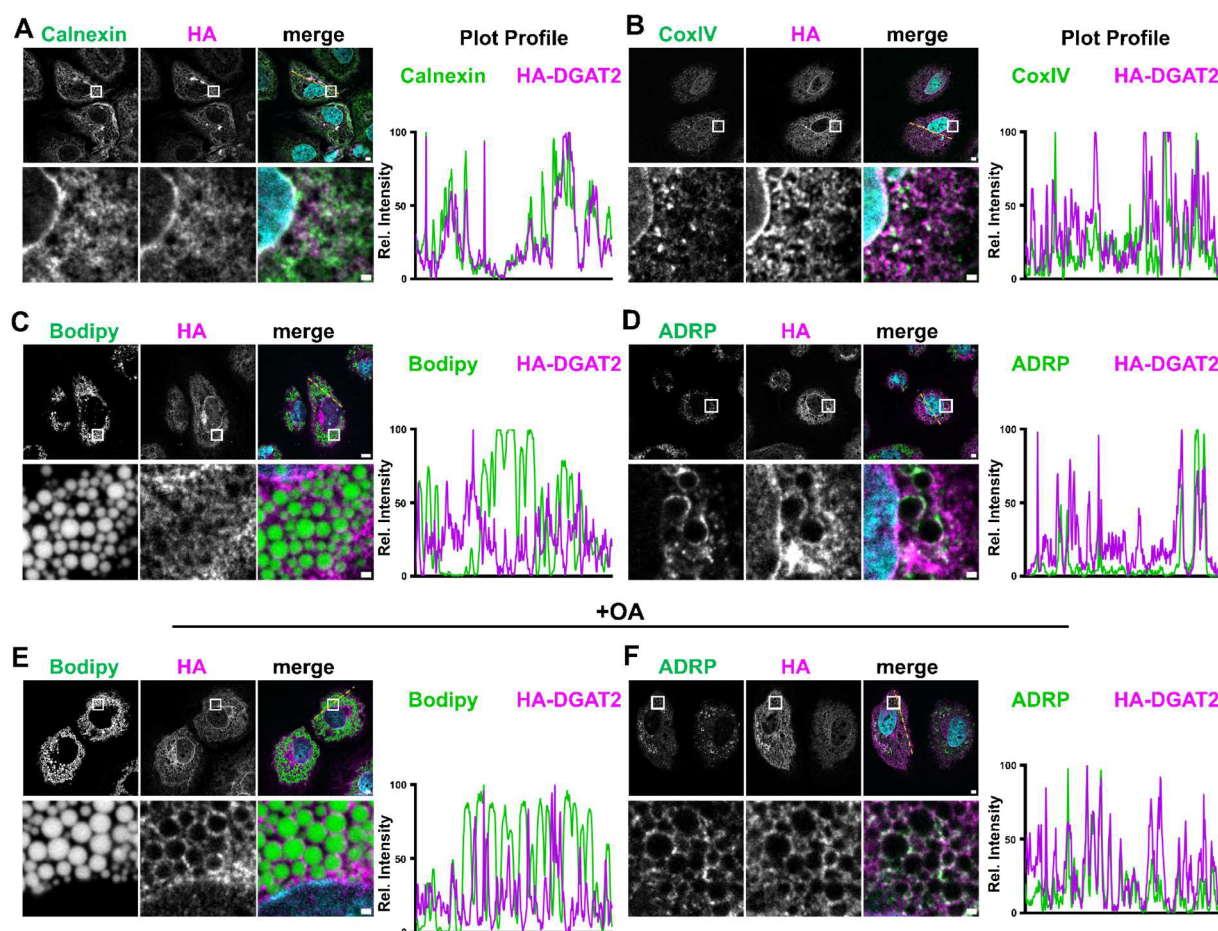


Figure 18: Subcellular localization of HA-DGAT2. (A-F) Lunet N hCD81 cells were transduced with lentiviruses to express HA-DGAT2. In (E) and (F), cells were treated with 360 μ M (oleic acid) OA 6 h prior to fixation. HA-DGAT2 was detected with anti-HA immunofluorescence staining and depicted in magenta. ER (Calnexin, (A)), mitochondria (CoxIV (B)) and LDs (BODIPY 493/503 (C,E), ADPR (D,F)) were co-stained and depicted in green. Nuclei were stained with DAPI and depicted in blue. The white box area in overview images (upper row of images in each panel) is enlarged in the lower row. Intensity plot profiles were computed along the depicted dotted line. Representative images of at least 3 independent experiments are shown.

Thanks to extensive topological studies on the mouse homologue of DGAT2, the protein domains of DGAT2 responsible for the different organelle associations are known (Fig. 5) [111,114,137].

To investigate whether the subcellular localization of the DGAT2 affects the antiviral activity of the protein, we cloned a set of selected previously published DGAT2 mutants to generate a variety of either ER, LD, or mitochondrial localization deficient and catalytically active or inactive proteins (Fig. 19A). All resulting DGAT2 mutants were fused to an HA-tag at the N-terminus to allow detection by WB and IF (Fig. 19). We successfully detected the tested HA-DGAT2 variants by WB around 40 kDa (Fig. 19B). Confirmatively, the protein bands of the deletion mutants DGAT2-del30-67 (mito mut2), DGAT2-del66-115 (ER mut) and DGAT2-del327-350 (LD mut2) were found to have a lower molecular weight due to the respective protein truncations (Fig. 19B). Of note, the expression of the wildtype DGAT2 and DGAT2_L83A protein seemed to be elevated in comparison to the tested DGAT2 mutants (Fig. 19B).

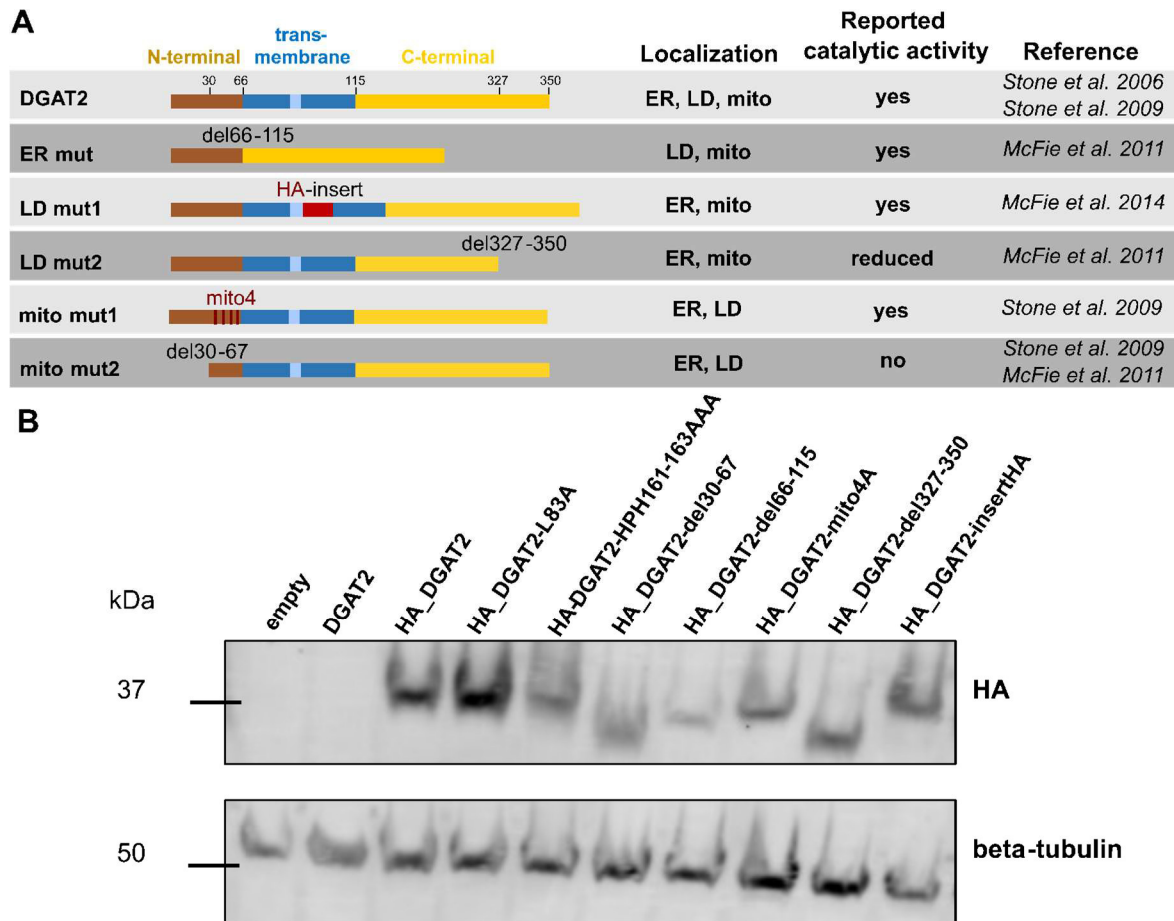
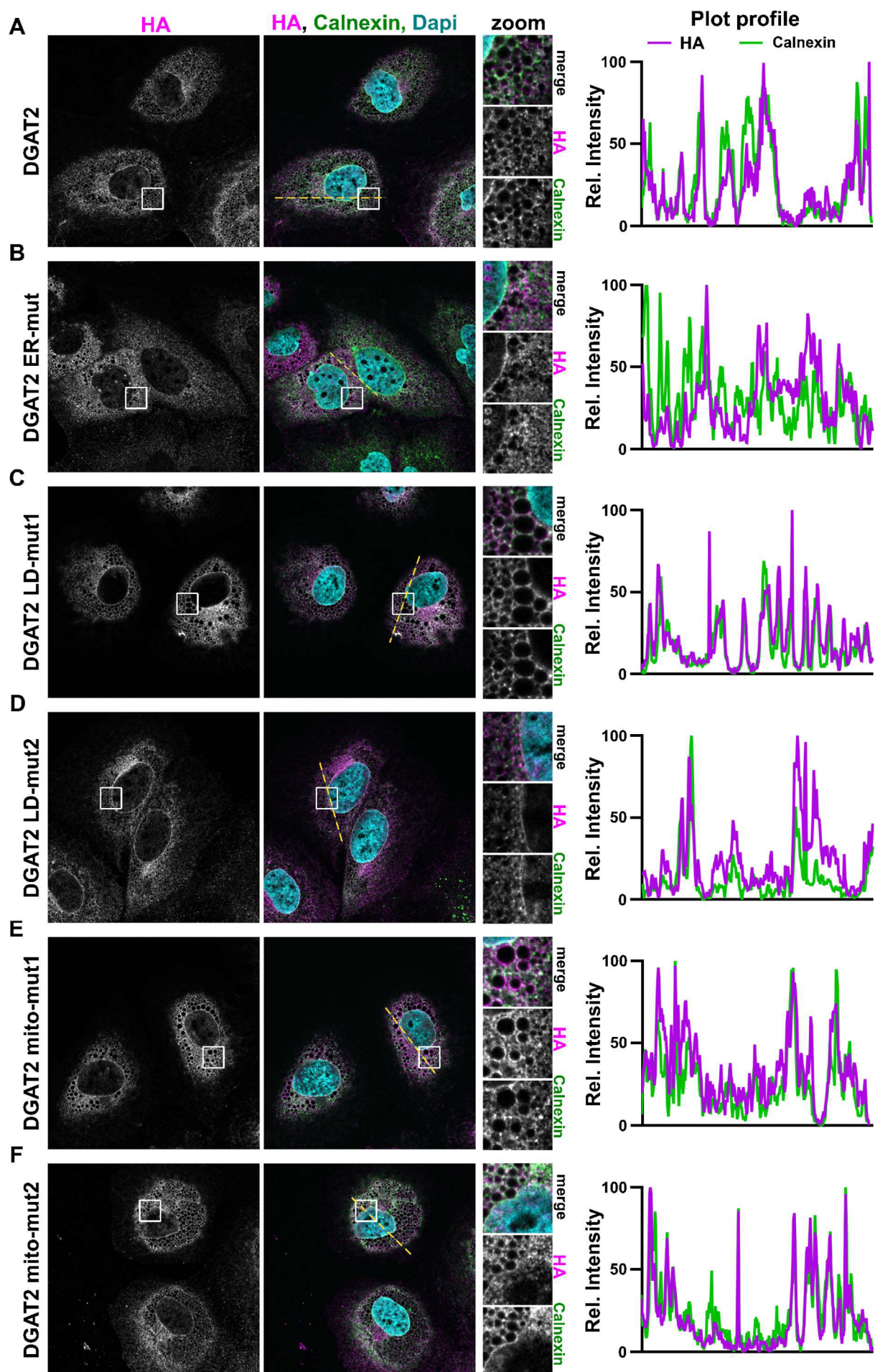


Figure 19: Subcellular localization mutants of DGAT2. (A) Mutant versions of DGAT2 that were reported to show abolished subcellular localization. The depicted panel includes DGAT2 versions with deficient ER (ER mut), LD (LD mut1 and LD mut2) or mitochondria (mito mut1, mito mut2) association. Truncations, insertions and point-mutations of the different protein domains of DGAT2, as well as reported protein localization and catalytic activity are indicated. **(B)** Detection of the HA-tagged versions of DGAT2 detected by Western Blot. Representative image of two independent experiments.

In the next step, we investigated the association of the different DGAT2 constructs with the ER membrane and LD by IF (Fig. 20). Due to the lack of a clear association with mitochondria of the wildtype protein, we did not further verify the localization to this organelle for the set of mutants.

Except for the ER-mutant DGAT2-del66-150, all constructs showed perinuclear ring localization, which is typical for the ER association of DGAT2 [113,115] (Fig. 20A-F). Furthermore, as expected, the LD-surface association of the two mutants DGAT2-del327-350 and DGAT2-insert-HA seemed to be abrogated, as the characteristic ring structure around the LDs was less pronounced (Fig. 20C, D, I, J).



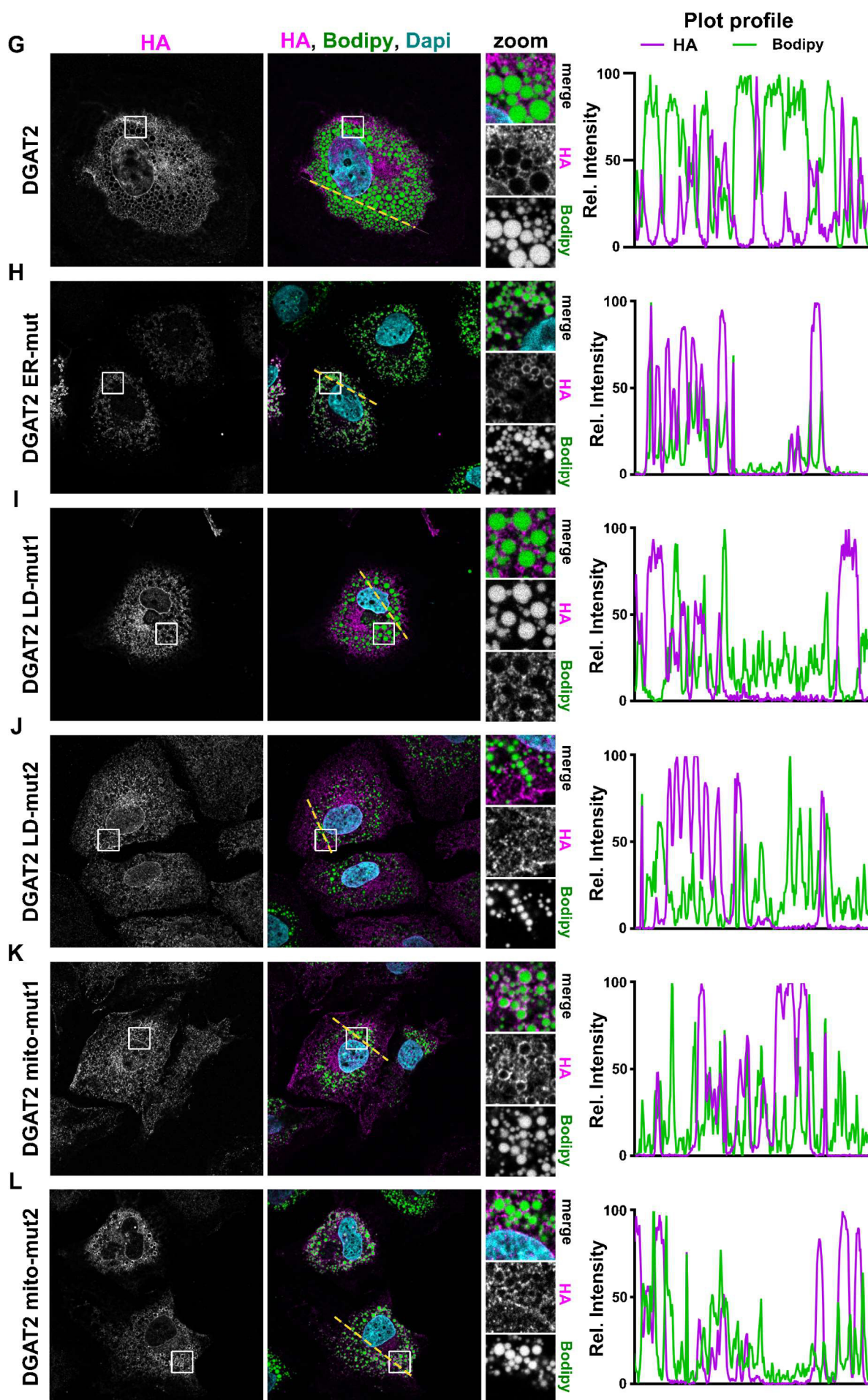


Figure 20: Subcellular localization of the DGAT2 mutant panel. Lunet N hCD81 cells expressing HA-tagged DGAT2 or different mislocalizing mutants of DGAT2 shown in Fig. 19 were treated with 100 μ M OA overnight prior to fixation. **(A-L)** HA-tagged DGAT2 and mutants were detected with an anti-HA antibody (magenta). ER (Calnexin **(A-F)**) or LDs (LD540 **(G-L)**) were co-stained (green). Nuclei were stained with DAPI (blue). The white box area in overview images (upper panel) is enlarged on the right side for each channel. Intensity plot profiles were computed along the depicted dotted yellow line. Representative images of at least 3 independent experiments are shown.

Next, we analyzed the LD accumulation and antiviral phenotype of the DGAT2 mutants by flow cytometry and luciferase assay, respectively (Fig. 21A). Strikingly, all DGAT2 mutants that triggered LD accumulation exhibited an inhibitory effect on HCV replication (Fig. 21B and C). This supports our previous findings, in which the enzymatic activity of DGAT2 and the resulting LD accumulation is a prerequisite for HCV inhibition. Surprisingly, the ER mutant DGAT2_{del66-150}, whose mouse homolog was described as catalytically active [137], neither induced LD accumulation nor inhibited HCV replication (Fig. 21B and C). Consequently, the ER localization of DGAT2, which was present in all other mutants tested, appears to be critical for both LD accumulation and HCV inhibition of DGAT2. In contrast, LD association of DGAT2 was not required for its antiviral effect, as the LD-deficient but catalytically active DGAT2 mutant still inhibited HCV replication (Fig. 21B and C).

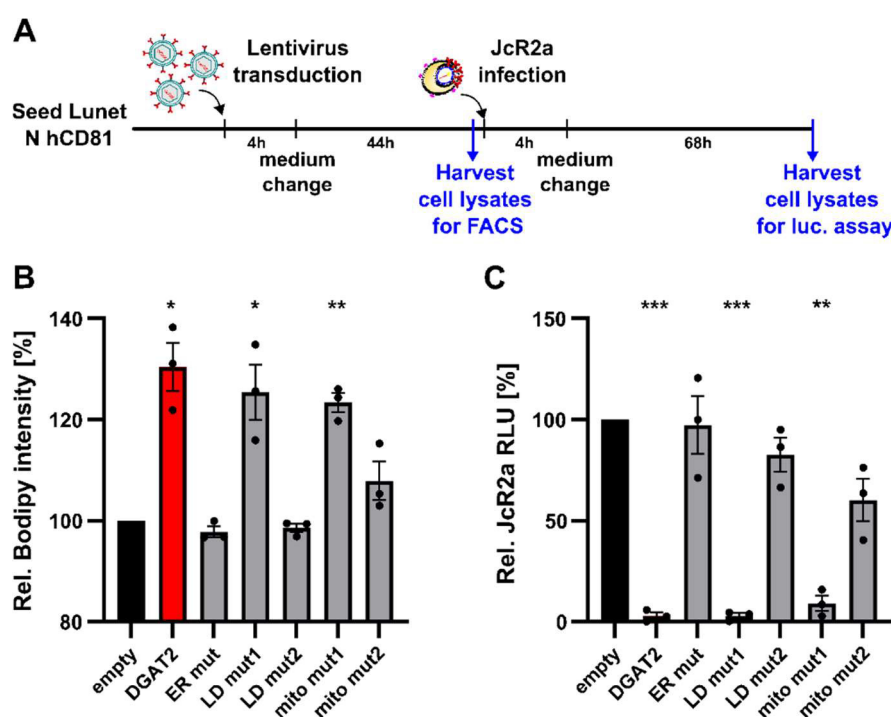


Figure 21: Effect of subcellular localization on the antiviral activity of DGAT2. **(A)** Lunet N hCD81/FLuc cells were transduced with lentiviruses to express the panel of localization deficient mutants described in Fig. 20. 48h after transduction, the cells were harvested for flow cytometry (FACS) or infected with JcR2a. At 72 hpi, the cells were lysed for luciferase assay. **(B)** Relative LD content in Lunet N hCD81 cells expressing the DGAT2 mutants. After staining with BODIPY 493/503, the LD content was measured by flow cytometry using [mRuby2] reference cells (see Fig. 13). Values were normalized to [empty] control cells ($n = 3$). **(C)** Effect of DGAT2 mutants on HCV replication was quantified by luciferase assay. RLuc values (correlating with viral RNA copies) were normalized to FLuc intensities (cell viability measure) of the Lunet N hCD81/FLuc cells. Values relative to the [empty] control cells are depicted. Mean \pm SEM of $n = 3$. Statistically significant changes (Welch's t-test) are indicated by asterisks.

4.2.4. Cell type dependence of the antiviral effect of the DGAT proteins

As HCV is a liver-tropic virus, hepatocytes are the most suitable cell culture system for HCV research. In particular, Huh-7.5 derived Lunet N cells overexpressing the HCV entry receptor CD81 were adapted for efficient HCV viral replication and are also mainly used in this study [138,139]. However, equipped with the required host-factors, various cell lines such as HEK293T cells can also efficiently be infected with HCV and are therefore used as a reference system to understand hepatocyte-specific effects of the HCV replication cycle, e.g. lipo-protein secretion [140–142]. LD biogenesis is a ubiquitous cellular process but is differentially pronounced in various cell types [135]. Consequently, the two ubiquitously expressed DGAT1 and DGAT2 proteins are believed to possess cell-type dependent functions [78] [120,143–146]. This raised the question whether overexpression of DGAT also has an antiviral effect in other HCV permissive hepatic and non-hepatic cell lines. Hence, we tested the sensitivity of HCV to DGAT protein expression in Huh-7.5, HuH6 and HepG2 hepatocytes, as well as in HEK293T (embryonic kidney), HeLa (cervix carcinoma), and Caco-2 (colon epithelia) cells. In order to efficiently infect the non-hepatic lines with HCV, we transfected the viral genome instead of using the classic infection set-up, to overcome cell type dependent differences of viral uptake. Furthermore, the micro RNA 122 (miR-122) required for viral translation initiation was ectopically expressed in HepG2, HEK293T, Caco-2 and HeLa cells, which otherwise express low levels of this host factor [140,147]. We determined successful replication in the utilized cell lines by comparison to Daclatasvir treatment, a replication inhibitor [148] that served as negative control (Fig. 22A-G). Additionally, we measured the expression of both DGAT1 and DGAT2 mRNA in the used cell lines by RT-qPCR (Fig. 22H and I).

As expected, HCV efficiently replicated in Lunet N hCD81, Huh-7.5, and HuH6 cells, indicated by increasing luciferase values over the course of infection (Fig. 22B and C). Furthermore, HCV also replicated in 293T-miR-122 cells (Fig. 22E). In contrast, luciferase values progressively decreased in HepG2-HFL and HeLa-miR-122 (Fig. 22D and G) and HCV did also not robustly replicate in Caco-miR-122 cells (Fig. 22F).

Consistently, DGAT2 overexpression exhibited also a strong inhibitory effect on JcR2a replication in Lunet N hCD81 cells in this transfection set-up (Fig. 22A). Moreover, DGAT2 overexpression was antiviral when expressed in Huh-7.5 cells, but not in HuH6 and 293T-miR-122 cells, although the level of mRNA expression was significantly increased in all these cell lines (Fig. 22B, C, E, H and I). Interestingly, DGAT1 overexpression did not hamper JcR2a replication in Lunet N hCD81 cells in this transient expression set-up (Fig. 22A), which supports our previous findings (Fig. 10). However, the transient expression of DGAT1 was inhibitory in Huh-7.5 cells and in 293T-miR-122 cells at 48 or 24 hours post transfection (hpt), respectively (Fig. 22C and E). Importantly, we detected DGAT1 mRNA expression in all of these cell lines (Fig. 22H and I). However, in contrast to earlier findings, DGAT1 overexpression did not affect DGAT2 mRNA expression levels in any of the tested cell lines (Fig. 22H).

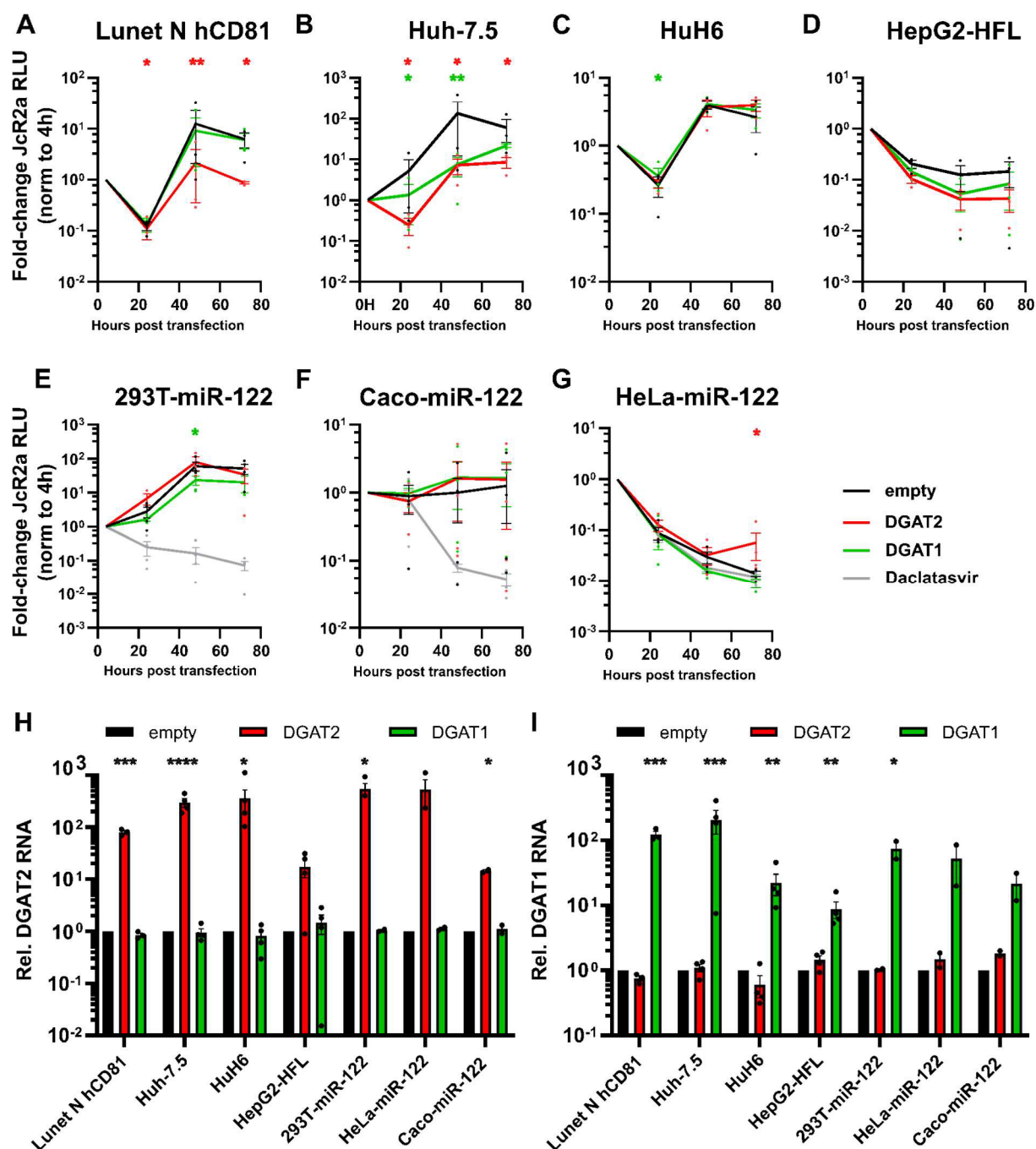


Figure 22: Cell type dependency of DGAT2 antiviral effect. (A-G) Lunet N hCD81, Huh-7.5, HuH6, HepG2-HFL, 293T-miR-122, Caco-miR-122 and HeLa-miR-122 cells were transduced with lentiviruses to express [empty], [DGAT2] or [DGAT1]. 72 h later, cells were transfected with JcR2a *in vitro* transcripts (IVTs) using lipofectamine. In (E-G), 1 nM Daclatasvir was added to transfected Lunet N hCD81 [empty] cells as control for viral replication. Viral replication was measured by luciferase assay 4, 24, 48 and 72 hpt. Mean \pm SEM values normalized to 4 hpt are depicted ($n = 3$). (H, I) Relative DGAT2 (H) or DGAT1 (I) mRNA expression 48 h after lentiviral transduction. Mean \pm SEM values normalized to [empty] control are depicted ($n = 2-3$). Statistically significant changes of the log-transformed values compared to the empty control group ((A-G) ANOVA, Dunnet's test, (H,I) Welch's t-test) are indicated by asterisks.

Since no antiviral effect of DGAT2 expression was observed in HuH6 and 293T-miR-122 cells, it was then investigated whether the missing antiviral effect reflects in the lack of LD accumulation upon DGAT2 expression. Subsequently, we measured the LD content of the cell lines which efficiently replicated HCV upon DGAT1 and DGAT2 expression by flow cytometry (Fig. 23).

Matching previous results, DGAT2 expression significantly stimulated LD accumulation in Lunet N hCD81 cells and had a stronger increase in LD content compared to treatment with 100 μ M OA (Fig. 23A). Also, DGAT1 stimulated the LD content in comparable levels to 36 μ M OA induction, but much milder than DGAT2 (Fig. 23A). Interestingly, in Huh-7.5 cells, overexpression of both DGAT2 and DGAT1 had a stronger effect than in Lunet N hCD81 cells, and we found LD accumulation exceeding the addition of 360 μ M and 100 μ M OA, respectively (Fig. 23B). In HuH6 cells, we detected an 1.8-fold LD content increase upon DGAT2 overexpression, which was comparable to the addition of 360 μ M OA or the effect of DGAT2 expression in Lunet N hCD81 cells (Fig. 22A and C). In contrast, the effect on LD accumulation in 293T-miR-122 cells was milder (1.2-fold increase) and comparable to 100 μ M OA addition (Fig. 23D). In summary, despite LD stimulation in HuH6 and 293T-miR-122 cells, DGAT2 expression did not hamper HCV in these cell lines.

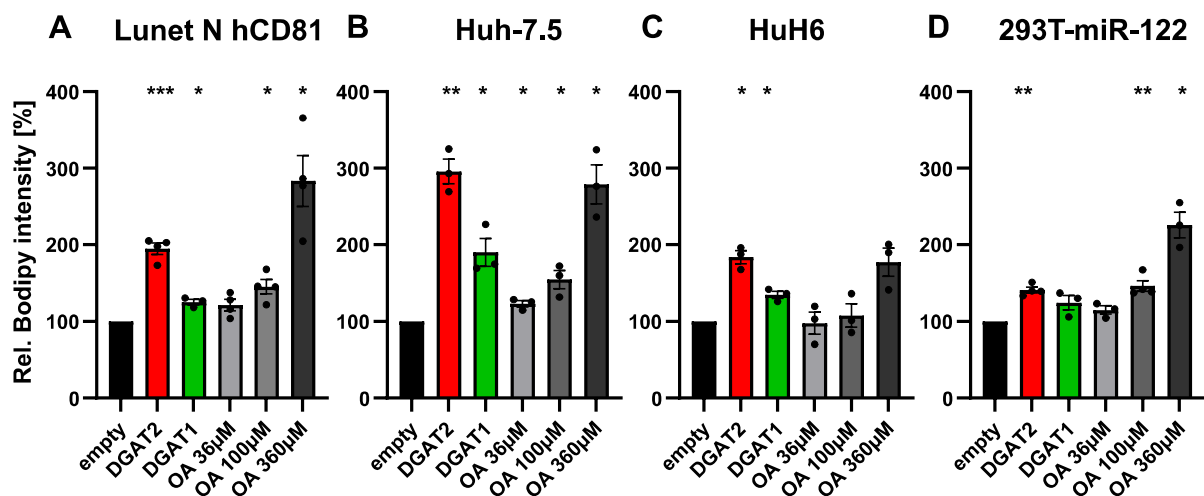


Figure 23: DGAT2 effect on LD accumulation in different cell lines. Lunet N hCD81, Huh-7.5, HuH6 and 293T-miR-122 cells were transduced with lentiviruses to express DGAT2, DGAT1 or empty vector control. Cells were harvested 48 h after transduction and the LD content was measured by flow cytometry utilizing mRuby2-positive control cells (as described in Fig. 13). OA (36, 100 or 360 μ M, 6 h prior harvest) treated mock-transduced cells were included as positive control. Mean \pm SEM values normalized to [empty] control are depicted (n = 3). Statistically significant changes (Welch's t-test) are indicated by asterisks.

To verify this finding, we tested the antiviral effect and LD accumulation also in HuH6 and 293T-miR-122-cell lines that stably overexpressed DGAT2 (Fig. 24). Thereby, lower transduction rates that were observed in 293T-miR-122 and HuH6 cells (data not shown) were circumvented.

Also in this set-up, DGAT2 expression did not impair HCV replication in HuH6 and in 293T-miR-122 cells (Fig. 24A-C). Consistent with the results in transient transduction, LDs were accumulated in HuH6 cells also under stable DGAT2 expression (Fig. 24E). In contrast, we detected no LD accumulation in 293T-miR-122 cells under stable DGAT2 expression (Fig. 24F).

Therefore, the lack of LD upregulation correlates with the missing antiviral effect in 293T-miR-122 stable cell lines but fails to explain the missing antiviral effect of DGAT2 in HuH6 cells. This suggests that there might be a further factor besides LD accumulation that determines the cell-type dependent sensitivity of HCV replication to DGAT2 overexpression. Subsequently, JcR2a infection assays in HuH6 and 293T-miR-122 cells are suitable tools to further decipher the mechanism behind the DGAT2 antiviral activity due to being insensitive to DGAT overexpression.

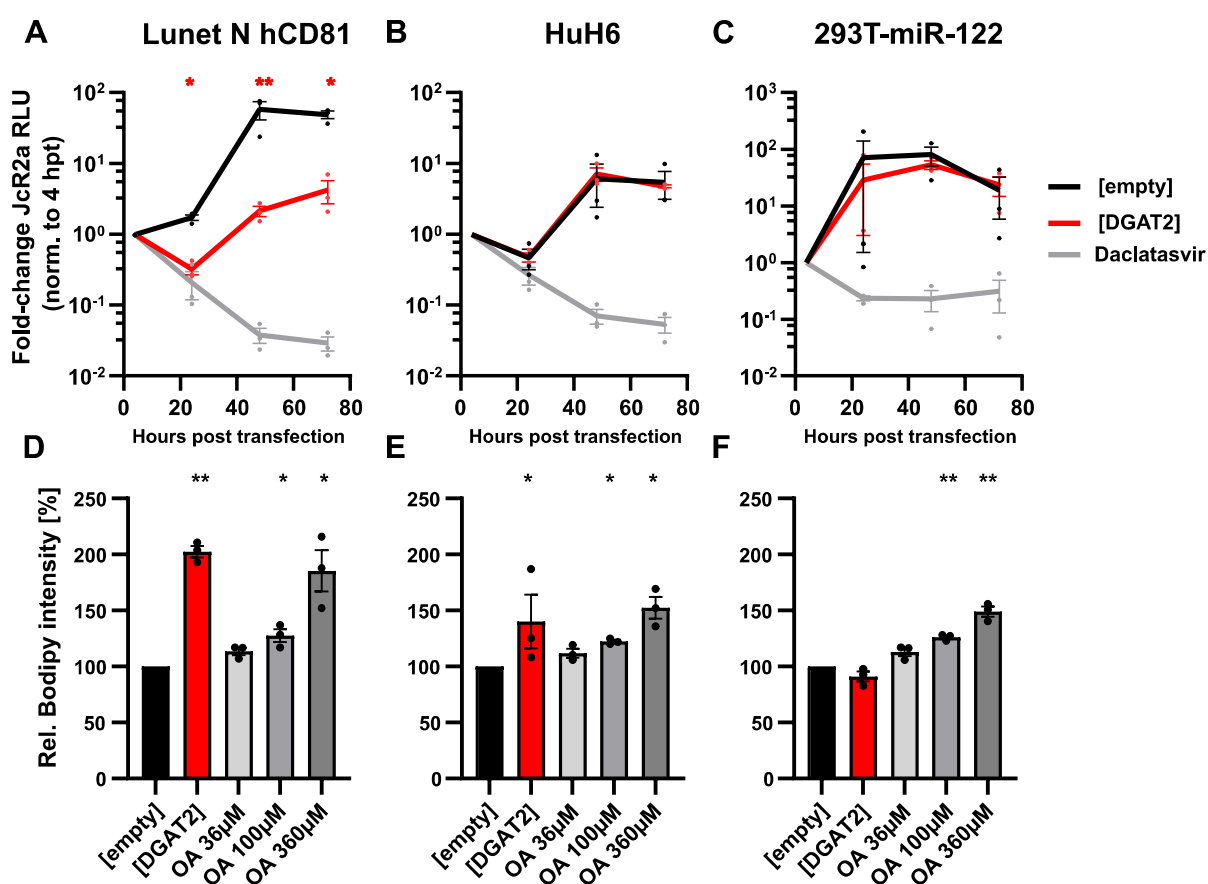


Figure 24: Antiviral effect of DGAT2 in stable cell lines. (A-C) Lunet N hCD81, HuH6, and 293T-miR-122 cells stably expressing [DGAT2] or [empty] vector control were transfected with JcR2a IVTs by using lipofectamine. 1 nM Daclatasvir was added to transfected Lunet N hCD81 [empty] cells as control for viral replication. Viral replication was measured by luciferase assay 4, 24, 48 and 72 hpt. Mean \pm SEM values normalized to 4 hpt are depicted ($n = 3$). (D-F) LD content of Lunet N hCD81, HuH6, and 293T-miR-122 cells stably expressing [DGAT2] or [empty] vector control measured by flow cytometry utilizing mRuby2-positive control cells (as described in Fig. 13). OA (36, 100 or 360 μ M, 6 h prior harvest) treated mock-transduced cells were included as positive control. Mean \pm SEM values normalized to [empty] control are depicted ($n = 3$). Statistically significant changes ((A-C) ANOVA, Dunnet's test, (D-F) Welch's t-test) are indicated by asterisks.

4.3. Viral determinants of the DGAT2 antiviral activity

4.3.1. Effect of DGAT2 expression on various HCV genotypes

Not only the expression of DGAT proteins, but also HCV infection itself triggers LD accumulation in hepatocytes, leading to steatohepatitis [149]. The severity of this effect varies among different HCV genotypes and is most prominent for infection with HCV genotype 3 [4].

Since we established a correlation between DGAT2 antiviral activity and LD accumulation upon DGAT protein expression, we wondered whether the highly steatogenic genotype 3a would respond differently to DGAT2 overexpression. To this end, we transfected a subgenomic replicon of the genotype 3a (DBN3a NS3-5B) into the stable DGAT Lunet N hCD81 cell lines. We compared the replication to the full-length reporter virus JcR2a of genotype 2 and the SGRs of the genotypes 2a (JFH1-NS3-5B) and 1b (Con1-NS3-5B) (Fig. 25). JcR2a, JFH1-NS3-5B, and Con1-NS3-5B kinetics were performed by G.V..

Interestingly, despite different replication kinetics, all tested HCV constructs were sensitive to the overexpression of DGAT2 (Fig. 25A-D). In detail, DGAT2 expression delayed the onset of replication of JFH1 SGR similar as in JcR2a replication and decreased the replication efficiency about 100-fold at 72 hpt (Fig. 25A and B). Furthermore, DGAT2 also affected the replication of Con1 and of DBN3a, although in a milder (~3 to 4-fold at 72 hpt) but still significant manner (Fig. 25C and D). In agreement with our previous observations, we detected lower antiviral activity of the two tested DGAT2 mutants against all tested genotypes (Fig. 25A-D). Altogether, these results indicate that the DGAT2 inhibitory effect is conserved across different HCV genotypes. Since overexpression of DGAT2 also hindered HCV replication in this transfection set-up, the antiviral effect of DGAT2 likely affects HCV replication after the entry step (Fig. 25).

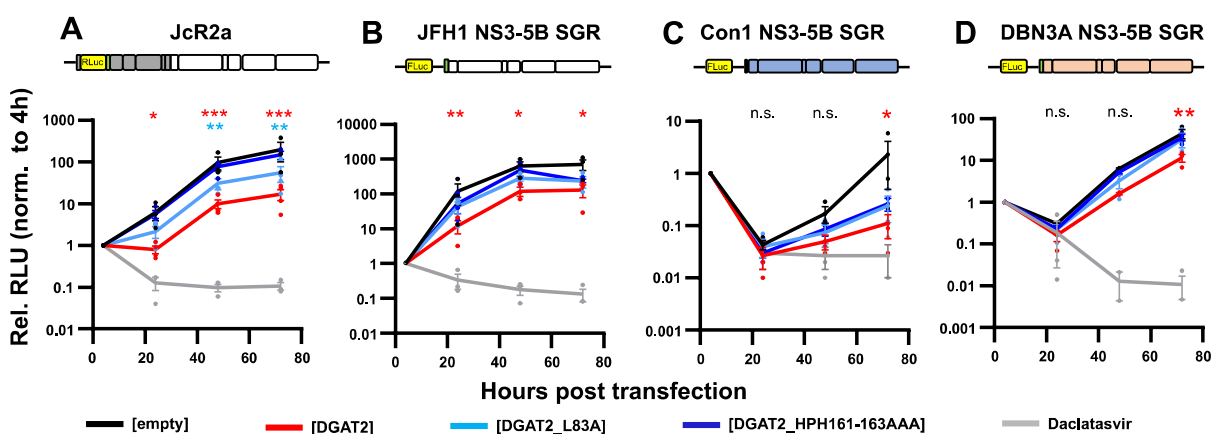


Figure 25: Effect of DGAT2 expression on sub-genomic replicons of different HCV genotypes. (A-D) Full-length JcR2a, JFH1 NS3-5B subgenomic replicon (SGR), Con1 NS3-5B SGR or DBN3A NS3-5B SGR were transfected in Lunet N hCD81 [empty], [DGAT2], [DGAT2_L83A], or [DGAT2_HPH161-163AAA] cell lines by electroporation. 1 nM Daclatasvir was added to transfected Lunet N hCD81 [empty] cells as control for viral replication. Viral replication was measured by luciferase assay at 4-72 hpi. Mean values normalized to 4 hpi \pm SEM are depicted ($n = 3$). Statistically significant changes of log-transformed values compared to the [empty] control group (ANOVA, Dunnet's test) are indicated by asterisks.

4.3.2. Timing of the DGAT2 antiviral effect on HCV replication

To verify the finding that DGAT2 expression affects HCV replication post-entry we used the doxycycline (Dox) inducible TetR-Tet-On expression system (Fig. 26) [150]. In this system, the target protein is ectopically expressed under control of a tetracycline operator (Tet-O) and constitutively suppressed by a repressor (Tet-R). In presence of Doxycycline (Dox), Tet-R is released from the Tet-O, which allows the transcription of the target protein [150]. Here, we generated Dox inducible Lunet N hCD81 cell lines expressing HA-DGAT2 or an empty vector control and verified the inducible expression of HA-DGAT2 by WB (Fig. 26A and B). Remarkably, we observed a strong accumulation of HA-DGAT2 protein already 8 h after induction (Fig. 26B). Consistently, the LD content of Lunet N hCD81/TetR [HA-DGAT2] cells increased to 120 % after 16 h of induction and increased linearly with the duration of Dox treatment (Fig. 26C).

Finally, we used the inducible system to determine at which treatment time point the expression of DGAT2 impairs HCV replication (Fig. 26D). HA-DGAT2 expression was induced either 24 h prior infection or at different times after infection (Fig. 26D). We subsequently measured the HCV replication kinetic by luciferase assay (Fig. 26E). Confirming earlier results, HA-DGAT2 induction prior infection was deleterious for virus replication (Fig. 26E). Interestingly, HA-DGAT2 expression reduced viral replication at late infection time points even when induced 4 or 24 hpi. (Fig. 26E). This suggests that HCV viral replication is sensitive to overexpression of DGAT2 even after its initiation and supports the hypothesis that excess DGAT2 affects a post-entry step of the viral life cycle.

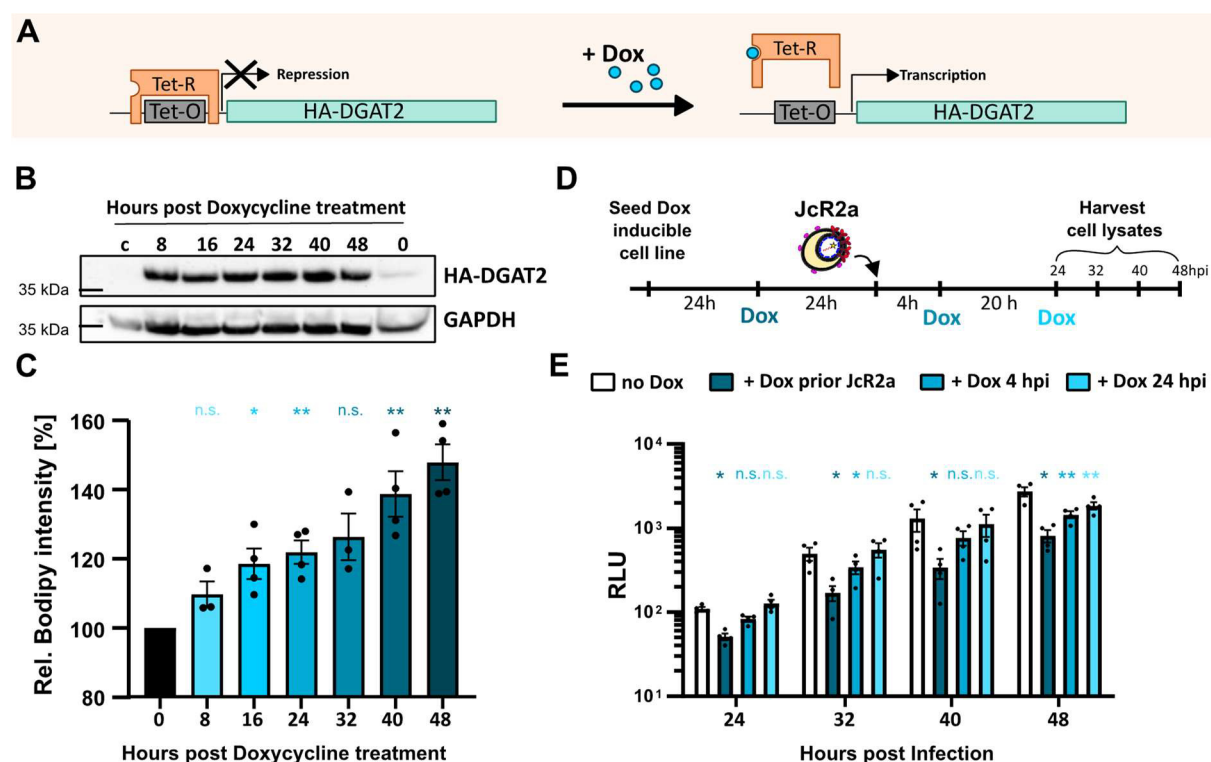


Figure 26: Assessment of the timing of the antiviral effect of DGAT2 in doxycycline-inducible cell line. (A) Schematic representation of the Doxycycline (Dox)-inducible Tet-On system. Expression of the gene of interest (here HA-DGAT2) is controlled by an upstream Tet-Operator (Tet-O) and constitutively repressed by the Tet-Repressor (Tet-R). In presence of Dox, TetR is released from Tet-O, enabling gene transcription. (B) The expression of HA-DGAT2 upon Dox treatment was tested by Western Blot analysis. The first lane shows Lunet N hCD81 [empty] control cell lysate. HA-DGAT2 (~45-50 kDa) was detected by an anti-HA antibody, GAPDH (~36 kDa) was stained as loading control. Representative blot of two independent experiments. (C) The LD content upon Dox treatment was measured by utilizing mRuby2-positive reference cells (see Fig. 13). Mean \pm SEM values normalized to 0 h Dox treatment are depicted (n = 4). (D, E) Dox-inducible HA-DGAT2 Lunet N hCD81 cells were infected with JcR2a and treated with 10 μ g/mL Dox at different times prior to and post infection (untreated, 24 h prior to infection, 4 or 24 hpi). Cell lysates were harvested for luciferase assay at 24, 32, 40 and 48 hpi. Mean \pm SEM values of are depicted (n = 4). Statistically significant changes (compared to 0 h Dox treatment (C) or no Dox treatment (E)) are indicated by asterisks (Welch's test (C), ANOVA, Dunnett' test (E)).

4.3.3. Effect of DGAT protein expression on HCV translation

To further pinpoint the replication step of HCV affected by DGAT2 overexpression, we investigated the effect of DGAT1 and DGAT2 expression on IRES-mediated translation by using the bicistronic dual-luciferase reporter construct pIRF1b [151]. This construct allows to simultaneously measure IRES-mediated translation of the encoded Renilla luciferase and cap-mediated translation of *firefly* luciferase (Fig. 27A).

Neither cap- nor IRES-mediated translation was affected by DGAT1 or DGAT2 expression (Fig. 27B). However, the addition of the translation inhibitor cycloheximide (CHX) strongly reduced the expression of both Renilla and *firefly* luciferase, indicating that the assay was functional. Therefore, it is unlikely that the antiviral activity of DGAT expression is coupled to HCV translation.

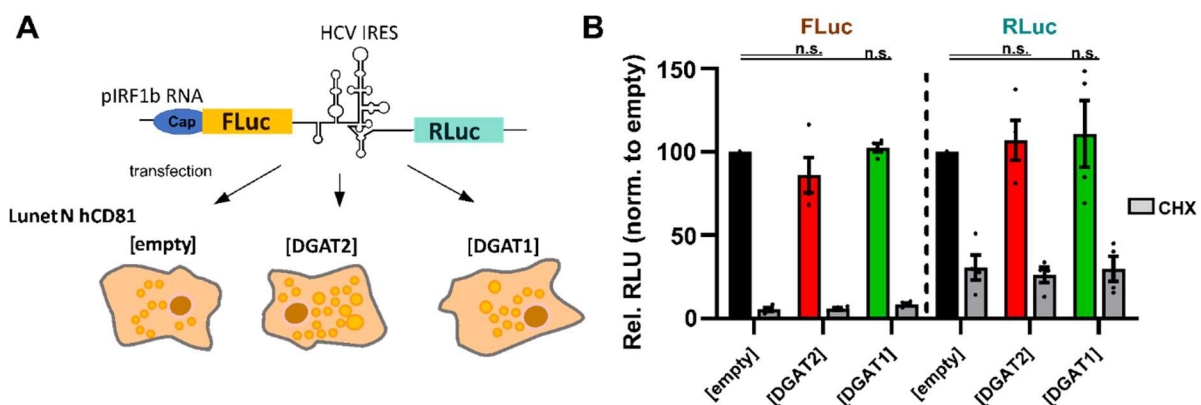


Figure 27: Effect of DGAT expression on HCV IRES-mediated translation. pIRF1b dual luciferase reporter IVTs encoding were transfected in Lunet N hCD81 [empty], [DGAT2] or [DGAT1] cells followed by 8 h incubation in the presence or absence of 20 μ M cycloheximide (CHX). Cap-mediated translation of *firefly* luciferase (FLuc) and HCV IRES-mediated RLuc signals were measured by luciferase assay and plotted normalized to Lunet N hCD81 [empty]. Mean \pm SEM values of are depicted (n = 4). Results of statistical analysis compared to control group are depicted (Welch's t-test).

4.3.4. Effect of DGAT2 on HCV membranous web formation

HCV replication relies on the formation of a replication compartment, the so-called membranous web, which mainly consists of ER-derived double- and multi-membrane vesicles (DMVs and MMVs) [41]. Since previous results suggested an impairment of the HCV replication step by DGAT2 expression, we subsequently investigated the formation of the HCV RO. To this end, we used a pTM-based expression construct encoding the HCV NS3 to NS5B polyprotein under the control of the T7 RNA polymerase promoter to induce membranous web formation independent of viral replication in LunetT7 cells (Fig. 28) [152]. The utilized construct contained GFP-tagged NS5A, which allowed the detection of successfully transfected, NS5A-positive, cells by fluorescence microscopy (Fig. 28 and 29) [41,152].

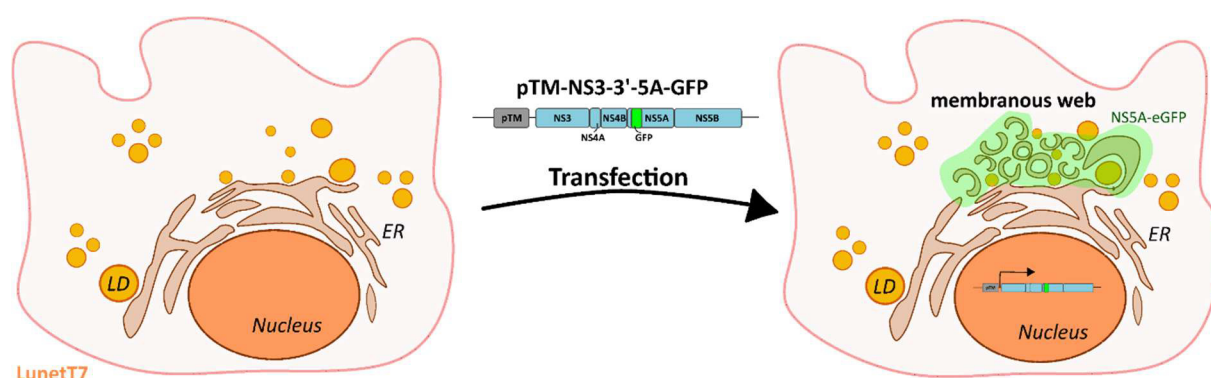


Figure 28: Schematic representation of HCV replication organelle formation induced by the expression of the pTM-NS3-5B-5A-GFP construct. By transfection of Lunet T7 cells with a pTM construct encoding the HCV polyprotein HCV NS3-5B/5A-eGFP, the formation of the HCV membranous web is induced. The eGFP-tagged NS5A enables detection of transfected cells via fluorescence microscopy. The formation of HCV ROs can be analyzed with correlated light electron microscopy.

We investigated the formation of the HCV membranous web in cells expressing empty vector, DGAT2, DGAT2_HPH161-163AAA, or DGAT1 by transmission electron microscopy (Fig. 29). Correlated light electron microscopy (CLEM) experiments and quantification were carried out by Ji Young Lee and Ralf Bartenschlager. As described in previous studies, we detected the accumulation of DMVs and MMVs in the cytoplasm and confirmed the formation of a membranous web-like structure upon expression of the pTM construct in LunetT7 [empty] cells (Fig. 29) [41]. Interestingly, we observed less DMVs in DGAT2-expressing cells and instead a strong accumulation of LDs (Fig. 29B).

We next evaluated the DMV formation quantitatively (Fig. 30). Strikingly, the amount of the DMVs was reduced by DGAT2 and DGAT1, but not by DGAT2_HPH161-163AAA expression (Fig. 30A). In contrast, the DMV size distribution was not affected by neither DGAT2 nor DGAT1 expression (Fig. 30B).

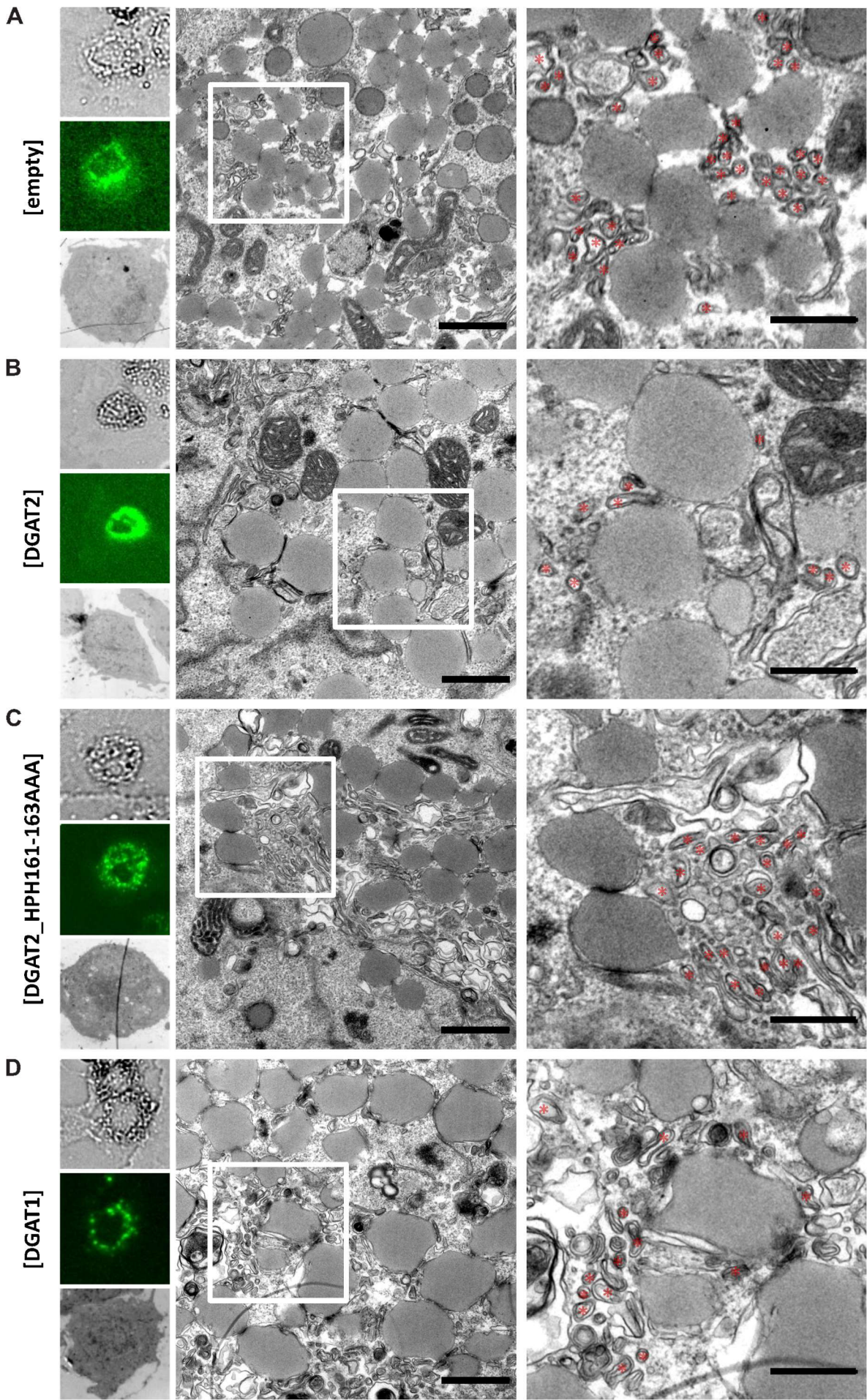


Figure 29: Effect of DGAT protein expression on the HCV membranous web formation. Stable Lunet T7 cells overexpressing [empty] (A), [DGAT2] (B), [DGAT2_HPH161-163AAA] (C) or [DGAT1] (D) were transfected with the pTM expression vector encoding HCV NS3-5B/5A-eGFP. Cells were fixed 24 hpt. Transfected cells were first identified by GFP signal then fixed and further processed for correlated light electron microscopy (CLEM) analysis. The left panel shows from top to bottom bright-field, fluorescent and electron microscopy overview images of a representative cell. The transmission electron microscopy (TEM) image in the middle panel is further enlarged in the white box area and depicted in the right panel. Red asterisks indicate double membrane vesicles (DMVs). Representative images of two independent experiments. Scale bar for middle image, 1 μm ; for magnified image, 500 nm.

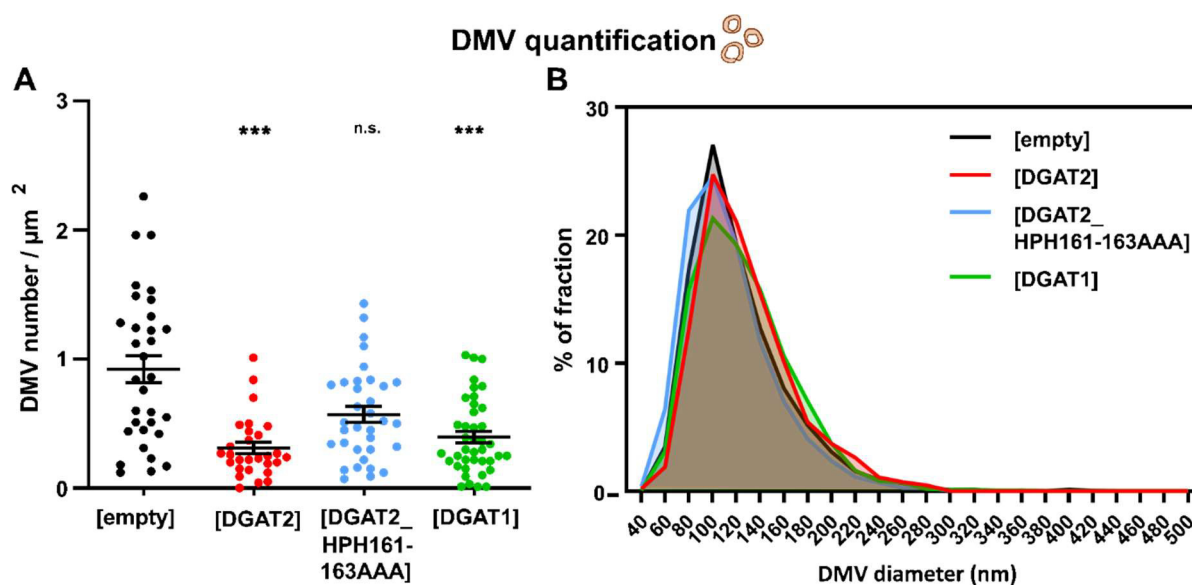


Figure 30: Effect of DGAT protein expression on HCV double membrane vesicles (DMVs). DMV profiles were analyzed using TEM images taken at x4 k magnification. (A) Number of DMVs per μm^2 and (B) size of DMVs in histograms respectively. Statistically significant changes (ANOVA, Dunnet's test) compared to [empty] control group are indicated by asterisks.

Additionally, in line with previous results, excess DGAT2 and DGAT1 expression stimulated LD accumulation (Fig. 31). While the LD numbers were mildly but not significantly increased, the proportion of larger LDs was drastically elevated in DGAT2 and DGAT1-expressing cells (Fig. 31A and B). This trend was reflected in the increased average LD size upon DGAT expression and was consistent with previous IF imaging results (Fig. 31C and Fig. 16).

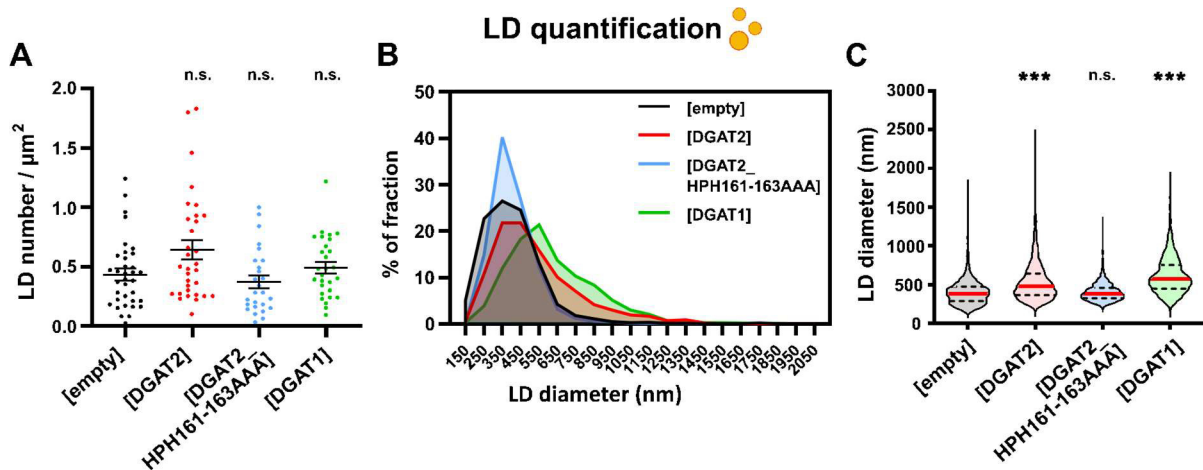


Figure 31: Effect of DGAT proteins on the LD profile in pTM-NS3-3'-NS5A-GFP expressing Lunet T7 cells. LD profiles of stable Lunet T7 cells overexpressing [DGAT2], [DGAT2_HPH161-163AAA] or [DGAT1] transfected with the pTM expression vector encoding HCV NS3-5B/5A-eGFP were analyzed using TEM images taken at x4 k magnification. **(A)** Number of LDs per μm^2 , **(B)** size distribution of LDs in histograms and **(C)** average size in nm, respectively. Statistically significant changes (ANOVA, Dunnet's test) compared to [empty] control group are indicated by asterisks.

Subsequently, it was necessary to test whether the increase in occupancy of the acquired image fields by accumulated LDs affected the observation of decreased DMVs in the examined cell lines. As shown above, OA addition also strongly induced LD accumulation while only mildly affecting HCV infection (Fig. 13 and 14). Therefore, we investigated the effect of DGAT2 expression on the formation of DMVs in comparison to OA or vehicle control addition (Fig. 32, SFig. 2). As expected, both DGAT2 overexpression and OA treatment elevated the LD content of the respective cells (Fig. 32A-C). OA addition enhanced the fraction of larger LDs and had an increasing effect on the average LD size (Fig. 32B and C). More importantly, OA treatment did not impair DMV formation and only had a mild increasing effect on the DMV diameter, while DGAT2 expression significantly reduced the DMV amount (Fig. 32D and E).

In conclusion, the antiviral effect of DGAT2 expression was pinpointed to a deficiency in the HCV RO formation and could not be reproduced through mere LD accumulation by OA addition.

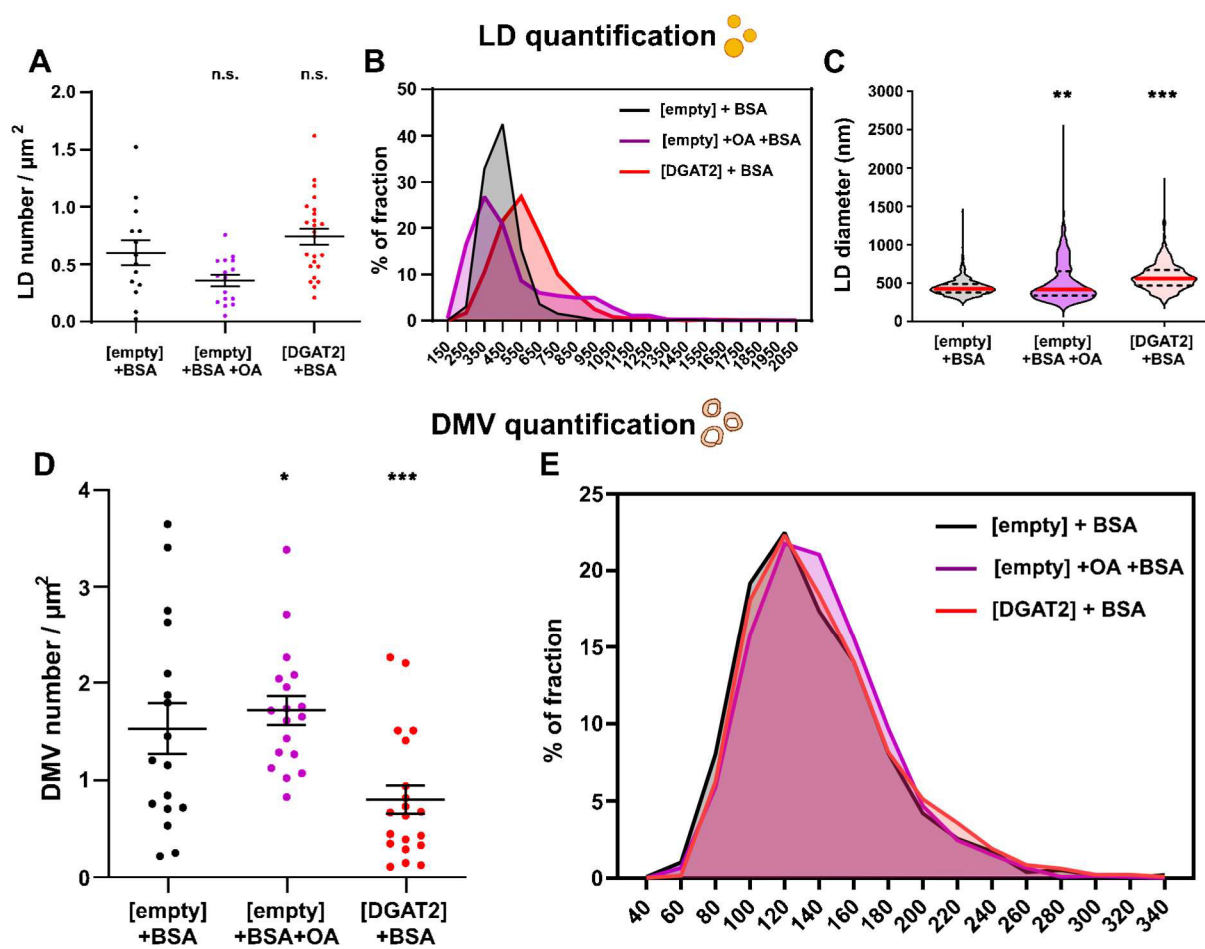


Figure 32: Comparison of DMV formation in pTM- NS3-3'-NS5A-GFP expressing Lunet T7 cells upon OA treatment and DGAT2 expression. Lunet T7 cells stably overexpressing [DGAT2] or [empty] vector were transfected with the pTM expression vector encoding HCV NS3-5B/5A-eGFP and treated with BSA (30 $\mu\text{g}/\text{mL}$) or 360 μM OA combined with BSA 18 hpt. Cells were fixed 24 hpt and LD (A-C) and DMV (D, E) profiles were analyzed by using TEM images taken at x4 k magnification. **(A)** LD number per μm^2 , **(B)** size distribution in histograms and **(C)** average size in nm. **(D)** DMV number per μm^2 and **(E)** size distribution in histograms. Statistically significant changes (ANOVA, Dunnet's test) compared to [empty] control group are indicated by asterisks.

During the experiments, we repeatedly observed LDs enwrapped by ER membranes in the immediate vicinity of DMVs, as already described in [30] (Fig. 33). Surprisingly, these enwrapped LDs were also found in DGAT2-overexpressing cells (Fig. 33A). The amount of ER enwrapped LDs per inspected image field was even higher in DGAT2 compared to the control cells (Fig. 33B). The effect was independent of the catalytic activity of DGAT2, as the numbers of ER-enwrapped LDs in DGAT2-expressing cells was similar to the mutant expressing cells (Fig. 33B). However, DGAT1 expression did not elevate the amount of ER-enwrapped LD content compared to the control (Fig. 33).

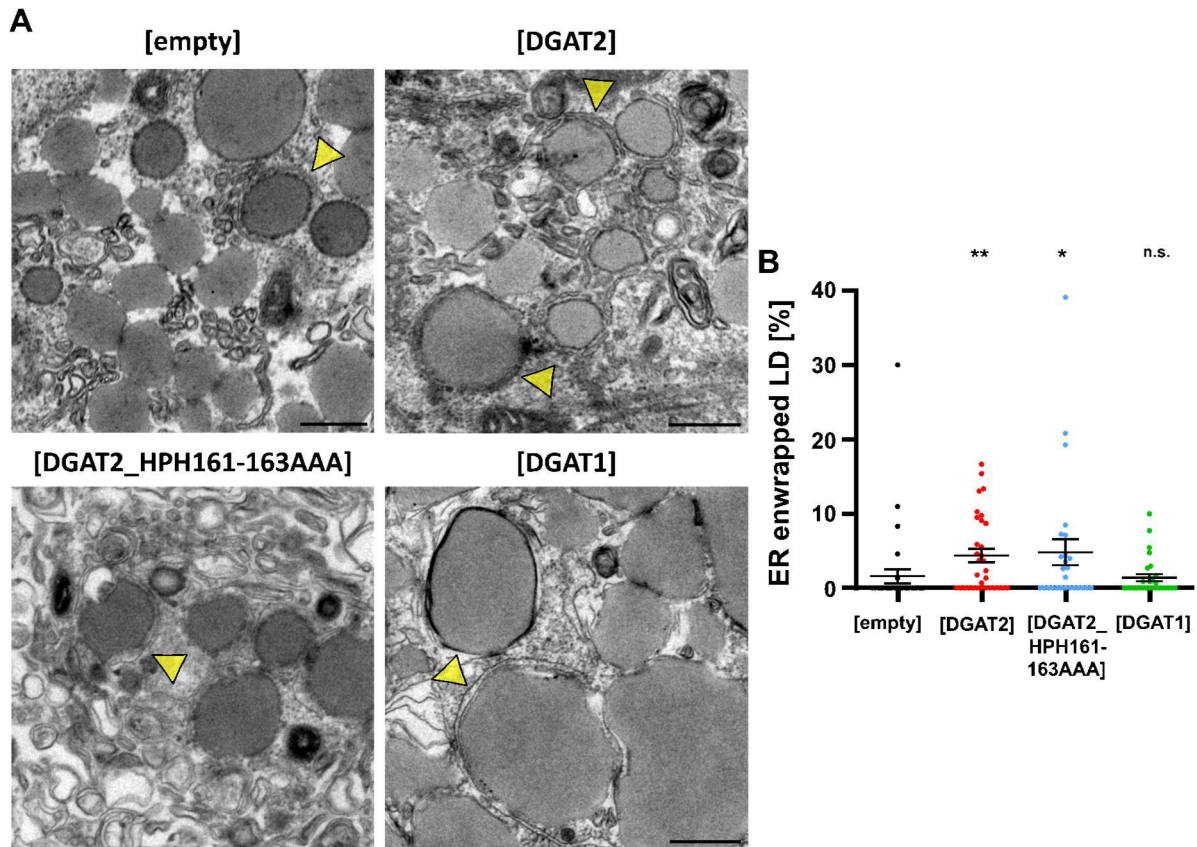


Figure 33: Effect of DGAT protein expression on the enwrapment of LDs in the HCV membranous web. Lunet T7 cells stably overexpressing [DGAT2], [DGAT2_HPH161-163AAA], [DGAT1] or [empty] vector were transfected with the pTM expression vector encoding HCV NS3-5B/5A-eGFP. Cells were fixated 24 hpt and LDs enwrapped by ER membranes as indicated in (A) by yellow arrows were counted. (B) Percentage of LDs enwrapped by ER per quantified. Statistically significant changes (ANOVA, Dunnet's test) compared to the [empty] control group are indicated by asterisks. Scale bar, 500 nm.

4.3.5. Effect of DGAT protein expression on single-stranded positive-sense RNA viruses

Due to the inhibitory effect on the formation of the HCV membranous web, we wondered whether the expression of DGAT2 also has an inhibitory effect on other viruses that rely on the formation of a membranous RO. Therefore, we tested the replication of two Flaviviruses, ZIKV and LGTV, as well as human coronavirus (HCoV-229E) and Hepatitis E virus (HEV), for their sensitivity to DGAT2 or DGAT1 overexpression (Fig. 34). ZIKV and LGTV were tested together with Lina Schlaeger, while HCoV-229 was tested by G.V. and HEV in collaboration with Volker Kinast.

Interestingly, both tested flaviviruses, ZIKV and LGTV, were slightly sensitive to overexpression of DGAT2 and DGAT1 (Fig. 34A and B). Same as for HCV, the DGAT2 catalytic activity was crucial for the antiviral effect (Fig. 34A and B). Remarkably, DGAT1 showed a strong antiviral effect on LGTV replication and reduced viral titers 10-fold (Fig. 34B). Compared with the positive control in the form of knockdown of the flavivirus host factor ATP6VOC [153], however, the effect of DGAT expression was much milder (Fig. 34B). Neither HCoV229E nor HEV were hampered by DGAT2 nor DGAT1 expression (Fig. 34C and D). These findings suggest that not only HCV but also other flaviviruses are sensitive to DGAT2 overexpression, although the extent of the effect may differ between viruses.

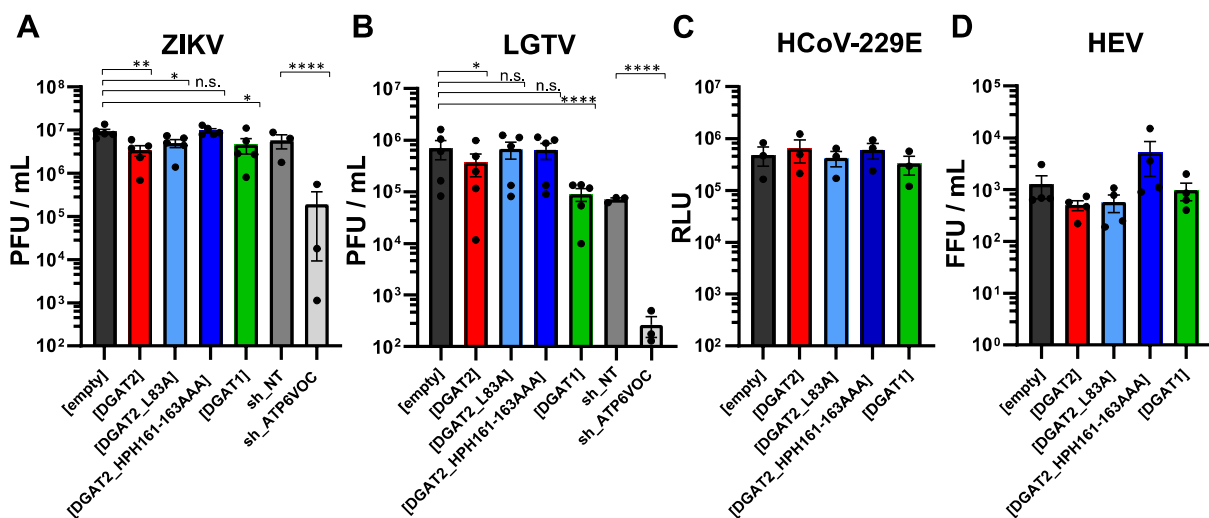


Figure 34: Effect of DGAT protein expression on positive-sense single-stranded RNA viruses dependent on RO formation. **A)** Zika virus (ZIKV) and **(B)** Langat virus (LGTV) titers produced in Lunet N hCD81 cells expressing [empty], [DGAT2], [DGAT2_L83A], [DGAT2_HPH161-163AAA] or [DGAT1] or Lunet N hCD81 cells expressing an shRNA against the ATP6VOC host factor (sh_ATP6VOC [153]) or a non-targeting shRNA (sh_NT). The cell lines were infected with ZIKV or LGTV at a multiplicity of infection of 0.1 for 96 h. Released infectious titers were measured by plaque assay and plotted as plaque forming units (PFU) per mL (n = 3-5). **(C)** Human coronavirus 229E (HCoV-229E) replication in stable DGAT Lunet N hCD81 cells. Cells were infected with HCoV-229E RLuc for 24 h and viral replication was measured by luciferase assay (n = 3). **(D)** Hepatitis E virus (HEV) progeny virus particles production in stable Lunet N hCD81 cell lines infected with HEV genotype 3 (Kernow-C1 p6 clone). Non-enveloped progeny virus was quantified by titration on naïve HepG2/C3A cells. Titers were determined by IF and plotted as focus forming units (FFU) per mL (n=4). Statistically significant changes of the log-transformed values compared to the [empty] control or sh_NT expressing cells (ANOVA, Dunnett's test) are indicated by asterisks.

4.4. Attempts to reverse the DGAT2 inhibitory phenotype

As shown above, LD accumulation as well as ER- rather than LD association seems to be important for the DGAT2 antiviral activity. In line with this, the inhibitory effect of DGAT2 expression affected the DMV formation of the HCV RO-, a highly complex membrane reshuffling process, that occurs at the ER [41,79]. As both DMVs and LDs originate from the ER-membrane, these findings suggest that the ER-located DGAT-mediated TAG biosynthesis might alter the host cell lipid landscape in a way that is deleterious for the formation of the membranous web.

Based on the hypothesis that overexpression of DGAT2 leads to an imbalance of membrane lipids, we further tested whether targeted alteration of the lipid landscape could compensate for excess TAG formation in DGAT2-expressing cells and thereby restore functional HCV replication. Therefore, in the next step, we attempted to reduce the antiviral effect of DGAT2 either by the co-expression of lipid-metabolizing enzymes (section 4.4.1) or by the addition of various lipid analogues (section 4.4.2).

4.4.1. Co-expression of lipid-metabolizing enzymes

We selected several proteins upstream of DGAT2 in the TAG biogenesis pathway and co-expressed them with DGAT2 or an empty vector control prior to infection with HCV (Fig. 35). The panel of co-expressed proteins consisted of the following: (i) AGPAT1 and 2, which generate PA from lyso-PA [72], (ii) Lipin 1 and 2, which convert PA to DAG [74], (iii) the lipase ATGL and its activator ABHD5 in wildtype and mutant versions, which hydrolyze TAG into DAG [92,93], and, finally, (iv) PCYT1A, which catalyzes the rate-limiting step of the PC-biosynthesis and provides the required phospholipids during LD growth [91] (Fig. 35). ATGL, ABHD5, and PCYT1A constructs have been prepared by G.V. priorly. The protein expression of the utilized ATGL and ABHD5 constructs upon lentiviral transduction was shown in [129]. Furthermore, we fused both Lipin and AGPAT constructs to a Flag-tag at the C-terminus and tested the antiviral effect of these tagged constructs in parallel to the untagged proteins (Fig. 35 and SFig. 3). Importantly, we detected the expression of Flag-tagged Lipin2, AGPAT1, AGPAT2, and PCYT1A in Lunet N hCD81 cells by WB, but not Flag-tagged Lipin1 (SFig. 3).

We subsequently expressed all constructs in Lunet N hCD81 [empty] or [DGAT2] cell lines and measured the replication of JcR2a in each condition by luciferase assay (Fig. 35B and C). Additionally, we assessed the impact of the expressed constructs on cell viability using Lunet N hCD81/FLuc cells (Fig. 35D).

Surprisingly, the expression of the panel of tested proteins involved in the TAG biosynthesis did not affect virus replication in neither empty vector nor DGAT2-expressing cells (Fig. 35C). We observed a mild, but not statistically significant increase in viral titers in DGAT2-expressing cells under ABHD5 expression (Fig. 35C). However, the observed regulations did not exceed the fluctuation range of the luciferase values (Fig. 35D). Additionally, we observed no effect on viral replication upon expression of the Flag-tagged constructs (SFig. 3).

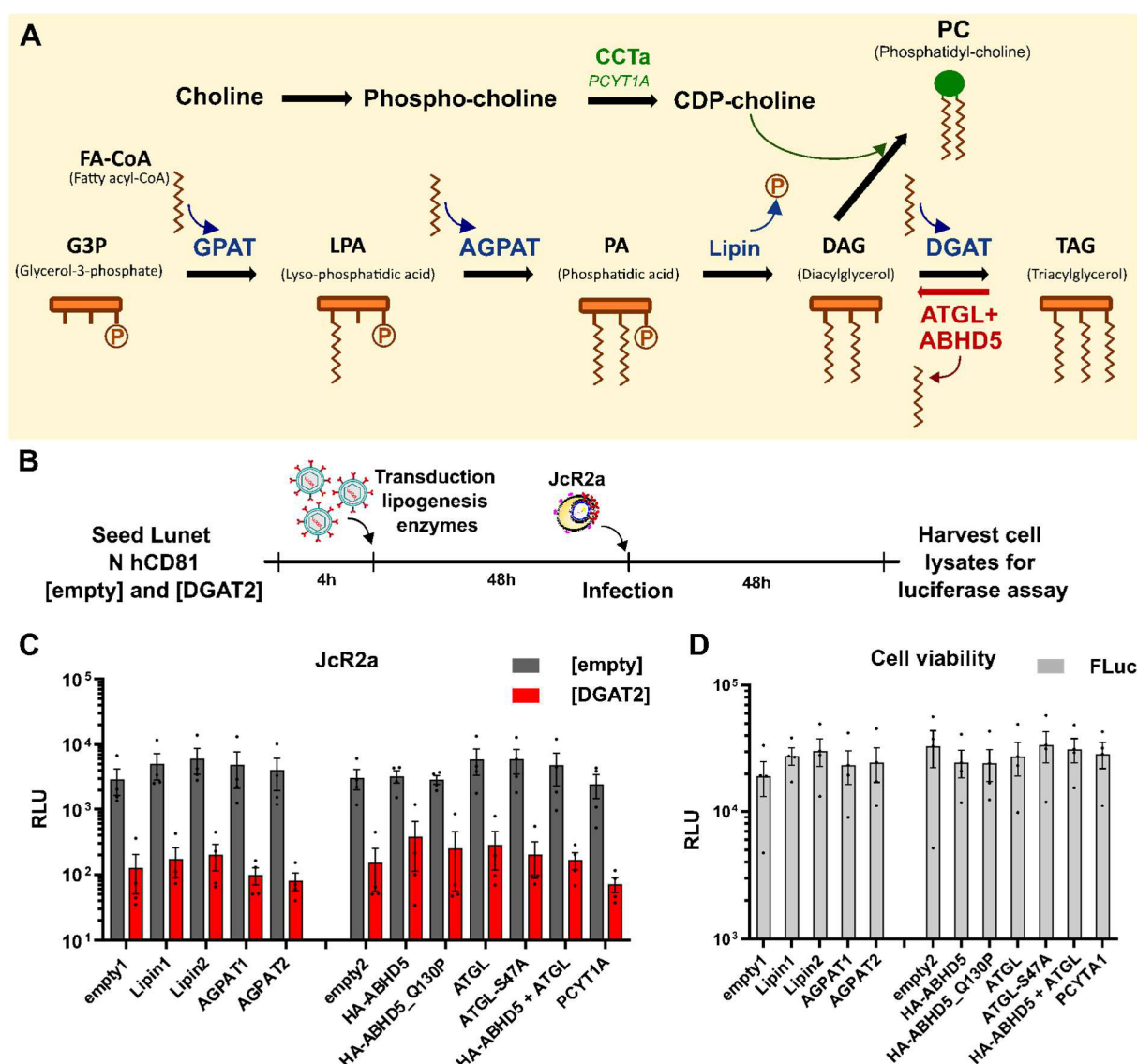


Figure 35: Co-expression of DGAT2 with enzymes of TAG and phospholipid synthesis pathways. (A) Overview of the targeted metabolic pathways and **(B)** experimental set up to test the effect of proteins involved in the TAG or PC synthesis pathway together on the DGAT2 antiviral activity. Lunet N hCD81 cells stably expressing [empty], [DGAT2] or [FLuc] were transduced with lentiviruses to co-express Lipin1, Lipin2, AGPAT1, AGPAT2, HA-tagged ABHD5 (WT or Q130P), ATGL (WT or S47A), HA-tagged ABHD5 and ATGL together or PCYT1A. The transduced cells were infected with JcR2a 48 h post transduction and cell lysates were harvested 48 hpi. **(C)** RLuc values were measured to monitor HCV JcR2a replication and **(E)** FLuc values to verify cell viability. Note that the graphs are divided into two sets with separate empty controls, corresponding to their respective plasmid background (empty1 = pWPI_Puro for Lipin and AGPAT constructs; empty2 = pWPI_BLR for ABHD5, ATGL and PCYT1A constructs).

4.4.2. Supplementation of lipid analogs

Apart from modulating the host cell lipid landscape indirectly by the co-expression of lipid metabolizing enzymes, we also challenged the DGAT2 antiviral activity by direct addition of cell permeable lipid analogs (Fig. 36 and 37). First, we tested the effect of DAG addition, the substrate of DGAT2, on HCV replication by utilizing the two short chain DAG analogs, sn-1,2-di-octanoyl-glycerol (1,2-DOG) and rac-1,3-DOG (Fig. 36A and B). We tested two different times of addition – 24 h before and 4 h after infection- and a concentration range from 25 μ M and 200 μ M and assessed the effect on cell viability in parallel (Fig. 36A, C-E).

The addition of DOG did not increase viral replication but had a rather decreasing effect at higher concentrations (Fig. 36C and D). Of note, the reduction of viral replication is most likely caused by the impairment of the cell-viability measured at concentrations above 100 μ M (Fig. 36E). However, these results indicated that DAG addition can not revert the DGAT2 antiviral phenotype.

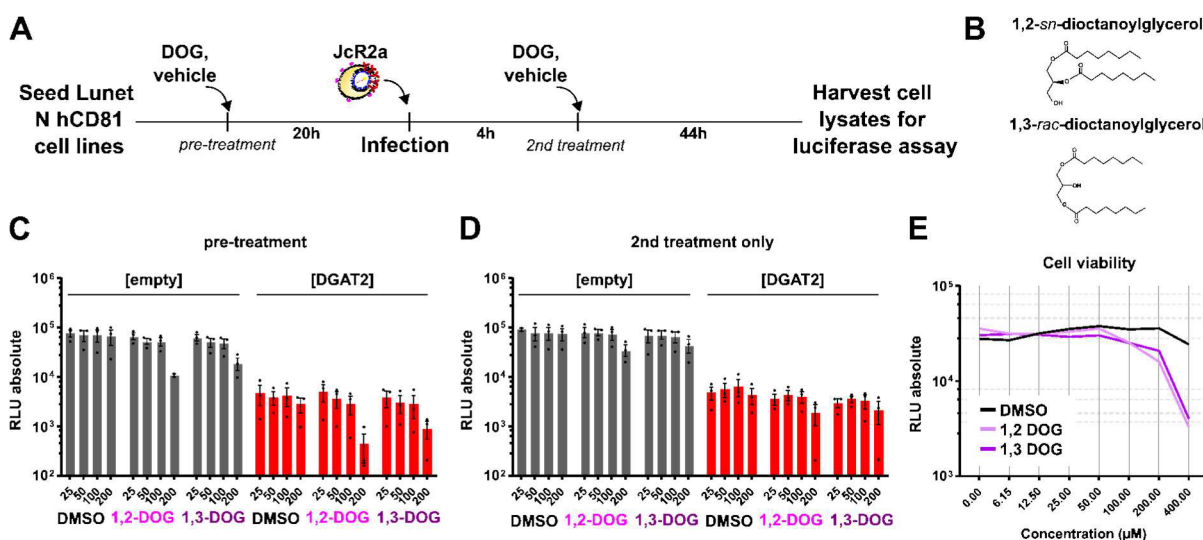


Figure 36: Effect of the cell permeable DAG analogs sn-1,2-di-octanoyl (DOG) and 1,3-DOG on the antiviral activity of DGAT2. (A) Lunet N hCD81 cells stably expressing [empty] or [DGAT2] were infected with JcR2a and cell lysates were harvested 48 hpi for luciferase assay. 1,2-DOG, 1,3-DOG or DMSO vehicle control were added to the cells either 20 hours prior and/ or 4 hpi (pretreatment vs. 2nd treatment only). (B) Chemical structures of the DOG analogs. (C) luciferase values of the infected, DOG treated cells. The compounds were added in a concentration range of 25-200 μ M. Mean \pm SEM of n = 4. (E) Cell viability of Lunet N hCD81 /FLuc cells treated with either 1,2-DOG, 1,3-DOG or DMSO vehicle control measured by FLuc values.

Furthermore, we extended the panel of tested lipid analogs to various other membrane lipid classes that were partially used in supplementation assays by other groups [58,77,154–157]. These included CER, PC, PE, SM, lyso-PC and PA classes (Fig. 37). Where possible, we chose nitrobenzoxadiazole (NBD)-labelled short-chain analogues to potentially visualize the cellular uptake of the lipid analogues. For CER, both the D- and the non-metabolizable enantiomer L-C6-CER were tested to distinguish whether membrane incorporation of CER itself or rather enhancement of the CER- metabolizing pathway would reverse the antiviral effect of DGAT2 (Fig. 37) [157]. Besides these lipid analogs, we included the addition of the DGAT2 inhibitor, which alleviated viral replication in DGAT2-expressing cells (Fig. 12, 37). Where available, we chose the lipid concentration range of the individual analogs to cover the concentrations used by other groups in lipid supplementation experiments [58,77,154–157]. We first assessed the cytotoxicity of the constructs by utilizing Lunet N hCD81/FLuc cells (Fig. 37A). Based on this cell-viability data, we chose the highest non-cytotoxic concentration and a respective 5-fold dilution and applied the lipid dilutions shortly after induction of DGAT2 by Dox addition (Fig. 37B). To rule out the possibility that the missing rescue of viral titers was due to an overwhelming effect of DGAT2 in stable expression, we modified the experimental set-up and utilized the previously introduced Dox-inducible cell line (Fig. 37B). While the addition of DGAT2 inhibitor alleviated viral replication in Dox treated inducible HA-DGAT2 Lunet N hCD81 cells, none of the tested lipid analogs increased viral replication (Fig. 37C). The cell viability, monitored by FLuc values in the infected and treated Lunet N hCD81/FLuc cells, was not strongly affected by either of the tested analogs (Fig. 37D). Note that in the same experiment, we also tested pretreatment with the lipid analogs prior infection as well as the effect on viral luciferase values at 72 hpi (data not shown). However, in none of the tested set-ups could viral replication be restored by the addition of lipid analogs.

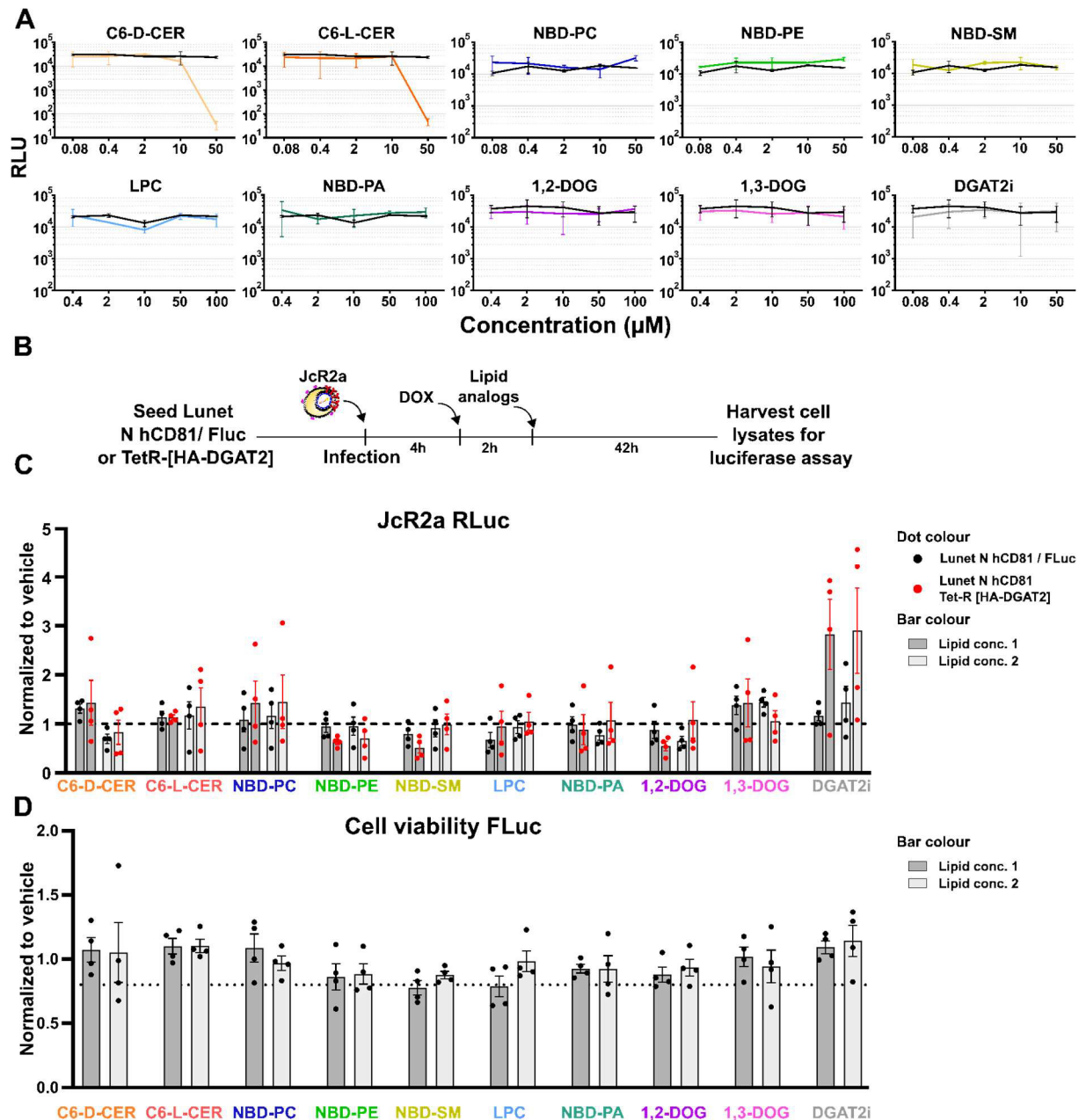


Figure 37: Effect of different lipid analogs on the antiviral effect of DGAT2 expression. (A) Cell viability of Lunet N hCD81 / FLuc cells treated for 48 h with lipid analogs. The concentration ranges from 0.08-50 μ M in the upper and 0.4-100 μ M in the lower panel. In each graph, the respective vehicle control is depicted in black (DMSO for 1,2-DOG, 1,3-DOG and DGAT2i, every else EtOH). **(B,C)** Assay to test the effect of lipid analogs on the antiviral effect of DGAT2. Lunet N hCD81 / FLuc or Lunet N hCD81-TetR [HA-DGAT2] cells were seeded in 96-well format and infected with JcR2a on the next day. 10 μ g/mL Dox was added to induce HA-DGAT2 expression in the inducible cell line 4 hpi. 2 h later, the medium was changed supplemented with the different lipid analogs in two chosen concentrations. For CER, PC, PE, SM and DGAT2i 10 μ M and 2 μ M lipid concentrations were tested. For LPC, PA and DOG 50 μ M and 10 μ M were tested. Fill colour of bars in (C,D): grey - higher concentration, light grey - lower concentration. **(C)** Relative RLuc values normalized to the vehicle control for each cell line and lipid analog. Black dots represent values measured in the control (Lunet N hCD81 / FLuc) cells, red dots in the HA-DGAT2 inducible cell line. **(D)** Relative FLuc values of Lunet N hCD81 cells treated with the indicated lipid analogs. Dotted line at y = 0.8 indicates the threshold of 80 % cell viability to distinguish cytotoxic effects. Mean \pm SEM of n = 4.

4.5. Effect of DGAT expression and HCV infection on the localization of host cell lipids

Earlier studies elucidated that the local regulation of several lipids and lipid classes is detrimental for the formation of the HCV RO [81]. As such, PI4P is enriched at the membranous web and is required for the recruitment of NS5A [52,54,57]. Moreover, accumulation of free Chol is observed at the HCV RO and necessary for the DMV biosynthesis [20,57]. Recently, the role of PA in the formation of DMVs was shown [31]. In the following, we examined the influence of DGAT2 expression on the localization of these lipids by fluorescence microscopy.

4.5.1. Effect of DGAT2 expression on PI4P and Cholesterol localization

To investigate the effect of DGAT2 overexpression on PI4P or Chol localization, we utilized the co-culture system with Lunet N hCD81 [mRuby2] cells, which allowed the direct comparison of DGAT2-expressing with control cells (Fig. 38 and 39). We used the anti-PI4P antibody and Filipin III complex, to stain PI4P or free Chol in the co-cultured cells, respectively (Fig. 38).

PI4P and Chol were detected throughout the whole cytoplasm of both control as well as DGAT2-expressing cells (Fig. 38A and B). As expected, Filipin often accumulated at the cell surface and in perinuclear regions (Fig. 38B). We did not detect obvious differences between DGAT2-expressing and control cells for neither PI4P nor Chol localization (Fig. 38A and B). Incidentally, the Filipin signal sometimes formed ring-shaped structures typical of LD localization, which was more common in DGAT2-overexpressing cells (Fig. 38B). Unfortunately, the LD association of Chol could not be further verified, as the addition of LD dyes such as LD540 or lipid-tox resulted in a strong association of Filipin with LDs, making co-staining of LD and Chol impossible (data not shown).

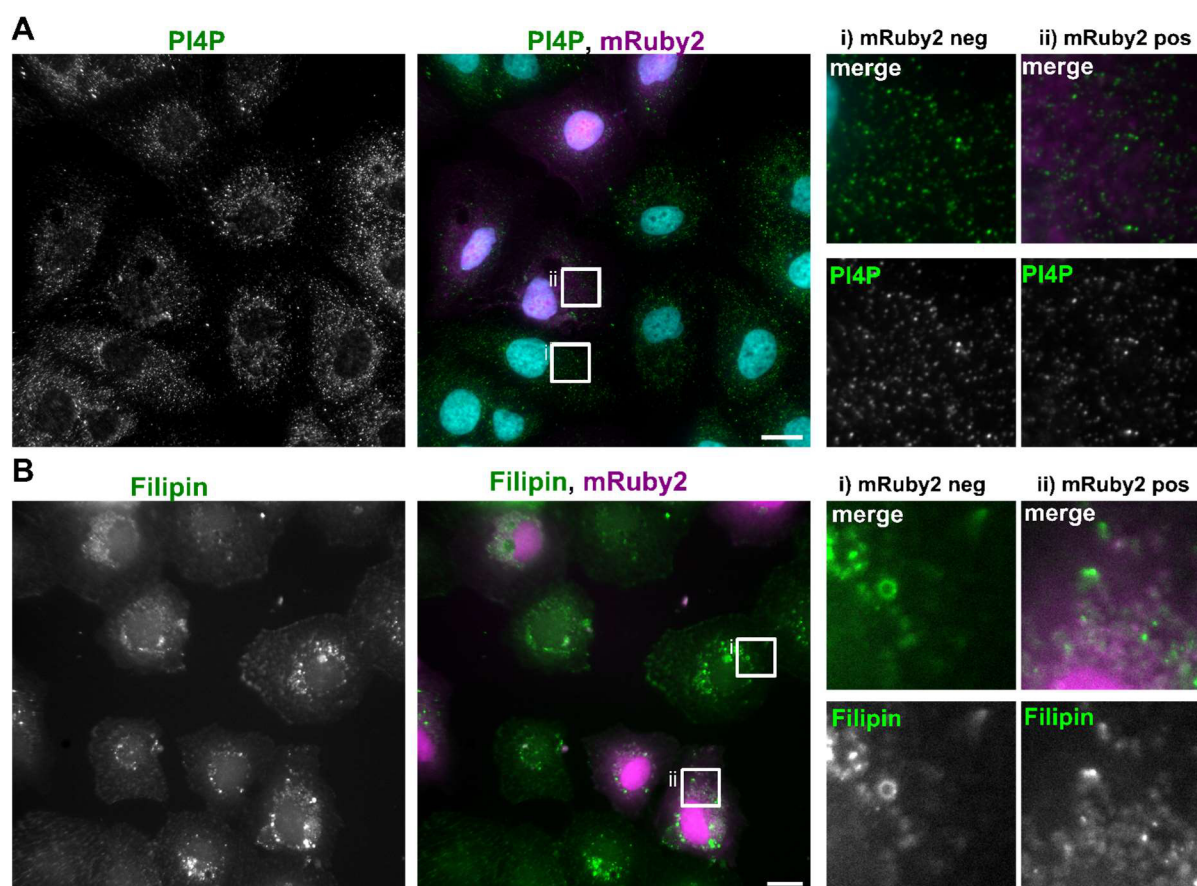


Figure 38: Effect of DGAT expression on cholesterol localization. Stable HA-DGAT2-expressing Lunet N hCD81 cells were co-seeded mRuby2-positive reference cells and cholesterol (Chol) was detected by staining with Filipin III complex. White boxes in the middle panel show mRuby2-negative or -positive cells and are enlarged on the right side. Representative image of 2 independent experiments. Scale bar, 20 μm.

4.5.2. Effect of DGAT2 expression on PA localization

Besides PI4P and Chol, PA accumulation was shown to be important for the formation of DMVs [31]. The authors of the latter study used a PA-biosensor composed of a PA-binding domain from Raf1 protein fused to a fluorophore, which allows the detection of cellular PA upon transduction of the sensor [31]. Here, we cloned the described biosensor and a mutant version fused to mNeonGreen (Fig. 39A). We expressed the wild-type or mutated version (Raf1-PABD-4E; R391E, R398E, K399E, R401E) of these sensors in Lunet N hCD81 cells. The PA-sensor signal was rather low, occasionally speckled and localized in the cytoplasm (Fig. 39B). The localization of wildtype and mutant PA-sensor was very similar, except for the accumulation of the mutant sensor in the nuclei (Fig. 39B). Indeed, the signal intensity of the mutant sensor seemed to be slightly brighter (Fig. 39B).

More importantly, the expression of HA-DGAT2 did not influence the localization of the PA-sensor (Fig. 39C).

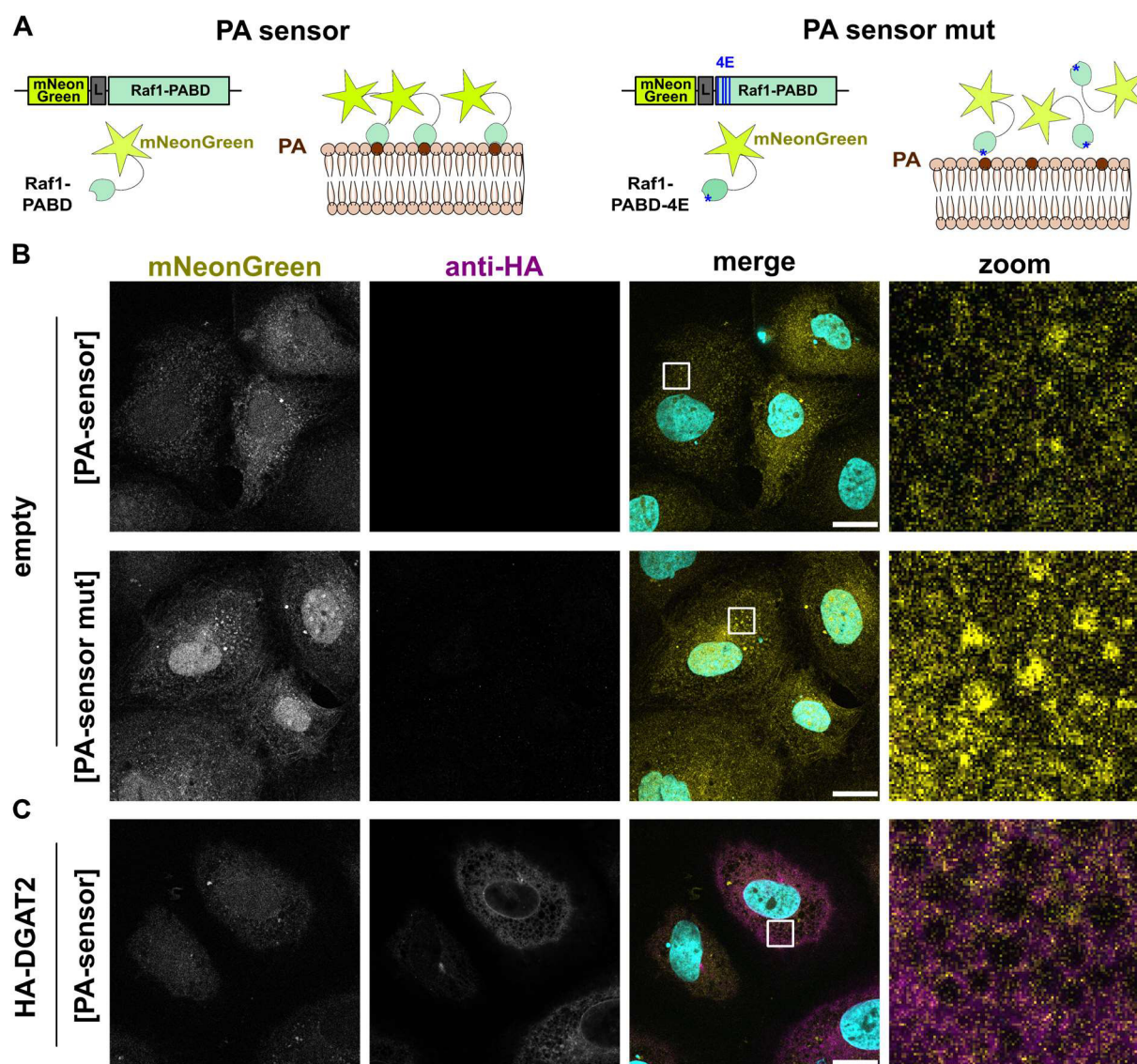


Figure 39: Effect of DGAT2 on phosphatidic acid (PA)-sensor localization. (A) Schematic representation of the PA sensor. The PA-binding domain of Raf1 fused to mNeonGreen fluorophore was used to detect PA within cellular membranes. A mutant sensor construct with four point mutations at the PABD domain (4E) was tested in parallel. **(B, C)** PA sensor (B upper panel, C) or mutated PA sensor (B lower panel) were stably expressed in Lunet N hCD81 cells. Localization of the sensor was tested in cells transduced with [empty] vector control (B) or HA-DGAT2 (C) 48. HA-DGAT2 was detected by anti-HA staining. Nuclei were stained with Dapi. White boxes in merge images are enlarged in right panel. Representative images of four independent experiments Scale bar, 20 μ m.

However, the functionality of the PA-sensor was not completely evident, as we could not reproduce the described phenotype of PA accumulation in HCV-infected cells [31]. Both the PA-sensor and the mutant sensor occasionally formed speckles in the cytoplasm, independent of HCV infection (Fig. 40). Thus, the influence of DGAT2 overexpression on the localization of PA could not be clearly determined by using the described PA-sensor.

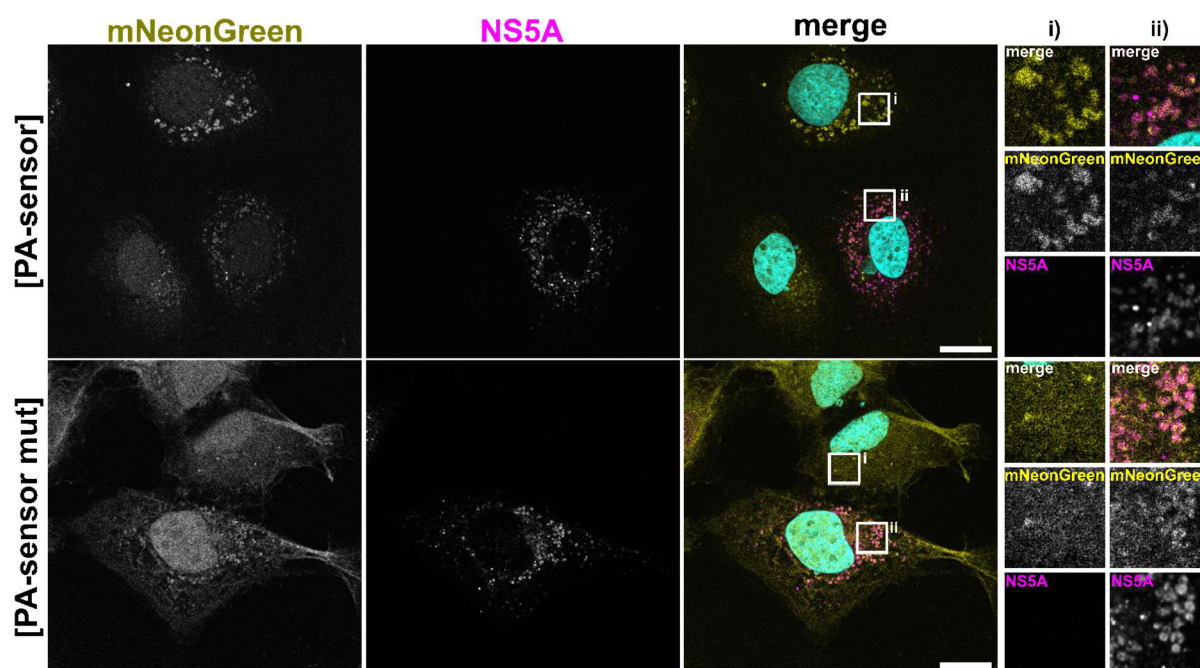


Figure 40: Localization of PA-sensor in HCV-infected cells. Lunet N hCD81 cells stably expressing the PA-sensor (top panel) or mutant version PA-sensor mut (bottom panel) were infected with HCV. 48 hpi, cells were fixed and the localization of both sensor constructs was investigated by fluorescence microscopy (yellow). NS5A was detected by immunofluorescence (magenta) and nuclei were stained with Dapi (blue). White boxes in merge picture are enlarged on the right side: i) NS5A negative, ii) NS5A positive cell. Representative images of two independent experiments Scale bar, 20 μ m.

4.5.3. Effect of DGAT2 expression on DAG localization

Considering that DAG is the main substrate of DGAT and serves as a precursor of various membrane lipids, we investigated whether DAG stores could be affected by overexpression of DGAT2, thereby impeding DMV synthesis, although a direct function of DAG in the context of DMV biogenesis has not yet been described. Subsequently, we cloned a further lipid biosensor construct, consistent of the DAG-binding domain C1a-C1b of the protein kinase C epsilon (PKC ϵ) fused to mRuby3 fluorophore, and transiently expressed it in control or DGAT2-expressing cells (Fig. 41) [77]. Additionally, we generated a mutated DAG-sensor construct (DAG-mut) by introducing a point-mutation at the catalytic domain (W294G) [77,158] to test the specificity of the DAG-binding (Fig. 41).

The wild-type DAG-sensor construct showed a strong cytoplasmic signal with reticular, perinuclear localization in the control cells, which fits to earlier findings [77] (Fig. 41A). In contrast, the signal of the mutant sensor was very weak and distributed throughout the whole cell (Fig. 41A). Strikingly, under influence of HA-DGAT2 expression, a great proportion of the DAG-sensor signal was re-localized and accumulated in cytoplasmic speckles, often in proximity to LDs (Fig. 41B).

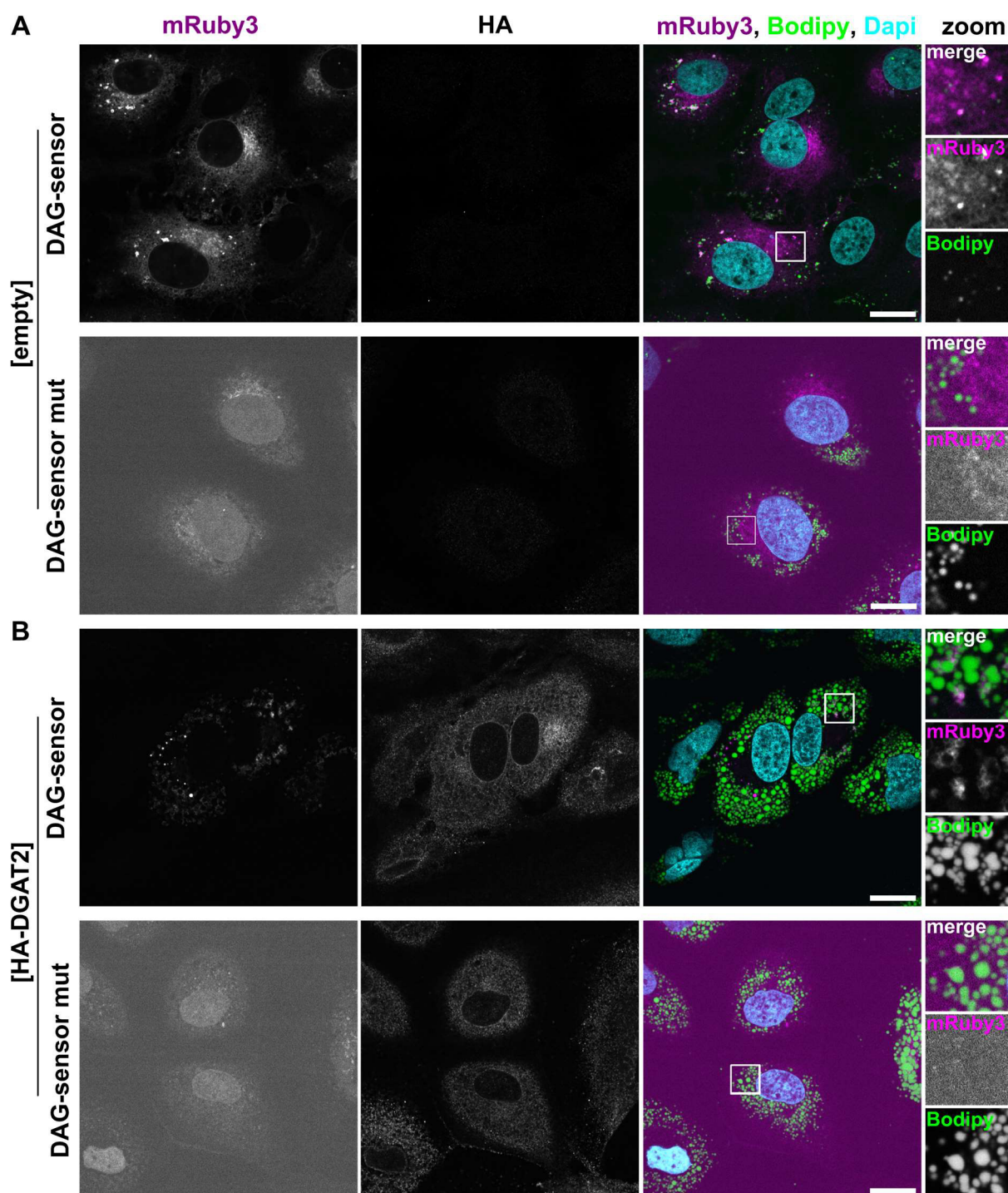


Figure 41: Effect of DGAT2 on diacylglycerol (DAG) sensor localization. (A, B) A DAG sensor consisting of the DAG-binding cassette of protein kinase C epsilon (PKC ϵ -C1a-C1b) attached to the mRuby3-fluorophore was utilized to detect the localization of DAG upon expression within [empty] (A) or [HA-DGAT2] (B) stably expressing Lunet N hCD81 cells. Additionally, a mutant sensor construct with a point mutation at the DAG binding domain (W294G) was tested in parallel (lower panels). DAG sensor localization was assessed by fluorescence microscopy (magenta). HA-DGAT2 was detected by immunofluorescence using an anti-HA antibody (middle large image, not in merge). LDs were stained with BODIPY 493/504 (green) and nuclei with Dapi (blue). White boxes in merge images are enlarged in right panel. Representative images of four independent experiments. Scale bar, 20 μ m.

As DAG is required for the TAG production, we wondered whether the DAG accumulation around LDs might be caused by excessive LD biogenesis. We therefore also tested the effect of OA treatment on the localization of the DAG sensor (Fig. 42).

Interestingly, we observed an intermediate phenotype with partially perinuclear, partially cytoplasmic speckle forming DAG stores in OA treated cells (Fig. 42). Therefore, the DAG re-localization might be an effect of increased LD formation, rather than a DGAT2 specific phenotype. As OA treatment itself did not hamper DMV synthesis, this argues that DAG re-localization might not be the detrimental factor for the antiviral effect of DGAT2 overexpression.

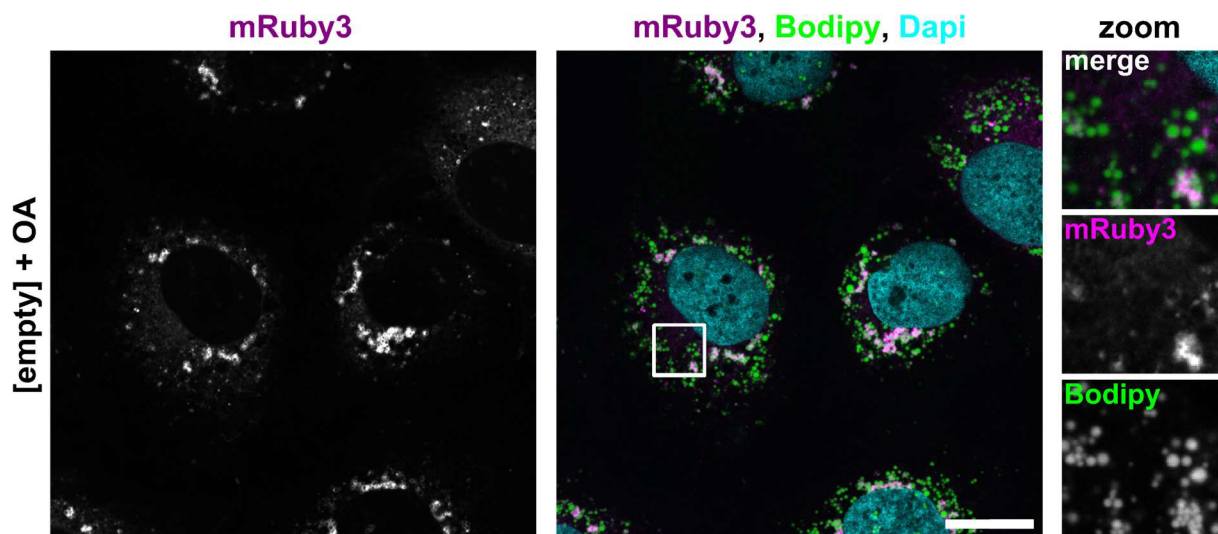


Figure 42: Effect of OA addition DAG sensor localization. (A, B) The DAG sensor (mRuby3-PKC ϵ -C1a-C1b) was expressed in [empty] Lunet N hCD81 cells. 6 h prior fixation, the cells were treated with 360 μ M OA combined with BSA. DAG sensor localization was assessed by fluorescence microscopy (magenta). LDs were stained with BODIPY 493/504 (green) and nuclei with Dapi (blue). White boxes in merge images are enlarged in right panel. Representative images of three independent experiments. Scale bar, 20 μ m.

Furthermore, in a preliminary experiment, the effect of HCV infection on the localization of the DAG-sensor was tested (Fig. 43). Interestingly, we observed the re-localization of DAG stores towards LDs also in infected cells and the DAG-speckles seemed to co-localize with NS5A (Fig. 43A). However, NS5A also co-localized with the mutant DAG-sensor construct (Fig. 43B), which suggests that this finding might be caused by an interaction of NS5A and the DAG-binding domain and rather independent of the localization of DAG.

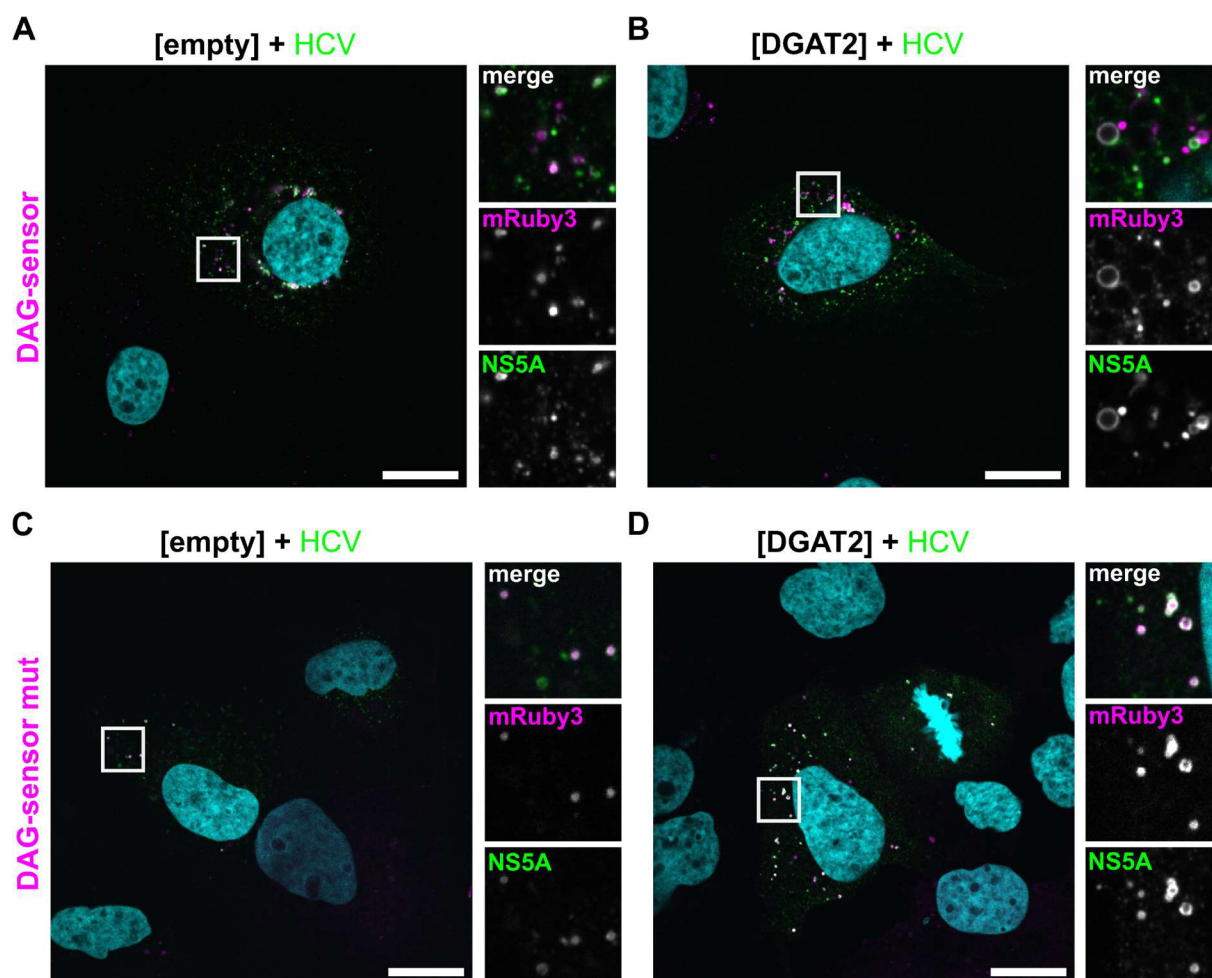


Figure 43: DAG sensor localization in HCV-infected cells. (A, B) The DAG sensor (mRuby3-PKCε-C1a-C1b) or mutant DAG sensor (mRuby3-PKCε-C1a-C1b_W294G) constructs were expressed in [empty] Lunet N hCD81 cells by lentiviral transduction. Cells were infected 48 hpt and fixed 48 hpi. DAG sensor localization was assessed by fluorescence microscopy (magenta). HCV NS5A was detected by anti-NS5A staining (green). Nuclei were stained with Dapi (blue). White boxes in merge images are enlarged in right panel. Scale bar, 20 μm.

Finally, we tested the DAG re-localization in 293T-miR-122 and in HuH6 cells (Fig. 44). Similar as in Lunet N hCD81, the DAG sensor signal was detected perinuclear in the control cells of both HuH6 and 293-miR-122 cells (Fig. 44). In HuH6 cells expressing HA-DGAT2, the sensor drastically re-localized to form cytoplasmic, LD adjacent speckles, which resembles the phenotype in Lunet N hCD81 cells (Fig. 44A). As HCV is not sensitive to DGAT2 overexpression when replicating in HuH6 cells, this finding strengthens the point that the observed DAG re-localization might not be prerequisite for the DGAT2 antiviral effect. In 293T-miR-122 cells, we observed occasionally a similar re-localization phenotype of the DAG sensor (Fig. 44B). However, due to the low signal of HA-DGAT2 and low transfection rates, it was difficult to clearly distinguish HA-DGAT2-overexpressing from control 293T-miR-122 cells.

In summary, although DGAT2 overexpression showed a strong phenotype of DAG-storage re-localization, this effect appears to be independent of the DGAT2 antiviral activity, as we also detected it in OA treated cells and in cell lines, in which HCV is insensitive to DGAT2 expression.

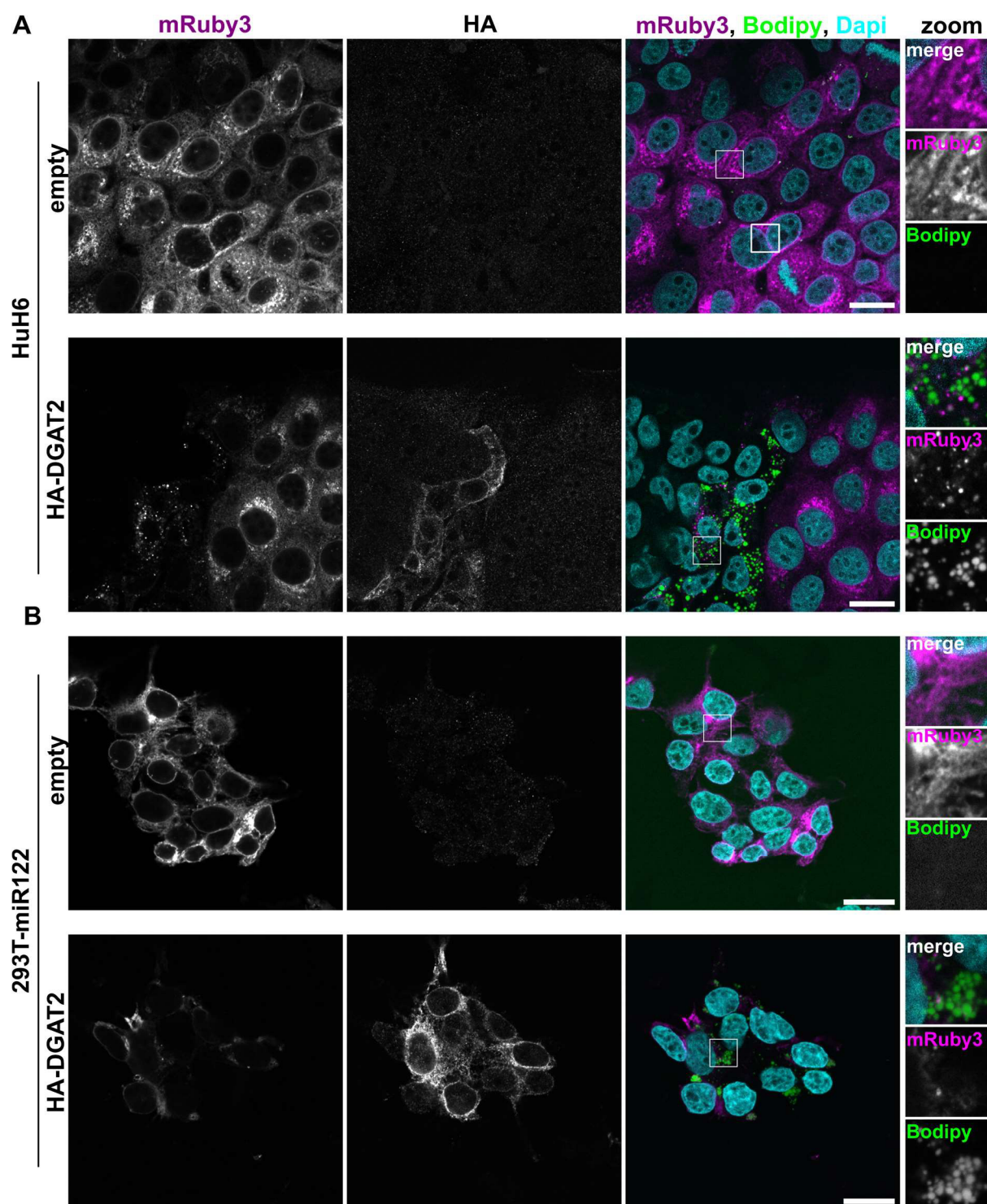


Figure 44: DAG sensor localization in HuH6 and 293T-miR-122 cells. The DAG sensor (mRuby3-PKC ϵ -C1a-C1b) was co-expressed with empty (upper panel) or HA-DGAT2 (lower panel) by lentiviral transduction in HuH6 (A) or 293T-miR-122 cells (B). DAG sensor localization was assessed by fluorescence microscopy (magenta). HA-DGAT2 was detected by immunofluorescence using an anti-HA antibody (middle large image, not in merge). LDs were stained with BODIPY 493/504 (green) and nuclei with Dapi (blue). White boxes in merge images are enlarged in right panel. Representative images of at least two independent experiments. Scale bar, 20 μ m.

4.6.Changes of the host cell lipidome upon DGAT protein expression, OA treatment or HCV infection

Besides the localization of Chol, PI4P and PA, previous studies have found a tremendous effect of HCV infection on the regulation of various PL and sphingolipid (SL) species [44,45]. Therefore, in the next step, we utilized lipidomic analysis to obtain a more holistic picture of the changes in the host cell lipid profile upon DGAT2 overexpression and HCV infection.

By using electrospray ionization tandem mass spectrometry (LC-ESI-MS/MS) and the Lipidyzer™ kit, we assessed the concentrations of 13 lipid classes including PLs, sphingolipids (SLs), glycerolipids, CE and FFA. Note that the FFA class had to be excluded from the analysis because of unusually high concentration values in all samples, probably caused by TAG hydrolysis during preparation. The utilized approach enabled to examine the absolute lipid concentrations (nmol / million cells) on lipid class, fatty acyl chain and individual lipid species levels (Fig. 46). Note that LC-ESI-MS/MS and MS data analysis was performed by Manka Fuh and Jörg Heeren.

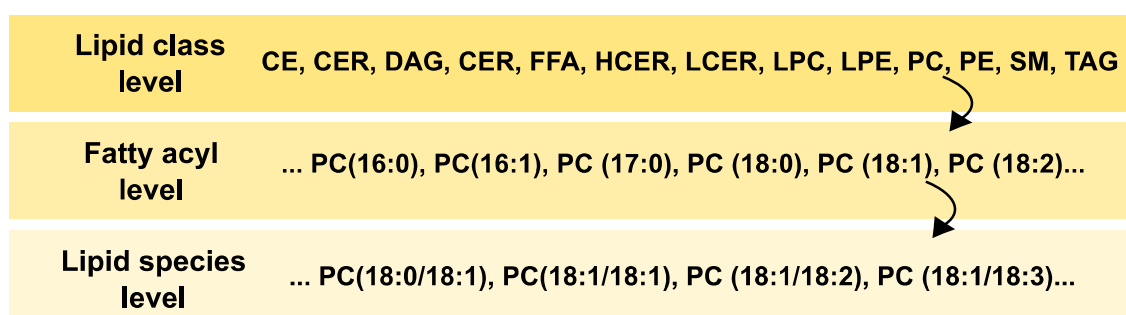


Figure 45: Lipidomics data overview measured with the Lipidyzer™ kit. Absolute lipid concentrations were measured using electrospray ionization tandem mass spectrometry (LC-ESI-MS/MS). The concentrations of lipid species were summarized in the fatty acyl or lipid classes dependent on their acyl chain or lipid class, respectively, which allows analysis of the data on lipid class, fatty acyl and lipid species level. TAG, triacylglycerol; CE, cholesteryl ester, CER, ceramide; DAG, diacylglycerol; DCER, dihydroceramide; HCER, hydroxyceramide; LCER, lactosylceramide; LPC, lyso-phosphatidylcholine; LPE, lyso-phosphatidylethanolamine; PC, phosphatidylcholine; PE, phosphatidylethanolamine; SM, sphingomyelin.

4.6.1. Set up of the lipidomics experiment and primary test

As described above, the DGAT2 antiviral effect was expected to mostly affect the ER membrane, the organelle where both DMVs and LDs originate. Therefore, in a first attempt, we analyzed samples of both microsomal fractions and whole cell lysates by lipidomics. We isolated the microsomal fractions by stepwise centrifugation and subsequently analyzed the fractions by Western Blot utilizing cytoplasmic (beta-Tubulin), ER (Calnexin), LD (ADRP), and mitochondria (CoxIV) markers (Fig. 46). As expected, Calnexin accumulated in cytoplasmic, microsomal, and mitochondrial fractions (Fig. 46B). In contrast, the microsomal fraction was free of beta-Tubulin and ADRP (Fig. 46B). Consistently, CoxIV accumulated only in the mitochondrial fraction (Fig. 46B).

Subsequently, we prepared samples of DGAT2, DGAT2_L83A, DGAT2_HPH161-163AAA, DGAT1 or empty vector expressing cells (Fig. 46A). Additionally, we analyzed empty vector or DGAT2-expressing cells infected with HCV for 48 h, as well as OA treated cells (Fig. 46A).

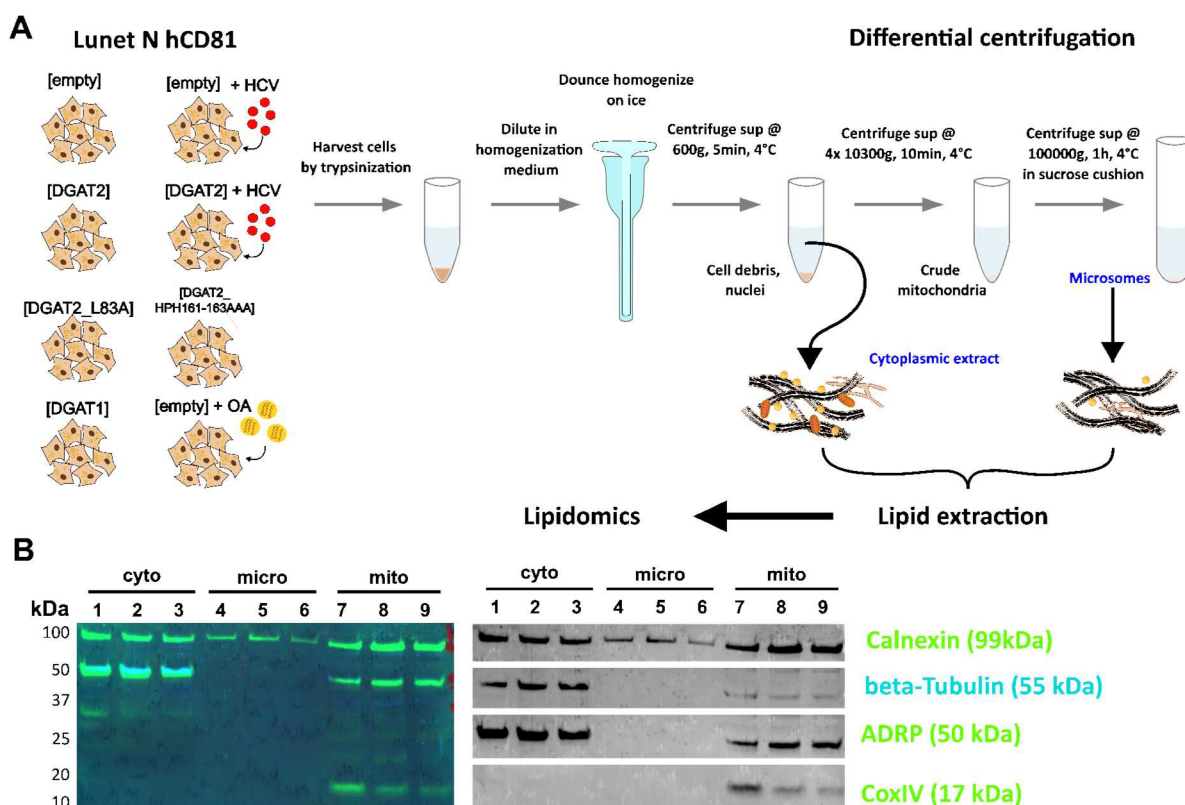


Figure 46: Sample preparation for first lipidomics attempt. (A) Lunet N hCD81 cells stably expressing [empty] vector control, [DGAT2], [DGAT2_L83A], [DGAT2_HPH161-163AAA] or [DGAT1] were harvested by trypsinization. Additionally, [empty] and [DGAT2] cells infected for 48 h with HCV Jc1 and [empty] cells treated overnight (20 h) with 360 μ M OA were harvested. Cell pellets were lysed by dounce homogenization and cytoplasmic extracts, mitochondrial, and microsomal fractions were harvested by differential centrifugation. Lipids were extracted from cytoplasmic extracts and microsomal fractions for lipidomic analysis. **(B)** Western Blot of [empty] (lanes 1, 4, 7), Jc1 infected (2, 5, 8) or OA treated (3, 6, 9) cellular fractions. ER (Calnexin, 99 kDa), cytosolic (beta-tubulin), LD (ADRP, 50 kDa) or mitochondrial (CoxIV, 17 kDa) markers were detected with primary antibodies and either Starbright B520 (beta-tubulin) or B700 (Calnexin, ADRP, CoxIV) secondary antibodies for fluorescent WB readout.

Differences in the lipid composition of the cytoplasmic and microsomal fractions of Lunet N hCD81 [empty] cells were easily recognized (Fig. 47). While the cytoplasmic fraction is enriched with TAG and CE species and make ~25 or 12 % of the total lipid content, respectively, these lipid classes are less abundant in the purified microsomes (~9 or 4 %) (Fig. 47). As the purified microsomal fractions are almost devoid of LDs, the main storage organelles of neutral lipids, these differences were expected [44]. Furthermore, the total concentration of measured lipids was reduced 10-fold, and less lipid species were detected in microsomal vs. cytoplasmic fractions (Fig. 47).

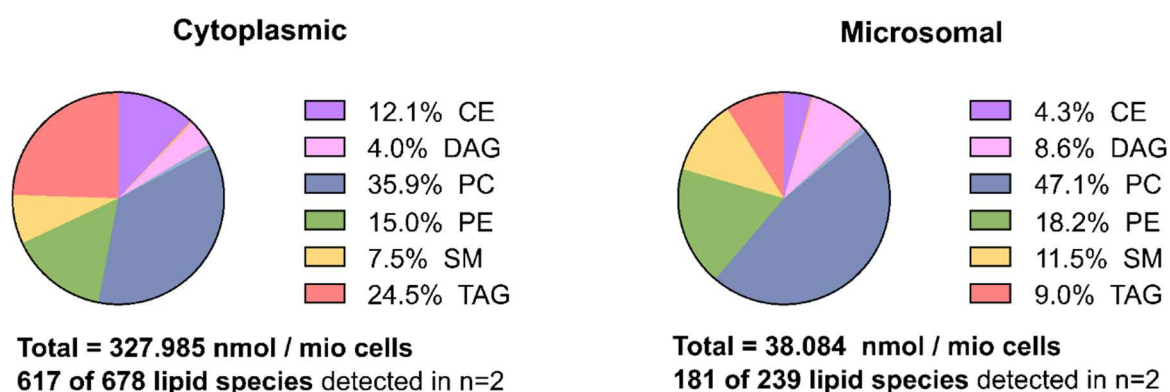


Figure 47: Total lipid composition of cytoplasmic and microsomal fractions. Cytoplasmic and microsomal fractions of stable Lunet N hCD81 [empty] cells were harvested as described in Fig. 46 and lipid concentrations were measured by lipidomic analysis using the Lipidizer® kit. The proportions of the lipid classes are depicted for cytoplasmic (left) and microsomal (right) fractions. The percentages of the six most abundant lipid classes (CE, DAG, PC, PE, SM, TAG) and the total lipid content (in nmol per million cells). Additionally, the amount of total detected lipid species and species, that were present in both replicates are indicated.

Extending the comparison to all measured conditions, we observed overall similar trends in the regulation of various lipid classes in cytoplasmic and microsomal samples (Fig. 48A and B). However, the absolute lipid concentrations of the microsomal fractions were rather low, resulting in many missing values (Fig. 48B). For example, both DGAT2 overexpression and HCV infection increased the concentration of various lipid classes including CE, PE, and TAG (Fig. 48B). Also, the changes on fatty acyl level, depicted for the PC class in (Fig. 48C), were comparable between cell-lysate and microsomal fractions. Interestingly, HCV-infected Lunet N hCD81 [DGAT2] cells showed almost the same changes compared to mock infected DGAT2-expressing cells (Fig. 48C). However, due to the strong antiviral effect of DGAT2 expression, this result is biased by the low infection rate and the resulting high number of uninfected DGAT2-expressing cells in the sample. Thus, we did not follow up the DGAT2-expressing HCV-infected samples in the further analysis.

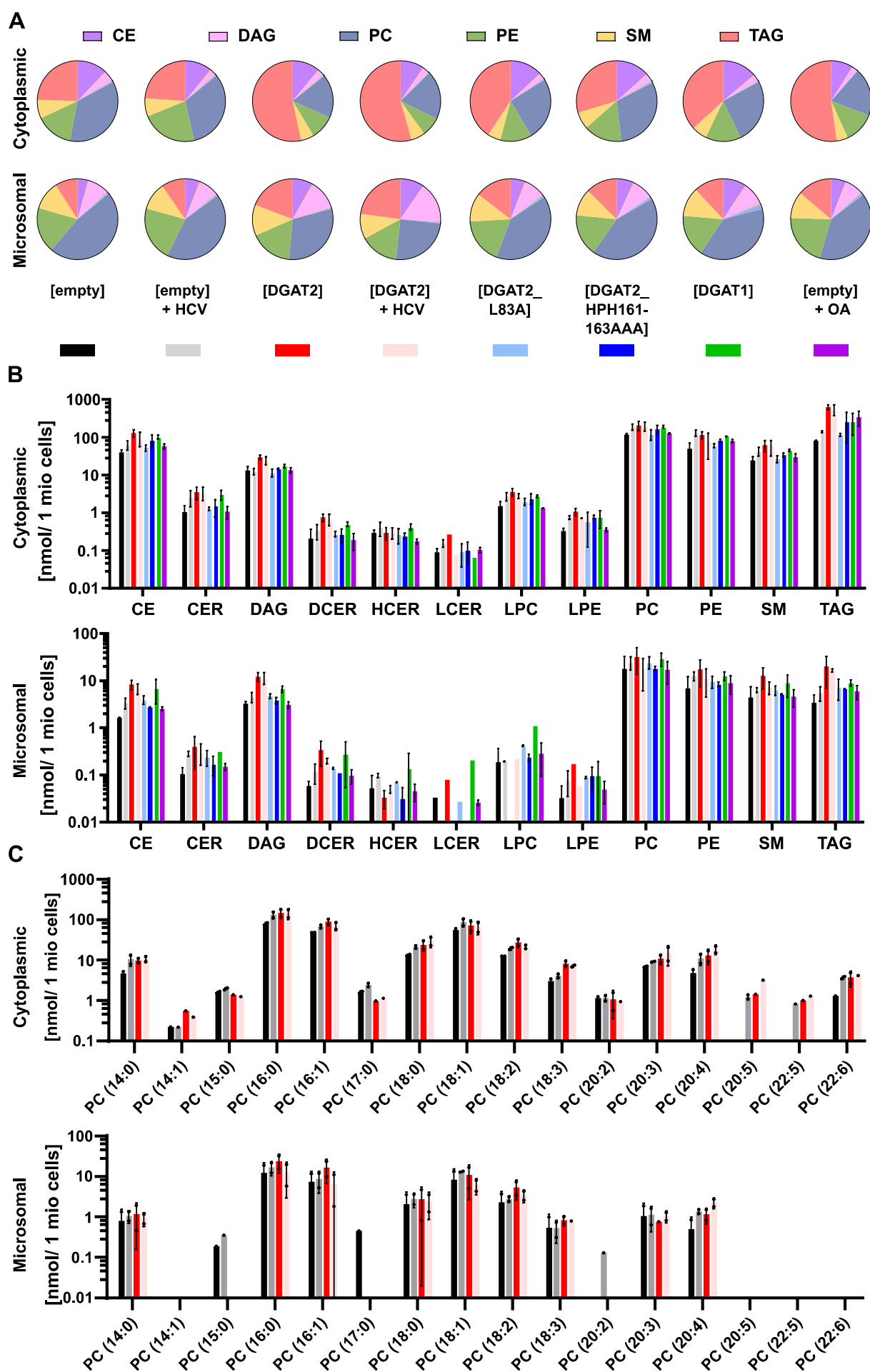


Figure 48: Comparison of lipid concentrations of cytoplasmic and microsomal fractions on lipid class and fatty acyl chain level. Cytoplasmic and microsomal fractions cells expressing [empty] vector control, [DGAT2], [DGAT2_L83A], [DGAT2_HPH161-163AAA] or [DGAT1] were harvested by differential centrifugation as described in Fig. 46. Additionally, fractions of [empty] and [DGAT2] cells infected for 48 h with HCV Jc1 and [empty] cells treated overnight (16 h) with 360 μ M OA were harvested. Lipid concentrations were measured by lipidomic analysis using the Lipidizer[®] kit. **(A)** Proportions of the lipid classes are depicted for cytoplasmic (top) and microsomal (bottom) fractions. Colour code of lipid classes is indicated on the top. **(B)** Absolute concentrations of lipid classes measured in cytoplasmic (top) and microsomal (bottom) fractions of the different conditions. Colours of bars indicate tested condition (legend above B). **(C)** Absolute concentrations of PC species on fatty acyl chain level of [empty] or [DGAT2] expressing cells with or without HCV infection measured in cytoplasmic (top) and microsomal (bottom) fractions. Colours of bars indicate tested condition (legend above B).

4.6.2. Analysis of the combined lipidomics datasets

Due to the overall similar changes within cytoplasmic and microsomal fractions, but the high amount of missing values within the latter, we decided to concentrate the further lipidomic analysis on the cell lysate fractions only. Furthermore, to gain a better understanding of the specific effects of DGAT1 and DGAT2 proteins on the lipid profile, we included DGAT1-expressing cells treated with the DGAT2 inhibitor (Fig. 49). The statistical analysis of the combined data sets was performed in collaboration with Chris Lauber.

Overall, we detected 859 lipid species in the combined data set, of which 710 lipid species were considered for further analysis after exclusion of lipid species that were absent in more than 25 % of the samples.

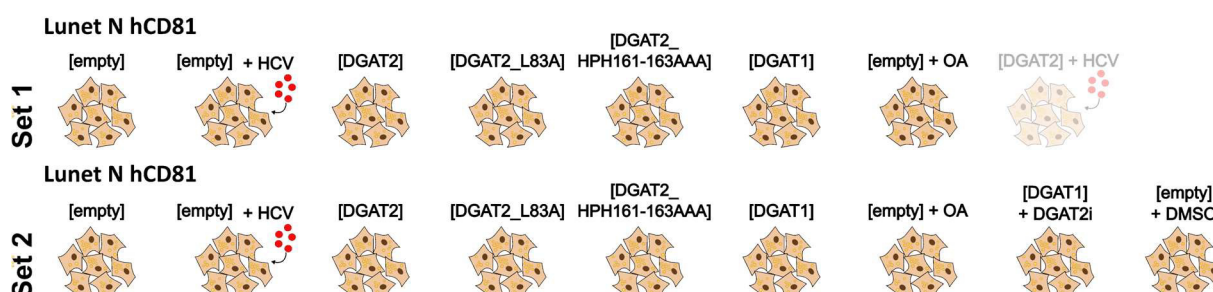


Figure 49: Overview about different conditions tested by lipidomic analysis. Samples for lipidomic analysis were harvested and measured in three sets. Samples of in total 4-6 independent experiments per conditions were measured. Only data of cytoplasmic fractions was included in the statistical analysis. Data of identical conditions were analyzed together.

4.6.3. Changes on lipid class level

When comparing the total lipid content between all conditions, the most noticeable differences were caused by strong TAG level accumulation in DGAT2- and DGAT1-expressing or OA treated cells (Fig. 50A). As expected, the highest TAG increase was found in DGAT2 wildtype-expressing cells and in cells treated with OA (Fig. 50B), which is consistent with the observed LD accumulation (Fig. 13). We detected a milder increase of TAGs in cells expressing DGAT1 or the catalytic mutants of DGAT2, which is consistent with reduced LD accumulation in these conditions (Fig. 13). Furthermore, CE, which is produced from free Chol and stored within LDs, was significantly upregulated upon DGAT2 and DGAT1 expression (Fig. 50B). In contrast, in HCV-infected cells, the upregulation of neutral fats was rather mild and not statistically significant on lipid class level (Fig. 50B).

In contrast to the neutral lipid classes, the membrane lipid biogenesis was strongly affected by HCV infection. Of note, the absolute concentrations of all detected membrane lipid classes were upregulated by HCV infection with the exception of DAG (Fig. 50B). In particular, CER, PC, and PE classes were significantly increased, which confirms the findings of Hofmann *et al.* [44] and others [45] and might be related to the increased membrane biosynthesis required for the formation of the HCV RO.

Interestingly, in Lunet N hCD81 cells, DGAT2 overexpression enhanced several membrane lipid classes, although to a lesser and not statistically significant extent (Fig. 50B). In line with previous results, these changes correlated with the catalytic activity of the tested DGAT2 variants (Fig. 50B). DGAT1 overexpression had a similar effect on the absolute membrane lipid concentrations, except for CER and dihydroceramide (DCER) levels, that were significantly increased in DGAT1-overexpressing cells (Fig. 50B). Remarkably, this effect was attenuated in the DGAT2 inhibitor treated cells, which suggests that both DGAT proteins might contribute to the upregulation of CER and DCER (Fig. 50B). These findings suggest that the increased LD biogenesis mediated by DGAT2 or DGAT1 overexpression affect not only the neutral lipid content, but also various other membrane lipid classes, and even influence CER lipid classes, that are not directly related to the TAG biosynthesis pathway (Fig. 35).

To gather more information about lipid composition changes in HCV-infected, DGAT-expressing or OA treated cells, we normalized the absolute lipid concentrations of the membrane lipids to the total membrane lipid amount (total lipid amount without CE and TAG) (Fig. 50C). This normalization allows to adjust for the strong global increase of lipids upon DGAT protein expression or OA treatment.

Interestingly, most of the observed shifts in absolute lipid concentrations were even more pronounced in membrane lipid composition (Fig. 50C). As such, HCV infection significantly increased PE and CER classes, and the proportion of DAG in the membrane lipid composition was significantly downregulated (Fig. 50C). Strikingly, despite an increase of absolute PC concentrations, the proportion of PCs in the membrane lipid content was significantly downregulated in both HCV infection. Furthermore,

proportions of lactosyl- (LCER) and hydroxyceramide (HCER) classes were significantly reduced in HCV-infected cells.

Interestingly, many of the lipid classes affected by HCV infection, including PC, PE, and CER classes, were similarly regulated by DGAT2 overexpression (Fig. 50C). Additionally, DGAT2 expression significantly elevated lyso-PE and SM lipid classes (Fig. 50C). Surprisingly, the proportion of DAG lipids was not strongly affected by DGAT2 overexpression, which was in contrast to HCV infection and also to DGAT1 overexpression, which both significantly depleted the DAG class (Fig. 50C).

In summary, both HCV infection and DGAT2 overexpression had a strong influence on the host cell lipid profile. Thereby, many of the affected lipid classes were similarly regulated by either HCV infection or DGAT2 overexpression, which might indicate similar lipid requirements for the HCV RO formation and the excessive LD biogenesis in DGAT2-expressing cells. Importantly, the observed lipid changes were reduced in the DGAT2 mutant-expressing cells, indicating that the catalytic activity of DGAT2 is crucial for its impact on the host lipid landscape and supporting our previous observations.

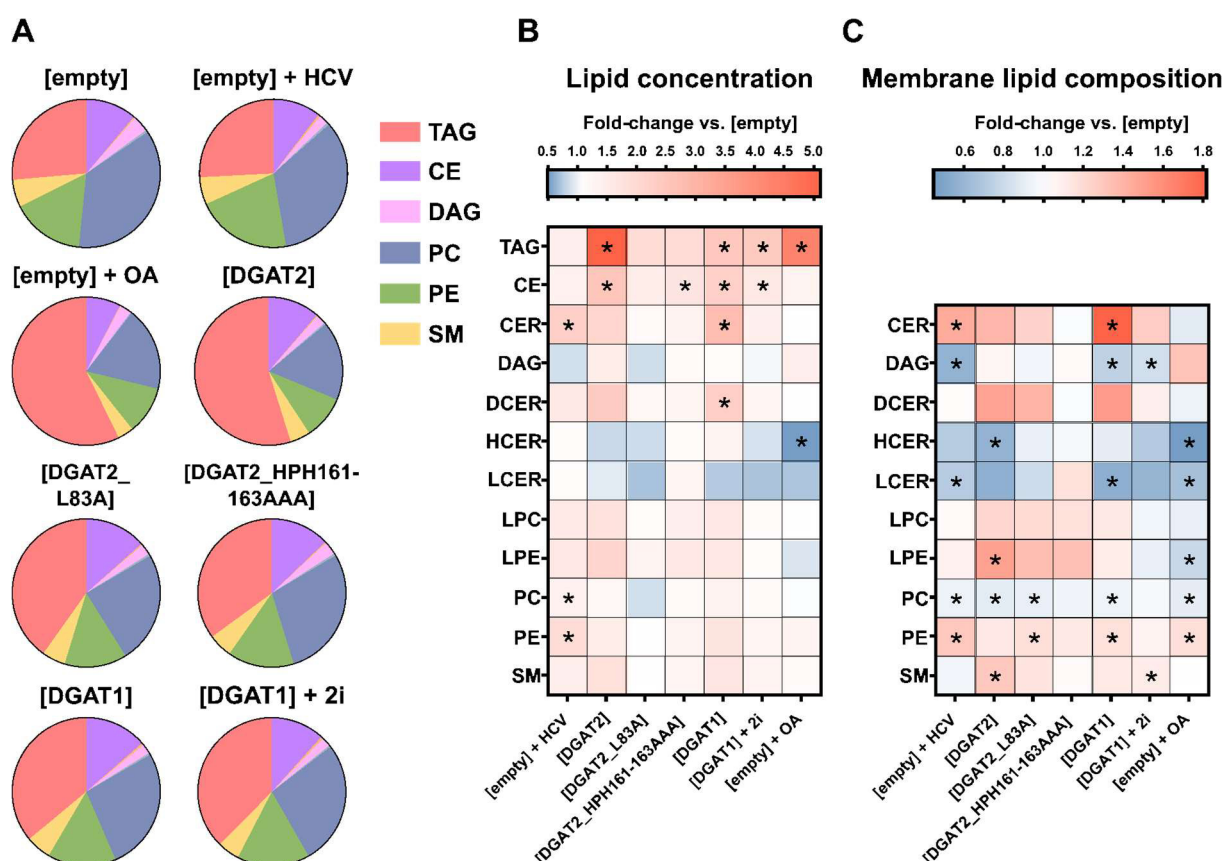


Figure 50: Effect of HCV infection, DGAT protein expression and OA treatment on the lipid profile analyzed on lipid class level. (A) Relative proportions (pie-charts) of lipid classes in whole lipidome of cytoplasmic extracts of the different tested cell lines. **(B)** Heatmap of fold changes of lipid class concentrations in infected, DGAT overexpressing or 360 μ M OA treated cells. **(C)** Heatmap of fold changes of membrane lipid composition calculated by normalization to the whole lipid content without TAG and CE classes. Values relative to the relative control cells ([empty]) or [empty] + DMSO for DGAT1 + DGAT2i). Significant changes are indicated by asterisks, ($P < 0.05$).

4.6.4. Changes on lipid species and FA-subspecies level

Furthermore, we analyzed the lipid profiles on lipid species level (Fig. 51-53). Due to the impact of DGAT2 overexpression on the HCV RO, we focused on the regulation of the membrane lipid composition, which plays a crucial role during the membranous web formation [39,44,81].

Importantly, the individual lipid species of a specific lipid class possess different biochemical and biophysical properties dependent on their FA chain. The diversity of this FA composition, in particular the PL classes, influences the flexibility and curvature of lipid membranes [50,159]. Dependent on the degree of saturation, one distinguishes between saturated, mono-unsaturated (MUFA), and polyunsaturated fatty acyl (PUFA) chains. We therefore analyzed the changes of the membrane lipid profiles on lipid species level with regard to the FA characteristics (Fig. 51).

Consistent with the trends on the lipid class level, we observed a strong increase of several PE species in HCV-infected cells, while DAG lipid species were rather down-regulated (Fig. 51A). Interestingly, although few PC lipid species were upregulated by HCV infection, we detected several depleted PC species, predominantly with PUFA chains (Fig. 51A). Moreover, while CER species were rather upregulated upon HCV infection, some of the low abundant glycosphingolipids (HCER, DCER) were significantly downregulated. In contrast, the proportion of SM species was not affected by HCV infection.

Interestingly, supporting the findings on lipid class level, we observed similar trends for various lipids when overexpressing DGAT2 compared to HCV infection. For example, we detected mutually upregulated CER and downregulated HCER lipids, and a strong increase in PE species, especially PUFA-PEs (Fig. 51B). However, in contrast to HCV infection, several saturated and MUFA-PC species were downregulated in DGAT2 expression, whereas PUFA-PCs were differentially regulated (Fig. 51B). Additionally, DGAT2 overexpression had a stimulating effect on LPC and SM species (Fig. 51B).

The changes of the lipid species profile caused by the catalytic mutants of DGAT2 mirrored the effect of DGAT2 wild-type expression, albeit in a milder form (Fig. 51C and D). Similarly, DGAT1 overexpression enhanced various PUFA-PLs, also in the presence of the DGAT2 inhibitor (Fig. 51E and F). Remarkably, CER species were strongly upregulated in DGAT1-overexpressing cells. Interestingly, this effect was reduced in DGAT2 inhibitor treated cells, matching the observations on lipid class level (Fig. 50C).

Conversely, in OA treated cells, several PUFA-PLs were strongly downregulated while various saturated and MUFA-PL were enhanced (Fig. 51E). Interestingly, this effect was the opposite for DAG species, where PUFA-DAG species were rather upregulated, while saturated and MUFA-DAG species were depleted (Fig. 51C). Overall, the lipid composition changes upon OA treatment differed substantially from the overexpression of the DGAT proteins.

In summary, these results indicate, on the one hand, a vast overlap of lipid changes, also on FA-species level, mediated by HCV infection and DGAT2-induced LD biogenesis, and on the other hand, a strong depletion of selected saturated and MUFA-lipid species upon DGAT2 overexpression. Importantly, both effects were dependent on the catalytic activity of the DGAT2 protein and might contribute to the antiviral effect.

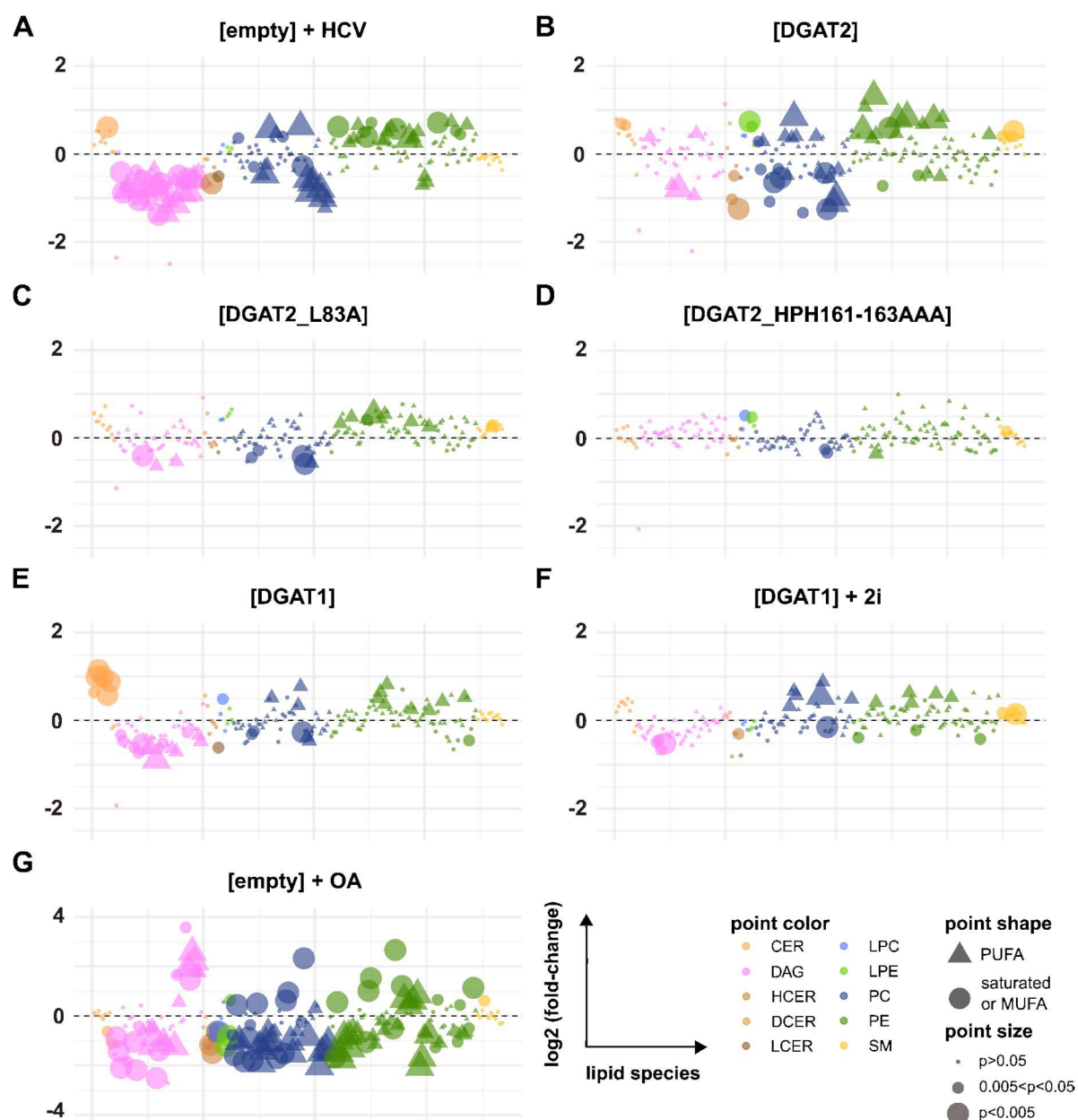


Figure 51: Membrane lipid profile changes upon HCV infection, DGAT expression or OA treatment on lipid species level. Bubble plots of log₂ fold changes of membrane lipids relative to the control cells ([empty] (A-E, G) or [empty] + DMSO (F)). Each point represents one individual lipid species. Point color indicates the lipid classes. Point size is respective to the p-value from t-test with unequal variances. Lipids are divided into species with saturated and mono-unsaturated (MUFA) (represented by bubbles) and species with polyunsaturated fatty acyl (PUFA) chains (represented by triangles). Note that the y-axis scale was adjusted in G while the same scale was used in all other plots.

To have a closer look at the effect of HCV infection and DGAT2 expression on the regulation of saturated and unsaturated lipid species, we further analyzed the changes within PC and PE lipid classes on FA species level (Fig. 52). The length and saturation degree of the FA chain can impact the biophysical properties of lipid membranes, such as membrane fluidity and bending ability. These properties are thought to be important for the formation of the HCV RO formation [44,70]. Accordingly, HCV infection was shown to upregulate various MUFA- and PUFA-PL species [44,45,160].

Aligned with the observations of Hofmann et al. [44], HCV infection specifically increased PLs with highly unsaturated fatty acyl (UFA) chains, including lipids with (C20:4), (C20:5), (C22:4), and (C22:6) FA chains (Fig. 52A and B). In contrast, several (C18:2), (C18:3), (C20:2), and (C20:3) PL species were downregulated (Fig. 52A and B). Moreover, while (C16:0), (C18:0), and (C18:1) PE species were upregulated (Fig. 52B), we detected a decrease of lipids with these FA chains in the PC class (Fig. 52A). Surprisingly, the expression of DGAT2 also increased several PLs with highly UFA chains, particularly (C20:4) and (C20:5) PLs (Fig. 52C and D). In contrast to HCV, species with (C18:2) and (C18:3) FA chains were strongly upregulated (Fig. 52C and D). Moreover, we observed a strong depletion of lipids with (C16:0), (C16:1) and (C18:1) FA chains upon DGAT2 overexpression, including the highly abundant PC (16:0/16:0), PC (16:0/18:1) and PE (18:1/18:1), which were not affected or upregulated in HCV-infected cells (Fig. 52C and D).

Importantly, we detected similar trends in cells expressing the catalytically impaired DGAT2 mutants and DGAT1, although in attenuated form (Fig. 52E-J). Furthermore, PLs with long FA chains were specifically increased in DGAT1-overexpressing cells treated with the DGAT2 inhibitor (Fig. 52K and L). Interestingly, the effect of OA addition on the PL profile strongly differed from DGAT expression or HCV infection. As expected, due to the higher abundance of OA, oleyl-(C18:1) PL species were selectively increased in the membrane lipid composition, whereas other lipid species were rather downregulated (Fig. 52M and N).

In summary, both DGAT2 overexpression and HCV infection elevated lipids with long PUFA chains, whereas opposing effects were observed for (C18:2), (C18:3) and MUFA-PL species with (C18:1) and (C16:1) FA chains.

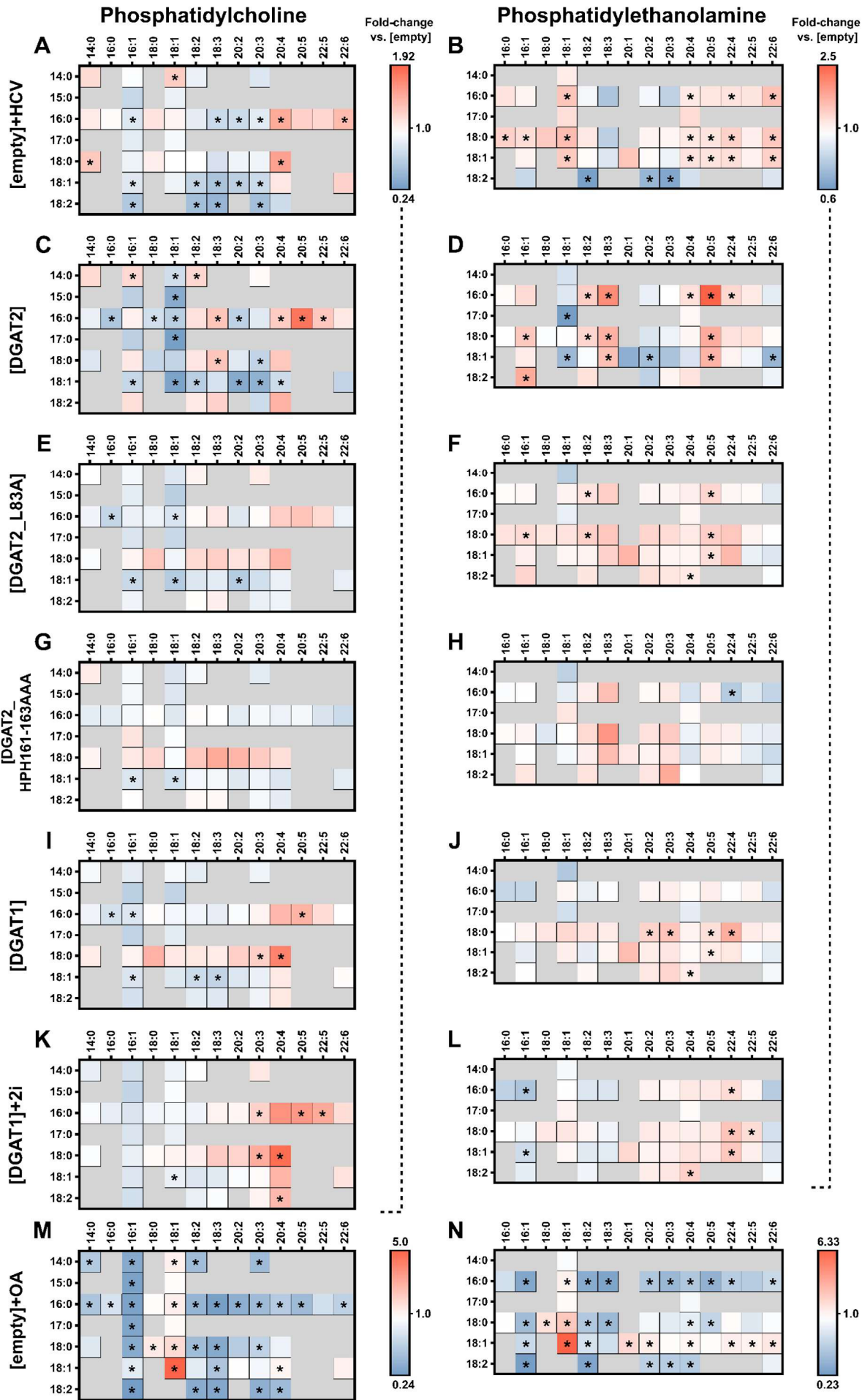


Figure 52: Changes of PC and PE lipid species on fatty acid subspecies level upon HCV infection, DGAT expression and OA addition. (A-N) Heatmaps of PC (left panel) and PE (right panel) lipid species profiles upon HCV infection, DGAT2 expression or OA treatment. Fold changes relative to the control cells ([empty] (A-J, M, N) or [empty] + DMSO (K,L)) are depicted. Significant changes ($P < 0.05$) are highlighted with asterisks. Note the adjusted color scale for fold-changes in OA treated cells (M and N) compared to the heatmaps in the other panels.

Furthermore, we determined the major regulated lipid species in HCV infection and DGAT2 overexpression among all 107 membrane lipid species, which were significantly affected by either HCV infection or DGAT2 overexpression (Fig. 53A). Of these, 22 lipid species were significantly regulated by both HCV infection and DGAT2 overexpression (Fig. 53A and B).

As observed above, various lipid species with PUFA-PLs were upregulated by both DGAT2 expression and HCV infection (Fig. 53C). This applied especially to PLs containing arachidonoyl-(AA, C20:4) or eicosapentaenoyl-(EPA, 20:5) FA chains (Fig. 53C). Moreover, several PC and DAG species were mutually downregulated upon HCV infection and DGAT2 overexpression, including the highly abundant PC (18:1/16:1) (Fig. 53C). In contrast, we detected 6 lipid species that were significantly but differentially regulated upon HCV infection and DGAT2 infection. These included on the one hand the oleoyl-(C18:1) FA-containing PE (18:1/18:1), PC (18:1/22:6), and PE (14:0/18:1) species, which were upregulated upon HCV infection but downregulated by DGAT2 overexpression, and on the other hand PC (18:0/18:3), DAG (16:1/20:4), and DAG (14:0/18:2), which were downregulated upon HCV infection but upregulated by DGAT2 overexpression (Fig. 53C).

Interestingly, the regulation of these lipids was mirrored in cells overexpressing the DGAT2 mutants or DGAT1, but not in OA-treated cells, in which oleyl-PLs were predominantly increased and other PL species were downregulated (Fig. 53C).

Altogether, these results show that long-chain PUFA-PLs are similarly regulated by HCV infection and DGAT2-overexpression, while MUFA and saturated PLs are rather up-regulated upon HCV infection and downregulated upon DGAT2 overexpression. Therefore, we hypothesize that excessive LD biogenesis in DGAT2-overexpressing cells either requires similar lipid species, particularly PUFA-PLs, which are also required for HCV replication, or lacks specific lipids essential for HCV RO formation.

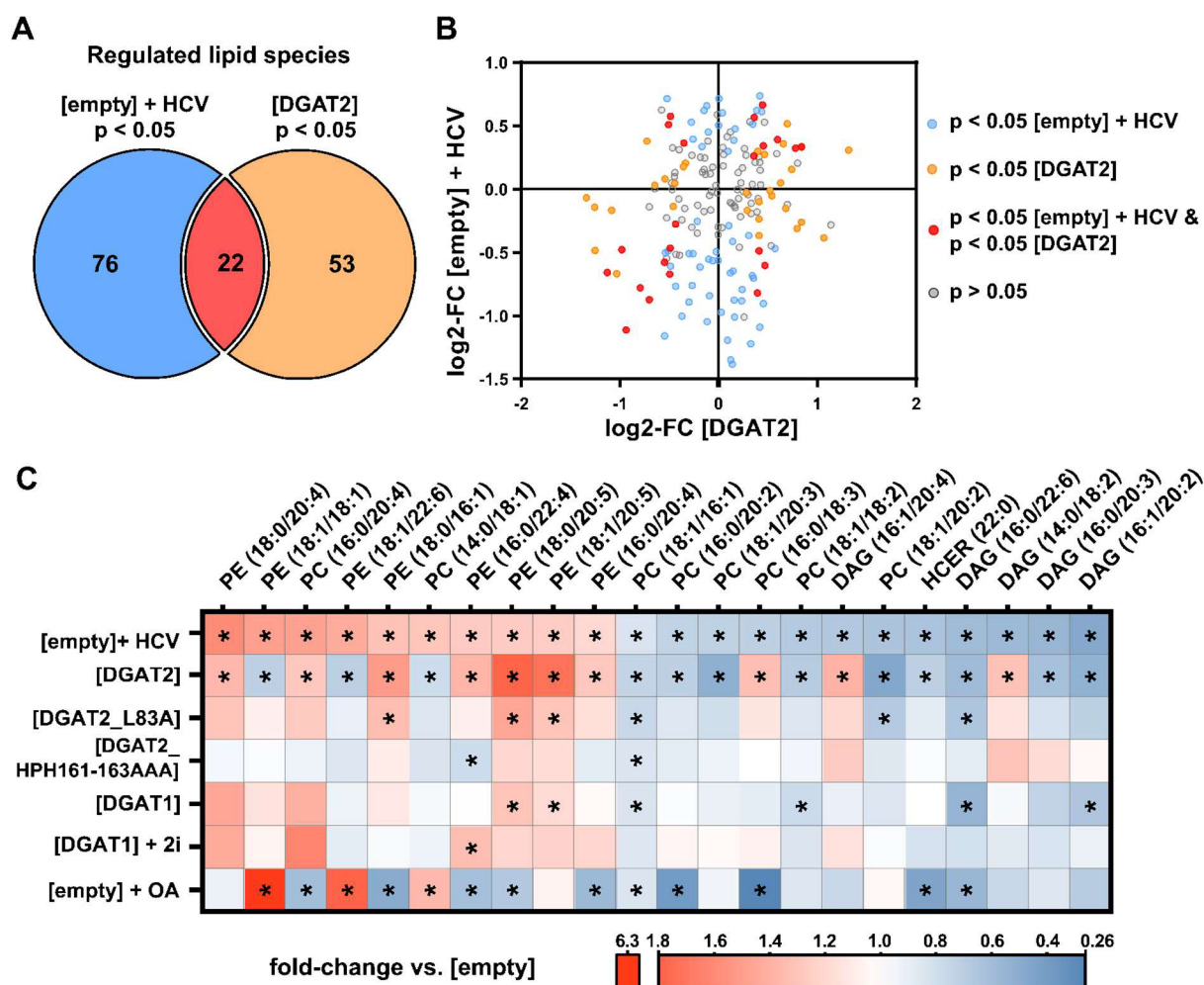


Figure 53: Top regulated membrane lipid species upon HCV infection and DGAT2 expression. (A) Of the 185 measured membrane lipid species identified in the Lunet N hCD81 cell background, 107 lipid species were identified that were significantly up- or down-regulated upon HCV infection (76 lipid species, blue) or DGAT2 expression (53 lipid species, yellow) or both (22 lipid species, red) in Lunet N hCD81 cells compared to the control cells. Log2 fold changes of these lipid species are shown in (B) as a scatterplot with the same color code. (C) Fold changes of membrane lipid species significantly regulated in both HCV infection and DGAT2 overexpression. Fold-changes of HCV-infected, DGAT-overexpressing or OA-treated cells relative to control [empty] cells are depicted in a heatmap. Significant changes ($P < 0.05$) are highlighted with asterisks.

4.6.5. Changes of the TAG lipid landscape on FA-level

The cellular FA metabolism is tightly regulated and dependent on both FA uptake as well as remodeling of incorporated FA between different lipid classes [161,162]. Here, the preference of lipid transport or lipogenic enzymes for binding to substrates with certain FA chains influences the frequency and distribution of FAs in the different lipid classes [161]. As we observed the accumulation of specific MUFA and PUFA species in the PL classes upon DGAT2 expression and HCV infection, we wondered whether these changes are also reflected in the TAG profile. We therefore compared the proportions of different TAG lipids on the FA level.

HCV infection mostly elevated PUFA-TAG species, especially (C20:4) and (C20:5), while TAGs with lower chain length (C12-18) were less strong and rather downregulated with exception of (C12:0), which matches previous findings and is in line with the overall increase of PUFA-FAs, which we also detected in the PL classes [19].

In contrast to HCV, various long-chain saturated and MUFA-TAG species were remarkably increased in DGAT2-overexpressing cells (Fig. 54). This confirms previous publications which reported a substrate preference of DGAT2 for the incorporation of *de novo* generated fatty acid species in TAGs [22,23] and may contribute to the depletion of these lipids in the PC and PE classes described above (Fig. 53). However, the most upregulated TAG species upon DGAT2 overexpression were the PUFA-TAGs with (C18:3) and (C20:5) FA chains (Fig. 54), which were also enriched in PC and PE classes (Fig. 52).

Moreover, the TAG FA profiles of the catalytic mutants resembled those of wild-type DGAT2-expressing cells in an attenuated form. The TAG FA profile was similarly affected by DGAT1 overexpression compared to DGAT2 overexpression (Fig. 54). Especially (C12-14) FA TAG species were elevated upon DGAT1 expression, which is consistent with previous reports of a substrate preference of DGAT1 for medium-chain fatty acids [24] (Fig. 57). However, similar to DGAT2 expression, (C18:3) and (C20:5) TAG species were strongly upregulated in DGAT1-expressing cells (Fig. 54).

Taken together, these results suggest that different FA species are incorporated in TAG in HCV-infected or DGAT2-expressing cells, which could be caused by different substrate channeling and lipid uptake in both conditions.

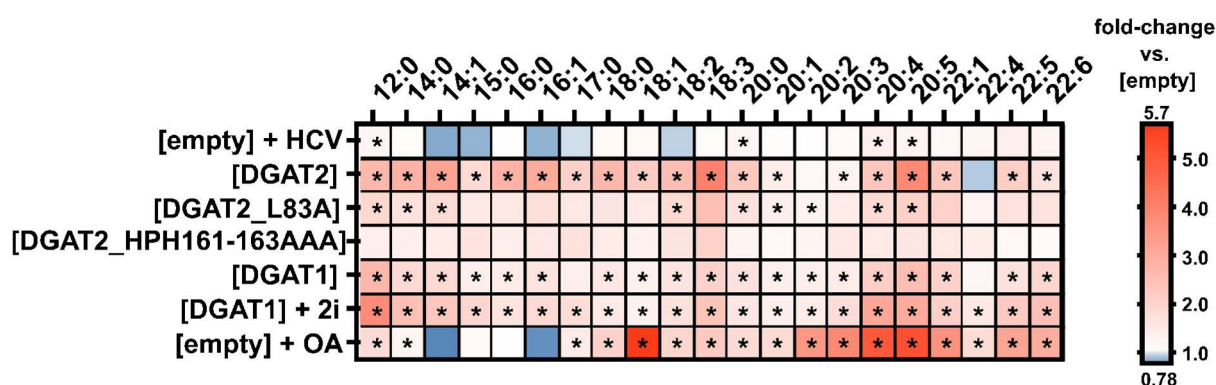


Figure 54: Fatty acyl profile of TAG species upon HCV infection, DGAT protein expression or OA treatment. Heatmaps of TAG FA profile changes. Fold-changes were calculated based on TAG-FA proportions of total lipid percentages compared to the control cells ([empty] or [empty] + DMSO for [DGAT1] + 2i). Significant changes are highlighted with asterisks for $P < 0.05$.

5. Discussion

5.1. HCV infection is inhibited by DGAT2-mediated LD biogenesis

Over the last years, the so-far underrated LD organelle gained more attention and has shown to be involved in the life cycle of various viruses. HCV infection in particular is tightly connected to the LD biogenesis [23,121,122,163]. Increasing LD content has been observed *in vitro* but also *in vivo* upon infection with HCV and is clinically associated with development of steatohepatitis [164,165]. LDs are entangled within the convoluted membranes of the HCV MW and are utilized as energy reservoirs, as well as assembly platform for the production of HCV lipo-viro-particles [121]. The lipogenesis enzyme DGAT1 plays an essential role in HCV assembly, as its expression is crucial for the recruitment of both Core and NS5A proteins to the viral assembly site at the ER-LD interface [127,166]. Of note, the enzymatic activity of DGAT1, which catalyzes the esterification of DAG to TAG, is required to fulfill the role as an HCV assembly factor [127]. Interestingly, although the other DGAT isoform in humans, DGAT2, catalyzes the same enzymatic reaction, DGAT2 is not able to fulfill the role as HCV assembly factor and its knock-down or inhibition does not have an effect on HCV replication [126].

Strikingly, in our lab, the overexpression of DGAT2 revealed a remarkable inhibitory effect on HCV replication (Fig. 7). JcR2a luciferase values were decreased about 2-log fold, an effect that is comparable to the strong antiviral effect of PI4K-IIIa reduction [52]. The inhibitory phenotype of DGAT2 expression was observed for all tested HCV genotypes, including genotype 1b, 2a, and the highly steatogenic genotype 3a (Fig. 25). Despite the strong antiviral effect upon DGAT2 overexpression, endogenous DGAT2 unlikely plays a role as an HCV restriction factor itself, as the inhibition of endogenous DGAT2 by a small molecule inhibitor did not elevate HCV replication (Fig. 12). In contrast to the control cells, the addition of the DGAT2 inhibitor to DGAT2-overexpressing cells could partially restore viral replication and increased JcR2a luciferase values up to 3-fold (Fig. 12). This indicates that the catalytic activity of DGAT2 is required for the inhibitory effect on HCV infection. Interestingly, we observed a link between the anti-viral effect and excess LD biogenesis caused by the overexpression of DGAT proteins: The expression of DGAT1 or catalytically impaired DGAT2 variants had a milder effect on both LD accumulation and, simultaneously, a reduced antiviral effect on HCV infection compared to the wild-type DGAT2 protein (Fig. 7, 13, 21).

Furthermore, we tested the antiviral effect of DGAT2 expression in various HCV permissive cell lines (Fig. 22). Interestingly, we identified two cell lines, in which the overexpression of DGAT2 did not impair HCV infection- HuH6 and 293T-miR-122 cells. Consistent with the earlier findings, the overexpression of DGAT2 led only to a mild induction of LDs in 293T-miR-122 cells (Fig. 22E), which supports the hypothesis, that the DGAT2 antiviral activity is linked to the LD accumulation.

However, although DGAT2 expression drastically increased the LD content in HuH6 cells, HCV was not inhibited by DGAT2 expression in this cell line mode (Fig. 22C). This indicates that the mere increase of the LD content is not solely responsible for the antiviral effect of DGAT2.

5.2. DGAT1 overexpression has a mild effect on HCV infection

Besides DGAT2, we also observed an antiviral effect in DGAT1-overexpressing cells (Fig. 7). This finding was surprising at the first glance, as DGAT1 was shown to have a proviral role in the HCV virus particle production [126]. However, so far, the role of DGAT1 in HCV assembly was investigated by inhibition or knockdown of endogenous DGAT1 and thus differed from the overexpression system that we used in our study [126,127]. Therefore, the results of the present study do not contradict previous publications. In contrast, they highlight that the tight regulation of LD biogenesis is essential for the HCV life-cycle and both depletion as well as excess DGAT1 (and DGAT2) expression are detrimental for HCV infection. Importantly, the antiviral effect of DGAT1 overexpression was weaker than that of DGAT2 and not as robust across different experimental set-ups (Fig. 7). As such, we did not observe an inhibitory effect of DGAT1 in Lunet N hCD81 cells transduced with lentiviruses, although the DGAT1 mRNA level and LD accumulation indicated successful expression of the construct (Fig. 10 and 11). Interestingly, we detected upregulated DGAT2 mRNA expression in Lunet N hCD81 cells stably expressing DGAT1 in which the antiviral effect of DGAT1 was observed (Fig. 8). Moreover, while treating the DGAT1-expressing cells with the DGAT1 inhibitor did not rescue the antiviral effect, we observed a reduced antiviral effect in the DGAT1-expressing cells treated with the DGAT2 inhibitor, although the effect was not statistically significant (Fig. 12). These findings suggest a time-dependent cross-regulation of DGAT1 and DGAT2 expression, which might have an impact on observed antiviral effect of stable DGAT1 expression. Therefore, the results obtained in stable Lunet N hCD81 DGAT1-expressing cell lines should be interpreted with caution and considering a possible cross-regulation.

For example, we performed the quantification of LD profiles in stably expressing Lunet N hCD81 cell lines to ensure that each individually quantified target cell successfully expressed the corresponding DGAT construct. Both DGAT1 and DGAT2 overexpression caused enlarged, but not increased numbers of LDs. We observed this phenotype both in untreated cells and in cells expressing the HCV polyprotein, which form a membranous web-like structure. (Fig. 16 and 31). Overall, we did not detect any obvious differences in the LD profiles of DGAT1 and DGAT2-overexpressing cells, except for a mild but not statistically significant reduction of LD numbers in DGAT1-overexpressing cells (Fig. 16 and 31).

These results differ from previous publications [98,167], which reported that DGAT1 and DGAT2 give rise to different LD subsets. It was shown in *Drosophila* and mammalian cell models that the ectopic expression of DGAT1 and DGAT2 accumulates small and large LDs, respectively [90].

Importantly, the aforementioned cross-regulation of DGAT2 expression within the stable DGAT1-expressing cells might contribute to this finding and could explain, why we did not observe differential effects of DGAT1 or DGAT2 expression on the LD profile. Furthermore, both image quantification methods underestimate the amount of very small LDs, as they are not easily distinguished from the background or other vesicular structures in fluorescence and EM image analysis, respectively. Therefore, this experiment should be repeated in the presence of the respective DGAT inhibitors to suppress the possible cross-regulation. Additionally, the LD quantification in DGAT1 and DGAT2-expressing cells would also benefit from using other LD markers that are more suitable for the detection of nascent LDs, such as the LD dye Live Drop [98].

5.3. The localization of DGAT2 at LDs is not important for the antiviral phenotype

DGAT1 and DGAT2 belong to different protein families and differ both in subcellular localization and substrate specificity [76,168]. While the localization of DGAT1 is restricted to the ER-membrane, DGAT2 can also associate with LDs and was detected at mitochondria and mitochondria-associated membranes [113–115,134]. Therefore, in the current model, DGAT1 is believed to be responsible for the fraction of ER-bound LDs that are preferentially hijacked by HCV [126,127]. We thus wondered whether the subcellular localization of DGAT2 plays a role for its antiviral properties. We hypothesized that LD association of DGAT2 and growth of cytosolic rather than ER-bound LDs is detrimental to HCV replication, as HCV might have evolved to utilize ER-bound LDs rather than cytosolic LDs.

Surprisingly, we found that inhibition of DGAT2 localization to the LD surface did not impair the antiviral activity of the protein (Fig. 21), which speaks against this hypothesis. Of note, localization at mitochondria does also not appear to play a role in the antiviral phenotype of DGAT2 overexpression (Fig. 21). In contrast, deletion of the transmembrane domain of DGAT2, which is required for ER association, resulted in loss of antiviral activity of the protein, although functional catalytic activity of the murine version of this DGAT2 mutant was reported (Fig. 21) [137]. Of note, the functional activity of the described DGAT2 mutant with abolished ER-association should be addressed by further experiments.

Against our initial hypothesis, these results indicated that, rather than enhanced TAG biogenesis at the LD surface, the overstimulation of ER-localized LD biogenesis caused the antiviral effect of DGAT2 overexpression. Therefore, besides the catalytic activity of DGAT2, the association of DGAT2 with the ER-membrane appears to be important for the inhibition of HCV infection.

5.4. DGAT2 overexpression affects HCV replication and the formation of the HCV replication organelle

To better understand the mechanism behind the antiviral effect, we wanted to determine the step of the HCV life cycle that is affected by DGAT2 overexpression. The results of the whole replication cycle experiment showed that the DGAT2-mediated inhibition targeted the HCV life cycle before the formation of viral progeny and the second round of infection (Fig. 7). Additionally, the overexpression of DGAT2 impaired viral replication of both full-length HCV and various SGR constructs despite bypassing the entry step by transfection of the viral genomes (Fig. 25). Moreover, using the pIRF1b translation reporter construct, we did not observe any change in IRES-mediated translation upon expression of DGAT2 (Fig. 26). These results suggest that the antiviral effect of DGAT2 most likely targets a replication step after viral entry but before HCV progeny release.

Of note, we also tested the formation of HCV replicase complex formation in DGAT2-expressing cells by fluorescence imaging of NS5A puncta in HCV-infected cells (performed by G.V., data not shown). The numbers of NS5A punctae were significantly reduced in DGAT2-expressing cells and dependent on the catalytic activity of the protein (data not shown). In order to prevent possible biases related to the reduced infection rate in DGAT2-expressing cells, this experiment should be repeated in a replication-independent system, such as the ectopic expression of the HCV polyprotein NS3-5B [41,152].

Subsequently, we investigated the formation of the HCV RO in Lunet-T7 cell lines stably expressing the DGAT proteins after transfection of the pTM-NS3-5B-NS5A construct, which enables the formation of the HCV membranous web independently of viral RNA replication (Fig. 28). Strikingly, we observed a reduction of DMV numbers in Lunet N hCD81 [DGAT2] cells, which indicates an impairment of the HCV RO formation (Fig. 29 and 30). Consistently, the depletion of DMVs was weaker in the catalytically inactive DGAT2 mutant expressing cells (Fig. 30). These findings suggest that excess DGAT2 expression targets the formation of the HCV membranous web, dependent on the catalytic activity of the protein. Since DMVs originate from the ER membrane, this result is consistent with the importance of ER-localization of DGAT2 for the antiviral effect of the protein (Fig. 21).

Importantly, the addition of OA did not reduce the number of DMVs, despite a strong effect on LD accumulation (Fig. 14 and 32). Thus, the observed decline in DMVs in DGAT2-expressing cells is not due to a mere accumulation of LDs pushing DMVs out of the field of view. In agreement with these results, OA treatment did not affect HCV replication when added directly after infection (Fig. 14). However, we observed a very mild effect of OA on JcR2a luciferase values when administered prior to HCV infection (Fig. 14). Nevertheless, the antiviral effect was marginal compared to the strong antiviral effect of DGAT2 overexpression (Fig. 7 and 14). Moreover, in contrast to OA, the induction of DGAT2 also affected virus replication when induced 4 or 24 hours after infection (Fig. 26). As HCV ROs are

continuously generated *de novo* at different cellular locations [169,170], the later induced DGAT2 expression might directly interfere with the ongoing RO formation and HCV replication. In summary, these results suggest that the extensive LD accumulation upon DGAT2 overexpression, but not upon OA treatment, is detrimental to HCV RO formation.

Of note, the effect of various FAs, including OA, on HCV replication was also investigated by Hofmann et al [44]. The study reported an effect of prolonged OA treatment on the integrity of HCV membranous web five days after infection. Apart from the expected accumulation of LDs, we did not observe such effects in our study (Fig. 21 and SFig. 2). The different protocol and the use of the pTM construct may explain why the results of our study differ from the previous publication [44]. Moreover, Hofmann et al. described no effect of OA treatment on the DMV biogenesis itself, which is in agreement with our observations (Fig. 32).

Altogether, these results indicate that excess LD formation upon DGAT2 overexpression has a detrimental effect on the formation of the HCV RO, leading to a strong antiviral effect that also impairs ongoing viral replication. As both DMV and LD biogenesis are localized at the ER-membrane, and the ER-localization of DGAT2 seems to be important for the antiviral effect of the protein (Fig. 21), we hypothesize that the overstimulation of LDs at the ER membrane by excess DGAT2 expression might lead to changes of the lipid composition, that are detrimental for the formation of the HCV RO.

5.5. The inhibitory effect of DGAT2 expression is specific for HCV

Not only the HCV membranous web, but also the ROs of other viruses of the *Flaviviridae*, *Coronaviridae*, and *Hepeviridae* families derive from the ER-membrane [30]. Both membrane invaginations and protrusions, including DMVs, are common RO architectures formed at the ER membrane [30]. Due to the strong effect of DGAT2 on the HCV DMV abundance, we speculated, that excess DGAT2 might also affect the replication of other +ssRNA viruses, that induce a DMV-shaped RO, and subsequently tested the sensitivity of HCoV-229E to DGAT2 overexpression. However, surprisingly, the replication of HCoV-229E, which also forms DMVs at the ER-membrane [171], was not affected by DGAT2 overexpression (Fig. 34C). Interestingly, recently DGAT2 was shown to have a proviral function in the SARS-CoV-2 life cycle and act as regulator of the lipid flux between ER, LDs and mitochondria in a complex with the viral ORF6 protein [172]. Therefore, coronaviruses may have evolved to utilize DGAT2-mediated LDs and might consequently not be affected by DGAT2 overexpression. However, this hypothesis requires further investigation, and it would be interesting to also test the effect of DGAT2 overexpression on SARS-CoV-2.

In contrast to HCoV-229E, we observed a mild inhibitory effect of DGAT2 overexpression on ZIKV and LGTV (Fig. 34A and B). However, the reduction of viral titers upon DGAT protein expression was not comparable to the positive control (Fig. 34A and B). As we investigated the effects on both viruses after 96 h of infection, the observed reduction of viral titers might also be related to the impaired cell growth upon DGAT2 expression (SFig. 1). Of note, the overexpression of DGAT1 had a stronger antiviral effect on LGTV expression, that exceeded the probably cell-viability related reduction of DGAT2 overexpression (Fig. 34B). So far, there are no reports about the importance of DGAT1 or DGAT2 in LGTV expression, and it would be interesting to further investigate this effect. Additionally, also the infection of HEV, which belongs to the *Hepeviridae* family and also forms its RO at the ER-membrane [173,174], was not impaired by DGAT2 overexpression (Fig. 34D).

Altogether, these findings indicate that the DGAT2 mediated antiviral effect is specific to HCV replication and might be related to the unique interplay of LD biogenesis and the HCV membranous web. However, it would be interesting to test the effect of DGAT2 expression on DENV or poliovirus replication, which are also tightly linked to LD metabolism [83,175].

5.6. The balance of neutral and membrane lipids is affected by DGAT protein expression and OA treatment

The formation of viral ROs comes along with vast membrane reshuffling and reshaping that require increased membrane lipid biogenesis [30,43]. Accordingly, various +ssRNA viruses have been shown to regulate the expression of lipogenic enzymes and lipid transport proteins in order maintain the high demand of membrane building blocks [68,176–178]. As the DGAT2-mediated LD accumulation caused reduced DMV numbers, a possible mechanism behind the antiviral effect could be that DGAT2 might affect the balance of neutral and membrane lipids in the host cell crucial for the formation of viral ROs. In particular, excessive DGAT2 expression could favor the formation of TAG over membrane lipid biogenesis, which require DAG or FAs as substrate and are important for the formation of HCV RO.

Indeed, we observed a tremendous increase of neutral lipids in DGAT2-overexpressing cells, dependent on the catalytic activity of the protein (Fig. 50). Thereby, the proportion of neutral lipids within the total lipid composition was drastically increased upon DGAT2 overexpression (Fig. 50A). However, the expression of DGAT2 and the misbalance of neutral vs. membrane lipids did not impair other tested +ssRNA viruses, that also rely on the formation of a membranous RO (Fig. 34). This was a first indication against the hypothesis that the imbalance between neutral and membrane lipids is responsible for the antiviral activity of DGAT2. Furthermore, we observed a similar increase of neutral lipids in OA treated cells, which itself was not deleterious for HCV infection (Fig. 14 and 34). Therefore, the sole increase in neutral lipids relative to membrane lipids is not detrimental to viral replication.

Instead, regulation of specific lipid classes or species, rather than bulk membrane lipids, might be responsible for the antiviral phenotype of DGAT2 overexpression on HCV.

Importantly, the esterification of DAG by DGAT2 is the last step in a row of consecutive enzymatic reactions that lead to the formation of TAG but are also involved in the biogenesis of different membrane lipid classes. Interestingly, various of these lipogenic enzymes play a role during the HCV membranous web formation. As such, AGPAT1 or AGPAT2, which mediate the biogenesis of PA, were recently shown to be crucial for both HCV and SARS-CoV-2 DMV biogenesis [31]. Furthermore, both Lipin1 and Lipin2, which convert PA to DAG, have been implicated in the HCV RO formation [179,180]. However, despite their function in the formation of the HCV RO, overexpression of neither of these enzymes could revert or reproduce the antiviral phenotype of DGAT2 expression (Fig. 35). Furthermore, the overexpression of PCYT1A, which is required for the PC homeostasis of growing LDs [91], did not affect viral replication (Fig. 35). Remarkably, not even the co-expression of ABHD5 or ATGL could revert the inhibitory effect of DGAT2, although they catalyze the hydrolysis of TAG to DAG, the opposite reaction of DGAT2 (Fig. 35) and exhibit a proviral function during the HCV particle formation [128,129]. These results demonstrate both the robustness and uniqueness of the antiviral effect mediated by DGAT2 overexpression, which could not be reproduced or rescued by any of the co-expressed enzymes. Moreover, the supplementation with cell-permeable lipid analogs of various membrane lipid classes could also not revert the antiviral effect of DGAT2 overexpression (Fig. 36 and 37). It is noteworthy that the addition of such lipid analogs has been successfully used by other groups to reverse different deleterious effects of lipid depletions [58,77,154–157].

Of note, both rescue experiments could benefit from further optimizations. As such, the co-expression of the different enzymes could be tested in the context of the Dox-inducible cell-lines, as the timing and expression level of the proteins might be essential to revert the antiviral effect of DGAT2.

Furthermore, although the various tested lipid analogs were previously shown to possess cell membrane permeability [58,77,154–157], their successful cellular uptake should be verified in the used set-up. Packaging into artificial liposomes could be beneficial to facilitate the uptake of the lipid analogs, as was done in [77,156]. Moreover, it should be noted that following cellular uptake, lipid analogs are susceptible to conversion to other lipid classes [181,182]. Additionally, various of the supplemented lipids, such as lyso-PC, DAG, CER, and PA possess signaling functions that could overshadow their role as membrane lipid in the formation of the HCV RO [73,76,183,184]. Due to these limitations, it is difficult to draw definite conclusions from lipid supplementation experiments and should therefore be addressed with caution.

5.7.Re-localization of DAG is unlikely responsible for the antiviral effect of DGAT2

Although the role of DAG in HCV replication organelle formation has not yet been described, due to its importance as a substrate for DGAT2, we decided to investigate the localization of DAG pools in DGAT2-overexpressing cells by using a previously described DAG lipid sensor [77]. This sensor allowed us to compare the localization of DAG in DGAT2-expressing and control cells (Fig. 41). Unfortunately, the localization of DAG in HCV-infected cells could not be observed without bias: The HCV-NS5A protein co-localized with both the DAG and the DAG-mutated sensor, suggesting that the co-localization was independent of DAG localization, but caused by the interaction with the sensor constructs (Fig. 43).

In control cells, the DAG-sensor was detected in the cytoplasm and showed a reticular, perinuclear staining that suggested ER and Golgi localization and fits observations of others [77]. Strikingly, the DAG sensor accumulated in the cytoplasm of DGAT2-expressing cells, often in close proximity to LDs, while the perinuclear signal vanished (Fig. 41). Consistently, the enhanced LD biogenesis by DGAT2 expression was shown to increase the DAG content at LDs in a previous study [115]. Interestingly, the accumulation of DAG around LDs was observed in yeast and is believed to play a role in the ER-embedment of LDs [185]. In addition to its importance for TAG and LD biogenesis, DAG plays a role in the formation of extreme membrane curvatures due to its inverted-cone shape, for example in the bending of the inner nuclear membrane during interphase [77,186]. Therefore, we hypothesized that the re-localization of the DAG sensor from the ER and Golgi to LDs might be required for excess LD accumulation in DGAT2-overexpressing cells but detrimental for HCV RO formation, as DAG might be required for membrane bending processes during DMV formation at the ER. However, this hypothesis is contradicted by our observation that several DAG lipid species were downregulated in HCV-infected cells (Fig. 50 and 54). Further evidence against the importance of DAG sensor re-localization for the inhibitory effect of DGAT2 is the fact that DAG sensor re-localization was also observed in HuH6 and 293T-miR-122 cells, in which HCV infection is not inhibited by DGAT2 expression (Fig. 22 and 44). Thus, it is unlikely that the observed re-localization of DAG alone explains the inhibitory effect of DGAT2 overexpression.

5.8.HCV infection and DGAT2 overexpression upregulate similar membrane lipid classes and highly unsaturated phospholipid species

The extensive membrane remodeling and expansion processes involved in viral RO formation require interference with host cell lipid pathways during viral infection. Hence, a specialized lipid environment is created, which facilitates membrane bending and cleavage processes and is crucial for the formation of the vesicular structures of viral ROs [30,81]. Accordingly, shifts both at the lipid class and lipid species

levels have been observed upon HCV infection. The role of PI4P [52,54], Chol [20,57], SM [58], CER [45,64], PC [69], PE [44,45] and PA [31] lipids has been reported or discussed by others.

In our study, we found increased CER, but not SM species upon infection with HCV via lipidomic analysis, which is in line with previous observations [45]. An upregulating effect on CER was also detected upon DGAT2 overexpression and, even stronger, upon DGAT1 (Fig. 50B). Surprisingly, the addition of the DGAT2 inhibitor attenuated the CER upregulation effect in DGAT1-overexpressing cells, suggesting that the balance of DGAT1 and DGAT2 expression is involved in the abundance of CER (Fig. 50C, 51E and F). This finding matches previous publications, which described an increase of CER species upon DGAT2 inhibition due to DGAT2's function in the formation of acyl-ceramide [187].

Furthermore, we detected an increase in absolute concentrations of both PC and PE classes upon HCV infection, which is in agreement with previous publications [44,45,68] (Fig. 50). Interestingly, looking at the membrane lipid composition, the proportion of PC in HCV-infected cells was reduced compared to the control cells (Fig. 51). As PCs possess a rather cylindrical shape, which is important for the formation of flat rather than bent membranes, the reduction in PC in the membrane lipid composition might be in exchange for the increase of other lipid classes with higher curvature favoring shapes, e.g. PE [188]. Interestingly, previous publications have reported the increase of PC at the HCV RO [68], but also a decrease of the total PC concentration was described [189], fitting our results. Furthermore, since the previous studies focused on effects on the lipid profile after 72 hpi [44,45], the observed downregulation of PC lipids could also be related to the earlier time of infection in our study.

Interestingly, also DGAT2 overexpression had a stimulating effect on PC and PE lipid classes, although not statistically significant (Fig. 50). However, several specific PC and PE species were significantly regulated by DGAT2 overexpression (Fig. 51). Additionally, the proportions of various lyso-PC and lyso-PE species were significantly enhanced in DGAT2-overexpressing cells and in DGAT2_HPH161-163AAA-expressing cells, albeit in attenuated form (Fig. 51B and D). These lower abundant lipids play an essential role in lipid signaling and are important intermediates of the PL remodeling pathway, the so-called Land's cycle [161,183]. Lyso-PLs are formed by the hydrolysis of PC and PE to LPC and LPE respectively and free fatty acid. The corresponding responsible enzyme, phospholipase 2, is directly involved in the LD biogenesis [190,191]. Due to their inverted conical shape, accumulation of lyso-PLs induces positive membrane curvature, which is thought to be crucial for LD growth [192]

Importantly, not only the lipid headgroup, but also the saturation level and length of the PL FA chains essentially influence the biophysical properties of lipids and lipid membranes [161,193] and are crucial for various cellular processes, such as the formation of endocytic vesicles [50]. Due to the kinked shape of UFA chains, incorporation of UFA-PLs lead to higher membrane disorder that comes along with increased membrane fluidity, bending rigidity and altered protein binding capacities [50,193].

Additionally, lipids with certain PUFA species, such as docosahexaenoic acid (DHA, C22:6), play a role in the formation of specialized membrane domains, the so-called lipid rafts [194].

These properties are thought to be important for the HCV RO formation, and HCV infection was shown to upregulate various MUFA and PUFA-PL species [44,45,160].

In line with previous publications [44,160], we observed an increase of several PUFA-PL species, especially arachidonoyl-(AA, C20:4), eicosapentaenoyl- (EPA, C20:5), and DHA PLs in HCV-infected cells (Fig. 52A and B). Surprisingly, various of the PUFA-PLs which were upregulated during HCV infection were also strongly increased upon DGAT2 overexpression (Fig. 52A-D). As such, AA- and EPA-PLs were enriched in DGAT2-overexpressing cells (Fig. 52C and D). Consistently, the upregulation of these lipid species correlated with the catalytic activity of DGAT2 and was reduced in the DGAT2 mutant expressing cells (Fig. 52E - J). Interestingly, the stimulating effect on PUFA-PLs has to our knowledge not been reported in the context of DGAT2 overexpression so far. However, AA-PLs were shown to be important for LD biogenesis [195,196]. Mechanistically, increased amounts of PUFA-PLs are thought to support membrane bending and LD budding by decreasing the surface tension between the ER membrane and LD [192,195]. These findings indicate that both HCV infection and DGAT2 overexpression regulate lipid classes and species that are important for membrane curvature and fluidity. The high overlap of the regulation of various lipid classes and FA species between HCV infection and DGAT2 overexpression suggests similar requirements for DMV and LD biogenesis. Subsequently, both processes might compete for specific host cell lipid pools in the DGAT2-overexpressing cells. Importantly, the upregulation of the above-mentioned PUFA-PLs was not detected in OA treated cells, speaking for its relevance for the antiviral effect of DGAT2.

5.9. DGAT2 overexpression depletes saturated and MUFA-PL-species, essential for the HCV RO formation

In addition to these similarly regulated lipids, we also detected individual lipid species that were differentially regulated in DGAT2 overexpression and HCV infection. As such, both linoleyl-(LA, C18:2) and alpha-linoleyl-(ALA, C18:3) PLs were strongly upregulated in DGAT2-overexpressing but downregulated in HCV-infected cells (Fig. 52). Interestingly, the enrichment of ALA-PLs was reported in the context of LD biogenesis [197], which could be relevant for the excess LD biogenesis in DGAT2-overexpressing cells. Additionally, ALA and LA play a role as precursors for other PUFAs, which can be produced by the action of elongases and desaturases [161]. Importantly, both ALA and LA, as well as all other PUFAs, except for mead-acid (C20:3) cannot be generated *de novo* in cells and must be obtained by exogenous uptake [159]. As the proportion of LA and ALA was increased in both PL and TAG classes, the uptake of these lipids might be affected in DGAT2-overexpressing cells.

In contrast to ALA and LA, the oleyl-(C18:1) PL proportions were strongly downregulated in DGAT2-overexpressing cells. This included the highly abundant PE (18:1/18:1), as well as PE (18:1/22:6), which was significantly reduced unlike other PUFA-PL species.

Curiously, this trend was inverted in HCV-infected cells, where oleyl-PLs and other mono-unsaturated- or saturated PLs were rather increased, especially in the PE class (Fig. 52A and B). Matching this observation, the *de novo* biogenesis of MUFAs, such as OA, was described to be crucial for the integrity of the HCV membranous web [44,70,71]. Additionally, the membrane bending properties of DHA [198] and its role in the formation of lipid rafts [194] might be beneficial for the HCV RO formation. Given their downregulation upon DGAT2 overexpression, but not OA treatment, we speculate that the DGAT2-mediated antiviral effect could also be caused by the depletion of these lipid species.

Interestingly, it has been reported, that DGAT2 preferentially utilizes lipids of the *de novo* lipogenesis pathway, including lipids with C12-C14 as well as (C16:0), (C16:1), (C18:0) and (C18:1) acyl chains [120,199]. This is reflected in the TAG-FA profile of DGAT2-overexpressing cells, where those FAs were strongly upregulated alongside the globally increased ALA and EPA species (Fig. 54). Therefore, the substrate channeling of DGAT2 might contribute to the depletion of the aforementioned lipid species. However, further experiments would be required to determine the source of the altered FA remodeling in DGAT2-expressing cells compared to HCV-infected cells.

5.10. Model, conclusions, and future outlook

Based on the highly overlapping lipid changes that favor membrane curvature and bending on the one hand, and decreased proportion of specific, often *de novo* generated lipids on the other hand, we propose a model in which excessive LD formation in DGAT2-overexpressing cells creates an unfavorable environment for the formation of DMVs (Fig. 55). Thereby, both competition for various curvature-inducing lipids as well as enzyme-specific substrate channelling, leading to depletion of specific lipids essential for DMV formation, might contribute to an altered lipid landscape which is detrimental for the HCV RO formation (Fig. 55). Apart from impaired physical membrane properties due to the changed lipid landscape, also the association of HCV replication cofactors could subsequently be affected.

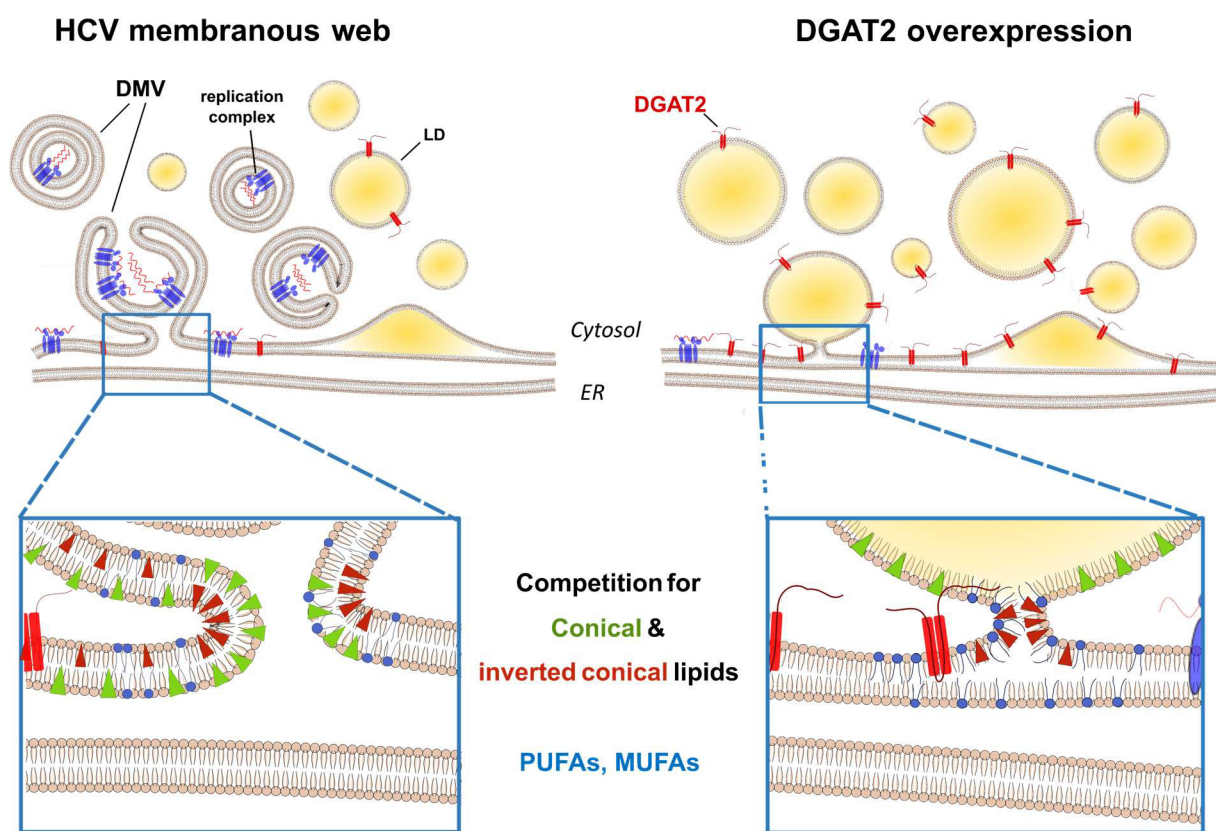


Figure 55: Proposed model of overlapping lipid requirements for HCV DMV synthesis and LD biogenesis upon increased DGAT2 expression. Both HCV membranous web and LD biogenesis reshuffle the host cell lipid landscape in favor for higher membrane curvature and flexibility such as conical and inverted-conical lipids as well as PUFAs and MUFAs, as described in the main text. We hypothesize that due to excessive LD biogenesis and DGAT2-specific substrate preferences, lipids critical for DMV synthesis are channeled toward LD expansion sites upon DGAT2 overexpression and their abundance becomes limiting for HCV RO formation.

Although DGAT2 unlikely acts as host restriction factor and the overexpression of the protein is a rather artificial system, we believe that the lipid changes we observed globally in DGAT2-expressing cells might be relevant for the interaction of LD biogenesis and DMV formation at the ER-membrane on a local level. In the recent decades, it has become increasingly evident that lipid membranes, especially the multifunctional ER membrane, are organized into lipid subdomains characterized by a specific lipid

signature and protein binding [161,200,201]. Such subdomains and their lipid compositions are especially dynamically regulated at membrane contact sites between different organelles .

We believe that the specific lipid composition due to the lipid flux at the ER-LD interface might provide the essential building blocks for the vast expansion of growing LDs, but simultaneously presents an advantageous environment for the HCV DMV formation. In other words, the specific lipid environment created for or caused by LD biogenesis could direct the HCV RO formation sites at the ER-membrane.

Supporting this hypothesis, DMVs are often found in close proximity to LDs [79–81]. In addition to DMVs, ER-enwrapped LDs were observed at the HCV-membranous web by others [79] and also in our study (Fig. 33). This enwrapment is believed to serve the spatio-temporal regulation of HCV replication and virion morphogenesis [79]. Interestingly, we also detected an increased amount of ER-enwrapped LDs in DGAT2-overexpressing cells, which was not dependent on the catalytic activity of the protein (Fig. 33B). Considering the previous publication, it is unlikely that the increased LD enwrapment is antiviral *per se*. However, in addition to the effects on the lipid landscape mediated by DGAT2 expression, the protein's function as a link between ER and LDs, as reported for *Caenorhabditis elegans* [117], could lead to increased lipid flux between ER and LD organelle, supporting our model.

In future, it would be crucial to further test this model and the hypothesis that ER domains specialized for LD biogenesis are used for HCV RO formation. Importantly, further investigations should also focus on the spatially regulated lipid compositions and determine the changes of the lipid landscape, both spatially and temporally resolved. In our study, we decided to concentrate the lipidomics analysis on the whole cell-lysates due to seemingly similar changes between cytoplasmic and microsomal fractions and in order to investigate various different conditions within a reasonable sample size. However, the isolation of microsomal membranes or HCV RO membranes, have been proven to be useful to acquire a spatially resolved view on the lipid changes and should be re-considered for investigations of the here-described model [31,44].

Moreover, microscopy analysis will be essential to unravel the role of LDs in the DMV biogenesis and to investigate lipid localization at the HCV membranous web. In our study, we tested the localization of PI4P and free Chol (Fig. 38), which have been reported to accumulate at the HCV RO and are important for the integrity of the HCV membranous web [20,52,54,57]. We utilized the anti-PI4P antibody or the Filipin III complex to assess the localization of PI4P and Chol in DGAT2-overexpressing or control cells (Fig. 38). However, neither PI4P nor Chol localizations were strongly affected by DGAT2 overexpression, except for occasionally appearing ring-structures of the Filipin dye in DGAT2-overexpressing cells (Fig. 38B), which suggests LD localization. It would be interesting to further evaluate this finding in presence of LD markers, which was so far not successful due to a staining artifact. Additionally, the localization of both PI4P and Chol should also be investigated in DGAT2-overexpressing cells in the

context of HCV membranous web formation, by using the HCV polyprotein expression construct (pTM-NS3-3'-NS5A-eGFP) as described above.

In addition to IF staining, lipid biosensors, such as the DAG and PA sensor applied in this study, are valuable tools for investigating the localization of lipids in cells. However, since the signal intensity of such sensors depends not only on the amount of detected lipid, but also on the expression level of the respective construct, the interpretation of such fluorescent biosensors must be done carefully. In our hands, only the DAG sensor construct showed a specific signal and could be utilized in the present study (Fig. 41-43), while the PA-sensor signal was rather unspecific (Fig. 39). Therefore, other PA-sensor constructs, as described in [205], should be tested and applied to investigate the role of PA-localization in the inhibitory effect of DGAT2 overexpression. Moreover, the localization of these alternative PA-sensor constructs and also of the DAG sensor should be investigated in live cells upon induced expression of DGAT2, and in the context of HCV membranous web formation.

Furthermore, labelled lipid analogs, which enable localization studies both in fixed and live cells, could be utilized to visualize the hypothesized lipid flux and accumulation at the HCV membranous web. At present, extensive research is ongoing to improve the stability and physiological functionality of various lipid analogs [206]. In addition, various lipid analogs, whose dyes change their fluorescent wavelength characteristics upon incorporation into a specific lipid environment, have been described and could be used to study the membrane properties at the HCV membranous web like packaging density and fluidity [207]. For example, an FA analog with an azapyrene dye was described, which changes its absorption and emission dependent on the polarity of its microenvironment [208]. Thereby, the localization of non-polar lipids, such as TAGs stored in LDs, medium-polar membranes and the polar aqueous cytoplasm can be visualized. This could be interesting to decipher the uptake and distribution of MUFA and PUFA lipids, which appear to be crucial for both, the DGAT2-mediated antiviral effect and the formation of the HCV membranous web. Combined with specialized microscopy techniques, such as lipid expansion [209], or super-resolution microscopy [210], the use of lipid analogs and lipid biosensors enables the detection of lipid changes also on nanodomain level and will be fundamental to unravel the role of lipid flux between LDs and ER for the HCV RO.

Besides these fluorescence microscopy based approaches, Raman spectroscopy might be useful to test our hypothesized model: Due to the Stokes shift mediated by the high amount of double bonds, UFAs can be visualized by Raman scattering microscopy [211,212]. Hence, it would be interesting to study the localization of differentially saturated FAs at the HCV membranous web and the effect of both DGAT2 and DGAT1 proteins on LD biogenesis and lipid flux.

Because of the potential cross-regulation and since the antiviral effect of DGAT1 expression was considerably milder compared to DGAT2 expression, we focused our study on the strong antiviral effect of DGAT2. The aforementioned techniques will be crucial to understand why only DGAT1, but not

DGAT2, is utilized by HCV for the virus progeny assembly and the role of both proteins in the HCV RO formation.

In conclusion, based on (i) the unique role of DGAT1 in HCV assembly, (ii) the inhibitory effect of excessive DGAT2 activity on HCV replication (iii) and the close proximity between replication and assembly sites in HCV-infected cells [24,39], we suggest that HCV might have evolved to use DGAT1- rather than DGAT2-generated LDs as a platform for assembly. Further investigation are required to test this hypothesis.

6. Materials

6.1. Nucleotides

Table 1: Plasmids used in this study. Marked constructs (*) have been cloned during this work.

	Name	Reference
	pFK_i389_JcR2a_dg_Jc1 (JcR2a)	[54]
	pFK_JFH1/J6/XbaI/C-846_dg (Jc1)	[2]
	dbn3acc-sgr-cpg-low-luc2-ns5ac (SGR-DBN3A)	[214], gift from Mark Harris
	pFK_i389LucNS3-3'_JFH_dg.gb (SGR-JFH1)	[215]
	pFKi_341_PiLuc_NS3-3'_Con1 ET (SGR-Con1)	[216]
	pTM_NS3-3'_5A gfp 383_JFH.gb	[152]
	pIRF1b	[151], gift from Jean Dubuisson and Annie Cahour
	pWPI_DGAT2_Puro	This study
	pWPI_DGAT2_L83A_Puro	This study
	pWPI_DGAT2_HPH161-163AAA_Puro	This study
	pWPI_DGAT1-Puro	This study
	pWPI_HAHA-L-DGAT2_Puro	This study
*	pWPI_HAHA-L-DGAT2-del30-67_Puro	This study
*	pWPI_HAHA-L-DGAT2-del66-115_Puro	This study
*	pWPI_HAHA-L-DGAT2-mito4A_Puro	This study
*	pWPI_HAHA-L-DGAT2-del327-350_Puro	This study
*	pWPI_HAHA-L-DGAT2-insert-HA_Puro	This study
	pLenti_CMV_TetR_BLR	[217], gift from James Olzmann
	pLenti CMV TO Puro DEST APEX2-V5	[218],
*	pLenti_CMV-TO_HAHA-DGAT2_Puro	This study
*	pWPI_mRuby3_PKCe_C1a_C1b_Puro	This study
*	pWPI_mRuby3_PKCe-C1a-C1b-W264G_stop_Puro	This study
	pWPI-Nter mNeonGreen in frame-Puro	This study
*	pWPI_mNeonGreen_Raf1-PABD_Puro	This study
*	pWPI_mNeonGreen_Raf1-PABD-4E_Puro	This study
*	pWPI_Lipin1_Puro	This study
*	pWPI_Lipin2_Puro	This study
*	pWPI_AGPAT1_Puro	This study
*	pWPI_AGPAT2_Puro	This study
*	pWPI_Lipin1-3xFlag_Puro	This study
*	pWPI_Lipin2-3xFlag_Puro	This study
*	pWPI_AGPAT1-3xFlag_Puro	This study
*	pWPI_AGPAT2-3xFlag_Puro	This study
	pWPI-PCYT1A-shResist-BLR	This study
	pWPI-ABHD5-shResist-L-HAHA-BLR	[128]
	pWPI-ABHD5-shResist-Q130P-L-HAHA-BLR	[128]
	pWPI-ATGL-7siResist-BLR	[129]

pWPI-ATGL-S47A-7siResist-BLR	[129]
pCMV-Delta R8-74	[219]
pczVSV-Gwt	[220]

Table 2: RT-qPCR primers used in this study.

Primer name	Sequence	Final conc. (nM)	Reference
F-GAPDH	5'-GAA GGT GAA GGT CGG AGT C-3'	120	[221]
R-GAPDH	5'-GAA GAT GGT GAT GGG ATT TC-3'	120	[221]
F-DGAT1	5'-ACT GGG AGC TGA GGT GC-3'	150	This study
R-DGAT1	5'-ACC AGG ATG CCA TAC TTG ATG A-3'	150	This study
F-DGAT2	5'-GGC TCA TCG CTG TGC TCT-3'	120	This study
R-DGAT2	5'-GGG GGT GGT ATC CAA AGA TAT AG-3'	120	This study

Table 3: RT-qPCR probes used in this study.

Probe name	Sequence	5' and 3' modifications	Final conc. (nM)	Reference
GAPDH YYE BHQ-1	5'-CAA GCT TCC CGT TCT CAG CCT-3'	YYE – BHQ-1	200	[221]
huDGAT1 TM	5'-CCA GAA ATA ACC GGG CAT TGC TCA-3'	FAM – BHQ-1	200	This study
DGAT2 TM	5'-TGG TCA GCA GGT TGT GTG TCT TCA CC-3'	FAM – BHQ-1	200	This study

6.2. Bacteria

Table 4: Bacteria strains used in this study.

Bacteria strain	Description
<i>Escherichia coli</i> (<i>E.coli</i>) DH5α	F- endA1 glnV44 thi-1 recA1 relA1 gyrA96 deoR nupG 80dlacZΔM15 Δ (lacZYA-argF) U169, hsdR17(rK- mK+), λ–
<i>E.coli</i> Stable2	MAX Efficiency™ Stbl2™ Competent Cells 10268019

6.3. Eukaryotic cell lines

Table 5: Cell lines used in this study. Marked cell lines (*) have been prepared during this work.

	Name	Description	Selection marker
	Huh-7.5	Human hepatoma cell line for efficient HCV virus propagation derived from Huh7 cells [139].	
	Huh-7.5.1	Human hepatoma cell line derived from Huh-7.5, optimized for efficient HCV virus propagation [222].	
	Lunet N hCD81	Human hepatoma cell line derived from Huh7-Lunet cells, highly permissive for HCV RNA replication and ectopically expressing human CD81 receptor [138,139].	Blasticidin
	Lunet N hCD81/ FLuc	Lunet N hCD81 derived stable cell line ectopically expressing <i>firefly</i> luciferase (FLuc) [128]. Used for monitoring of cell viability.	Blasticidin
	Lunet N hCD81/ mRuby2	Lunet N hCD81 derived stable cell line ectopically expressing mRuby2 fluorophore [129]. Used as reference cells for fluorescence microscopy or flow cytometry.	Blasticidin, Puromycin
	Lunet N hCD81 [DGAT2]	Lunet N hCD81 derived stable cell line ectopically expressing human DGAT2.	Blasticidin, Puromycin
	Lunet N hCD81 [DGAT2_L83A]	Lunet N hCD81 derived stable cell line ectopically expressing human DGAT2_L83A mutant.	Blasticidin, Puromycin
	Lunet N hCD81 [DGAT2_HPH161-163AAA]	Lunet N hCD81 derived stable cell line ectopically expressing human DGAT2_HPH161-163AAA mutant.	Blasticidin, Puromycin
	Lunet N hCD81 [DGAT1]	Lunet N hCD81 derived stable cell line ectopically expressing human DGAT1.	Blasticidin, Puromycin
*	Lunet N hCD81 [HA-DGAT2]	Lunet N hCD81 derived stable cell line ectopically expressing human HA-tagged DGAT2.	Blasticidin, Puromycin
*	Lunet N hCD81 [mNeonGreen_Raf1-PABD_Puro]	Lunet N hCD81 derived stable cell line ectopically expressing the PA sensor mNeonGreen-Raf1-PABD.	Blasticidin, Puromycin
*	Lunet N hCD81 [mNeonGreen_Raf1-PABD-4E_Puro]	Lunet N hCD81 derived stable cell line ectopically expressing the mutant PA sensor mNeonGreen-Raf1-PABD-4E.	Blasticidin, Puromycin
*	Lunet N hCD81 /TetR-[HA-DGAT2]	Tet-inducible Lunet N hCD81 derived cell line, stably expressing the Tet-Repressor and Tet-Operator regulated HA-DGAT2.	Blasticidin, Puromycin
	Lunet T7 [empty]	Derived from Huh7-Lunet T7 cells stably expressing the T7 polymerase [223]. Stable expression of empty vector control.	Puromycin
	Lunet T7 [DGAT2]	Derived from Huh7-Lunet T7 cells ectopically expressing human DGAT2.	Puromycin

	Lunet T7 [DGAT2_HPH161-163AAA]	Derived from Huh7-Lunet T7 cells ectopically expressing human DGAT2_HPH161-163AAA mutant	Puromycin
	Lunet T7 [DGAT1]	Derived from Huh7-Lunet T7 cells ectopically expressing human DGAT1.	Puromycin
	HepG2-HFL	Human hepatocellular carcinoma cell line, derived from HepG2 cells ectopically expressing miR-122 and CD81 [147].	Blasticidin
	HuH6	Human hepatoblastoma cell line [224].	
*	HuH6 [empty]	Derived from HuH6, stably expressing empty vector control.	Puromycin
*	HuH6 [DGAT2]	Derived from HuH6, stably expressing empty vector DGAT2.	Puromycin
	HEK293T	Human embryonic kidney cell line that expresses the large T antigen of SV40 [225].	
	293T-miR-122	Derived from HEK293T, stably expressing miR-122 [140].	Puromycin
*	293T-miR-122 [DGAT2]	Derived from 293T-miR-122, stably expressing DGAT2.	Puromycin
*	293T-miR-122 [empty]	Derived from 293T-miR-122, stably expressing empty vector control.	Puromycin
	HeLa-miR-122	Human epitheloid cervix carcinoma cell line, derived from HeLa cells, ectopically expressing miR-122 [140].	Puromycin
	Caco-miR-122	Human colon carcinoma cell line, derived from Caco-2 cells, ectopically expressing miR-122 [140].	Puromycin
	Vero E6	Green monkey kidney epithelial cell line [226].	
	A549	Human adenocarcinoma alveolar basal epithelial cells [227].	

6.4. Viruses

Table 6: Virus stocks used in this study.

Name	Origin	Cell line for virus amplification
HCoV 229E Rluc	gift from Volker Thiel	Huh-7.5
ZIKV (strain H/PF/2013)	kindly provided by the Centre National de Référence des arbovirus IRBA at the Aix-Marseille University, France, and distributed via the European Virus Archive Global, EVAg Ref-SKU:001v-EVA1545	Vero E6
LGTV (strain TP21)	gift from Gerhard Dobler	Vero E6

Virus stocks were amplified and titrated by Stefanie Rößler (ZIKV, LGTV) and Corinne Ginkel (HCoV 229E). Stocks of HEV Kernow-C1 p6 used by V.K. were produced as described before [228].

6.5. Antibodies

Table 7: Primary antibodies used in this study.

Targeted antigen	Manufacturer	Order number	Species	Concentration ($\mu\text{g/mL}$) or dilution	
				Immuno-fluorescence	Western blot
Beta Tubulin	Abcam	ab15568	rabbit		1
Calnexin	Abcam	ab22595	rabbit	1	1
CoxIV (F8)	Santa Cruz	sc-376731	mouse	0.4	0.2
DGAT2	Abcam	ab237613	rabbit	1-5	0.05-0.2
DGAT2	Santa Cruz	sc-293211	mouse	1-5	0.05-0.2
GAPDH	Santa Cruz	sc-47724	mouse		0.2
HA tag	Novus Biologicals	NB600-362	goat	40	
HA tag (clone 16B12)	BioLegend	901502	mouse	2	1
HCV NS5A (9E10)	Gift from Charles Rice, produced by Cell Essentials		mouse	6.66	
Perilipin 2 (ADRP (AP125))	Progen	610102	mouse	1	1
PCYT1A (CCT α (F-6))	Santa Cruz	sc-376107	mouse		0.4
PI4P	Echelon Bioscience	Z-P004	mouse	33.33	

Table 8: Secondary antibodies used in this study.

Name	Manufacturer	Order number	Species	Concentration ($\mu\text{g/mL}$) or dilution	
				Immuno-fluorescence	Western blot
Goat anti-Mouse IgG Secondary Antibody, Alexa Fluor Plus 488	Invitrogen	A32723	goat, anti-mouse	2	
Goat anti-Rabbit IgG Secondary Antibody, Alexa Fluor Plus 488	Invitrogen	A32731	goat, anti-rabbit	2	
Goat anti-Mouse IgM Secondary Antibody, Alexa Fluor 568	Invitrogen	A21043	goat, anti-mouse	2	
Chicken anti-Goat IgG Secondary Antibody, Alexa Fluor 647	Invitrogen	A21469	chicken, anti-goat	2	
Goat anti-Mouse IgG Peroxidase Conjugate	Sigma Aldrich	A 4416	goat, anti-mouse		1/15,000
Goat anti-Rabbit IgG Secondary Antibody, HRP	Invitrogen	G-21234	goat, anti-rabbit		1/15,000
Goat Anti-Mouse IgG StarBright Blue 520	BioRad	12005866	goat, anti-mouse		1/2500
Goat Anti-Rabbit IgG StarBright Blue 520	BioRad	12005869	goat, anti-rabbit		1/2500

Goat Anti-Mouse IgG StarBright Blue 700	BioRad	12004158	goat, anti-mouse		1/2500
Goat Anti-Rabbit IgG StarBright Blue 700	BioRad	12004161	goat, anti-rabbit		1/2500

6.6. Buffers

Table 9: Buffers for bacteria culture and agarose-gel electrophoresis.

Name	Components
Lysogeny broth medium	2.5 % (m/v) LB broth in dH ₂ O
LB agar medium	1.5 % (m/v) Agar-Agar in LB medium
TAE buffer	100 mM Tris, 1mM Na ₂ EDTA, 20 mM acetic acid, in dH ₂ O

Table 10: Buffers used for *in vitro* transcription.

Name	Components
IVT reaction buffer	80 mM HEPES, 12 mM MgCl ₂ , 2 mM spermidine, 40 mM DTT, 3.125 mM of each NTP, 1 U/μL Rnasein, in dH ₂ O
IVT reaction buffer with m7G Cap analog	80 mM HEPES, 12 mM MgCl ₂ , 2 mM spermidine, 40 mM DTT, 3.125 mM of ATP, CTP, UTP, 1.5625 mM GTP, 0.25 mM Ribo m7G Cap analog (Promega) 1 U/μL Rnasein, in dH ₂ O

Table 11: Buffers and solutions for luciferase assay.

Name	Components
Luciferase assay buffer	25mM Gly-Gly pH 7.8, 15 mM KPO ₄ pH 7.8, 15 mM MgSO ₄ , 4 mM EGTA, 1 mM DTT, 2 mM ATP, in dH ₂ O
D-Luciferine solution	25mM Gly-Gly, 200 mM D-Luciferin, in dH ₂ O
Coelenterazine solution	0.424 μg/mL Coelenterazine, in dH ₂ O

Table 12: Buffers for SDS-PAGE and Western Blot.

Name	Components
RIPA buffer	1 % (v/v) TritonX-100, 300 mM NaCl, 100 mM Tris-HCl pH 7.4, 2 mM EDTA pH 8, in dH ₂ O
5x SDS-PAGE Sample buffer	75 mM Tris-HCl pH 6.8, 4 % (m/v) SDS, 40 % (v/v) glycerol, 200 mM beta-mercaptoethanol, bromphenolblue, in dH ₂ O
6x SDS-PAGE Sample buffer	0.875 M Tris-HCl (pH 6.8), 12.5 % (v/v) glycerol, 12.5 % (m/v) SDS, 11.625 % (m/v) DTT in dH ₂ O with brom-phenol blue
MES Running buffer	0.1 M 2-(N-morpholino)ethanesulfonic acid (MES) monohydrate, 0.1 M Tris Base, 0.2 % (m/v) SDS, 2 mM EDTA, in dH ₂ O
Resolving gel (10-12%)	10-12% (v/v) Rothiphorese Gel 30 (30 % acrylamide and bisacrylamide stock solution), 0.38 M Tris pH 8.8, 0.1 % (m/v) SDS, 0.2 % (v/v) tetramethylethylenediamine (TEMED), 0.1 % (v/v) ammoniumperoxisulphate (APS) saturated solution, in dH ₂ O
Stacking gel (4%)	4 % (v/v) Rothiphorese Gel 30, 0.13 M Tris pH 6.8, 0.1 % (m/v) SDS, 0.2 % (v/v) TEMED, 0.1 % (m/v) APS saturated solution, in dH ₂ O
Transfer buffer	25 mM Tris, 192 mM Glycine, 20 % (v/v) Methanol, in dH ₂ O pH 8.3
PBST	0.5 % (v/v) Tween 20 in PBS
WB blocking solution	5 % (m/v) milk powder in PBST

Table 13: Buffers used for flow-cytometry.

Name	Components
FACS fixation buffer	0.5 % (m/v) paraformaldehyde, 1 % (v/v) FCS in PBS
FACS wash buffer	1 % (v/v) fetal calf serum (FCS) in PBS
BODIPY FACS staining solution	0.5 µg/mL BODIPY in FACS fixation buffer

Table 14: Buffers for immuno fluorescence (IF) staining.

Name	Components
Permeabilization buffer	0.1 % (v/v) TritonX-100 in dH ₂ O
IF blocking solution 1	5 % goat serum in PBS
IF blocking solution 2	0.1 % (m/v) BSA in PBS

Table 15: Buffers for cell culture and cell based assays.

Name	Components
PBS	137 mM NaCl, 2.7mM KCl, 10 mM Na ₂ HPO ₄ , 1.8 mM KH ₂ PO ₄ , in dH ₂ O
Cell culture medium	10 % (v/v) FCS, 100 U/mL penicillin, 100 U/mL streptomycin, 2 mM L-Glutamine, non-essential aminoacids, in Dulbecco's Modified Eagle Medium (DMEM)
Homogenization medium	0.25 M sucrose, 10 mM HEPES, 1 cOmplete™ Mini Protease Inhibitor Cocktail tablet per 10 mL medium, in dH ₂ O
Cytomix	10 mM K ₂ HPO ₄ /KH ₂ PO ₄ , 120 mM KCl, 0.15 mM CaCl ₂ , 25 mM HEPES, 2 mM EGTA, 5 mM MgCl ₂ , in dH ₂ O

6.7. Reagents and Kits

Table 16: Reagents used for cell culture and cell based assays.

Name	Company
Blasticidine	Capricorn
BSA Fraction V IgG Free Fatty Acid Poor	Fisher Scientific
DMEM High Glucose (4.5 g/l)	Capricorn
Fetal Bovine Serum (FBS) Advanced	Capricorn
HEPES 1M solution, Gibco™	Fisher Scientific
L-Glutamine (200 mM), Gibco™	Fisher Scientific
Lipofectamine 2000	Invitrogen
MEM Non-Essential Amino Acids	Capricorn
Oleic acid	Sigma Aldrich
Opti-MEM™ I Serumreduziertes M	Gibco
Penicillin/Streptomycin (100x)	Capricorn
Polyethylenimine, branched (PEI)	Sigma Aldrich
Poly-L-lysine hydrobromide	VWR

Materials

Puromycin	Capricorn
Triton® X 100	Carl Roth
Trypsin-EDTA (0.5 %), no phenol red, Gibco™	Fisher Scientific
Trypan blue	Carl Roth

Table 17: Small molecule inhibitors used for different assays.

Name	Company	Stock solution
Cycloheximide	Sigma Aldrich	10 mM in DMSO
Daclatasvir (BMS-790052)	Absource Diagnostic GmbH	10 mM in DMSO
Doxycycline (hyclate)	Biomol GmbH	10 mM in DMSO
PF-06424439 (DGAT2 inhibitor)	Sigma Aldrich	10 mM in DMSO
T863 (DGAT1 inhibitor)	Sigma Aldrich	25 mM in DMSO

Table 18: Reagents used for fluorescence microscopy or flow cytometry stainings. Stock solutions were prepared as indicated in the right column.

Name	Company, origin	Stock solution
Filipin III complex from <i>Streptomyces Filipinensis</i>	Sigma Aldrich	5 mg/mL in DMSO
LD540	Gift from C. Thiele	2.5 mg/mL in EtOH
DAPI	Life Technologies	5 mg/mL in dH ₂ O
BODIPY 493/503	Fisher Scientific	1 mg/mL in DMSO

Table 19: Lipids used in this study. Stock solution and final working concentrations are indicated. NBD, 4-Chlor-7-nitrobenzo-2-oxa-1,3-diazol.

Abbreviation	Name	Company	Stock solution	Final conc.
OA	18:1 Oleic acid	Sigma Aldrich	3.15 M in EtOH	assay dependent
1,2-DOG	1,2-Dioctanoyl-sn-glycerol	Avanti Polar	20 mM in DMSO	50 µM
1,3-DOG	1,3-Dioctanoyl- glycerol	Avanti Polar	20 mM in DMSO	50 µM
C6-L-Cer	N-Hexanoyl-L-erythro-Sphingosine	Avanti Polar	10 mM in EtOH	10 µM
C6-D-Cer	N-Hexanoyl-D-erythro-Sphingosine	Avanti Polar	10 mM in EtOH	10 µM
NBD-SM	NBD-hexanoyl-sphingosine-1-phosphocholine	Avanti Polar	10 mM in EtOH	10 µM
NBD-PC	1-oleyl-2-NBD-hexanoyl-sn-glycero-3-phosphocholine	Avanti Polar	10 mM in EtOH	10 µM

NBD-PE	1-oleyl-2-NBD-hexanoyl-sn-glycero-3-phosphoethanolamine	Avanti Polar	10 mM in EtOH	10 μ M
Lyso-PC	1-octadecenoyl-sn-glycero-3-phosphocholine	Avanti Polar	20 mM in EtOH	50 μ M
NBD-PA	1-oleoyl-2-NBD-hexanoyl-sn-glycero-3-phosphate	Avanti Polar	20 mM in EtOH	50 μ M

Table 20: Kits and enzymes used in this study sorted by application.

Name	Purpose	Company
Antarctic Phosphatase	Cloning	NEB
Gibson assembly Master Mix	Cloning	NEB
Monarch DNA Gel Extraction Kit	Cloning	NEB
NucleoSpin Gel and PCR Clean-up Kit	Cloning	Macherey & Nagel
Q5® High-Fidelity DNA Polymerase and Buffer	Cloning	NEB
Restriction endonucleases (various)	Cloning	NEB
T4 Ligase	Cloning	NEB
NucleoSpin RNA, Mini kit for RNA purification	IVT	Macherey & Nagel
Qiaquick Spin mini prep kit)	IVT	Quiagen
RNA Cap Struc. Analog, m7G(5)ppp(5)G	IVT	NEB
T7 RNA Polymerase	IVT	NEB
NucleoBond Xtra Midi Plus EF,	Plasmid preparation	Macherey & Nagel
NucleoSpin Plasmid, Mini kit for plasmid DNA	Plasmid preparation	Macherey & Nagel
QIAfilter Plasmid Maxi Kit	Plasmid preparation	Qiagen
QIAGEN Plasmid Midi Kit	Plasmid preparation	Qiagen
LightCycler 480 RNA Master Hydrolysis Probes kit	RT-qPCR	Roche
Luna Universal Probe One-Step RT-qPCR kit	RT-qPCR	NEB
NucleoSpin RNA extraction kit	RT-qPCR	Macherey-Nagel
SuperSignal West Pico Plus ECL	WB	Thermo Scientific

6.8. Software

Table 21: Softwares used in this study.

Name	Purpose
Cell Profiler	Image analysis
Fiji	Image analysis
FlowJo	Flow cytometry analysis
GIMP	Image processing
GraphPad Prism	Statistics
Inkscape	Figure creation
Microsoft Excel	Data processing
Rstudio	Statistics
SA3800	Flow cytometry analysis
Snap Gene	Cloning

7. Methods

7.1. Molecular biology methods

7.1.1. Cloning and plasmid preparation techniques

7.1.1.1. Amplification of DNA fragments by Polymerase Chain Reaction (PCR)

PCRs were performed in a PCR thermocycler using the Q5 High-Fidelity DNA Polymerase kit (NEB) according to the manufacturer's protocol in 50 μ L total volume. The general reaction mix and amplification program are listed in the tables below. Annealing temperatures were adapted depending on the primer's melting temperatures and extension times were adapted to the size of the amplicon.

Table 22: Standard Q5-PCR reaction mix. F- and R-primer: forward and reverse primers.

Reagent	Volume [μ L]
Template Plasmid (1 ng/ μ L)	2.5
F-Primer (10 μ M)	2.5
R-Primer (10 μ M)	2.5
Q5-Polymerase	0.5
Q5 5xBuffer	10
dNTP (10 mM)	1
H ₂ O (ad.to 50 μ L)	31
Total volume	50 μL

Table 23: Standard Q5-PCR amplification program.

	Temperature [$^{\circ}$ C]	Time [s]	Number of cycles
Initial denaturation	98	30	1
Denaturation	98	10	25-35
Annealing	50-72	20-30 s/kb	
Extension	72	36	
Final Extension	72	120	1
Hold	4	∞	1

7.1.1.2. Fusion-PCR

Fusion-PCR was used for site-directed mutagenesis or insertion of short sequences. A complementary primer pair was designed to contain the desired mutation of the gene of interest and to anneal together for at least 15 nt. First, two PCR reactions were performed to amplify the gene of interest either upstream or downstream of the targeted sequence. The two resulting PCR products were then combined in a third, fusion-PCR by using nested primers.

Table 24: Reaction mix for Fusion-PCR.

Reagent	Volume [μ L]
PCR 1 product (10 ng/ μ L)	1
PCR 2 product (10 ng/ μ L)	1
Nested Primer F (10 μ M)	2.5
Nested Primer R (10 μ M)	2.5
Q5-Polymerase	0.5
Q5 5xBuffer	10
dNTP (10 mM)	1
H2O (ad.to 50 μ L)	31.5
Total volume	50 μL

7.1.1.3. DNA restriction

Restriction endonuclease reactions were performed using enzymes from NEB and according to the manufacturer's instructions. In brief, 5 μ g of DNA were digested with 10 U of enzyme per μ g DNA and incubated for 1 h at 37°C. To reduce backbone re-ligation, Antarctic Phosphatase (NEB) was added to digested vectors prior ligation according to the manufacturer's protocol. Digested fragments were purified with or without gel extraction using the NucleoSpin Gel and PCR Clean-up Kit (Machery Nagel, Thermo Fisher Scientific, NEB).

7.1.1.4. DNA ligation

Linear DNA fragments resulting from restriction digestion were ligated using the T4-ligase (NEB). In brief, backbone vector and insert were mixed in a 1:3 or 1:10 molecular ratio (8 μ L DNA in total) and 1 μ L of each T4-Ligase and T4-Ligase buffer were added. The reaction mixes were incubated at 16 °C overnight.

Alternatively, linear DNA fragments were ligated with Gibson assembly Master Mix (NEB) in 1:2 backbone vector and insert ratio, according to the manufacturer's protocol.

7.1.1.5. Cloning of lentiviral vectors

All utilized plasmids, including the pWPI lentiviral vectors cloned in this study, are listed in table 5. The DGAT wild-type and HA-tagged constructs as well as the two catalytical mutants DGAT2_L83A, DGAT2_HPH161-163AAA were cloned by G.V. before. In brief, the human DGAT2 sequence was ordered as a g-Block (Integrated DNA technologies, IDT) and the DGAT1 sequence as vector from DNAsu (pDONR221) and cloned between *Ascl* and *SpeI* in the pWPI_Puro vector. HA-tagged DGAT2 was cloned by insertion of a double HA-tag (YPYDVPDYA, twice) preceded by a linker (GGGGSG) by PCR. Furthermore, the point mutants DGAT2_L83A, DGAT2_HPH161-163AAA were generated by fusion-PCR.

For the panel of cloned DGAT2 mutants pWPI_HAHA-L-DGAT2-del30-67_Puro, pWPI_HAHA-L-DGAT2-del66-115_Puro, pWPI_HAHA-L-DGAT2-mito4A_Puro, pWPI_HAHA-L-DGAT2-del327-350_Puro and pWPI_HAHA-L-DGAT2-insert-HA_Puro, the DGAT2 sequence was amplified in three fragments by PCR (N-terminal, middle part, C-terminal). g-Blocks carrying the desired deletions or mutations within the respective fragment were ordered (IDT) and the fragments were inserted into the pWPI_Puro vector by Gibson assembly.

pLenti_CMV-TO_HAHA-DGAT2_Puro was cloned from pLenti_CMV-TO_Puro_DEST_APEX2-V5 by restriction-based cloning. In brief, the HA-DGAT2 sequence from pWPI_HAHA-DGAT2_Puro was amplified by PCR. The resulting fragment was inserted between the *Ascl* and *XbaI* restriction sites of pLenti_CMV-TO_Puro_DEST_APEX2-V5.

The DAG-sensor pWPI_mRuby3_PRKCe_C1a_C1b_Puro was cloned as described in [77]. The sequence of *Homo sapiens* protein kinase C epsilon (PKCε) (NM_005400.3) C1a-C1b (aa170-294) cassette fused with mRuby3 was ordered as g-Block (IDT) and inserted between *Ascl* and *SpeI* in the pWPI_Puro vector. The W264 point mutation [77,158] was inserted by fusion PCR.

The PA-sensor pWPI_mNeonGreen_Raf1-PABD_Puro was cloned as described in [31]. The sequence of *Homo sapiens* Raf1 (NM_001354689.3) PA-binding domain (PABD) (aa 390-426) or 4E mutant (R391E, R398E, K399E and R401E) were ordered as g-Block (IDT). The sequences were inserted between *Ascl* and *XbaI* in pWPI_Nter-mNeonGreen-in-frame_Puro.

AGPAT1 (NM_006411.4:281-1132), AGPAT2 (NM_006412.4:101-937), Lipin1 (NM_001349206.2:50-2830) and Lipin2 (NM_001375808.2:68-2758) sequences were codon optimized using the IDT-online tool and ordered as g-Blocks (IDT) fused to a C-terminal triple Flag-tag (DYKDHDG-DYKDHDIDYKDDDDK). Untagged versions were generated by insertion of a stop codon before the triple Flag motif. Sequences were inserted into the pWPI_Puro vector between the *Ascl* and *SpeI* restriction sites. All cloned constructs were verified by multiple restriction analyses and by sequencing (Microsynth SeqLab).

7.1.1.6. Bacteria transformation

For plasmid amplifications, *E. coli* DH5α or Stable2 cells were incubated with the plasmid for 20-45 min on ice. After a heat-shock at 42 °C for 90s, the transformed bacteria were incubated for 1 h at 30 °C in LB medium, shaking, and plated on LB agar plates containing 100 µg/mL Ampicillin. Plates were incubated at 37 °C (DH5α) or 30 °C (Stable2) overnight.

7.1.1.7. Plasmid extraction and control digestion

For plasmid preparations, single colonies obtained from transformation were picked and added to LB medium supplemented with Ampicillin. 5 or 100 mL inoculum were prepared for Mini- or Midipreparations respectively. Bacterial cultures were incubated at 37 °C (DH5α) or 30 °C (Stable2) overnight, shaking. Plasmid preparations were performed by using the kits indicated in table 20 and following the manufacturer's protocol. Plasmid DNA concentrations were measured via spectrophotometry (A260). To confirm integrity of plasmids, control digestions were performed on 0.5 µg plasmid using 1-2 restriction enzymes (NEB) resulting in defined patterns of restriction fragments. Reactions were separated on agarose gels containing GelRed® in TAE buffer and visualized under UV light.

7.1.2. *In vitro* transcription

For the generation of *in vitro* transcripts (IVTs), plasmids were digested with MluI, XbaI or SpeI (NEB). Linearized plasmid DNA was extracted and dissolved in RNase free water. 0.2 µg/µL restricted plasmid DNA were mixed with IVT reaction buffer (with m7G Cap analog in case of pIRF1b IVT) and 0.6 U/µL T7 RNA polymerase to a total of 100 µL reaction volume. Reactions were incubated for 2 h at 37 °C, and additional 0.3 U/µL T7 RNA polymerase was added to the mixture, following another 2 h incubation. Transcription was terminated by addition of 3.25 U of RNase free DNase per µg of plasmid DNA and incubation for 30 min at 37°C. RNAs were extracted and eluted in RNase free water. RNA concentration was determined with a spectrophotometer and degradation of RNA was inspected on an agarose gel. IVTs were stored at - 80°C.

7.1.3. Luciferase activity assays

For Renilla (RLuc) and *firefly* (FLuc) luciferase measurements, cells were lysed in Milli-Q water (400 µL per well for 6-well dishes, 150 µL per well for 12- or 24-well dishes, 40-50 µL per well for 96-well dishes) and froze the plates at - 20°C or - 80°C until luciferase readout. Assays were performed following previously published protocols [7]. In brief, 20 µL lysed cells were transferred to white 96-well plates. For FLuc assay, 72 µL luciferase assay buffer was added. Luminescence was measured after adding 40 µL D-luciferin solution per well. For RLuc assay, Luminescence was measured after adding 40 µL Coelenterazine solution per well. Luciferase readout was performed using the Berthold Centro XS luminometer (Berthold).

7.1.4. SDS-PAGE and Western Blot

7.1.4.1. Sample preparation for SDS-PAGE

Cells cultured in 6-well or 12-well plates were harvested by trypsinization and cell pellets were washed twice with PBS. Cell pellets were frozen and stored at -20 °C. After thawing at RT, cell pellets were resuspended in 30 µL 1 % TritonX100-PBS and incubated for 10 min on ice. Cell debris was removed by centrifugation at 10 min at 130000 rpm. The samples were supplemented with 5x SDS-PAGE loading buffer and incubated for 10 min at 80 °C. The samples were stored on ice before loading on the SDS-PAGE buffer.

Alternatively, the thawed cell pellets were resuspended in 200 or 330 µL RIPA buffer supplemented with protease inhibitor followed by incubation for 20 min on ice. Cell debris was removed by centrifugation at 10 min at 130000 rpm. Samples were supplemented with 6x SDS-PAGE loading and incubated for 15 min at 70 °C. Samples were frozen at -20 °C or stored on ice before loading on the SDS-PAGE gel.

7.1.4.2. SDS-PAGE

Bis-Tris SDS-PAGE gels composed of resolving gel (10-12.5 % BAA, bottom) and stacking gel (4 % BAA, with loading pockets, top) were prepared and placed in an SDS-PAGE gel chamber. Cell lysate samples and markers were pipetted into the gel pockets of the stacking gel and electrophoresis was performed in MES buffer at 80-130 V.

7.1.4.3. Western Blot (WB)

For the protein transfer, a PVDF membrane (Amersham™ Hybond® P Western blotting membrane, Sigma-Aldrich) was cut according to the SDS-PAGE gel size and activated in methanol 99.9%. The membrane was incubated in water and followed by short equilibration in transfer buffer. For the semi-dry blotting method, the SDS-PAGE gel was placed onto the pre-activated PVDF membrane and sandwiched between two thick Whatman papers soaked with transfer buffer (table 12). The transfer was conducted at 70 mA per minigel for 70 minutes with a semi-dry blotting chamber (Thermo Fisher Scientific). Alternatively, the Trans-Blot® Turbo™ Transfer System (Biorad) was used according to the manufacturer's instructions.

7.1.4.4. WB Immunodetection

The WB membranes were blocked in WB blocking solution for 1 h at RT or at 4°C overnight, shaking. Primary antibody and secondary antibody solutions were prepared in blocking solution and concentrations according to tables 7 and 8. The WB membranes were first incubated with primary antibody solution for 1 hour at RT or overnight at 4°C, shaking overnight. The membranes

were washed in 3 washing steps in PBST for 5 min (mouse) or 15 min (rabbit) dependent on the primary antibody origin species. Followingly, membranes were incubated with horseradish peroxidase- (HRP) or fluorophore-coupled secondary antibody for 1 h at RT. The same washing procedure was performed again to wash away unbound antibodies. Proteins stained with the HRP-coupled antibodies were detected using an SuperSignal West Pico Plus ECL system (Thermo Fisher Scientific) with the ChemoStar Imaging System (Intas). Proteins stained with the fluorophore-coupled antibodies were detected using the Odyssey®CLx imaging System (LI-COR) or the ChemiDoc MP system (BioRad).

7.1.5. RT-qPCR

RNA extraction, qRT-PCR and analysis were performed by Laura Weber. Cellular RNA was extracted using the NucleoSpin RNA extraction kit (Macherey-Nagel) according to the manufacturer's instructions. The quality of the extracted RNA was assessed by agarose gel electrophoresis. RNA transcripts of GAPDH, DGAT1 and DGAT2 were quantified by one-step primer-probe RT-qPCR using the LightCycler 480 RNA Master Hydrolysis Probes kit (Roche) or the Luna Universal Probe One-Step RT-qPCR kit (NEB) following the manufacturer's instructions. Utilized primers and probes can be found in tables 2 and 3. In one reaction, primers and probes for GAPDH and DGAT1 or DGAT2 were combined and the concentrations of all oligonucleotides were optimized by titration. Each sample was measured in technical triplicates on a Lightcycler 480 instrument (Roche) or with the 7900HT Fast Real-Time PCR system (Applied Biosystems). The data was analyzed by the $2^{-\Delta\Delta C_t}$ method.

The 8 PHH samples used here were the same as previously reported and therefore were isolated following the same procedure [129]. All tissue donors gave written informed consent for experimental use of clinical data and liver specimen prior to surgery. The protocol was approved by the ethics commission of Hanover Medical School (#252–2008 and #2148–2014).

7.1.6. Flow cytometry-based quantification of the lipid droplet content

The cell harvest, addition of reference cells, fixation, and staining for flow cytometry was performed as described in [129]. In brief, cells were grown in 12-well plates and treated according to the experimental requirements. After harvest by trypsinization, cells were combined with Lunet N hCD81/mRuby2 reference cells in an approximate 1:1 ratio. The cells pellets were washed with PBS and resuspended in FACS fixation buffer before storing 4 °C. Prior staining, the fixed cells were washed in FACS wash buffer and pelleted by centrifugation at 600 g for 3 min at 4 °C. Followingly, the cells were resuspended in BODIPY FACS staining solution and incubated for 20 min on ice in the dark. After two washing steps, the cell pellets were re-suspended in FACS wash buffer for flow cytometry.

The analysis was performed with the BD Accuri C6 flow cytometer (BD Biosciences), SA3800 Spectral Cell Analyzer (Sony Biotechnology) or the BD LSR Fortessa™ Cell Analyzer (BD Biosciences),

In all cases, the gates were set to exclude cell debris by using the FSC-A and SSC-A channels, and doublet cells by using the FSC-A and FSC-H channels. BODIPY 493/503 and mRuby2 fluorescence signals were obtained by using the FL1 and FL3 (BD Accuri) or B2 and YG3 (BD Fortessa) channels, or the Spectral Analyzer (Sony) respectively. Color compensation or spectral unmixing were performed following the manufacturer's instructions. Further analysis was performed with FlowJo (BD Biosciences). The test cells were distinguished from the spiked-in control cells by their red fluorescence as shown above (Fig. 13) and compared the ratios of the BODIPY fluorescence between the test and the control cells as explained in the main text.

7.1.7. Microscopy methods

7.1.7.1. Fluorescence microscopy - general staining protocol

Cells were seeded on 1.5 mm glass coverslips in 24-well plates to be ~60-70 % confluent on the day of fixation. For fixation, the cell culture medium was aspirated and the cells were washed with PBS prior incubation with 3 % PFA-PBS for 10 min at RT. To permeabilize the cells, they were incubated with 0.5 % TritonX-100-PBS for 5 min at RT. cells were stained with antibodies (primary, followed by fluorophore-labelled secondary antibodies) or fluorescent dyes dependent on the experiment set-up. Antibody dilutions were prepared in 5% goat serum-PBS or 0.01 % BSA-PBS (for staining with HA antibody from Novus Biologicals (goat)) in concentrations according to table 7 and 8.

7.1.7.2. Fluorescence microscopy - image acquisition and analysis

All fluorescence microscopy images were taken with a 60x Nikon CFI Apochromat TIRF objective (CFI Apochromat TIRF 60x Oil/ 1.49/ 0,13). The images for LD quantification by fluorescence microscopy were acquired with a Nikon Ti-E microscope equipped with a Yokogawa CSU-X1 spinning disc and an EMCCD DU-888 camera from Andor and an additional 2x magnification lens inside the spinning-disc unit. For the detection of Filipin and PI4P, the Nikon Ti microscope equipped with a pco.panda 4.2 bi UV sCMOS camera (Excelitas Technologies) was used. All other images were taken with a Nikon Ti2 microscope equipped with an Ai plus laser scan confocal unit.

The shown images were adjusted in Fiji [229] with equal background subtraction and contrast enhancement parameters for all samples of a figure panel. Fluorescence intensity profiles were measured along the indicated lines in Fiji and plotted with GraphPad Prism after normalization to the maximum intensity (set to 100 %) of each respective channel.

For the lipid droplet (LD) quantification, the mRuby2-positive cells were automatically segmented with a Fiji macro to generate binary masks in order to distinguish mRuby2-positive and negative cells. Nuclei

and LDs of both populations were then automatically segmented. Images with successful segmentation were further analyzed with CellProfiler [230] using the same parameters throughout all conditions.

7.1.7.3. Correlated light electron microscopy (CLEM) and quantification of double membrane vesicle (DMV) and LDs

The DMV characterization and by CLEM microscopy was performed by Ji Young Lee and Ralf Bartenschlager following the protocol described in [31]. 5×10^4 Lunet/T7 [empty], [DGAT2], [DGAT2_HPH161-163AAA] or [DGAT1] cells were transfected with 2.5 μ g HCV NS3-5B/5AEGFP pTM expression plasmid by lipofetamine transfection according to the manufacturer's protocol. After 24 h, transfected cells were identified by GFP signal by using a widefield fluorescence microscope (Nikon Eclipse) with 10x objective lens. Cells were fixed with EM Fixative (1 % GA, 4 % PFA, 50 mM KCl, 2.6 mM MgCl₂, 2.6 mM Calcium chloride, 2 % Sucrose, 50 mM CacO) and further processed for EM analysis. TEM images were acquired at x4 k magnification with JEOL JEM-1400.

For the DMV and LD quantification, systematic random sampling was used. Rectangle areas of $\sim 100 \mu\text{m}^2$ were placed on whole cell images to count and measure DMVs and LDs manually. At least 10 GFP-positive cells in each sample were counted ($n \geq 10$).

7.1.8. Lipidomic analysis

7.1.8.1. Sample preparation for lipidomic analysis

Lunet N hCD81, HuH6 and 293T-miR-122 stable DGAT cell lines were seeded in 10 cm dishes to be confluent on day 4. When relevant, the cells were infected on day 2 with Jc1 and the medium was changed at 4 hpi or treated with 360 μ M OA combined with BSA day 3 overnight. The cells were harvested by trypsinization on day 4 (48 hpi) and counted with a Neubauer chamber (section 7.2.4). The harvested cells were washed with PBS (500 g, 5 min) and resuspended in homogenization buffer. The cells were mechanically lysed with a Dounce homogenizer on ice controlling the cell rupture by Trypan Blue staining (same stroke number per cell type for all conditions). The cell lysates were separated from the cell debris and nuclei by centrifugation (500 g, 5 min).

For the microsome extraction, the remaining supernatant was centrifuged at 10300 g for 10 min at 4°C to separate crude mitochondria. The procedure was repeated two more times before transferring the remaining lysate into ultracentrifugation tubes filled with homogenization medium. The samples were centrifuged at 100000 g for 1 h at 4 °C. Afterwards, the supernatant was discarded and the pellets containing the microsomal membranes were re-suspended in homogenization medium. Both cytoplasmic and microsomal extracts were stored at -80°C until lipid extraction. Before transfer of the samples to the Mass Spectrometry facility, they were supplemented with Methanol and Methyl-tert-butyl-ester (MTBE) in a volume ratio of 1 : 1.5 : 5 (sample : MeOH : MTBE).

7.1.8.2. Mass Spectrometry based lipidomic analysis

Lipidomic analysis was performed by Manka Fuh and Jörg Heeren as described in [231] using the Lipidizer platform™. This included a triple quadrupole mass spectrometer (QTRAP 5500; AB SCIEX, Darmstadt, Germany) equipped with a differential mobility spectrometer (DMS) interface operating with SelexION technology. In this case, an ultra-high pressure liquid chromatography system (Nexera X2, Shimadzu, Japan) was used as an autosampler. The Lipidizer™ Platform was tuned using the SelexION Tuning Kit (AB SCIEX) and a system suitability test was performed using the System Suitability Kit (AB SCIEX) according to the manufacturer's instructions. To the cell lysates, 100 µL of water was added and shortly vortexed. The lipid extraction process was then carried out as previously described [231]. The generated data was processed using Lipidomics workflow manager (AB SCIEX) and Shotgun Lipidomic Shortgun Assistant (SLA) software according to the SLA guidelines [232].

7.2. Cell culture methods

7.2.1. Culture and passaging of mammalian cell lines

All cell lines were cultivated at 37°C with 5 % CO₂ in DMEM complete medium. For selection, 5 µg/mL Blasticidin or 2.5 µg/mL Puromycin was added to the cell culture medium. Cells were sub-passaged 2-3 weekly before reaching confluence. Therefore, the cell culture medium was aspirated and cells were washed with PBS. Trypsin/EDTA solution was added followed by incubation at 37 °C until cells started to detach. Fresh cell culture medium was added and the detached cells were resuspended and seeded into a new cell culture dish or flask at lower density.

7.2.2. Generation of stable cell lines

Cells were seeded in 6-well dishes to reach confluency four days post seeding. One day after seeding, cells were transduced with lentiviral vectors expressing the gene of interest and the medium was changed after 6 h. Upon reaching confluency, the cells were detached by trypsinization and transferred to a larger cell culture dish. Simultaneously, transduced cells were selected by addition of 5 µg/mL Blasticidin or 2.5 µg/mL Puromycin according to the selection marker of the utilized lentiviral vector plasmid. Transduction and selection controls were performed to evaluate growth defects caused by the transgene and as control for the antibiotic selection, respectively.

7.2.3. Cryopreservation and thawing of mammalian cell lines

Cells were grown in 15-cm culture dishes to reach ~80 % confluency. Cells were detached by trypsinization and resuspended in fresh cell culture medium. After centrifugation 5 min at 500 g, the cell pellet was resuspended in cryomedium. The cell solutions were transferred to cryotubes and gradually cooled to -80 °C before storage at -150 °C or in liquid nitrogen.

Frozen cells were thawed at 37 °C in a waterbath and transferred to 10 mL cell culture medium before pelleting at 200 g for 7 min. Cells were resuspended in fresh cell culture medium and plated in cell culture dishes or flasks. The respective selective antibiotics were added after the first sub-passaging.

7.2.4. Cell counting

Cells were harvested by trypsinization and resuspended in cell culture medium. 10 µL cell suspension was mixed with 10 µL trypan blue and transferred to a Neubauer haemocytometer chamber. Living cells in the four quadrants were counted and the mean value was used to determine the total number of cells per milliliter: $\text{cells/mL} = \text{total count of cells} * 10^4 / 4$. If more than ~20 cells were counted per quadrant, cell suspension was diluted with cell culture medium before counting. For the sample preparation of the lipidomics experiment, the procedure was repeated four times and the average cell count was calculated.

7.2.5. MTT assay

MTT assays were performed by G.V.. To monitor growth and viability of the DGAT2-overexpressing cell lines, each cell line was seeded with 10^4 cells/well in 96-well dishes and an MTT assay was performed at 4, 24, 48, 72 and 96 h post seeding. MTT (Sigma Aldrich) was dissolved in PBS at 5 mg/mL and this stock was diluted 10 times in complete DMEM before usage. At each time point, the cell supernatant was discarded and the cells incubated with 50 µL per well of MTT-containing complete medium, previously prewarmed at 37°C. After 1 h incubation at 37°C, the medium was discarded, MTT precipitates were dissolved by adding 50 µL per well of DMSO, and absorbance was read at 570 nm in a Biotek Synergy 2 plate reader (Agilent).

7.2.6. Cell viability assessment using Lunet N hCD81/FLuc

Cytotoxic effects of ectopic expression of lentiviral constructs or treatment with inhibitors or lipid analogs were monitored by Lunet N hCD81/FLuc cells. Lunet N hCD81/FLuc cells were seeded in 24-well or 96-well dishes according to the individual experiment format. Cells were treated in the same way as the tested experiment conditions. Cell lysates were harvested for luciferase assay.

7.2.7. Translation reporter assay

For the translation reporter assay, Lunet N hCD81 cell lines were seeded in 96-well plates (10^4 cells/well). On the next day, the medium was changed and supplemented with 20 µM CHX or DMSO control 1 h before transfection with IVTs obtained from the pIRF1b construct. We lysed the cells 8 hpt for FLuc and RLuc luciferase readout.

7.3. Virological methods

7.3.1. Lentivirus stock preparation

Lentivirus stocks were prepared using HEK293T cells and following previously described protocols [128]. In brief, 3.1×10^6 HEK293T cells were seeded on poly-L-lysine coated cell culture dishes. On the next day, cells were transfected via PEI transfection with 5 μ g of the lentiviral packaging plasmids pCMV-Delta R8-74, pczVSV-Gwt, and a third plasmid expressing the protein of interest. On the next day, cells were induced by adding 10 mM sodium butyrate and infectious supernatants were harvested two and three days post transfection. Combined supernatants were sterile filtered (0.45 μ m) and stored at -80 °C.

7.3.2. General lentivirus transduction protocol

Cells were seeded in either 6-, 12-, 24- or 96-well plates to reach confluency on the last day of the respective experiment. The cell culture medium was aspirated and cells were incubated for 6-8 h or overnight with undiluted lentivirus stocks according to the inoculum volumes in table 24. The cells were further treated dependent on the individual experimental conditions. The specific assay treatments are indicated in the respective figure legends.

Table 25: Usual inoculum volumes for different well-plate formats and incubation times.

	Incubation time	6-well	12-well	24-well	96-well
Volume [μ L]	4-8 h	600	350	300	35
	Overnight	1000	600	500	-

7.3.3. HCV virus stock preparation

Huh-7.5 or Huh-7.5.1 cell lines were used for HCV Jc1 and JcR2a virus production following previously described protocols [128]. In brief, Huh-7.5 cells were grown in 15-cm dishes and harvested when they reach ~70-80 % confluency by trypsinization. 6×10^6 cells were transferred to a falcon and washed with PBS before resuspension in 400 μ L cytomix supplemented with 2 mM ATP and 5 mM glutathione. Cells were mixed with 10 μ g Jc1 or JcR2a in vitro transcript and electroporated using the BioRad Gene-pulser (975 μ F, 270 V). Upon electroporation, cells were resuspended with cell culture medium and incubated at 37 °C. Medium was changed 6-24 hours post transfection (hpt). Supernatants of transfected cells were harvested starting at 24 hpt or 48 hpt for Jc1 or JcR2a, respectively, 1-2 times daily until 96 hpt. Combined supernatants were sterile filtered (0.45 μ m) and stored at -80 °C. Infectious titers were determined by TCID50.

7.3.4. TCID₅₀

Tissue culture infectious dose 50 (TCID₅₀) of HCV stocks were determined as previously described [6,7]. Huh-7.5 cells were seeded in 96-well plates (1x10⁴ cells/well). On the next day, infectious supernatants were added in 10-fold (Jc1) or 5-fold (JcR2a) serial dilutions. 72 hpi, inoculum was aspirated and cells were washed with PBS prior fixation with MeOH at -20 °C. After histochemistry staining of NS5A positive cells using Carbazole, infected wells were determined by microscopy. TCID₅₀/mL was calculated as described previously [6,7].

7.3.5. Replication of HCV sub-genomic replicons (SGR) and full-length JcR2a upon electroporation

Lunet N hCD81 cell lines were grown in 10 cm dishes to reach ~80 % confluence and harvested by trypsinization. After washing with PBS, cell dilutions of 10⁷ cells/mL were prepared in Cytomix supplemented with 2 mM ATP and 5 mM glutathione. For transfection by electroporation, 400 µL of cell suspension was mixed with 5 µg IVT of the respective HCV construct and electroporated with the BioRad Gene-pulser (975 µF, 270 V). The cell suspensions of the individual construct/cell line combinations were transferred to 24-well plates and incubated at 37 °C. The cell lysates were harvested at 4, 24, 48 and 72 hpi for luciferase assay.

7.3.6. JcR2a replication in different cell lines upon lipofectamine transfection

The cell lines Lunet N hCD81, Huh-7.5, HuH6 and HepG2-HFL, 293T-miR-122, HeLa-miR-122 and Caco-miR-122 were seeded in 24-well plates to reach confluency on day 4. On day 2, cells were transduced with lentiviruses to express DGAT2, DGAT1 or empty control vectors. Cells were reseeded into 96-well plates 2 or 3 days after transduction and transfected with JcR2a IVTs 72 h after transduction. For this, both 0.1 µg JcR2a IVT and 0.2 µg Lipofectamine were diluted in 5 µL OptiMem each, combined and incubated for 5 min at RT. The mixture was applied to the cells and the medium was changed 4 hpt. 1 nM Daclatasvir was added to transfected Lunet N hCD81 [empty] cells as viral replication control. Cell lysates were harvested at 4, 24, 48 and 72 hpi for luciferase assay.

7.3.7. General HCV infection protocol

For the HCV infection assays, the cells were seeded in 12-, 24- or 96-well plates to reach confluency on the last day of the respective experiment. For infection, the cell culture medium was aspirated and 350, 250 or 35 µL (12-, 24- or 96-well plates) of undiluted Jc1 or JcR2a virus stock was added. The medium of the infected cells was changed 4 hpi, and the cells were further treated according to the required experimental conditions. The specific assay treatments are indicated in the respective figure legends. If the HCV infection experiment included transduction with lentiviral vectors, cells were transduced at

least 48 h prior to infection. Cells were reseeded between 48 and 72 h after transduction if the total assay exceeded five days.

7.3.8. HCV whole replication cycle

To assess the whole replication cycle of HCV, stable Lunet N hCD81 cell lines were seeded in 12-well plates and infected on the next day with HCV JcR2a virus stock. Medium of infected cells was changed 4 hpi. Cell lysates were harvested 48 hpi for luciferase readout (producers) and supernatant were transferred onto Huh-7.5 target cells in triplicates in 24-well plates, seeded the day before. Cell lysates of producer cells were harvested 72 hpi for luciferase assay (see above).

7.3.9. ZIKV and LGTV replication in stable DGAT cell lines

Lunet N hCD81 cell lines were seeded in 12-well plates (8×10^4 cells/well) and transduced with Lentiviruses to express the shRNA constructs targeting ATP6VOC or non-targeting shRNAs. Two days later, the cells were re-seeded in 24-well dishes and stable Lunet N hCD81 DGAT cell lines were seeded in parallel (2×10^4 cells/well). On the next day, cells were infected with ZIKV or LGTV at MOI=0.1. Infectious supernatants were harvested 96 hpi and stored at -80°C . The infectious titers were determined by plaque forming unit (PFU) assay.

7.3.10. Plaque forming unit (PFU) assay (for ZIKV and LGTV)

For ZIKV and LGTV PFU assays, 2.5×10^4 Vero E6 or A549 cells/well were seeded in 96-well plates. On the next day, infectious supernatants were titrated in serial dilution to the cells. At 2 hpi infection, the medium was replaced with overlay medium and cells were incubated 96 h. Cells were fixed with 10 % formaldehyde and plaques were visualized by crystal violet staining and manually counted.

7.3.11. HEV replication assay

HEV intracellular progeny virus formed in the DGAT stable cell lines were harvested and analyzed by Volker Kinast and Sarah Schlienkamp as previously described [228]. In brief, stable Lunet N hCD81 cells were seeded in a 24-well plate (5×10^4 cells/well) and infected with non-enveloped HEV Kernow-C1 p6 at a multiplicity of infection of 0.5. The medium was changed at 24 hpi. Cells were harvested by trypsinization 3 days post infection and intra-cellular progeny virus was harvested by cell lysis via three freeze-thaw cycles. To remove cell debris, lysates were centrifuged for 10 min at 10,000 g. Supernatants containing the recovered HEV particles were titrated in duplicates on HepG2/C3A cells, which were seeded 24 h before titration with 10^4 cells/well on 96-well plates. The cells were fixed 7 days post infection with 3 % PFA and permeabilized with 0.5 % TritonX-100 as described below. The focus-forming units were counted after IF staining as described in [228].

7.4. Statistics

Mean \pm standard error of the mean (SEM) values were depicted in bar plots and mean \pm standard deviation (SD) in all other plots, if not indicated differently. For statistical analysis we used GraphPadPrism, R [233] and RStudio [234]. Statistical tests were performed as indicated in the figure legends. Significant changes are indicated by asterisks in the respective figures and shown as * $P < 0.05$; ** $P < 0.01$; *** $P < 0.005$; **** $P < 0.001$.

For the lipidomics analysis, the two data sets were combined (as described in the results part) and filtered for lipid species which were present in more than 75 % of the samples. Concentrations of FFA were excluded. The absolute measured lipid concentrations were normalized to the cell number, to calculate the concentration per million cells. Where indicated, the lipid concentrations per million cells were normalized to the total or total membrane lipid (without TAG and CE classes) content, to calculate the total lipid or membrane lipid percentages, respectively. The lipidomics results were tested by two-tailed students t-test and non-adjusted p-values were depicted. Note that, for clarity reasons, significant changes in lipidomics heatmaps were depicted with only one asterisk (* $P < 0.05$), not distinguishing between significant and highly significant p-values.

8. Bibliography

1. Pietschmann T, Brown RJP. Hepatitis C Virus. *Trends Microbiol.* 2019 Apr;27(4):379–80.
2. World Health Organization. Hepatitis C [Internet]. Hepatitis C. 2023 [cited 2023 Nov 1]. Available from: <https://www.who.int/news-room/fact-sheets/detail/hepatitis-c>
3. Goto K, Roca Suarez AA, Wrensch F, Baumert TF, Lupberger J. Hepatitis C Virus and Hepatocellular Carcinoma: When the Host Loses Its Grip. *International Journal of Molecular Sciences.* 2020 Jan;21(9):3057.
4. Keikha M, Eslami M, Yousefi B, Ali-Hassanzadeh M, Kamali A, Yousefi M, Karbalaeei M. HCV genotypes and their determinative role in hepatitis C treatment. *VirusDisease.* 2020 Sep;31(3):235.
5. Choo QL, Kuo G, Weiner AJ, Overby LR, Bradley DW, Houghton M. Isolation of a cDNA cLone Derived from a Blood-Borne Non-A, Non-B Viral Hepatitis Genome. *Science.* 1989 Apr 21;244(4902):359–62.
6. Lindenbach BD, Evans MJ, Syder AJ, Wölk B, Tellinghuisen TL, Liu CC, Maruyama T, Hynes RO, Burton DR, McKeating JA, Rice CM. Complete replication of hepatitis C virus in cell culture. *Science.* 2005 Jul 22;309(5734):623–6.
7. Vieyres G, Pietschmann T. Entry and replication of recombinant hepatitis C viruses in cell culture. *Methods.* 2013 Feb;59(2):233–48.
8. Pileri P, Uematsu Y, Campagnoli S, Galli G, Falugi F, Petracca R, Weiner AJ, Houghton M, Rosa D, Grandi G, Abrignani S. Binding of Hepatitis C Virus to CD81. *Science.* 1998 Oct 30;282(5390):938–41.
9. Bartosch B, Vitelli A, Granier C, Goujon C, Dubuisson J, Pascale S, Scarselli E, Cortese R, Nicosia A, Cosset FL. Cell Entry of Hepatitis C Virus Requires a Set of Co-receptors That Include the CD81 Tetraspanin and the SR-B1 Scavenger Receptor. *Journal of Biological Chemistry.* 2003 Oct 24;278(43):41624–30.
10. Blanchard E, Roingeard P. The Hepatitis C Virus-Induced Membranous Web in Liver Tissue. *Cells.* 2018 Nov;7(11):191.
11. Niepmann M, Gerresheim GK. Hepatitis C Virus Translation Regulation. *Int J Mol Sci.* 2020 Mar 27;21(7):2328.
12. Tabata K, Neufeldt CJ, Bartenschlager R. Hepatitis C Virus Replication. *Cold Spring Harb Perspect Med.* 2020 Mar 1;10(3):a037093.
13. Tsukiyama-Kohara K, Iizuka N, Kohara M, Nomoto A. Internal ribosome entry site within hepatitis C virus RNA. *J Virol.* 1992 Mar;66(3):1476–83.
14. Spahn CMT, Kieft JS, Grassucci RA, Penczek PA, Zhou K, Doudna JA, Frank J. Hepatitis C Virus IRES RNA-Induced Changes in the Conformation of the 40S Ribosomal Subunit. *Science.* 2001 Mar 9;291(5510):1959–62.
15. Moradpour D, Penin F. Hepatitis C virus proteins: from structure to function. *Curr Top Microbiol Immunol.* 2013;369:113–42.

16. Egger D, Wölk B, Gosert R, Bianchi L, Blum HE, Moradpour D, Bienz K. Expression of Hepatitis C Virus Proteins Induces Distinct Membrane Alterations Including a Candidate Viral Replication Complex. *Journal of Virology*. 2002 Jun 15;76(12):5974–84.
17. Gosert R, Egger D, Lohmann V, Bartenschlager R, Blum HE, Bienz K, Moradpour D. Identification of the Hepatitis C Virus RNA Replication Complex in Huh-7 Cells Harboring Subgenomic Replicons. *Journal of Virology*. 2003 May;77(9):5487–92.
18. Ferraris P, Blanchard E, Roingeard P. Ultrastructural and biochemical analyses of hepatitis C virus-associated host cell membranes. *Journal of General Virology*. 2010;91(9):2230–7.
19. Wolff G, Melia CE, Snijder EJ, Bárcena M. Double-Membrane Vesicles as Platforms for Viral Replication. *Trends in Microbiology*. 2020 Dec 1;28(12):1022–33.
20. Paul D, Hoppe S, Saher G, Krijnse-Locker J, Bartenschlager R. Morphological and Biochemical Characterization of the Membranous Hepatitis C Virus Replication Compartment. *J Virol*. 2013 Oct;87(19):10612–27.
21. André P, Komurian-Pradel F, Deforges S, Perret M, Berland JL, Sodoyer M, Pol S, Bréchet C, Paranhos-Baccalà G, Lotteau V. Characterization of low- and very-low-density hepatitis C virus RNA-containing particles. *J Virol*. 2002 Jul;76(14):6919–28.
22. Diaz O, Delers F, Maynard M, Demignot S, Zoulim F, Chambaz J, Trépo C, Lotteau V, André P. Preferential association of Hepatitis C virus with apolipoprotein B48-containing lipoproteins. *J Gen Virol*. 2006 Oct;87(Pt 10):2983–91.
23. Vieyres G, Pietschmann T. HCV Pit Stop at the Lipid Droplet: Refuel Lipids and Put on a Lipoprotein Coat before Exit. *Cells*. 2019 Mar 12;8(3):233.
24. Syed GH, Khan M, Yang S, Siddiqui A. Hepatitis C Virus Lipovirions Assemble in the Endoplasmic Reticulum (ER) and Bud off from the ER to the Golgi Compartment in COPII Vesicles. *J Virol*. 2017 Jul 12;91(15):e00499-17.
25. Agaogué S, Perrin-Cocon L, André P, Lotteau V. Hepatitis C lipo-Viro-particle from chronically infected patients interferes with TLR4 signaling in dendritic cell. *PLoS One*. 2007 Mar 28;2(3):e330.
26. Wensch F, Crouchet E, Ligat G, Zeisel MB, Keck ZY, Fong SKH, Schuster C, Baumert TF. Hepatitis C Virus (HCV)-Apolipoprotein Interactions and Immune Evasion and Their Impact on HCV Vaccine Design. *Front Immunol*. 2018;9:1436.
27. Thursz M, Fontanet A. HCV transmission in industrialized countries and resource-constrained areas. *Nat Rev Gastroenterol Hepatol*. 2014 Jan;11(1):28–35.
28. Bailey JR, Barnes E, Cox AL. Approaches, Progress, and Challenges to Hepatitis C Vaccine Development. *Gastroenterology*. 2019 Jan;156(2):418–30.
29. Brunner N, Bruggmann P. Trends of the Global Hepatitis C Disease Burden: Strategies to Achieve Elimination. *J Prev Med Public Health*. 2021 Jul;54(4):251–8.
30. Nguyen-Dinh V, Herker E. Ultrastructural Features of Membranous Replication Organelles Induced by Positive-Stranded RNA Viruses. *Cells*. 2021 Sep;10(9):2407.

31. Tabata K, Prasad V, Paul D, Lee JY, Pham MT, Twu WI, Neufeldt CJ, Cortese M, Cerikan B, Stahl Y, Joecks S, Tran CS, Lüchtenborg C, V'kovski P, Hörmann K, Müller AC, Zitzmann C, Haselmann U, Beneke J, Kaderali L, Erfle H, Thiel V, Lohmann V, Superti-Furga G, Brügger B, Bartenschlager R. Convergent use of phosphatidic acid for hepatitis C virus and SARS-CoV-2 replication organelle formation. *Nat Commun.* 2021 Dec 14;12:7276.
32. Neufeldt CJ, Joyce MA, Buuren NV, Levin A, Kirkegaard K, Jr MG, Tyrrell DLJ, Wozniak RW. The Hepatitis C Virus-Induced Membranous Web and Associated Nuclear Transport Machinery Limit Access of Pattern Recognition Receptors to Viral Replication Sites. *PLOS Pathogens.* 2016 Oct 2;12(2):e1005428.
33. Twu WI, Lee JY, Kim H, Prasad V, Cerikan B, Haselmann U, Tabata K, Bartenschlager R. Contribution of autophagy machinery factors to HCV and SARS-CoV-2 replication organelle formation. *Cell Rep.* 2021 Nov 10;37(8):110049.
34. Mackenzie JM, Khromykh AA, Parton RG. Cholesterol Manipulation by West Nile Virus Perturbs the Cellular Immune Response. *Cell Host & Microbe.* 2007 Oct;2(4):229–39.
35. Arakawa M, Morita E. Flavivirus Replication Organelle Biogenesis in the Endoplasmic Reticulum: Comparison with Other Single-Stranded Positive-Sense RNA Viruses. *International Journal of Molecular Sciences.* 2019 Jan;20(9):2336.
36. Welsch S, Miller S, Romero-Brey I, Merz A, Bleck CKE, Walther P, Fuller SD, Antony C, Krijnse-Locker J, Bartenschlager R. Composition and Three-Dimensional Architecture of the Dengue Virus Replication and Assembly Sites. *Cell Host & Microbe.* 2009 Apr 23;5(4):365–75.
37. Cortese M, Goellner S, Acosta EG, Neufeldt CJ, Oleksiuk O, Lampe M, Haselmann U, Funaya C, Schieber N, Ronchi P, Schorb M, Pruunsild P, Schwab Y, Chatel-Chaix L, Ruggieri A, Bartenschlager R. Ultrastructural Characterization of Zika Virus Replication Factories. *Cell Reports.* 2017 Feb 28;18(9):2113–23.
38. Miorin L, Romero-Brey I, Maiuri P, Hoppe S, Krijnse-Locker J, Bartenschlager R, Marcello A. Three-Dimensional Architecture of Tick-Borne Encephalitis Virus Replication Sites and Trafficking of the Replicated RNA. *Journal of Virology.* 2013 Jun;87(11):6469–81.
39. Roingeard P, Eymieux S, Burlaud-Gaillard J, Hourieux C, Patient R, Blanchard E. The double-membrane vesicle (DMV): a virus-induced organelle dedicated to the replication of SARS-CoV-2 and other positive-sense single-stranded RNA viruses. *Cell Mol Life Sci.* 2022 Jul 16;79(8):425.
40. Wolff G, Limpens RWAL, Zevenhoven-Dobbe JC, Laugks U, Zheng S, de Jong AWM, Koning RI, Agard DA, Grünewald K, Koster AJ, Snijder EJ, Bárcena M. A molecular pore spans the double membrane of the coronavirus replication organelle. *Science.* 2020 Sep 11;369(6509):1395–8.
41. Romero-Brey I, Merz A, Chiramel A, Lee JY, Chlanda P, Haselman U, Santarella-Mellwig R, Habermann A, Hoppe S, Kallis S, Walther P, Antony C, Krijnse-Locker J, Bartenschlager R. Three-Dimensional Architecture and Biogenesis of Membrane Structures Associated with Hepatitis C Virus Replication. *PLOS Pathogens.* 2012 Jun 12;8(12):e1003056.
42. Kopek BG, Settles EW, Friesen PD, Ahlquist P. Nodavirus-Induced Membrane Rearrangement in Replication Complex Assembly Requires Replicase Protein A, RNA Templates, and Polymerase Activity. *J Virol.* 2010 Dec;84(24):12492–503.
43. Paul D, Bartenschlager R. Flaviviridae Replication Organelles: Oh, What a Tangled Web We Weave. *Annual Review of Virology.* 2015;2(1):289–310.

44. Hofmann S, Krajewski M, Scherer C, Scholz V, Mordhorst V, Truschow P, Schöbel A, Reimer R, Schwudke D, Herker E. Complex lipid metabolic remodeling is required for efficient hepatitis C virus replication. *Biochimica et Biophysica Acta (BBA) - Molecular and Cell Biology of Lipids*. 2018 Sep 1;1863(9):1041–56.
45. Diamond DL, Syder AJ, Jacobs JM, Sorensen CM, Walters KA, Proll SC, McDermott JE, Gritsenko MA, Zhang Q, Zhao R, Metz TO, Li DGC, Waters KM, Smith RD, Rice CM, Katze MG. Temporal Proteome and Lipidome Profiles Reveal Hepatitis C Virus-Associated Reprogramming of Hepatocellular Metabolism and Bioenergetics. *PLOS Pathogens*. 2010 Jan 8;6(1):e1000719.
46. Leier HC, Weinstein JB, Kyle JE, Lee JY, Bramer LM, Stratton KG, Kempthorne D, Navratil AR, Tafesse EG, Hornemann T, Messer WB, Dennis EA, Metz TO, Barklis E, Tafesse FG. A global lipid map defines a network essential for Zika virus replication. *Nat Commun*. 2020 Jul 21;11(1):3652.
47. Farley SE, Kyle JE, Leier HC, Bramer LM, Weinstein JB, Bates TA, Lee JY, Metz TO, Schultz C, Tafesse FG. A global lipid map reveals host dependency factors conserved across SARS-CoV-2 variants. *Nat Commun*. 2022 Jun 17;13(1):3487.
48. Bigay J, Antonny B. Curvature, Lipid Packing, and Electrostatics of Membrane Organelles: Defining Cellular Territories in Determining Specificity. *Developmental Cell*. 2012 Nov 13;23(5):886–95.
49. Vanni S, Hirose H, Barelli H, Antonny B, Gautier R. A sub-nanometre view of how membrane curvature and composition modulate lipid packing and protein recruitment. *Nat Commun*. 2014 Sep 15;5:4916.
50. Pinot M, Vanni S, Pagnotta S, Lacas-Gervais S, Payet LA, Ferreira T, Gautier R, Goud B, Antonny B, Barelli H. Polyunsaturated phospholipids facilitate membrane deformation and fission by endocytic proteins. *Science*. 2014 Aug 8;345(6197):693–7.
51. Belov GA, van Kuppeveld FJ. (+)RNA viruses rewire cellular pathways to build replication organelles. *Current Opinion in Virology*. 2012 Dec 1;2(6):740–7.
52. Berger KL, Kelly SM, Jordan TX, Tartell MA, Randall G. Hepatitis C Virus Stimulates the Phosphatidylinositol 4-Kinase III Alpha-Dependent Phosphatidylinositol 4-Phosphate Production That Is Essential for Its Replication. *Journal of Virology*. 2011 Sep;85(17):8870–83.
53. Hsu NY, Ilnytska O, Belov G, Santiana M, Chen YH, Takvorian PM, Pau C, van der Schaar H, Kaushik-Basu N, Balla T, Cameron CE, Ehrenfeld E, van Kuppeveld FJM, Altan-Bonnet N. Viral Reorganization of the Secretory Pathway Generates Distinct Organelles for RNA Replication. *Cell*. 2010 May 28;141(5):799–811.
54. Reiss S, Rebhan I, Backes P, Romero-Brey I, Erfle H, Matula P, Kaderali L, Poenisch M, Blankenburg H, Hiet MS, Longerich T, Diehl S, Ramirez F, Balla T, Rohr K, Kaul A, Bühler S, Pepperkok R, Lengauer T, Albrecht M, Eils R, Schirmacher P, Lohmann V, Bartenschlager R. Recruitment and activation of a lipid kinase by hepatitis C virus NS5A is essential for integrity of the membranous replication compartment. *Cell Host Microbe*. 2011 Jan 20;9(1):32–45.
55. Bishé B, Syed GH, Field SJ, Siddiqui A. Role of Phosphatidylinositol 4-Phosphate (PI4P) and Its Binding Protein GOLPH3 in Hepatitis C Virus Secretion. *Journal of Biological Chemistry*. 2012 Aug 10;287(33):27637–47.
56. Amako Y, Sarkeshik A, Hotta H, Yates J, Siddiqui A. Role of Oxysterol Binding Protein in Hepatitis C Virus infection. *Journal of Virology*. 2009 Sep 15;83(18):9237–46.

57. Wang H, Perry JW, Lauring AS, Neddermann P, De Francesco R, Tai AW. Oxysterol-Binding Protein Is a Phosphatidylinositol 4-Kinase Effector Required for HCV Replication Membrane Integrity and Cholesterol Trafficking. *Gastroenterology*. 2014 May 1;146(5):1373-1385.e11.
58. Gewaid H, Aoyagi H, Arita M, Watashi K, Suzuki R, Sakai S, Kumagai K, Yamaji T, Fukasawa M, Kato F, Hishiki T, Mimata A, Sakamaki Y, Ichinose S, Hanada K, Muramatsu M, Wakita T, Aizaki H. Sphingomyelin Is Essential for the Structure and Function of the Double-Membrane Vesicles in Hepatitis C Virus RNA Replication Factories. *Journal of Virology*. 2020 Nov 9;94(23):e01080-20.
59. Róg T, Pasenkiewicz-Gierula M, Vattulainen I, Karttunen M. Ordering effects of cholesterol and its analogues. *Biochimica et Biophysica Acta (BBA) - Biomembranes*. 2009 Jan 1;1788(1):97–121.
60. Rothwell C, LeBreton A, Young Ng C, Lim JYH, Liu W, Vasudevan S, Labow M, Gu F, Gaither LA. Cholesterol biosynthesis modulation regulates dengue viral replication. *Virology*. 2009 Jun 20;389(1):8–19.
61. Bezemer B, van Cleef KWR, Overheul GJ, Miesen P, van Rij RP. The calcium channel inhibitor lacidipine inhibits Zika virus replication in neural progenitor cells. *Antiviral Research*. 2022 Jun 1;202:105313.
62. Aizaki H, Lee KJ, Sung VMH, Ishiko H, Lai MMC. Characterization of the hepatitis C virus RNA replication complex associated with lipid rafts. *Virology*. 2004 Jul 1;324(2):450–61.
63. Kawano M, Kumagai K, Nishijima M, Hanada K. Efficient Trafficking of Ceramide from the Endoplasmic Reticulum to the Golgi Apparatus Requires a VAMP-associated Protein-interacting FFAT Motif of CERT. *Journal of Biological Chemistry*. 2006 Oct 6;281(40):30279–88.
64. Amako Y, Syed GH, Siddiqui A. Protein Kinase D Negatively Regulates Hepatitis C Virus Secretion through Phosphorylation of Oxysterol-binding Protein and Ceramide Transfer Protein. *Journal of Biological Chemistry*. 2011 Apr 1;286(13):11265–74.
65. Aktepe TE, Pham H, Mackenzie JM. Differential utilisation of ceramide during replication of the flaviviruses West Nile and dengue virus. *Virology*. 2015 Oct;484:241–50.
66. Dawaliby R, Trubbia C, Delporte C, Noyon C, Ruysschaert JM, Van Antwerpen P, Govaerts C. Phosphatidylethanolamine Is a Key Regulator of Membrane Fluidity in Eukaryotic Cells. *J Biol Chem*. 2016 Feb 12;291(7):3658–67.
67. van der Veen JN, Kennelly JP, Wan S, Vance JE, Vance DE, Jacobs RL. The critical role of phosphatidylcholine and phosphatidylethanolamine metabolism in health and disease. *Biochimica et Biophysica Acta (BBA) - Biomembranes*. 2017 Sep 1;1859(9, Part B):1558–72.
68. Zhang J, Zhang Z, Chukkapalli V, Nchoutmboube JA, Li J, Randall G, Belov GA, Wang X. Positive-strand RNA viruses stimulate host phosphatidylcholine synthesis at viral replication sites. *Proceedings of the National Academy of Sciences*. 2016 Feb 23;113(8):E1064–73.
69. Xu K, Nagy PD. RNA virus replication depends on enrichment of phosphatidylethanolamine at replication sites in subcellular membranes. *Proceedings of the National Academy of Sciences*. 2015 Apr 7;112(14):E1782–91.

70. Lyn RK, Singaravelu R, Kargman S, O'Hara S, Chan H, Oballa R, Huang Z, Jones DM, Ridsdale A, Russell RS, Partridge AW, Pezacki JP. Stearoyl-CoA desaturase inhibition blocks formation of hepatitis C virus-induced specialized membranes. *Sci Rep*. 2014 Apr 1;4(1):4549.
71. Nguyen LN, Lim YS, Pham LV, Shin HY, Kim YS, Hwang SB. Stearoyl Coenzyme A Desaturase 1 Is Associated with Hepatitis C Virus Replication Complex and Regulates Viral Replication. *Journal of Virology*. 2014 Nov 1;88(21):12311–25.
72. Athenstaedt K, Daum G. Phosphatidic acid, a key intermediate in lipid metabolism. *Eur J Biochem*. 1999 Nov;266(1):1–16.
73. Wang X, Devaiah SP, Zhang W, Welti R. Signaling functions of phosphatidic acid. *Progress in Lipid Research*. 2006 May 1;45(3):250–78.
74. Reue K, Wang H. Mammalian lipin phosphatidic acid phosphatases in lipid synthesis and beyond: metabolic and inflammatory disorders. *Journal of Lipid Research*. 2019 Apr 1;60(4):728–33.
75. Goñi FM, Alonso A. Structure and functional properties of diacylglycerols in membranes. *Prog Lipid Res*. 1999 Jan;38(1):1–48.
76. Eichmann TO, Lass A. DAG tales: the multiple faces of diacylglycerol—stereochemistry, metabolism, and signaling. *Cell Mol Life Sci*. 2015 Oct 1;72(20):3931–52.
77. Domart MC, Hobday TMC, Peddie CJ, Chung GHC, Wang A, Yeh K, Jethwa N, Zhang Q, Wakelam MJO, Woscholski R, Byrne RD, Collinson LM, Poccia DL, Larijani B. Acute Manipulation of Diacylglycerol Reveals Roles in Nuclear Envelope Assembly & Endoplasmic Reticulum Morphology. Guerrero-Hernandez A, editor. *PLoS ONE*. 2012 Dec 5;7(12):e51150.
78. Yen CLE, Stone SJ, Koliwad S, Harris C, Farese RV. Thematic Review Series: Glycerolipids. DGAT enzymes and triacylglycerol biosynthesis. *Journal of Lipid Research*. 2008 Nov 1;49(11):2283–301.
79. Lee JY, Cortese M, Haselmann U, Tabata K, Romero-Brey I, Funaya C, Schieber NL, Qiang Y, Bartenschlager M, Kallis S, Ritter C, Rohr K, Schwab Y, Ruggieri A, Bartenschlager R. Spatiotemporal Coupling of the Hepatitis C Virus Replication Cycle by Creating a Lipid Droplet-Proximal Membranous Replication Compartment. *Cell Reports*. 2019 Jun;27(12):3602–3617.e5.
80. Meyers NL, Fontaine KA, Kumar GR, Ott M. Entangled in a membranous web: ER and lipid droplet reorganization during hepatitis C virus infection. *Current Opinion in Cell Biology*. 2016 Aug;41:117–24.
81. Bley H, Schöbel A, Herker E. Whole Lotta Lipids—From HCV RNA Replication to the Mature Viral Particle. *International Journal of Molecular Sciences*. 2020 Jan;21(8):2888.
82. Tang WC, Lin RJ, Liao CL, Lin YL. Rab18 Facilitates Dengue Virus Infection by Targeting Fatty Acid Synthase to Sites of Viral Replication. *J Virol*. 2014 Jun;88(12):6793–804.
83. Laufman O, Perrino J, Andino R. Viral Generated Inter-Organellar Contacts Redirect Lipid Flux for Genome Replication. *Cell*. 2019 Jul 11;178(2):275–289.e16.
84. Olzmann JA, Carvalho P. Dynamics and functions of lipid droplets. *Nat Rev Mol Cell Biol*. 2019 Mar;20(3):137–55.

85. Chang TY, Li BL, Chang CCY, Urano Y. Acyl-coenzyme A:cholesterol acyltransferases. *Am J Physiol Endocrinol Metab*. 2009 Jul;297(1):E1–9.
86. Renne MF, Klug YA, Carvalho P. Lipid droplet biogenesis: A mystery “unmixing”? *Seminars in Cell & Developmental Biology*. 2020 Dec 1;108:14–23.
87. Arlt H, Sui X, Folger B, Adams C, Chen X, Remme R, Hamprecht FA, DiMaio F, Liao M, Goodman JM, Farese RV, Walther TC. Seipin forms a flexible cage at lipid droplet formation sites. *Nat Struct Mol Biol*. 2022 Mar;29(3):194–202.
88. Kim S, Chung J, Arlt H, Pak AJ, Farese RV Jr, Walther TC, Voth GA. Seipin transmembrane segments critically function in triglyceride nucleation and lipid droplet budding from the membrane. Delemotte L, Faraldo-Gómez JD, editors. *eLife*. 2022 May 18;11:e75808.
89. Salo VT, Ikonen E. Moving out but keeping in touch: contacts between endoplasmic reticulum and lipid droplets. *Current Opinion in Cell Biology*. 2019 Apr 1;57:64–70.
90. Wilfling F, Wang H, Haas JT, Krahmer N, Gould TJ, Uchida A, Cheng JX, Graham M, Christiano R, Fröhlich F, Liu X, Buhman KK, Coleman RA, Bewersdorf J, Farese RV, Walther TC. Triacylglycerol Synthesis Enzymes Mediate Lipid Droplet Growth by Relocalizing from the ER to Lipid Droplets. *Dev Cell*. 2013 Feb 25;24(4):384–99.
91. Krahmer N, Guo Y, Wilfling F, Hilger M, Lingrell S, Heger K, Newman HW, Schmidt-Supprian M, Vance DE, Mann M, Farese RV, Walther TC. Phosphatidylcholine Synthesis for Lipid Droplet Expansion Is Mediated by Localized Activation of CTP:Phosphocholine Cytidylyltransferase. *Cell Metabolism*. 2011 Oct;14(4):504–15.
92. Lass A, Zimmermann R, Oberer M, Zechner R. Lipolysis – A highly regulated multi-enzyme complex mediates the catabolism of cellular fat stores. *Progress in Lipid Research*. 2011 Jan 1;50(1):14–27.
93. Schott MB, Weller SG, Schulze RJ, Krueger EW, Drizyte-Miller K, Casey CA, McNiven MA. Lipid droplet size directs lipolysis and lipophagy catabolism in hepatocytes. *Journal of Cell Biology*. 2019 Aug 7;218(10):3320–35.
94. Granneman JG, Moore HPH, Mottillo EP, Zhu Z, Zhou L. Interactions of Perilipin-5 (Plin5) with Adipose Triglyceride Lipase. *Journal of Biological Chemistry*. 2011 Feb 18;286(7):5126–35.
95. Schulze RJ, Sathyanarayan A, Mashek DG. Breaking fat: The regulation and mechanisms of lipophagy. *Biochim Biophys Acta Mol Cell Biol Lipids*. 2017 Oct;1862(10 Pt B):1178–87.
96. Thiam AR, Beller M. The why, when and how of lipid droplet diversity. *J Cell Sci*. 2017 Jan 15;130(2):315–24.
97. Hugenholtz M, Bohnert M. Come a little bit closer! Lipid droplet-ER contact sites are getting crowded. *Biochimica et Biophysica Acta (BBA) - Molecular Cell Research*. 2020 Feb 1;1867(2):118603.
98. Wang H, Becuwe M, Housden BE, Chitraju C, Porras AJ, Graham MM, Liu XN, Thiam AR, Savage DB, Agarwal AK, Garg A, Olarte MJ, Lin Q, Fröhlich F, Hannibal-Bach HK, Upadhyayula S, Perrimon N, Kirchhausen T, Ejsing CS, Walther TC, Farese RV Jr. Seipin is required for converting nascent to mature lipid droplets. Young SG, editor. *eLife*. 2016 Aug 26;5:e16582.

99. Grippa A, Buxó L, Mora G, Funaya C, Idrissi FZ, Mancuso F, Gomez R, Muntanyà J, Sabidó E, Carvalho P. The seipin complex Fld1/Ldb16 stabilizes ER–lipid droplet contact sites. *Journal of Cell Biology*. 2015 Nov 16;211(4):829–44.
100. Petan T, Jarc E, Jusović M. Lipid Droplets in Cancer: Guardians of Fat in a Stressful World. *Molecules*. 2018 Aug;23(8):1941.
101. Bosch M, Sánchez-Álvarez M, Fajardo A, Kapetanovic R, Steiner B, Dutra F, Moreira L, López JA, Campo R, Marí M, Morales-Paytuví F, Tort O, Gubern A, Templin RM, Curson JEB, Martel N, Català C, Lozano F, Tebar F, Enrich C, Vázquez J, Del Pozo MA, Sweet MJ, Bozza PT, Gross SP, Parton RG, Pol A. Mammalian lipid droplets are innate immune hubs integrating cell metabolism and host defense. *Science*. 2020 Oct 16;370(6514):eaay8085.
102. Libbing CL, McDevitt AR, Azcueta RMP, Ahila A, Mulye M. Lipid Droplets: A Significant but Understudied Contributor of Host–Bacterial Interactions. *Cells*. 2019 Apr;8(4):354.
103. Monson EA, Trenerry AM, Laws JL, Mackenzie JM, Helbig KJ. Lipid droplets and lipid mediators in viral infection and immunity. *FEMS Microbiology Reviews*. 2021 Jul 1;45(4):fuaa066.
104. Vallochi AL, Teixeira L, Oliveira K da S, Maya-Monteiro CM, Bozza PT. Lipid Droplet, a Key Player in Host-Parasite Interactions. *Front Immunol*. 2018;9:1022.
105. Cases S, Smith SJ, Zheng YW, Myers HM, Lear SR, Sande E, Novak S, Collins C, Welch CB, Lusis AJ, Erickson SK, Farese RV. Identification of a gene encoding an acyl CoA:diacylglycerol acyltransferase, a key enzyme in triacylglycerol synthesis. *Proceedings of the National Academy of Sciences*. 1998 Oct 27;95(22):13018–23.
106. Lardizabal KD, Mai JT, Wagner NW, Wyrick A, Voelker T, Hawkins DJ. DGAT2 Is a New Diacylglycerol Acyltransferase Gene Family. *Journal of Biological Chemistry*. 2001 Oct;276(42):38862–9.
107. Cao H. Structure-Function Analysis of Diacylglycerol Acyltransferase Sequences from 70 Organisms. *BMC Research Notes*. 2011 Jul 21;4(1):249.
108. Cases S, Stone SJ, Zhou P, Yen E, Tow B, Lardizabal KD, Voelker T, Farese RV. Cloning of DGAT2, a Second Mammalian Diacylglycerol Acyltransferase, and Related Family Members. *Journal of Biological Chemistry*. 2001 Oct 19;276(42):38870–6.
109. McFie PJ, Stone SL, Banman SL, Stone SJ. Topological Orientation of Acyl-CoA:Diacylglycerol Acyltransferase-1 (DGAT1) and Identification of a Putative Active Site Histidine and the Role of the N Terminus in Dimer/Tetramer Formation. *Journal of Biological Chemistry*. 2010 Nov 26;285(48):37377–87.
110. Sui X, Wang K, Gluchowski NL, Elliott SD, Liao M, Walther TC, Farese RV. Structure and catalytic mechanism of a human triacylglycerol-synthesis enzyme. *Nature*. 2020 May;581(7808):323–8.
111. Stone SJ, Levin MC, Farese RV. Membrane Topology and Identification of Key Functional Amino Acid Residues of Murine Acyl-CoA:Diacylglycerol Acyltransferase-2. *Journal of Biological Chemistry*. 2006 Dec 29;281(52):40273–82.
112. Jin Y, McFie PJ, Banman SL, Brandt C, Stone SJ. Diacylglycerol Acyltransferase-2 (DGAT2) and Monoacylglycerol Acyltransferase-2 (MGAT2) Interact to Promote Triacylglycerol Synthesis. *Journal of Biological Chemistry*. 2014 Oct;289(41):28237–48.

113. McFie PJ, Jin Y, Banman SL, Beauchamp E, Berthiaume LG, Stone SJ. Characterization of the interaction of diacylglycerol acyltransferase-2 with the endoplasmic reticulum and lipid droplets. *Biochimica et Biophysica Acta (BBA) - Molecular and Cell Biology of Lipids*. 2014 Sep 1;1841(9):1318–28.
114. Stone SJ, Levin MC, Zhou P, Han J, Walther TC, Farese RV. The endoplasmic reticulum enzyme DGAT2 is found in mitochondria-associated membranes and has a mitochondrial targeting signal that promotes its association with mitochondria. *J Biol Chem*. 2009 Feb 20;284(8):5352–61.
115. Kuerschner L, Moessinger C, Thiele C. Imaging of Lipid Biosynthesis: How a Neutral Lipid Enters Lipid Droplets. *Traffic*. 2008;9(3):338–52.
116. McFie PJ, Banman SL, Stone SJ. Diacylglycerol acyltransferase-2 contains a c-terminal sequence that interacts with lipid droplets. *Biochimica et Biophysica Acta (BBA) - Molecular and Cell Biology of Lipids*. 2018 Sep 1;1863(9):1068–81.
117. Xu N, Zhang SO, Cole RA, McKinney SA, Guo F, Haas JT, Bobba S, Farese RV Jr, Mak HY. The FATP1–DGAT2 complex facilitates lipid droplet expansion at the ER–lipid droplet interface. *Journal of Cell Biology*. 2012 Aug 27;198(5):895–911.
118. Villanueva CJ, Monetti M, Shih M, Zhou P, Watkins SM, Bhanot S, Farese Jr. RV. Specific role for acyl CoA:Diacylglycerol acyltransferase 1 (Dgat1) in hepatic steatosis due to exogenous fatty acids. *Hepatology*. 2009;50(2):434–42.
119. Qi J, Lang W, Geisler JG, Wang P, Petrounia I, Mai S, Smith C, Askari H, Struble GT, Williams R, Bhanot S, Monia BP, Bayoumy S, Grant E, Caldwell GW, Todd MJ, Liang Y, Gaul MD, Demarest KT, Connelly MA. The use of stable isotope-labeled glycerol and oleic acid to differentiate the hepatic functions of DGAT1 and -2. *Journal of Lipid Research*. 2012 Jun 1;53(6):1106–16.
120. Wurie HR, Buckett L, Zammit VA. Diacylglycerol acyltransferase 2 acts upstream of diacylglycerol acyltransferase 1 and utilizes nascent diglycerides and de novo synthesized fatty acids in HepG2 cells. *The FEBS Journal*. 2012;279(17):3033–47.
121. Miyanari Y, Atsuzawa K, Usuda N, Watashi K, Hishiki T, Zayas M, Bartenschlager R, Wakita T, Hijikata M, Shimotohno K. The lipid droplet is an important organelle for hepatitis C virus production. *Nat Cell Biol*. 2007 Sep;9(9):1089–97.
122. Zhang J, Lan Y, Sanyal S. Modulation of Lipid Droplet Metabolism—A Potential Target for Therapeutic Intervention in Flaviviridae Infections. *Front Microbiol*. 2017 Nov 28;8:2286.
123. Camus G, Schweiger M, Herker E, Harris C, Kondratowicz AS, Tsou CL, Farese RV, Herath K, Previs SF, Roddy TP, Pinto S, Zechner R, Ott M. The Hepatitis C Virus Core Protein Inhibits Adipose Triglyceride Lipase (ATGL)-mediated Lipid Mobilization and Enhances the ATGL Interaction with Comparative Gene Identification 58 (CGI-58) and Lipid Droplets. *Journal of Biological Chemistry*. 2014 Dec 26;289(52):35770–80.
124. Vogt DA, Camus G, Herker E, Webster BR, Tsou CL, Greene WC, Yen TSB, Ott M. Lipid Droplet-Binding Protein TIP47 Regulates Hepatitis C Virus RNA Replication through Interaction with the Viral NS5A Protein. *PLOS Pathogens*. 2013 Nov 4;9(4):e1003302.
125. Lassen S, Grüttner C, Nguyen-Dinh V, Herker E. Perilipin-2 is critical for efficient lipoprotein and hepatitis C virus particle production. *Journal of Cell Science*. 2019 Jan 9;132(1):jcs217042.

126. Herker E, Harris C, Hernandez C, Carpentier A, Kaehlcke K, Rosenberg AR, Farese RV, Ott M. Efficient Hepatitis C Virus Particle Formation Requires Diacylglycerol Acyltransferase 1 (DGAT1). *Nat Med.* 2010 Nov;16(11):1295–8.
127. Camus G, Herker E, Modi AA, Haas JT, Ramage HR, Farese RV, Ott M. Diacylglycerol acyltransferase-1 localizes hepatitis C virus NS5A protein to lipid droplets and enhances NS5A interaction with the viral capsid core. *J Biol Chem.* 2013 Apr 5;288(14):9915–23.
128. Vieyres G, Welsch K, Gerold G, Gentzsch J, Kahl S, Vondran FWR, Kaderali L, Pietschmann T. ABHD5/CGI-58, the Chananin-Dorfman Syndrome Protein, Mobilises Lipid Stores for Hepatitis C Virus Production. *PLOS Pathogens.* 2016 Apr 28;12(4):e1005568.
129. Vieyres G, Reichert I, Carpentier A, Vondran FWR, Pietschmann T. The ATGL lipase cooperates with ABHD5 to mobilize lipids for hepatitis C virus assembly. *PLOS Pathogens.* 2020 Jun 15;16(6):e1008554.
130. Zhang Z, He G, Filipowicz N, Randall G, Belov G, Kopek B, Wang X. Host Lipids in Positive-Strand RNA Virus Genome Replication. *Frontiers in Microbiology.* 2019 Feb 26;10.
131. Shavinskaya A, Boulant S, Penin F, McLauchlan J, Bartenschlager R. The Lipid Droplet Binding Domain of Hepatitis C Virus Core Protein Is a Major Determinant for Efficient Virus Assembly. *Journal of Biological Chemistry.* 2007 Dec 21;282(51):37158–69.
132. Suzuki R, Tobe K, Aoyama M, Sakamoto K, Ohsugi M, Kamei N, Nemoto S, Inoue A, Ito Y, Uchida S, Hara K, Yamauchi T, Kubota N, Terauchi Y, Kadowaki T. Expression of DGAT2 in White Adipose Tissue Is Regulated by Central Leptin Action. *Journal of Biological Chemistry.* 2005 Feb 4;280(5):3331–7.
133. Cheng X, Geng F, Pan M, Wu X, Zhong Y, Wang C, Tian Z, Cheng C, Zhang R, Puduvalli V, Horbinski C, Mo X, Han X, Chakravarti A, Guo D. Targeting DGAT1 ameliorates glioblastoma by increasing fat catabolism and oxidative stress. *Cell Metab.* 2020 Aug 4;32(2):229-242.e8.
134. McFie PJ, Chumala P, Katselis GS, Stone SJ. DGAT2 stability is increased in response to DGAT1 inhibition in gene edited HepG2 cells. *Biochimica et Biophysica Acta (BBA) - Molecular and Cell Biology of Lipids.* 2021 Sep 1;1866(9):158991.
135. Harris CA, Haas JT, Streeper RS, Stone SJ, Kumari M, Yang K, Han X, Brownell N, Gross RW, Zechner R, Farese RV. DGAT enzymes are required for triacylglycerol synthesis and lipid droplets in adipocytes. *J Lipid Res.* 2011 Apr 1;52(4):657–67.
136. Farese RV, Walther TC. Glycerolipid Synthesis and Lipid Droplet Formation in the Endoplasmic Reticulum. *Cold Spring Harb Perspect Biol.* 2023 May 1;15(5):a041246.
137. McFie PJ, Banman SL, Kary S, Stone SJ. Murine diacylglycerol acyltransferase-2 (DGAT2) can catalyze triacylglycerol synthesis and promote lipid droplet formation independent of its localization to the endoplasmic reticulum. *J Biol Chem.* 2011 Aug 12;286(32):28235–46.
138. Bitzegeio J, Bankwitz D, Hueging K, Haid S, Brohm C, Zeisel MB, Herrmann E, Iken M, Ott M, Baumert TF, Pietschmann T. Adaptation of hepatitis C virus to mouse CD81 permits infection of mouse cells in the absence of human entry factors. *PLoS Pathog.* 2010 Jul 1;6(7):e1000978.
139. Blight KJ, McKeating JA, Rice CM. Highly permissive cell lines for subgenomic and genomic hepatitis C virus RNA replication. *J Virol.* 2002 Dec;76(24):13001–14.

140. Hueging K, Doepke M, Vieyres G, Bankwitz D, Frentzen A, Doerrbecker J, Gumz F, Haid S, Wölk B, Kaderali L, Pietschmann T. Apolipoprotein E Codetermines Tissue Tropism of Hepatitis C Virus and Is Crucial for Viral Cell-to-Cell Transmission by Contributing to a Postenvelopment Step of Assembly. *J Virol*. 2014 Feb;88(3):1433–46.
141. Da Costa D, Turek M, Felmler DJ, Girardi E, Pfeffer S, Long G, Bartenschlager R, Zeisel MB, Baumert TF. Reconstitution of the Entire Hepatitis C Virus Life Cycle in Nonhepatic Cells. *Journal of Virology*. 2012 Nov;86(21):11919–25.
142. Icard V, Diaz O, Scholtes C, Perrin-Cocon L, Ramière C, Bartenschlager R, Penin F, Lotteau V, André P. Secretion of Hepatitis C Virus Envelope Glycoproteins Depends on Assembly of Apolipoprotein B Positive Lipoproteins. *PLOS ONE*. 2009 Jan 21;4(1):e4233.
143. Zammit VA, Buckett LK, Turnbull AV, Wure H, Proven A. Diacylglycerol acyltransferases: Potential roles as pharmacological targets. *Pharmacology & Therapeutics*. 2008 Jun;118(3):295–302.
144. Irshad Z, Chmel N, Adya R, Zammit VA. Hepatic VLDL secretion: DGAT1 determines particle size but not particle number, which can be supported entirely by DGAT2. *Journal of Lipid Research*. 2019 Jan 1;60(1):111–20.
145. Chitraju C, Walther TC, Farese RV. The triglyceride synthesis enzymes DGAT1 and DGAT2 have distinct and overlapping functions in adipocytes. *Journal of Lipid Research*. 2019 Jun 1;60(6):1112–20.
146. Hung YH, Carreiro AL, Buhman KK. Dgat1 and Dgat2 regulate enterocyte triacylglycerol distribution and alter proteins associated with cytoplasmic lipid droplets in response to dietary fat. *Biochimica et Biophysica Acta (BBA) - Molecular and Cell Biology of Lipids*. 2017 Jun 1;1862(6):600–14.
147. Narbus CM, Israelow B, Sourisseau M, Michta ML, Hopcraft SE, Zeiner GM, Evans MJ. HepG2 cells expressing microRNA miR-122 support the entire hepatitis C virus life cycle. *J Virol*. 2011 Nov;85(22):12087–92.
148. Belema M, Meanwell NA. Discovery of Daclatasvir, a Pan-Genotypic Hepatitis C Virus NS5A Replication Complex Inhibitor with Potent Clinical Effect. *J Med Chem*. 2014 Jun 26;57(12):5057–71.
149. Kralj D, Jukić LV, Stojšavljević S, Duvnjak M, Smolić M, Čurčić IB. Hepatitis C Virus, Insulin Resistance, and Steatosis. *J Clin Transl Hepatol*. 2016 Mar 28;4(1):66–75.
150. Das AT, Tenenbaum L, Berkhout B. Tet-On Systems For Doxycycline-inducible Gene Expression. *Curr Gene Ther*. 2016 Jun;16(3):156–67.
151. Laporte J, Malet I, Andrieu T, Thibault V, Toulme JJ, Wychowski C, Pawlotsky JM, Huraux JM, Agut H, Cahour A. Comparative Analysis of Translation Efficiencies of Hepatitis C Virus 5' Untranslated Regions among Intraindividual Quasispecies Present in Chronic Infection: Opposite Behaviors Depending on Cell Type. *J Virol*. 2000 Nov;74(22):10827–33.
152. Backes P, Quinkert D, Reiss S, Binder M, Zayas M, Rescher U, Gerke V, Bartenschlager R, Lohmann V. Role of Annexin A2 in the Production of Infectious Hepatitis C Virus Particles. *J Virol*. 2010 Jun;84(11):5775–89.

153. Scaturro P, Stukalov A, Haas DA, Cortese M, Draganova K, Płaszczyc A, Bartenschlager R, Götz M, Pichlmair A. An orthogonal proteomic survey uncovers novel Zika virus host factors. *Nature*. 2018 Sep;561(7722):253–7.
154. Wüstner D, Mukherjee S, Maxfield FR, Müller P, Herrmann A. Vesicular and Nonvesicular Transport of Phosphatidylcholine in Polarized HepG2 Cells. *Traffic*. 2001;2(4):277–96.
155. Liebscher S, Ambrose RL, Aktepe TE, Mikulasova A, Prier JE, Gillespie LK, Lopez-Denman AJ, Rupasinghe TWT, Tull D, McConville MJ, Mackenzie JM. Phospholipase A2 activity during the replication cycle of the flavivirus West Nile virus. *PLOS Pathogens*. 2018 Apr 30;14(4):e1007029.
156. Henkels KM, Miller TE, Ganesan R, Wilkins BA, Fite K, Gomez-Cambronero J. A Phosphatidic Acid (PA) conveyor system of continuous intracellular transport from cell membrane to nucleus maintains EGF receptor homeostasis. *Oncotarget*. 2016 May 31;7(30):47002–17.
157. Duran JM, Campelo F, van Galen J, Sachsenheimer T, Sot J, Egorov MV, Rentero C, Enrich C, Polishchuk RS, Goñi FM, Brügger B, Wieland F, Malhotra V. Sphingomyelin organization is required for vesicle biogenesis at the Golgi complex. *The EMBO Journal*. 2012 Dec 12;31(24):4535–46.
158. Stahelin RV, Digman MA, Medkova M, Ananthanarayanan B, Melowic HR, Rafter JD, Cho W. Diacylglycerol-induced membrane targeting and activation of protein kinase Cepsilon: mechanistic differences between protein kinases Cdelta and Cepsilon. *J Biol Chem*. 2005 May 20;280(20):19784–93.
159. Barelli H, Antonny B. Lipid unsaturation and organelle dynamics. *Current Opinion in Cell Biology*. 2016 Aug 1;41:25–32.
160. Douglas DN, Pu CH, Lewis JT, Bhat R, Anwar-Mohamed A, Logan M, Lund G, Addison WR, Lehner R, Kneteman NM. Oxidative Stress Attenuates Lipid Synthesis and Increases Mitochondrial Fatty Acid Oxidation in Hepatoma Cells Infected with Hepatitis C Virus. *Journal of Biological Chemistry*. 2016 Jan 22;291(4):1974–90.
161. Harayama T, Riezman H. Understanding the diversity of membrane lipid composition. *Nat Rev Mol Cell Biol*. 2018 May;19(5):281–96.
162. Galli C, Risé P. Origin of fatty acids in the body: endogenous synthesis versus dietary intakes. *European Journal of Lipid Science and Technology*. 2006;108(6):521–5.
163. Boulant S, Douglas MW, Moody L, Budkowska A, Targett-Adams P, McLauchlan J. Hepatitis C Virus Core Protein Induces Lipid Droplet Redistribution in a Microtubule- and Dynein-Dependent Manner. *Traffic*. 2008;9(8):1268–82.
164. Elgretli W, Chen T, Kronfli N, Sebastiani G. Hepatitis C Virus-Lipid Interplay: Pathogenesis and Clinical Impact. *Biomedicines*. 2023 Feb;11(2):271.
165. Piodi A, Chouteau P, Lerat H, Hézode C, Pawlowsky JM. Morphological changes in intracellular lipid droplets induced by different hepatitis C virus genotype core sequences and relationship with steatosis. *Hepatology*. 2008;48(1):16–27.
166. Herker E, Harris C, Hernandez C, Carpentier A, Kaehlcke K, Rosenberg AR, Jr RVF, Ott M. Efficient Hepatitis C Virus Particle Formation Requires Diacylglycerol Acyltransferase 1 (DGAT1). *Nature Medicine*. :19.

167. Walther TC, Chung J, Jr RVF. Lipid Droplet Biogenesis. 2017;23.
168. Eichmann TO, Kumari M, Haas JT, Farese RV, Zimmermann R, Lass A, Zechner R. Studies on the Substrate and Stereo/Regioselectivity of Adipose Triglyceride Lipase, Hormone-sensitive Lipase, and Diacylglycerol-O-acyltransferases. *Journal of Biological Chemistry*. 2012 Nov;287(49):41446–57.
169. Wang H, Tai AW. Continuous de novo generation of spatially segregated hepatitis C virus replication organelles revealed by pulse-chase imaging. *Journal of Hepatology*. 2017 Jan 1;66(1):55–66.
170. Eyre NS, Fiches GN, Aloia AL, Helbig KJ, McCartney EM, McErlean CSP, Li K, Aggarwal A, Turville SG, Beard MR. Dynamic Imaging of the Hepatitis C Virus NS5A Protein during a Productive Infection. *J Virol*. 2014 Apr;88(7):3636–52.
171. Snijder EJ, Limpens RWAL, Wilde AH de, Jong AWM de, Zevenhoven-Dobbe JC, Maier HJ, Faas FFGA, Koster AJ, Bárcena M. A unifying structural and functional model of the coronavirus replication organelle: Tracking down RNA synthesis. *PLOS Biology*. 2020 Aug 6;18(6):e3000715.
172. Yue M, Hu B, Li J, Chen R, Yuan Z, Xiao H, Chang H, Jiu Y, Cai K, Ding B. Coronaviral ORF6 protein mediates inter-organelle contacts and modulates host cell lipid flux for virus production. *The EMBO Journal*. 2023 Jul 3;42(13):e112542.
173. Rehman S, Kapur N, Durgapal H, Panda SK. Subcellular localization of hepatitis E virus (HEV) replicase. *Virology*. 2008 Jan 5;370(1):77–92.
174. Liu X, Wang M, Yin X. Cellular Organelles Involved in Hepatitis E Virus Infection. *Pathogens*. 2021 Sep;10(9):1206.
175. Samsa MM, Mondotte JA, Iglesias NG, Assunção-Miranda I, Barbosa-Lima G, Poian ATD, Bozza PT, Gamarnik AV. Dengue Virus Capsid Protein Usurps Lipid Droplets for Viral Particle Formation. *PLOS Pathogens*. 2009 Oct 23;5(10):e1000632.
176. Vance DE, Trip EM, Paddon HB. Poliovirus increases phosphatidylcholine biosynthesis in HeLa cells by stimulation of the rate-limiting reaction catalyzed by CTP: phosphocholine cytidyltransferase. *Journal of Biological Chemistry*. 1980 Feb 10;255(3):1064–9.
177. Roe B, Kensicki E, Mohny R, Hall WW. Metabolomic Profile of Hepatitis C Virus-Infected Hepatocytes. Jhaveri R, editor. *PLoS ONE*. 2011 Aug 11;6(8):e23641.
178. Perera R, Riley C, Isaac G, Hopf-Jannasch AS, Moore RJ, Weitz KW, Pasa-Tolic L, Metz TO, Adamec J, Kuhn RJ. Dengue Virus Infection Perturbs Lipid Homeostasis in Infected Mosquito Cells. *PLOS Pathogens*. 2012 Mar 22;8(3):e1002584.
179. Mingorance L, Castro V, Ávila-Pérez G, Calvo G, Rodríguez MJ, Carrascosa JL, Pérez-Del-Pulgar S, Forns X, Gastaminza P. Host phosphatidic acid phosphatase lipin1 is rate limiting for functional hepatitis C virus replicase complex formation. *PLoS Pathog*. 2018 Sep;14(9):e1007284.
180. Castro V, Calvo G, Ávila-Pérez G, Dreux M, Gastaminza P. Differential Roles of Lipin1 and Lipin2 in the Hepatitis C Virus Replication Cycle. *Cells*. 2019 Nov 18;8(11):1456.

181. Pagano RE, Longmuir KJ, Martin OC, Struck DK. Metabolism and intracellular localization of a fluorescently labeled intermediate in lipid biosynthesis within cultured fibroblasts. *Journal of Cell Biology*. 1981 Feb 22;91(3):872–7.
182. Lipsky NG, Pagano RE. Intracellular translocation of fluorescent sphingolipids in cultured fibroblasts: endogenously synthesized sphingomyelin and glucocerebroside analogues pass through the Golgi apparatus en route to the plasma membrane. *Journal of Cell Biology*. 1985 Jan 1;100(1):27–34.
183. Kaffe E, Tisi A, Magkrioti C, Aidinis V, Mehal WZ, Flavell RA, Maccarrone M. Bioactive signalling lipids as drivers of chronic liver diseases. *Journal of Hepatology*. 2024 Jan 1;80(1):140–54.
184. Stith JL, Velazquez FN, Obeid LM. Advances in determining signaling mechanisms of ceramide and role in disease. *Journal of Lipid Research*. 2019 May 1;60(5):913–8.
185. Choudhary V, Golani G, Joshi AS, Cottier S, Schneider R, Prinz WA, Kozlov MM. Architecture of Lipid Droplets in Endoplasmic Reticulum Is Determined by Phospholipid Intrinsic Curvature. *Current Biology*. 2018 Mar;28(6):915-926.e9.
186. Peeters BWA, Piët ACA, Fornerod M. Generating Membrane Curvature at the Nuclear Pore: A Lipid Point of View. *Cells*. 2022 Jan 29;11(3):469.
187. Senkal CE, Salama MF, Snider AJ, Allopenna JJ, Rana NA, Koller A, Hannun YA, Obeid LM. Ceramide is metabolized to acylceramide and stored in lipid droplets. *Cell Metab*. 2017 Mar 7;25(3):686–97.
188. Li Z, Agellon LB, Allen TM, Umeda M, Jewell L, Mason A, Vance DE. The ratio of phosphatidylcholine to phosphatidylethanolamine influences membrane integrity and steatohepatitis. *Cell Metabolism*. 2006 May 1;3(5):321–31.
189. Wong MT, Chen SS. Human Choline Kinase- α Promotes Hepatitis C Virus RNA Replication through Modulation of Membranous Viral Replication Complex Formation. *J Virol*. 2016 Oct 15;90(20):9075–95.
190. Gubern A, Casas J, Barceló-Torns M, Barneda D, de la Rosa X, Masgrau R, Picatoste F, Balsinde J, Balboa MA, Claro E. Group IVA phospholipase A2 is necessary for the biogenesis of lipid droplets. *J Biol Chem*. 2008 Oct 10;283(41):27369–82.
191. Guijas C, Rodríguez JP, Rubio JM, Balboa MA, Balsinde J. Phospholipase A2 regulation of lipid droplet formation. *Biochimica et Biophysica Acta (BBA) - Molecular and Cell Biology of Lipids*. 2014 Dec 1;1841(12):1661–71.
192. Ben M'barek K, Ajjaji D, Chorlay A, Vanni S, Forêt L, Thiam AR. ER Membrane Phospholipids and Surface Tension Control Cellular Lipid Droplet Formation. *Developmental Cell*. 2017 Jun 19;41(6):591-604.e7.
193. Harayama T, Shimizu T. Roles of polyunsaturated fatty acids, from mediators to membranes. *Journal of Lipid Research*. 2020 Aug 1;61(8):1150–60.
194. Shaikh SR, Rockett BD, Carraway K. Docosahexaenoic Acid Modifies the Clustering and Size of Lipid Rafts and the Lateral Organization and Surface Expression of MHC Class I of EL4 Cells. *The Journal of Nutrition*. 2009 Sep 1;139(9):1632–9.

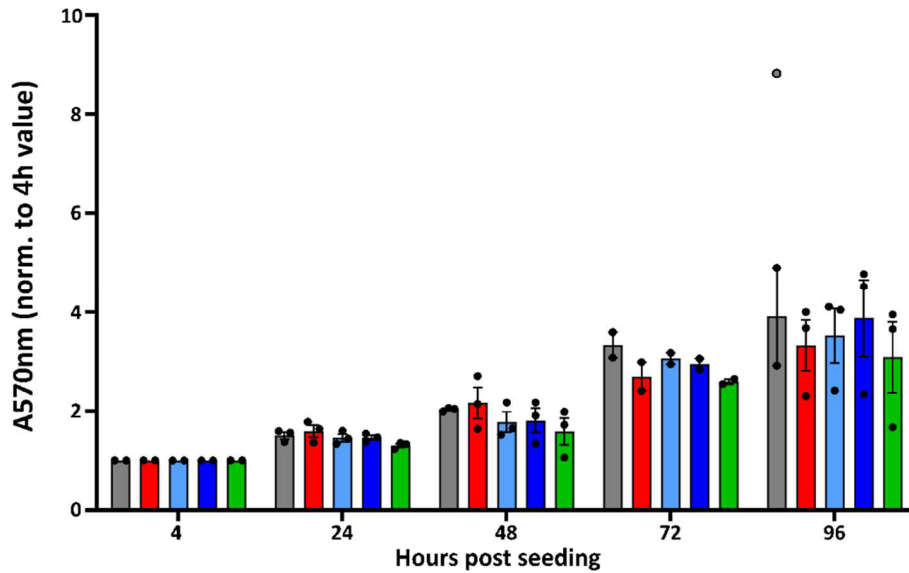
195. Rong X, Wang B, Dunham MM, Hedde PN, Wong JS, Gratton E, Young SG, Ford DA, Tontonoz P. Lpcat3-dependent production of arachidonoyl phospholipids is a key determinant of triglyceride secretion. Walther TC, editor. *eLife*. 2015 Mar 25;4:e06557.
196. Hashidate-Yoshida T, Harayama T, Hishikawa D, Morimoto R, Hamano F, Tokuoka SM, Eto M, Tamura-Nakano M, Yanobu-Takanashi R, Mukumoto Y, Kiyonari H, Okamura T, Kita Y, Shindou H, Shimizu T. Fatty acid remodeling by LPCAT3 enriches arachidonate in phospholipid membranes and regulates triglyceride transport. Cravatt B, editor. *eLife*. 2015 Apr 21;4:e06328.
197. Cao Z, Hao Y, Fung CW, Lee YY, Wang P, Li X, Xie K, Lam WJ, Qiu Y, Tang BZ, Shui G, Liu P, Qu J, Kang BH, Mak HY. Dietary fatty acids promote lipid droplet diversity through seipin enrichment in an ER subdomain. *Nat Commun*. 2019 Jul 1;10(1):2902.
198. Pinot M, Vanni S, Pagnotta S, Lacas-Gervais S, Payet LA, Ferreira T, Gautier R, Goud B, Antonny B, Barelli H. Lipid cell biology. Polyunsaturated phospholipids facilitate membrane deformation and fission by endocytic proteins. *Science*. 2014 Aug 8;345(6197):693–7.
199. Irshad Z, Dimitri F, Christian M, Zammit VA. Diacylglycerol acyltransferase 2 links glucose utilization to fatty acid oxidation in the brown adipocytes. *Journal of Lipid Research*. 2017 Jan;58(1):15–30.
200. Nettebrock NT, Bohnert M. Born this way – Biogenesis of lipid droplets from specialized ER subdomains. *Biochimica et Biophysica Acta (BBA) - Molecular and Cell Biology of Lipids*. 2020 Jan 1;1865(1):158448.
201. Kassan A, Herms A, Fernández-Vidal A, Bosch M, Schieber NL, Reddy BJN, Fajardo A, Gelabert-Baldrich M, Tebar F, Enrich C, Gross SP, Parton RG, Pol A. Acyl-CoA synthetase 3 promotes lipid droplet biogenesis in ER microdomains. *Journal of Cell Biology*. 2013 Dec 23;203(6):985–1001.
202. King C, Sengupta P, Seo AY, Lippincott-Schwartz J. ER membranes exhibit phase behavior at sites of organelle contact. *Proceedings of the National Academy of Sciences*. 2020 Mar 31;117(13):7225–35.
203. Vance JE. Inter-organelle membrane contact sites: implications for lipid metabolism. *Biol Direct*. 2020 Nov 11;15(1):24.
204. Scorrano L, De Matteis MA, Emr S, Giordano F, Hajnóczky G, Kornmann B, Lackner LL, Levine TP, Pellegrini L, Reinisch K, Rizzuto R, Simmen T, Stenmark H, Ungermann C, Schuldiner M. Coming together to define membrane contact sites. *Nature Communications*. 2019 Mar 20;10(1):1287.
205. Kassas N, Tanguy E, Thahouly T, Fouillen L, Heintz D, Chasserot-Golaz S, Bader MF, Grant NJ, Vitale N. Comparative Characterization of Phosphatidic Acid Sensors and Their Localization during Frustrated Phagocytosis. *Journal of Biological Chemistry*. 2017 Mar 10;292(10):4266–79.
206. Dadina N, Tyson J, Zheng S, Lesiak L, Schepartz A. Imaging organelle membranes in live cells at the nanoscale with lipid-based fluorescent probes. *Current Opinion in Chemical Biology*. 2021 Dec 1;65:154–62.
207. Umabayashi M, Takemoto S, Reymond L, Sundukova M, Hovius R, Bucci A, Heppenstall PA, Yokota H, Johnsson K, Riezman H. A covalently linked probe to monitor local membrane properties surrounding plasma membrane proteins. *Journal of Cell Biology*. 2022 Dec 26;222(3):e202206119.

208. Kajiwaru K, Osaki H, Greßies S, Kuwata K, Kim JH, Gensch T, Sato Y, Glorius F, Yamaguchi S, Taki M. A negative-solvatochromic fluorescent probe for visualizing intracellular distributions of fatty acid metabolites. *Nat Commun.* 2022 May 9;13(1):2533.
209. White BM, Kumar P, Conwell AN, Wu K, Baskin JM. Lipid Expansion Microscopy. *J Am Chem Soc.* 2022 Oct 12;144(40):18212–7.
210. Owen DM, Gaus K. Imaging lipid domains in cell membranes: the advent of super-resolution fluorescence microscopy. *Front Plant Sci.* 2013 Dec 12;4:503.
211. Yan S, Cui S, Ke K, Zhao B, Liu X, Yue S, Wang P. Hyperspectral Stimulated Raman Scattering Microscopy Unravels Aberrant Accumulation of Saturated Fat in Human Liver Cancer. *Anal Chem.* 2018 Jun 5;90(11):6362–6.
212. Freudiger CW, Min W, Saar BG, Lu S, Holtom GR, He C, Tsai JC, Kang JX, Xie XS. Label-Free Biomedical Imaging with High Sensitivity by Stimulated Raman Scattering Microscopy. *Science.* 2008 Dec 19;322(5909):1857–61.
213. Pietschmann T, Kaul A, Koutsoudakis G, Shavinskaya A, Kallis S, Steinmann E, Abid K, Negro F, Dreux M, Cosset FL, Bartenschlager R. Construction and characterization of infectious intragenotypic and intergenotypic hepatitis C virus chimeras. *Proceedings of the National Academy of Sciences.* 2006 May 9;103(19):7408–13.
214. Ward JC, Bowyer S, Chen S, Fernandes Campos GR, Ramirez S, Bukh J, Harris M. Insights into the unique characteristics of hepatitis C virus genotype 3 revealed by development of a robust sub-genomic DBN3a replicon. *J Gen Virol.* 2020 Nov;101(11):1182–90.
215. Krieger N, Lohmann V, Bartenschlager R. Enhancement of Hepatitis C Virus RNA Replication by Cell Culture-Adaptive Mutations. *J Virol.* 2001 May;75(10):4614–24.
216. Lohmann V, Hoffmann S, Herian U, Penin F, Bartenschlager R. Viral and Cellular Determinants of Hepatitis C Virus RNA Replication in Cell Culture. *J Virol.* 2003 Mar;77(5):3007–19.
217. Campeau E, Ruhl VE, Rodier F, Smith CL, Rahmberg BL, Fuss JO, Campisi J, Yaswen P, Cooper PK, Kaufman PD. A versatile viral system for expression and depletion of proteins in mammalian cells. *PLoS One.* 2009 Aug 6;4(8):e6529.
218. Bersuker K, Peterson CWH, To M, Sahl SJ, Savikhin V, Grossman EA, Nomura DK, Olzmann JA. A Proximity Labeling Strategy Provides Insights into the Composition and Dynamics of Lipid Droplet Proteomes. *Developmental Cell.* 2018 Jan 8;44(1):97–112.e7.
219. Dull T, Zufferey R, Kelly M, Mandel RJ, Nguyen M, Trono D, Naldini L. A Third-Generation Lentivirus Vector with a Conditional Packaging System. *J Virol.* 1998 Nov;72(11):8463–71.
220. Pietschmann T, Heinkelein M, Heldmann M, Zentgraf H, Rethwilm A, Lindemann D. Foamy virus capsids require the cognate envelope protein for particle export. *J Virol.* 1999 Apr;73(4):2613–21.
221. Haid S, Windisch MP, Bartenschlager R, Pietschmann T. Mouse-Specific Residues of Claudin-1 Limit Hepatitis C Virus Genotype 2a Infection in a Human Hepatocyte Cell Line. *Journal of Virology.* 2010 Jan 15;84(2):964–75.

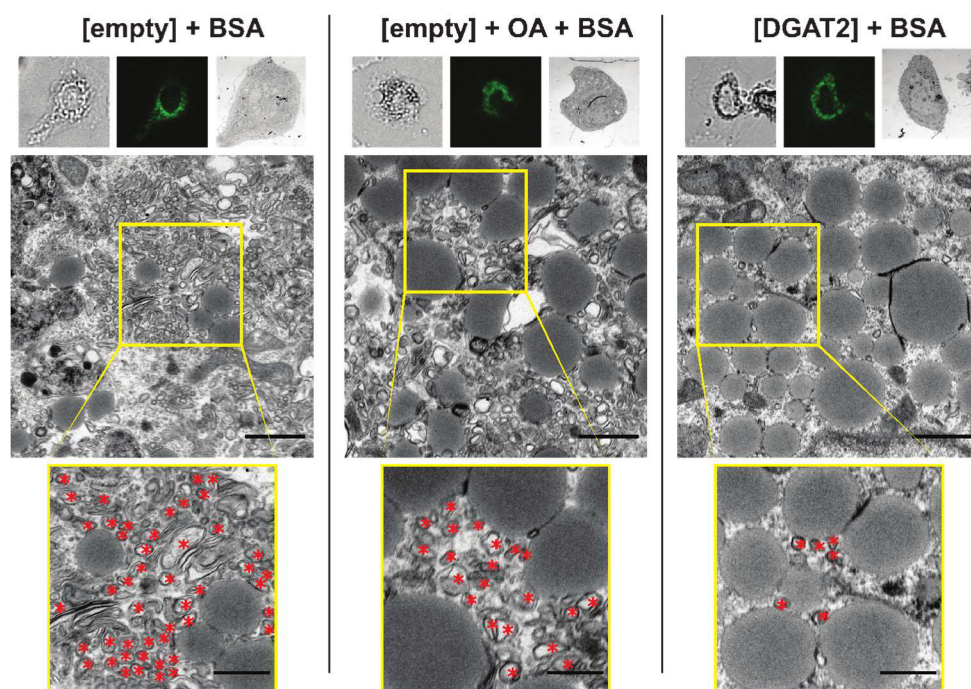
222. Zhong J, Gastaminza P, Cheng G, Kapadia S, Kato T, Burton DR, Wieland SF, Uprichard SL, Wakita T, Chisari FV. Robust hepatitis C virus infection in vitro. *Proceedings of the National Academy of Sciences*. 2005 Jun 28;102(26):9294–9.
223. Appel N, Pietschmann T, Bartenschlager R. Mutational analysis of hepatitis C virus nonstructural protein 5A: potential role of differential phosphorylation in RNA replication and identification of a genetically flexible domain. *J Virol*. 2005 Mar;79(5):3187–94.
224. Doi I. Establishment of a cell line and its clonal sublines from a patient with hepatoblastoma. *Gan*. 1976 Feb;67(1):1–10.
225. DuBridge RB, Tang P, Hsia HC, Leong PM, Miller JH, Calos MP. Analysis of mutation in human cells by using an Epstein-Barr virus shuttle system. *Mol Cell Biol*. 1987 Jan;7(1):379–87.
226. Ammerman NC, Beier-Sexton M, Azad AF. Growth and Maintenance of Vero Cell Lines. *Current Protocols in Microbiology*. 2008;11(1):A.4E.1-A.4E.7.
227. Giard DJ, Aaronson SA, Todaro GJ, Arnstein P, Kersey JH, Dosik H, Parks WP. In Vitro Cultivation of Human Tumors: Establishment of Cell Lines Derived From a Series of Solid Tumors. *JNCI: Journal of the National Cancer Institute*. 1973 Nov 1;51(5):1417–23.
228. Todt D, Friesland M, Moeller N, Praditya D, Kinast V, Brüggemann Y, Kneigendorf L, Burkard T, Steinmann J, Burm R, Verhoye L, Wahid A, Meister TL, Engelmann M, Pfankuche VM, Puff C, Vondran FWR, Baumgärtner W, Meuleman P, Behrendt P, Steinmann E. Robust hepatitis E virus infection and transcriptional response in human hepatocytes. *Proceedings of the National Academy of Sciences*. 2020 Jan 21;117(3):1731–41.
229. Schindelin J, Arganda-Carreras I, Frise E, Kaynig V, Longair M, Pietzsch T, Preibisch S, Rueden C, Saalfeld S, Schmid B, Tinevez JY, White DJ, Hartenstein V, Eliceiri K, Tomancak P, Cardona A. Fiji: an open-source platform for biological-image analysis. *Nat Methods*. 2012 Jul;9(7):676–82.
230. Carpenter AE, Jones TR, Lamprecht MR, Clarke C, Kang IH, Friman O, Guertin DA, Chang JH, Lindquist RA, Moffat J, Golland P, Sabatini DM. CellProfiler: image analysis software for identifying and quantifying cell phenotypes. *Genome Biology*. 2006 Oct 31;7(10):R100.
231. Dieckmann S, Strohmeyer A, Willershäuser M, Maurer SF, Wurst W, Marschall S, de Angelis MH, Kühn R, Worthmann A, Fuh MM, Heeren J, Köhler N, Pauling JK, Klingenspor M. Susceptibility to diet-induced obesity at thermoneutral conditions is independent of UCP1. *Am J Physiol Endocrinol Metab*. 2022 Feb 1;322(2):E85–100.
232. Su B, Bettcher LF, Hsieh WY, Hornburg D, Pearson MJ, Blomberg N, Giera M, Snyder MP, Raftery D, Bensinger SJ, Williams KJ. A DMS Shotgun Lipidomics Workflow Application to Facilitate High-Throughput, Comprehensive Lipidomics. *J Am Soc Mass Spectrom*. 2021 Nov 3;32(11):2655–63.
233. R: The R Project for Statistical Computing [Internet]. [cited 2023 May 18]. Available from: <https://www.r-project.org/>
234. Team Rs. RStudio: integrated development environment for R. RStudio. Inc, Boston, MA. 2015;14.

9. Supplementary information

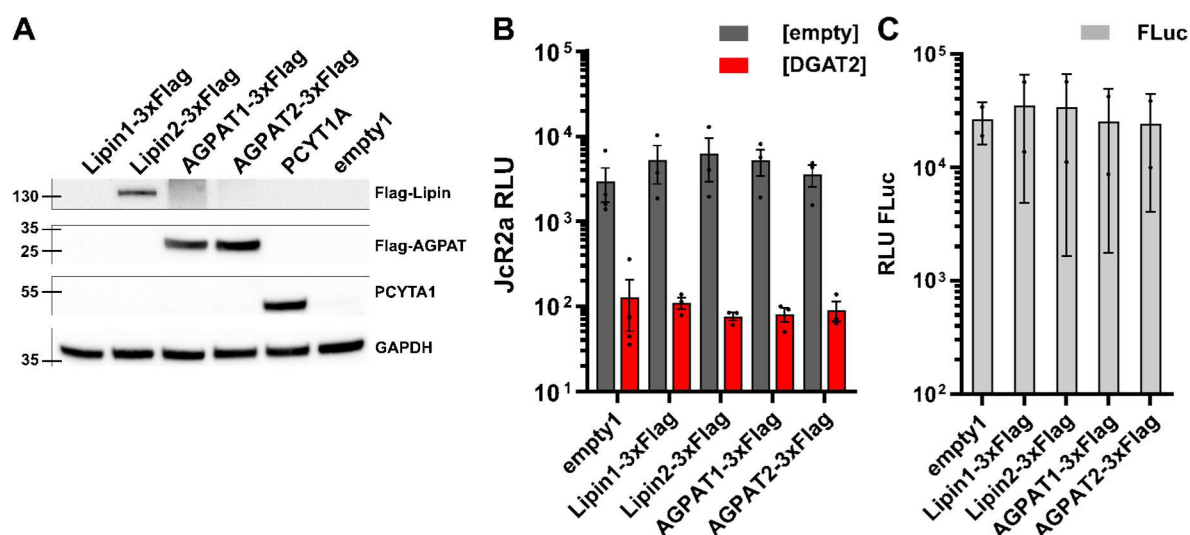
9.1. Supplementary figures



Supplementary figure 1: Cell viability of Lunet N hCD81 stably expressing DGAT constructs. Cell viability of Lunet N hCD81 [empty], [DGAT2], [DGAT2_L83A], [DGAT2_HPH161-163AAA] and [DGAT1] cells was measured by MTT assay at 4, 24, 48, 72 and 96 h post seeding. Normalized values (to 4 h post seeding) are depicted. Outlier (ROUT, Q = 1 %) is depicted in grey. Mean \pm SEM of (n = 2-3).































Supplementary figure 2: Effect of DGAT2 overexpression and oleic acid treatment on DMV formation. Stable Lunet T7 cells overexpressing [DGAT2] or [empty] vector control were transfected with the pTM expression vector encoding HCV NS3-5B/5A-eGFP. At 18 hpt, cells were treated with BSA (30 μ g) or 360 μ M oleic acid (OA) combined with BSA. Cells were fixed at 24 hpt. Transfected cells were first identified by GFP signal then fixed and further processed for correlated light electron microscopy (CLEM) analysis. The upper panel shows from left to right bright-field, fluorescent and electron microscopy overview images of a representative cell. The transmission electron microscopy (TEM) image in the middle panel is further enlarged in the yellow box area and depicted in the lower panel. Red asterisks indicate DMVs. Scale bar for middle image, 1 μ m; for magnified image, 500 nm.



Supplementary figure 3: Expression of Flag-tagged proteins of the TAG biosynthesis pathway and effect on HCV replication in control and DGAT2-expressing cells. Lunet N hCD81 [empty], [DGAT2] or /FLuc cells were transduced with lentiviruses to express Lipin1-3xFlag, Lipin2-3xFlag, AGPAT1-3xFlag, AGPAT2-3xFlag, PCYT1A, empty vector control. **(A)** Western Blot of cell lysates harvested 48 h post transduction. Protein expression was detected by anti-Flag or anti-PCYT1A antibody staining. **(B,C)** 48 h after transduction, Lunet N hCD81 [empty], [DGAT2] and FLuc cells were infected with JcR2a and cell lysates were harvested 48 hpi. RLuc values were measured to monitor HCV JcR2a replication (B) and FLuc values to monitor cell viability (C). This figure completes the data set shown in Fig. 35.

9.2. List of toxic chemicals

Name	Hazard pictogram	Hazard statements	Precautionary statements
Acetic acid		H226, H314	P210, P280, P301+330+331, P303+361+353, P305+351+338, P310
Ampicillin		H315, H317, H319, H334, H335	P261, P280, P305+351+338, P342, P311
APS		H272, H302, H315, H317, H319, H334, H335	P210, P221, P284, P305+351+338, P405, P501
Beta-mercaptoethanol		H301+H331-H310-H315-H317-H318-H373-H410	P273, P280, P302+352, P304+340 P305+351+338, P310
Bromphenolblue		H332, H302, H319	P261, P264, P280, P304, P340, P312, P301, P312, P330, P305, P351, P338, P337, P313
Carbazole		H314, H315, H413	P202, P273, P280, P308+313, P405, P501
cOmplete™ Mini Protease Inhibitor Cocktail		H315, H319	P264, P280, P302+352, P332+P313, P337+P313, P362+P364
Crystal violet		H302, H318, H351, H410	P202, P273, P280, P301+312, P305+351+338, P308+313
Cycloheximide		H300, H341, H360D, H411	P202, P264, P273, P280, P301+310, P391
Daclatasvir (BMS-790052)		H315, H319, H335	P261, P305+351+338, P302+352
DMSO		H227	P210, P280, P370, P378, P403, P235, P501
Doxycycline (hyclate)		H302, H315, H319, H335, H361fd, H412	P202, P273, P301+312, P302+352, P305+351+338, P308+313
DTT		H302, H315, H319, H335	P261, P302, 352, P305, P351, P338, P501
EDTA		H290-H314-H373	P280, P302+352, P305+351+338
EtOH		H225, H319	P210, P233, P305+351+338

Formaldehyde		H226, H302, H314, H317, H318, H331, H350, H401	P202, P210, P280, P303+361+353, P304+340+310, P305+351+338
MES monohydrate		H315, H319, H335	P261, P264, P280, P305+351+338, P308+311, P403+223, P501
Methanol		H225, H301, H311, H331, H370	P210, P270, P280, P303+361+353, P304+340, P308+311
MgSO₄		H302, H312, H332	P102, P202, P261, P64, P280
NA₂EDTA		H373	P260, P314, P501
Paraformaldehyde		H228, H302, H332, H315, H317, H318, H335, H341, H350	P210, P280, P301+312, P304+340+312, P305+351+338, P308+313
Penicillin		H317	P261, P272, P280, P302+352, P333+313, P362+364
PF-06424439 (DGAT2 inhibitor)		H301	P264, P270, P301+310, P405, P501
Polyethylenimine, branched (PEI)		H302, H317, H319, H411	P261, P273, P280, P301+312, P302+352, P305+351+338
Rotiphorese Gel 30		H302, H315, H317, H319, H340, H350, H361f, H372	P201, P280, P301+312, P302+352, P305+351+338, P308+313,
Spermidine		H314	P280, P303+361+353, P305+351+338, P310
TEMED		H225, H302, H332, H314	P210, P280, P301+330+331, P303+361+353, P305+351+338, P310
Triton® X 100		H302, H318, H411	P270, P273, P280, P305+351+338, P310

10. Acknowledgements

I would like to express my gratitude to Dr. Gabrielle Vieyres, for giving me the opportunity to work on this project and to perform my doctoral thesis under her supervision.

I would also like to thank Prof. Dr. Kay Grünewald and Prof. Dr. Caroline Barisch for the evaluation of the thesis and Dr. Pietro Scaturro and Prof. Dr. Wolfram Brune for being part of my thesis committee. In addition, I want to thank Prof. Kay Grünewald and Dr. Pietro Scaturro for their valuable insight during co-supervisor and lab-meetings. I would also like to thank all collaboration partners, with whom this work would not have been possible. In particular, I want to thank Chris Lauber and Manka Fuh for their time and support during the lipidomics data analysis and Prof. Dr. Thomas Pietschmann for his advice and supervision during the beginning of my PhD at the Twincore in Hannover. Furthermore, I want to thank Delaney, Haris, Janina, Laura, Ralf, Rodrigo, Sandro, and Tatjana for proofreading my thesis.

I also want to thank my practical student, Lina Schlaeger, for sharing my passion for viruses and lipid metabolism and for her contribution to the project. It was really amazing to work together with you and I enjoyed our literature discussions and lab memes!

I want to thank all members of the Leibniz Institute of Virology in Hamburg, and Experimental Virology group at the Twincore in Hannover, especially Dr. Yudi Zhang and Dr. Melina Winkler, for their warm welcome in the beginning of my PhD.

My heartfelt thanks go to Laura Weber and Janina Conradi, who significantly shaped my PhD-life and contributed to my well-being. Thank you so much for your support and for laughing, crying, worrying, celebrating, and bearing with me. I really enjoyed growing together as a group with you, especially after a bunch of challenging moments we experienced together. I also want to thank Katharina Remstedt who impressed me with her kind and humorous way and who often managed to temporally lift the dark clouds on rainy days.

I also want to thank my parents, my sisters, and my grandparents for their love and trust in me. Thank you so much for strengthen my back and for giving me the opportunity to pursue my goals and dreams. I also want to thank my band members who supported me with their never-ending encouragement and enabled me to fulfill one of my dreams.

Furthermore, I want to thank Sarah, Sandro, Ralf, Christoph, Lucia, Haris, my friends from Ulm, and the other mentees of the dynaMent programme, for their friendship and for fighting by my side.

I want to thank Belina and Christine for their guidance, encouragement and mentoring. Your advices were game-changers.

My last and deepest thanks go to Rodrigo Alarcon, who supported me in every possible way. Thank you for never stopping believing in me, for putting up with my scientific questions and flashes of inspiration, and for giving me confidence in foggy moments. I'm really excited for the future.

11. Declaration

I hereby declare upon oath that I have written the present dissertation independently and have not used further resources and aids than those stated in the dissertation. Results that were generated in collaboration with others are marked as such. I, the undersigned, declare that this bound copy of the dissertation and the dissertation submitted in electronic form (via the Docata upload) and the printed bound copy of the dissertation submitted to the Chemistry faculty for archiving are identical.

Ich erkläre hiermit an Eides statt, dass ich diese Arbeit selbst verfasst und keine anderen als die angegebenen Hilfsmittel benutzt habe. Ergebnisse, die in Zusammenarbeit mit anderen Personen entstanden sind, sind als solche gekennzeichnet. Die schriftliche Fassung entspricht der elektronisch eingereichten Thesis. Ich versichere, dass dieses gebundene Exemplar der Dissertation und das in elektronischer Form eingereichte Dissertationsexemplar (über den Docata-Upload) und das bei der Fakultät für Chemie (zur Archivierung eingereichte gedruckte und gebundene Exemplar der Dissertationsschrift identisch sind.

11.07.2024

Date/Datum

A handwritten signature in black ink, consisting of a stylized 'J' followed by a long horizontal stroke and a loop.

Signature/Unterschrift